P-ISSN 2525-2461 • E-ISSN 2615-9937

Vietnam Journal of Science, Technology and Engineering

JUNE 2022 • VOLUME 64 NUMBER 2

A new species of the genus Macrosemia from Vietnam

VIETNAM JOURNAL OF SCIENCE, TECHNOLOGY AND ENGINEERING * JUNE 2022 * VOLUME 64 NUMBER 2

vietnamscience.vn or vietnamscience.vjst.vn

Vietnam Journal of Science, Technology and Engineering (VJSTE) **is a quarterly double-blind peer-reviewed academic journal. VJSTE publishes research articles and review articles in all areas of science, technology and engineering with the focus on the physical sciences, life sciences and environmental sciences including the following topics:**

- **Physical Sciences**
- **Agriculture**
- **Medicine**
- **Pharmacology**
- **Biology**
- **Biotechnology**
- **Biomedical Applications**
- **Ecology**
- **Climatology**
- **Environmental Science.**

CLASSIFICATION SCHEME

1. **Mathematics and Computer Science**
   - **1.1. Mathematics**
   - **1.2. Computer Science**
   - **1.3. Computational Science**
2. **Physical Sciences**
   - **2.1. Physics**
   - **2.2. Chemistry**
   - **2.3. Engineering**
3. **Life Sciences**
   - **3.1. Agriculture**
   - **3.2. Medicine**
   - **3.3. Pharmacology**
   - **3.4. Biology**
   - **3.5. Biotechnology**
   - **3.6. Biomedical Applications**
4. **Earth Sciences**
   - **4.1. Geography**
   - **4.2. Geology**
   - **4.3. Geophysics**
   - **4.4. Oceanography**
5. **Environmental Sciences**
   - **5.1. Ecology**
   - **5.2. Climatology**
   - **5.3. Environmental Science**

CONTENTS

JUNE 2022 • VOLUME 64 NUMBER 2

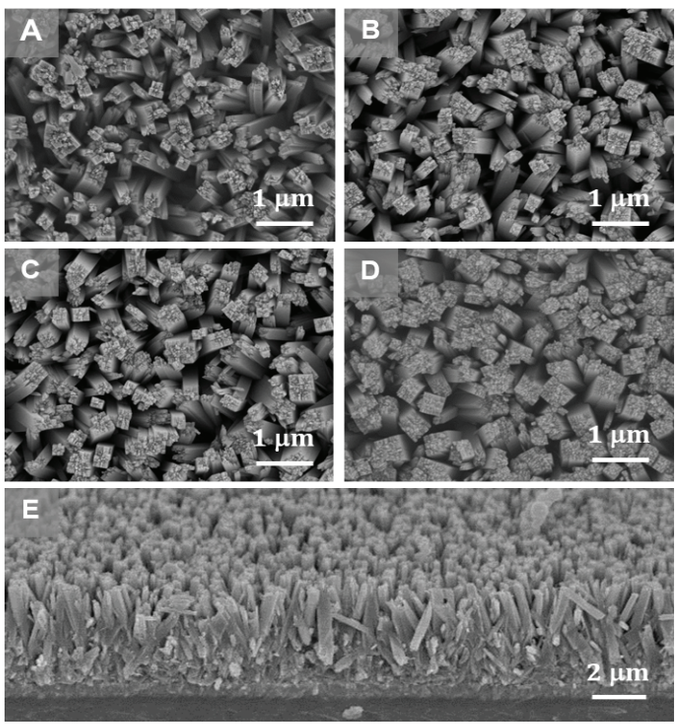

CONTENTS

JUNE 2022 • VOLUME 64 NUMBER 2

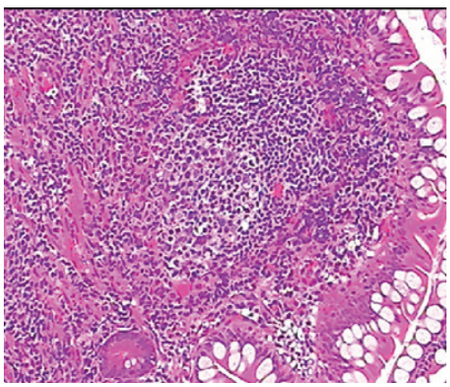

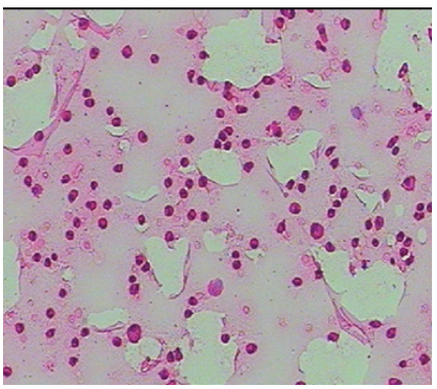

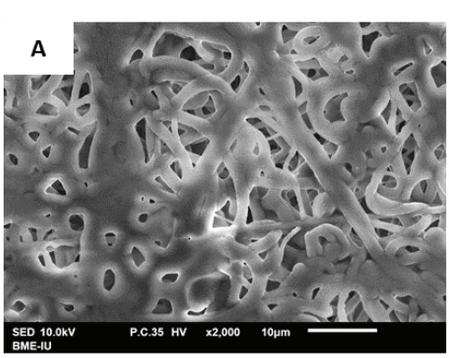

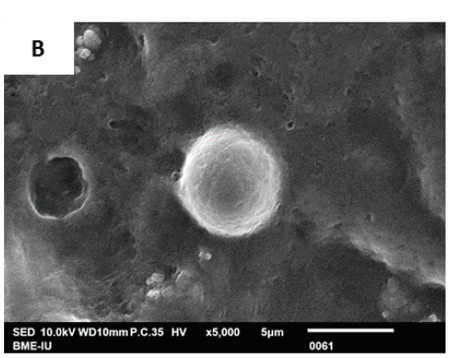

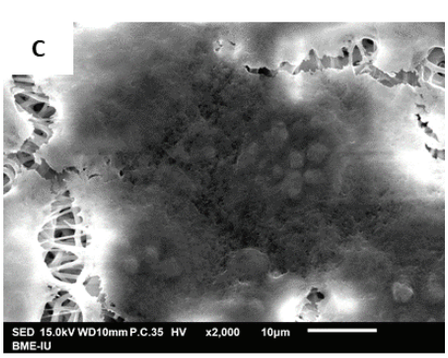

DOI: 10.31276/VJSTE.64(2).03-09

Investigation of the water states of poly(styrene sulfonic acid) grafted poly(ethylene-co-tetrafluoroethylene) copolymer using FT-IR analysis

Tran Trong Hieu Dinh[1], Hoang Hao Lam[2], Thanh Danh Tran[2], Quang Luan Le[3], Van Man Tran[2], Truc Phuong Huynh[2], Van Phuc Dinh[4], Anh Tuyen Luu[5], Kim Ngoc Pham[2], Duy Tap Tran[2*]

[1]Physics Laboratory, Le Thanh Ton High School, Ho Chi Minh City, 124 17 Street, Tan Kieng Ward, District 7, Ho Chi Minh City, Vietnam
[2]University of Science, Vietnam National University - Ho Chi Minh City, Quarter 6 Linh Trung Ward, Thu Duc City, Ho Chi Minh City, Vietnam
[3]Biotechnology Center of Ho Chi Minh City, 2374 Highway 1, Quarter 2, Trung My Tay Ward, District 12, Ho Chi Minh City, Vietnam
[4]Institute of Fundamental and Applied Sciences, Duy Tan University, 6 Tran Nhat Duat Street, Tan Dinh Ward, District 1, Ho Chi Minh City, Vietnam
[5]Center for Nuclear Technologies, Vietnam Atomic Energy Institute, 217 Nguyen Trai Street, Nguyen Cu Trinh Ward, District 1, Ho Chi Minh City, Vietnam

Received 19 April 2021; revised 15 June 2021; accepted 24 June 2021

Abstract:

The water states of poly(styrene sulfonic acid) (PSSA) grafted poly(ethylene-co-tetrafluoroethylene) copolymers (ETFE-PEMs) with grafting degree (GD)=8.8-30.5% are investigated under ambient conditions by using FT-IR analysis. Detailed analysis of the FT-IR spectra of ETFE-PEMs allows the observation of each component of water in the two broad bands of 1500-2000 cm^{-1} and 2400-3800 cm^{-1}. These components include protonated water (H_3O^+…$(H_2O)_n$), H-bonded water to sulfonic acid groups ((SO_3)…(H_3O^+)$(H_2O)_n$), H-bonded water to other water molecules ((H_2O)…(H_2O)), and non-H-bonded water (HOH…F). Of these water forms, ((SO_3)…(H_3O^+)$(H_2O)_n$) is predominantly represented. Free water (non-H-bonded water) is assumed to be trapped in the holes of the ETFE backbone and is thus difficult to remove at 50°C over a 24 h period. The total peak areas of the water molecules significantly increase with GD indicating that the ETFE-PEM with higher GD possesses higher water content. Moreover, the increase of the total peak area with GD via two steps reveals an interesting relationship between the hierarchical structures and the capacity of water content under ambient conditions. The observed water content at ambient conditions can significantly affect the conductance of ETFE-PEMs under conditions of low relative humidity such as during fuel cell operation or measurement procedures of specific characterisations or testing methods.

Keywords: **ETFE, FT-IR, pre-irradiation grafting, water states.**

Classification number: **2.1**

1. Introduction

A hydrogen fuel cell is an electrochemical device that converts energy from the chemical reaction of hydrogen fuel into electrical energy (electricity). This device exhibits several advantages such as high efficiency (60% or higher), low temperature operation (~100°C), and zero waste emission as the by-products are only heat, water, or steam when only hydrogen and air are the reactants [1]. Fuel cells are thriving in the automobile industry as this fuel source is being developed by the world's leading automobile companies such as General Motors (USA), Ford (USA), Daimler Benz (Germany), Renault (France), Toyota (Japan), Nissan (Japan), Honda (Japan), and Hyundai (Korea). Indeed, the potential of these fuel cells in life-service industries is enormous [2]. In addition to transportation, power generation, and heat applications, fuel cells are also utilised in mobile applications like mobile phones and laptops [3]. Proton exchange membranes or polymer electrolyte membranes (PEMs) are the core and most critical component of a proton exchange membrane fuel cell (PEMFC) because it acts to conduct protons from the anode to the cathode, prevents hydrogen and oxygen diffusion across the membrane, and thus is involved in energy efficiency and durability of fuel cells [4]. Currently, the most popular material used to make PEM is Nafion, but this material faces some limitations such as low proton conductivity with increasing temperature (>70°C) and decreasing relative humidity (RH) (RH <50%), high gas permeation, and high cost [5]. This has prompted scientists to find new materials to replace Nafion.

*Corresponding author: Email: tdtap@hcmus.edu.vn

Among the many new candidate materials, PSSA grafted ETFE-PEMs exhibit several advantages such as high proton conductivity, good heat resistance, good chemical stability, moderate water absorption, and high mechanical stability [6]. Thus, this graft-type PEM has been extensively investigated by our group and others [7-11]. During characterisation of PEMs for hydrogen fuel cell applications, many measurement procedures and testing methods have been realised to study the water content or water state in PEMs including ion exchange capacity (IEC), water uptake, mechanical strength, proton conductivity, thermogravimetric analysis (TGA), differential scanning calorimetry (DSC), positron annihilation spectroscopy, X-ray photoelectron spectra (XPS), etc. [12]. The amount of water absorbed in the surrounding environment can affect the subsequent water absorption when PEM is placed in an environment with higher RH or total hydration [9] and thus it is involved in the conductance of membranes under conditions of low RH [13, 14]. However, there have been no reports about this critical issue despite its importance in obtaining precise results from the abovementioned characterization methods and as the primary step toward understanding the water absorption and proton conductance mechanisms under various RH conditions and especially at very low RH.

Therefore, in this study, we report an examination of the water states of ETFE-PEMs with GD=8.8-30.5% by using FT-IR spectroscopy as this technique is very sensitive to the existence of water molecules even at a very small amount [14]. The states of water are investigated and discussed by using FT-IR analysis as a function of GD. This study provides the first insights into water states in graft-type PEMs in their ambient environment.

2. Materials and methods

2.1. Materials

ETFE films of 50-μm thickness were provided by Asahi Glass Co. Ltd., Japan. Styrene, sodium chloride, 1,2-dichloroethane, and sodium hydroxide were provided by Wako Pure Chemical Industries, Ltd., Japan. Acetone, sulfonic acid, toluene, and hydrogen peroxide were purchased from Wako Pure Chemical Industries, Ltd. All the organic chemicals were used without further purification [7, 8].

2.2. Preparation

The general procedures for preparation and an illustration of the chemical structures of ETFE and ETFE-PEM are depicted in Scheme 1. All materials, reagents, and details on the preparation of ETFE-PEMs using the pre-irradiation grafting method have been previously described [7, 8]. Briefly, the ETFE films were irradiated by gamma rays emitted from a ^{60}Co source (Japan Atomic Energy Agency in Takasaki, Japan) under argon conditions with an absorbed dose of 15 kGy and a dose rate of 15 kGy/h. The irradiated samples were then immersed in a styrene solution (in toluene solvent) with different concentrations at 60^{o}C for graft polymerization to obtain polystyrene-grafted ETFE films. The GD is determined based on the formula: GD (%) = 100*(W_g - W_0)/W_0, where W_0 and W_g are the weights of pristine ETFE and the grafted film, respectively. The grafted films were soaked in a 0.2-M chlorosulfonic acid solution in a 1,2 dichloroethane solvent at 50^{o}C for about 6 h of sulfonation to obtain ETFE-PEMs [8, 9].

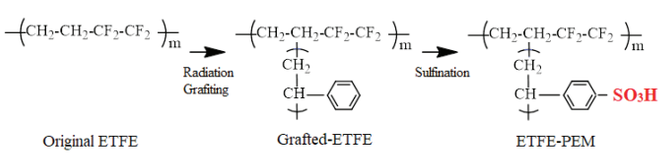

Scheme 1. Synthetic scheme and molecular structures for ETFE-PEMs using pre-irradiation grafting of styrene onto the ETFE substrate and subsequent sulfonation [9].

2.3. FT-IR measurement

The chemical structures and water states of the pristine ETFE and ETFE-PEMs were investigated by using Fourier-transform infrared (FT-IR) spectroscopy in absorption mode at the Center for Nuclear Technologies in Ho Chi Minh city, Vietnam. Before the FT-IR measurements, the ETFE-PEMs were dried in a vacuum oven at 50^{o}C for 24 h to remove the remaining water molecules inside the membranes. FT-IR spectra were recorded using a spectrometer (IRAffinity1, Shimadzu, Japan) at wavenumbers ranging from 400 to 7000 cm^{-1} over the course of 64 scans with a resolution of 4 cm^{-1} at room temperature.

3. Results and discussion

FT-IR spectra of the original ETFE and the ETFE-PEMs with GD ranging between 8.8-30.5% are shown in Fig. 1. The FT-IR spectrum of pristine ETFE was reported previously [10]. Briefly, the film is characterised by strong bands in the wavenumber range of 1000-1400 cm^{-1}, which identifies the CF_2 groups. In addition, the CH_2

asymmetric stretching vibration rises around 2974 and 2879 cm^{-1} and the sharp band at 1452 cm^{-1} is assigned to the -CH deformation [11]. After grafting and sulfonation, all the ETFE-PEMs show the similar characteristic peaks of original ETFE plus new peaks at 1492 and 1600 cm^{-1} that are ascribed to deformation of the conjugated C=C of the benzene ring. In addition, bands appeared at 756 and 698 cm^{-1}, which are assigned to CH out-of-plane vibration, and the bands found at 3020-3010 cm^{-1} are ascribed to C-H stretching [15]. These spectral features indicate that styrene was indeed grafted onto the ETFE film. Also observed are absorption bands at 840 and 607 cm^{-1} due to the stretching vibration of S=O and the two broader bands of 1500-2000 cm^{-1} and 2400-3800 cm^{-1} are due to the existence of water molecules. These peak features indicate that the grafted film was sulfonated by the introduction of the $-SO_3H$ group [15]. Also seen in Fig. 1 is the significant increase in the broad bands of 1500-2000 cm^{-1} and 2400-3800 cm^{-1} with the increase of GD, which indicates that ETFE-PEM with higher GD possesses more water content despite ambient conditions. Surprisingly, the source of the water content has not been clear until now. Indeed, the source may originate from the fact that the membranes re-absorbed water after treatment at 50°C for 24 h as described in the Experimental section and/or free waters, which are confined in the free-volume holes of the crystallite phases and/or bonded waters, which are assigned to the strong hydrogen bonding effect between sulfonic acid groups and water [11].

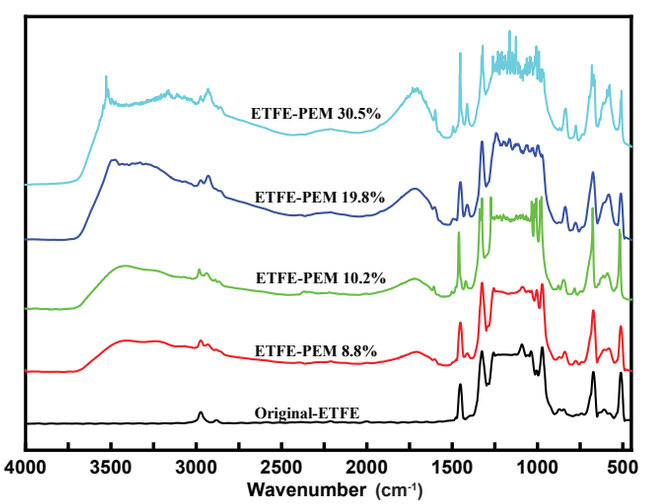

Fig. 1. FT-IR spectra of the original ETFE film and ETFE-PEMs with GD ranging between 8.8 and 30.5%.

There have been reports that water content dramatically affects several measurements of the graft-type PEMs such as XPS [15], IEC [15, 16], PALS [15], or the conductance of membranes at low RH [13]. Thus, in the following sections, we performed the analysis of FT-IR spectra in detail to explore the water states and water content in ETFE-PEMs with various GD values.

Figure 2 shows the FT-IR spectrum of ETFE-PEM (GD=10.2%) with a band at 1500-2000 cm^{-1} due to the bent oscillation of the -OH group plus a peak at 1600 cm^{-1} representing the C=C group of polystyrene grafted onto the pristine film as represented above. Thus, the spectrum is deconvoluted into four component peaks including peak1 at 1636 cm^{-1} (assigned to the -OH group's bending oscillation in $(H_2O)_n$), peak2 at 1700 cm^{-1} (attributed to the bending oscillation of the -OH group in hydronium (H_3O^+)), peak3 at 1788 cm^{-1} (representing the bending oscillation of -OH group in large protonate groups such as the ions Zundel ($H_5O_2^+$) and Eigen ($H_9O_4^+$)) [17], plus the peak at 1600 cm^{-1} of C=C. The above assignments are based on the fact that the O-H bond length in $(H_2O)_n$ is the smallest, followed by H_3O^+, and then the large protonate group. A considerable bond length leads to a small bonding force and, thus, the bending energy is enormous, which is why the large protonate group is located at the largest wavenumber [18].

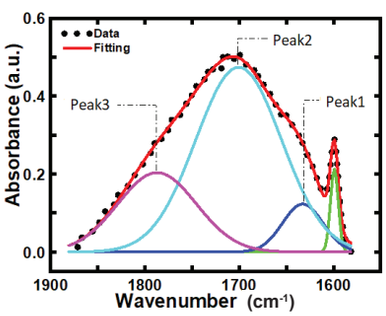

Fig. 2. A deconvolution model for FT-IR spectrum of ETFE-PEM with GD=10.2% in the spectral region of 1500-2000 cm^{-1}.

The oscillation frequency of the peaks represents the bent oscillation of the OH group so that the changes in the position of the peaks and peak intensity can be compared. Fig. 3A shows the spectrum of each component peak, and the results indicate that the peak positions of all membranes do not change with GD. However, contrary to the peak positions, the peak areas (Fig. 3B) change significantly with GD and follows the order of peak2 (H_3O^+) > peak3 ($H_5O_2^+$) > peak1 $(H_2O)_n$. Moreover, H_3O^+ is predominantly represented, which indicates that the hydrogen bonds connecting protonate and H_2O are preferred in all the ETFE-PEMs. The result can be explained by the fact that the PSSA groups can reach and elongate in free water clusters. These

free water clusters continue to participate in the group dissociation process, i.e., $-SO_3H + H_2O \rightarrow -SO_3^- + H_3O^+$ and the combines with free water $(H_2O)_n$ to create H_3O^+, $H_5O_2^+$, or larger clusters. Therefore, the content of free water $(H_2O)_n$ is small while the water component of H_3O^+, $H_5O_2^+$, and $H_9O_4^+$ increases with GD [19]. This result leads to an assumption that, under ambient conditions, the ETFE-PEMs possess water molecules that are mainly located around the PSSA groups but these amounts of water are not large enough to form water channels.

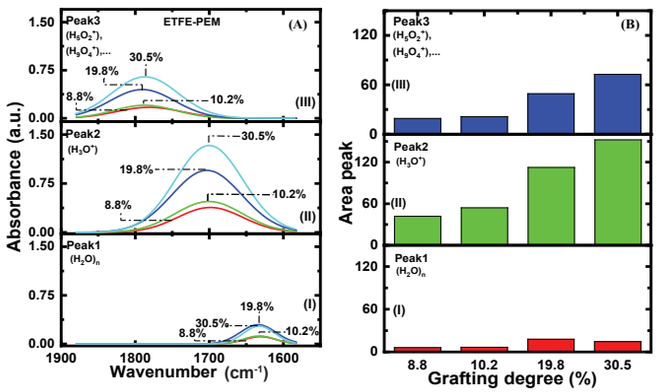

Fig. 3. FT-IR spectra of ETFE-PEMs with GD=8.8-30.5% in the band region of 1500-2000 cm^{-1} for (A) each component peak and (B) the corresponding peak area.

Figure 4 shows the FT-IR spectrum in the band region of 2400-3800 cm^{-1} of ETFE-PEM with GD=10.2%. This band represents the drag oscillation of the -OH group. In this region, water modes are classified into hydrogen-free water containing "mixture" waters located in the larger band region and a "continuum" of water possessing the hydrogen bonds that form a network located at the smaller band region [17]. Thus, the spectrum is deconvoluted into nine component peaks including five peaks relating to water molecules and four peaks representing PS grafts and pristine ETFE. Peak1 at 2669 cm^{-1} is assigned to the symmetric tensile oscillation of HO…H in the protonated water species hydronium (H_3O^+) [17, 20]. Peak2 at 3032 cm^{-1} is attributed to the tensile oscillation of the O-H bond in the protonate group that directly interacts with the $-SO_3^-$ group according to the model $(SO_3^-)…(H_3O^+)(H_2O)_n$ [21]. Peak3 at 3260 cm^{-1} is assigned to protonated water species in the form of a Zundel cation $(H_5O_2^+)$ [21]. Peak4 at 3441 cm^{-1} is attributed to O-H stretching vibrations of H-bonded water molecules to other water molecules $[(H_2O)…(H_2O)]$ and is also referred to as "bulk water" [21]. Because of the existence of the extracellular hydrogen spherical bonds HO…H in the form of a Zundel cation $(H_5O_2^+)$, peak3 is located at a position where the wavenumber is greater than peak1 and peak2 but smaller than peak4. Finally, peak5 at 2571 cm^{-1} represents the free water group, which has no hydrogen bond [20]. In the ETFE-PEMs, water molecules without hydrogen bonds can only be located in free-volume holes and only have physical interactions (HOH… F) or as surface waters [20, 22]. This water group is not affected by hydrogen bonds, so it has the highest energy and, thus, it is located at the largest wavenumber among the five water components. The above results indicate that even under dried conditions, the membranes contain water molecules in different states. It is interesting that free water (non-H-bonded water) is also trapped in the membranes.

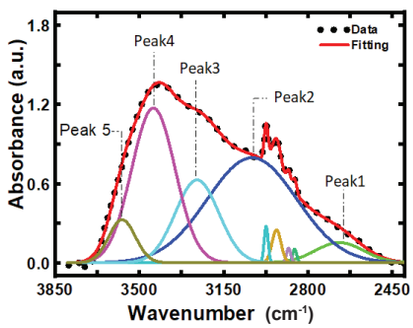

Fig. 4. A deconvolution model for the FT-IR spectrum of ETFE-PEM with GD=10.2% in the spectral region of 2400-3800 cm^{-1}.

Figure 5A shows the spectrum of each component's peak in the band region of 2400-3800 cm^{-1} and the results indicate that the peak positions of all samples are nearly unchanged with GD, which is similar to that in the spectral region of 1500-2000 cm^{-1}. Fig. 5B shows the peak area of each component peak, and the results indicate that the peak areas significantly change with GD and follow the order of peak2 $[(SO_3)…(H_3O^+)(H_2O)_n]$ > peak4 $(H_2O…H_2O)$ > peak3 $(H_5O_2^+)$ > peak1 (H_3O^+) > peak5 (HOH…F). Peak3 $(H_5O_2^+)$ is of the -OH group in the large protonate groups, which can form the Zundel $(H_5O_2^+)$ because as GD increases, the elongated PSSA chains reach local water clusters in the membrane. Simultaneously, the electrostatic binding force pulls water groups around PSSA chains, which leads to the increase of water content. As GD increases from 19.8 to 30.5%, the surrounding water content also increases. At the same time, the -OH bond in the large protonate groups is formed diverse, possibly in Zundel $(H_5O_2^+)$. Therefore, the same -OH group in large protonate groups exhibits multiple components leading to the increase of

peak area with GD [19, 22]. The water state of $((SO_3)\ldots(H_3O^+)(H_2O)_n)$ is the most dominant and located mainly around the PSSA chains, but these water amounts are not large enough to form water channels, which is entirely consistent with those in the spectral region of 2400-3800 cm^{-1}.

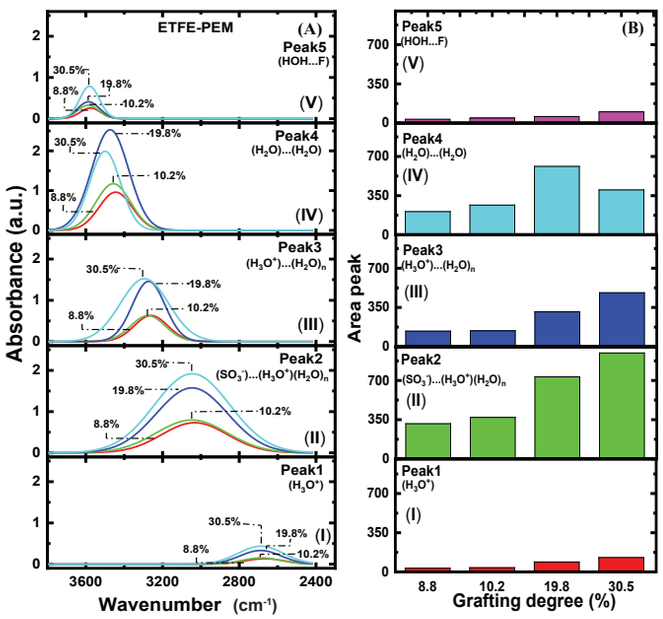

Fig. 5. FT-IR spectra of ETFE-PEMs with GD=8.8-30.5% in the band region of 2400-3800 cm^{-1} for (A) each component peak and (B) the corresponding peak area.

Figure 6 shows the total peak areas of the ETFE-PEMs with GD=8.8-30.5% in the spectral region of (A) 1500-2000 cm^{-1} and (B) 2400-3800 cm^{-1}. Interestingly, the total peak areas in both regions increase quickly and linearly with GD in the range of 8.8-19.8% and then increase more slowly as GD increases to 30.5%. In other words, the increase occurs via two steps even at ambient conditions. The increase of total peak area with GD can be explained by the fact that the membrane with higher GD possesses a higher number of $-SO_3H$ groups, thus possessing more water molecules [7]. The increase via two steps should be related to the hierarchical structure change of ETFE-PEMs, in which the lamellar period and oriented crystallite sizes (i.e., lamellar grain sizes) increased quickly in the GD of 0-19% and then more slowly with higher GD, as observed by small- and ultra-small angle X-ray scattering (SAXS/USAXS) [9]. The increase of the lamellar period and lamellar grain sizes indicate that the PSSA grafts were generated in the amorphous region of lamellar structures and/or in the regions between two lamellar grains. These newly generated graft phases can absorb water molecules as observed by SAXS/USAXS when measuring the ETFE-PEMs under dry and hydrated states [9]. Thus, the result depicted in Fig. 6 provides the first evidence that the higher-order structure change of ETFE-PEMs in the low GD range of 8.8-30.5% relates closely to their water content even at ambient conditions.

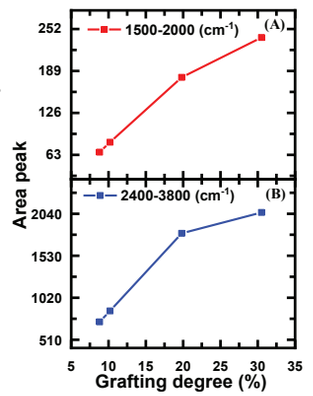

Fig. 6. The total peak area of ETFE-PEMs with GD=8.8-30.5% in the spectral region of (A) 1500-2000 cm^{-1} and (B) 2400-3800 cm^{-1}.

From the basic FT-IR analysis of ETFE-PEMs, the water states inside the membranes are classified into four types [20] including protonated water, water H-bonded to other water molecules, water H-bonded to sulfonic acid groups, and non-H-bonded water as depicted in Fig. 7. Protonated water plays an essential role in proton conductance for fuel cells since, in its hydronium form, protons are transported via a diffusion mechanism that occurs when the water content is low [19]. When the number of water molecules increases at low temperatures, water binds with H_3O^+ to form a hydrogen-bonding network such as Zundel ($H_5O_2^+$), Eigen ($H_9O_4^+$), etc., and thus are separated from the SO_3^- group and tend to diffuse through the membranes [23]. The water group, which directly interacts with the $-SO_3H$ group, results in the dissociation of hydrogen to form SO_3^- and H_3O^+ [19] and then to transport proton through the oscillations of polymer chains due to the attraction between the SO_3^- and H_3O^+ groups. The water form that does not interact with H_3O^+ but interacts through hydrogen bonds is the most important water group because they are sensitive to RH and play an important role in transporting protons across the membrane [24]. The remaining water form is the so-called free water as it may be trapped in the voids (or free-volume holes) without hydrogen or water bonds. This amount of water is not significant and does not contribute to proton conductance, nonetheless, it is difficult to remove even after drying and can also cause membrane swelling.

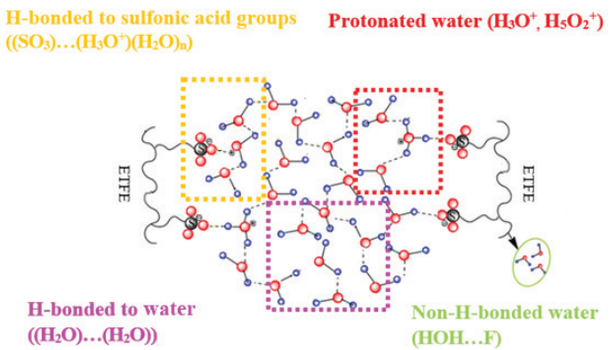

Fig. 7. A proposed model of the water states in ETFE-PEM.

4. Conclusions

Detailed analysis of the FT-IR spectra of ETFE-PEMs with GD=8.8-30.5% provides an observation of component waters in the two broader bands of 1500-2000 cm^{-1} and 2400-3800 cm^{-1} that include protonated water (H_3O^+, $H_5O_2^+$), H-bonded water to sulfonic acid groups $((SO_3)…(H_3O^+)(H_2O)_n)$, H-bonded water to other water molecules $((H_2O)…(H_2O))$, and non-H-bonded water (HOH…F) at ambient conditions in which the water form of $((SO_3)…(H_3O^+)(H_2O)_n)$ is mainly represented. The free water (non-H-bonded water) is assumed to be in the holes of the ETFE matrix and, hence, this is the most difficult water to remove under conditions of 50°C for 24 h. The total peak areas of the water molecules dramatically increase with the increase of GD indicating that the ETFE-PEM with higher GD possesses higher water content. The increase of these total peak areas with GD via two steps revealed the important relationship between the higher-order structures and the capacity for water content at ambient conditions. Note that these observed contents can have a significant effect on the conductance of ETFE-PEMs under the conditions of low relative humidity and on the results of measurements of certain characterisations or testing methods.

CRediT author statement

Tran Trong Hieu Dinh, Hoang Hao Lam, Thanh Danh Tran, Quang Luan Le: Data curation, Software, Visualisation; Van Man Tran, Truc Phuong Huynh, Van Phuc Dinh, Anh Tuyen Luu, Kim Ngoc Pham: Investigation, Writing original draft preparation, Conceptualization, Duy Tap Tran: Methodology, Supervision.

ACKNOWLEDGEMENTS

This work was funded by Vingroup Big Data Institute (VINBIGDATA), Vingroup and supported by Vingroup Innovation Foundation (VINIF) under project code VINIF.2020.DA08.

COMPETING INTERESTS

The authors declare that there is no conflict of interest regarding the publication of this article.

REFERENCES

[1] I. Staffell, D. Scamman, A.V. Abad, et al. (2019), "The role of hydrogen and fuel cells in the global energy system", *Energy & Environmental Science*, **12(2)**, pp.463-491, DOI: 10.1039/C8EE01157E.

[2] G. Frenette, D. Forthoffer (2009), "Economic & commercial viability of hydrogen fuel cell vehicles from an automotive manufacturer perspective", *International Journal of Hydrogen Energy*, **34(9)**, pp.3578-3588, DOI: 10.1016/j.ijhydene.2009.02.072.

[3] J. Garche, L. Jurissen (2015), "Applications of fuel cell technology: Status and perspectives", *The Electrochemical Society Interface*, **24(2)**, pp.39-43, DOI 10.1149/2.F02152if.

[4] B. Tylkowski, J.W. Kulikowska, J. Wolska, et al. (2017), "Polymers application in proton exchange membranes for fuel cells (PEMFCs)", *Physical Sciences Reviews*, **2(8)**, pp.293-348, DOI: 10.1515/psr-2017-0018.

[5] T. Li, J. Shen, G. Chen, et al. (2020), "Performance comparison of proton exchange membrane fuel cells with Nafion and Aquivion perfluorosulfonic acids with different equivalent weights as the electrode binders", *ACS Omega*, **5**, pp.17628-17636, DOI: 10.1021/acsomega.0c02110.

[6] H.B. Youcef, L. Gubler, S.A. Gürsel, et al. (2009), "Novel ETFE based radiation grafted poly (styrene sulfonic acid-co-methacrylonitrile) proton conducting membranes with increased stability", *Electrochemistry Communications*, **11(5)**, pp.941-944, DOI: 10.1016/j.elecom.2009.02.047.

[7] T.D. Tap, D.D. Khiem, L.L. Nguyen, et al. (2018), "Humidity and temperature effects on mechanical properties and conductivity of graft-type polymer electrolyte membrane", *Radiation Physics and Chemistry*, **151**, pp.186-191, DOI: 10.1016/j.radphyschem.2018.06.033.

[8] T.D. Tap, S. Sawada, S. Hasegawa, et al. (2013), "Poly(ethylene-co-tetrafluoroethylene) (ETFE)-based graft-type polymer electrolyte membranes with different ion exchange capacities: Relative humidity dependence for fuel cell applications", *Journal of Membrane Science*, **447**, pp.19-25, DOI: 10.1016/j.memsci.2013.07.041.

[9] T.D. Tap, S. Sawada, S. Hasegawa, et al. (2014), "Hierarchical structure-property relationships in graft-type fluorinated polymer electrolyte membranes using small- and ultrasmall-angle X-ray scattering analysis", *Macromolecules*, **47(7)**, pp.2373-2383, DOI: 10.1021/ma500111x.

[10] J. Chen, M. Asano, Y. Maekawa, et al. (2007), "Polymer electrolyte hybrid membranes prepared by radiation grafting of p-styryltrimethoxysilane into poly (ethylene-co-tetrafluoroethylene) films", *Journal of Membrane Science*, **296(1-2)**, pp.77-82, DOI: 10.1016/j.memsci.2007.03.017.

[11] J. Chen, M. Asano, T. Yamaki, et al. (2006), "Preparation and characterisation of chemically stable polymer electrolyte membranes by radiation - induced graft copolymerisation of four monomers into ETFE films", *Journal of Membrane Science*, **269(1-2)**, pp.194-204, DOI: 10.1016/j.memsci.2005.06.035.

[12] M.M. Nasef (2014), "Radiation-grafted membranes for polymer electrolyte fuel cells: Current trends and future directions", *Chemical Reviews*, **114**, pp.12278-12329, DOI: 10.1021/cr4005499.

[13] S. Slade, S.A. Campbell, T.R. Ralph, et al. (2002), "Ionic conductivity of an extruded Nafion 1100 EW series of membranes", *Journal of The Electrochemical Society*, **149(12)**, pp.1556-1564, DOI: 10.1149/1.1517281.

[14] M. Marechal, J.L. Souquet, J. Guindet, et al. (2007), "Solvation of sulphonic acid groups in Nafion® membranes from accurate conductivity measurements", *Electrochemistry Communications*, **9(5)**, pp.1023-1028, DOI: 10.1016/j.elecom.2006.12.021.

[15] G. Qelik, M. Barsbay, O. Güven (2016), "Towards new proton exchange membrane materials with enhanced performance via RAFT polymerization", *Polymer Chemistry*, **7(3)**, pp.701-714, DOI: 10.1039/C5PY01527H.

[16] T. Hamada, S. Hasegawa, H. Fukasawa, et al. (2015), "Poly(ether ether ketone) (PEEK)-based graft-type polymer electrolyte membranes having high crystallinity for high conducting and mechanical properties under various humidified conditions", *Journal of Materials Chemistry A*, **3(42)**, pp.20983-20991, DOI: 10.1039/C5TA05567A.

[17] M. Laporta, M. Pegoraro, L. Zanderighi (1999), "Perfluorosulfonated membrane (Nafion): FT-IR study of the state of water with increasing humidity", *Physical Chemistry Chemical Physics*, **1(19)**, pp.4619-4628, DOI: 10.1039/A904460D.

[18] M. Chaplin (2009), "Theory vs experiment: What is the surface charge of water", *Water*, **1**, pp.1-28.

[19] M. Eikerling, A.A. Kornyshev, A.M. Kuznetsov, et al. (2001), "Mechanisms of proton conductance in polymer electrolyte membranes", *The Journal of Physical Chemistry B*, **105(17)**, pp.3646-3662, DOI: 10.1021/jp003182s.

[20] D.W. Hofmann, L. Kuleshova, B. D'Aguanno, et al. (2009), "Investigation of water structure in Nafion membranes by infrared spectroscopy and molecular dynamics simulation", *The Journal of Physical Chemistry B*, **113(3)**, pp.632-639, DOI: 10.1021/jp806761h.

[21] J. Kim, U.W. Schmitt, J.A. Gruetzmacher, et al. (2002), "The vibrational spectrum of the hydrated proton: Comparison of experiment, simulation, and normal mode analysis", *The Journal of Chemical Physics*, **116(2)**, pp.737-746, DOI: 10.1063/1.1423327.

[22] H. Nishiyama, S. Takamuku, K. Oshikawa, et al. (2020), "Chemical states of water molecules distributed inside a proton exchange membrane of a running fuel cell studied by operando coherent anti-stokes Raman scattering spectroscopy", *The Journal of Physical Chemistry C*, **124(18)**, pp.9703-9711, DOI: 10.1021/acs.jpcc.0c00347.

[23] H. Gao, K. Lian (2014), "Proton-conducting polymer electrolytes and their applications in solid supercapacitors: A review", *RSCAdvances*, **4(62)**, pp.33091-33113, DOI: 10.1039/C4RA05151C.

[24] K.D. Kreuer, S.J. Paddison, E. Spohr, et al. (2004), "Transport in proton conductors for fuel-cell applications: Simulations, elementary reactions, and phenomenology", *Chemical Reviews*, **104(10)**, pp.4637-4678, DOI: 10.1021/cr020715f.

DOI: 10.31276/VJSTE.64(2).10-15

Effect of *in-situ* Fe doping on the visible light photoelectrochemical activity of TiO_2 nanorods

Nam Trung Tran*, Thi Minh Huong Pham, Tan Lam Nguyen

Faculty of Natural Sciences, Quy Nhon University, 170 An Duong Vuong Street, Nguyen Van Cu Ward, Quy Nhon City, Binh Dinh Province, Vietnam

Received 5 February 2021; revised 25 April 2021; accepted 4 May 2021

Abstract:

Considering its superior photocatalytic activity and excellent chemical stability, titanium dioxide (TiO_2) is an excellent candidate for photoelectrochemical (PEC) hydrogen production. Besides, many challenges exist ahead of improving the photoresponse of TiO_2 to visible light while maintaining high photocatalytic activity. Herein, the authors report recent efforts to improve the visible light PEC activity of TiO_2 nanorods by *in-situ* doping with various iron (Fe) concentrations using a hydrothermal method. The influences of Fe doping concentrations on the morphological and structural properties of TiO_2 nanorods were investigated by using scanning electron microscopy (SEM), X-ray diffraction (XRD), and Raman spectroscopy. Furthermore, this work demonstrates that Fe doping could improve the PEC activity of TiO_2 nanorods under visible light irradiation. The authors achieve a remarkable enhancement in the photocurrent density, as high as 2.9 mA/cm^2 at an applied voltage of 0.5 V, for the sample synthesised with an Fe doping concentration of 10 mM. These results reveal that Fe-doped TiO_2 nanorods can serve as ideal materials for PEC applications.

Keywords: **Fe-doped TiO_2, hydrothermal, in-situ doping, photoelectrochemical, TiO_2 nanorods.**

Classification number: **2.1**

1. Introduction

PEC water splitting is one of the most promising and environmentally friendly approaches to providing clean and renewable energy. The process of water splitting comprises two half-cell reactions of water oxidation and proton reduction to hydrogen, which require a minimum energy of 1.23 eV to drive the reactions [1]. In a PEC system, the photoelectrode is a key component that plays an important role in capturing and converting solar energy directly to chemical energy in the form of hydrogen and oxygen. Various semiconducting materials such as TiO_2, ZnO, $BiVO_4$, Fe_2O_3… have been extensively explored as photoelectrodes for efficient PEC water splitting [2-4].

Over the few past decades, TiO_2 has become known as one of the most widely used materials for research applications related to environmental concerns and solar energy conversion. Recently, the use of a TiO_2-based photoelectrode for PEC water splitting has been considered as the superior candidate due to its strong photocatalytic activity, excellent chemical stability, and cost savings [5, 6]. However, low electron mobility, fast recombination of the photoexcited carriers, and wide band gap (~3.2 eV for anatase and ~3.0 eV for rutile phases) hampers the application of TiO_2 in photocatalytic materials [7]. Among the different strategies to overcome these drawbacks of TiO_2 photocatalysts, metal ion doping of TiO_2 is an effective strategy that improves its electronic properties, optical sensitivity, and photocatalytic activities. Existing research on metal ion doping of TiO_2 has recognised the critical role played by cation doping to extend the photoresponse of TiO_2 into the visible spectral range and to achieve more efficient photocatalytic properties. In particular, doping with metal ions tailors the energy bandgap and increases the electric conductivity of TiO_2 [8, 9]. Among metal ions such as Fe, Co, Mn, W, Ni, etc., the Fe(III) ion has attracted much attention as a dopant into the TiO_2 lattice due the similarity of their ionic radii [10]. In addition, doping with Fe can induce charge trapping levels in the energy band of TiO_2 and

*Corresponding author: Email: trannamtrung@qnu.edu.vn

promote the interfacial charge transfer process resulting in the prevention of charge carrier recombination [11]. Many approaches have been employed to dope TiO_2 nanostructures such as sol-gel methods, impregnation techniques, hydrothermal methods, or some combination of these [12, 13]. However, among these approaches, the use of hydrothermal methods have the advantage of achieving a good crystalline phase of the TiO_2 nanostructures, which is a benefit to thermal stability and photocatalytic activities.

In the present work, we report our recent efforts to understand the effects of Fe dopant concentration on TiO_2 nanorods. To achieve this, different doping concentrations of Fe were introduced into TiO_2 nanorods via an *in-situ* doping process using a hydrothermal method. The structural properties, morphologies, and optical properties of the obtained samples were characterised in detail. Moreover, the visible light PEC activities of the Fe-doped TiO_2 nanorods were investigated to evaluate the effect of Fe doping concentrations on the PEC performance of the TiO_2 nanorods.

2. Experimental design

2.1. Materials and synthesis

All chemicals were purchased from Sigma Aldrich and were used without further purification. Titanium butoxide ($C_{16}H_{36}O_4Ti$, >97%) was used as the TiO_2 precursor. Fe(III) nitrate nonahydrate ($Fe(NO_3)_3.9H_2O$, >98%) was used as the Fe source for doping the TiO_2 nanorods. The aqueous solutions were prepared using hydrochloric acid (HCl, 37%) and deionised (DI) water. Another solvent of ethanol (C_2H_5OH) was used for substrate cleaning.

Undoped TiO_2 and Fe-doped TiO_2 nanorods were prepared on fluorine-doped tin oxide (FTO) glass substrates in a Teflon-lined stainless steel autoclave using a hydrothermal method. The FTO substrates were cleaned prior to use by ultrasonication using ethanol and DI water, and subsequently dried under nitrogen gas. For the synthesis of the TiO_2 nanorods, an aqueous solution containing 0.2 ml of $C_{16}H_{36}O_4Ti$, 9 ml of HCl, and 9 ml of DI water was vigorously stirred until the solution became transparent. The mixture was then transferred to a 25-ml Teflon-lined stainless steel autoclave containing cleaned FTO substrates, followed by hydrothermal treatment at 180°C for 8 h. After the reaction was cooled down to room temperature, these samples were rinsed extensively with DI water and were dried under nitrogen gas. Finally, the samples were annealed in air at 500°C for 1 h. *In-situ* Fe-doped TiO_2 nanorods were prepared in a similar process except that certain amounts of $Fe(NO_3)_3.9H_2O$ were added into the mixed solution. The Fe dopant was used with 5, 10, and 20 mM molar concentrations, and the Fe-doped TiO_2 nanorods samples were denoted as T-Fe5, T-Fe10, and T-Fe20, respectively.

2.2. Characterisation and PEC measurement

The morphologies and structures of the synthesised samples were investigated by using SEM (Hitachi 4800) and XRD (Siemens D5000), respectively. The structural properties of the samples were investigated via micro-Raman spectroscopy using an excitation of 532 nm and a charge-coupled device detector.

A three-electrode system was assembled for the PEC measurement, which was performed in 1 M KOH electrolyte solution under simulated solar light with a 150 W xenon lamp (Newport 94021A). The reference and counter electrodes were made of Ag/AgCl and a Pt coil, respectively. Linear sweep voltammetry (LSV) and photocurrent-time scans were measured by an electrochemical analyser (DY2300 Series Potentiostat/ Bipotentiostat, Digi-Ivy).

3. Results and discussion

3.1. XRD analysis

The structure of the synthesised materials was determined by XRD. Figure 1 shows the XRD patterns of the TiO_2 and Fe-doped TiO_2 samples with different Fe doping concentrations. The TiO_2 sample possesses diffraction patterns with strong characteristic peaks at 2θ angles of 26.8, 36.4, 41.6, 54.7, 63.1, and 70.2°, which can be assigned to (110), (101), (111), (211), (002), and (112) planes of the tetragonal rutile structure of TiO_2 (JCPDS No. 88-1175). The diffraction peaks of the FTO substrate were also observed and were marked by asterisk signs. The diffraction peaks of the Fe-doped TiO_2 samples with different Fe doping concentrations were all in good accord with the rutile phase of TiO_2. Additionally, any other crystalline phase containing metallic Fe or Fe oxides could not be observed. Compared to the pristine TiO_2 sample, the peaks of the Fe-doped TiO_2 sample were slightly broader and weaker. It is worth noting that

careful analysis of the main peak (110) of the rutile phase revealed a slight shift to lower angles for the Fe-doped TiO_2 sample, as can be seen from the inset of Fig. 1. It is also observed that the higher Fe doping concentration caused a larger shift toward lower angles. These shifts can be explained by the possible substitution of Ti^{4+} by Fe^{3+} in the crystal lattice of TiO_2. Due to the fact that the radius cation of Fe^{3+} (0.64 Å) is a little larger than that of Ti^{4+} (0.61 Å) [14], this replacement of Ti^{4+} by Fe^{3+} causes an increase in *d*-spacing that consequently causes a shift of the peak position to the lower angle side. Due to the change in the *d*-spacing, the crystal lattice of net TiO_2 was deformed, which resulted in a slightly weakened and broadened XRD peaks of the Fe-doped sample [15].

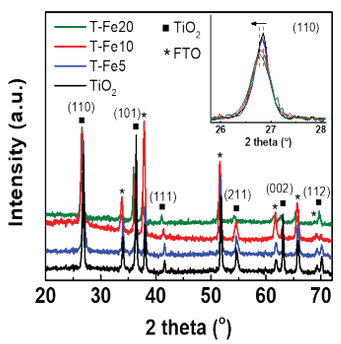

Fig. 1. XRD patterns of TiO_2 and Fe-doped TiO_2 nanorods on FTO substrates. The inset shows the peak (110) in the short range of diffraction angle.

3.2. Morphology

The morphologies and microstructures of the pristine and *in-situ* Fe-doped TiO_2 nanorod samples were investigated using SEM. Fig. 2 shows SEM images of the undoped TiO_2 nanorods and Fe-doped TiO_2 nanorods with different Fe doping concentrations. It can be seen from Fig. 2A that the nanorods uniformly formed at a relatively high density with large spaces between each nanorod. These nanorods appear in tetragonal shapes with a square base and the diameter of each nanorod was ~250 nm. A cross-sessional SEM image of the TiO_2 sample reveals that vertically aligned nanorods were uniformly grown on the FTO substrate, and the film had a thickness of ~3.5 μm (Fig. 2E). When Fe dopant was introduced into the TiO_2 nanorod via *in-situ* doping of concentrations of 5 and 10 mM, the morphology of the doped samples remained the same as shown in Fig. 2A, i.e., the nanorods maintained their tetragonal shape (Figs. 2B and 2C). However, when increasing the doping concentration to 20 mM, larger nanorods formed at a higher density and thus the space between nanorods were narrower in this sample (Fig. 2D).

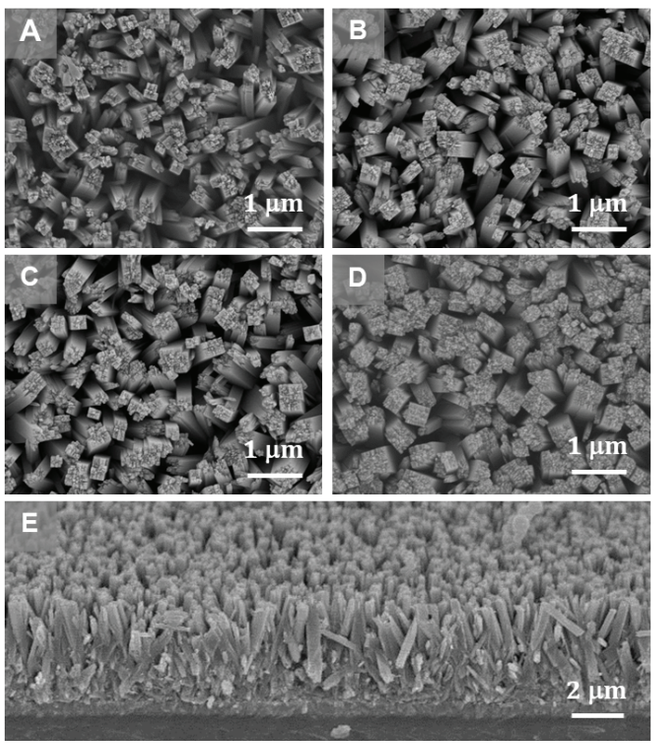

Fig. 2. SEM images of (A) undoped TiO_2 and Fe-doped TiO_2 with different doping concentrations of (B) 5, (C) 10, and (D) 20 mM; (E) cross-sessional SEM image of undoped TiO_2 nanorods.

3.3. Raman studies

To further investigate the structural properties and the effect of Fe doping on the TiO_2 nanorods, Raman spectroscopy was employed. It is well known that changes in Raman signals reflect a change of phase, bond, and/or structural defects in nanostructured materials [16, 17]. Fig. 3 shows the Raman spectra of undoped and Fe-doped TiO_2 nanorods with different Fe doping concentrations. For the pristine TiO_2 nanorod sample, three typical Raman active modes were detected near 145, 447, and 612 cm^{-1}, which were assigned to the B_{1g}, E_g, and A_{1g} vibrational modes of the rutile phase of TiO_2. Another Raman peak positioned around 240 cm^{-1} was attributed to the second-order effect (SOE) [18]. All doped samples also exhibited the four vibrational modes, and no Raman peaks related to Fe or Fe compounds were detected. In addition, the E_g mode of the doped samples slightly decreased in Raman intensity and were accompanied by a slight shift to lower

wavenumbers (red shift) as shown in the inset of Fig. 3. The red shift of the E_g mode was attributed to internal strains caused by doping the TiO_2 structure [19]. This result indicated the substitution of Ti^{4+} by Fe^{3+} within the crystal lattice of rutile TiO_2 and reconfirms the results obtained from XRD.

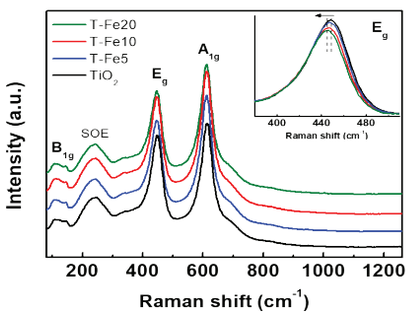

Fig. 3. Raman spectra of undoped TiO_2 and Fe-doped TiO_2 nanorods. The inset shows the Raman shift of the E_g mode in short range.

3.4. PEC performance

In order to investigate the effect of Fe doping concentration on the visible light PEC activity of the TiO_2 nanorods, photoelectrodes in the PEC cell were prepared from the synthesised samples. The working areas of all photoelectrodes were fixed at dimensions of 0.5×0.5 cm^2 by using non-conductive epoxy to cover the undesired area of the samples. LSV of the photoelectrodes was recorded under illumination of a solar light simulator to evaluate the PEC performance of the samples. Fig. 4A shows the current density-potential (J-V) curves of the undoped TiO_2 photoelectrode and Fe-doped TiO_2 photoelectrodes with different Fe doping concentrations of 5, 10, and 20 mM, hereafter referred to as the T-Fe5, T-Fe10, and T-Fe20 photoelectrodes, respectively. The PEC activity was greatly enhanced due to Fe doping into the TiO_2 nanorods. With an Fe doping concentration of 5 mM, the T-Fe5 photoelectrode showed a photocurrent density of 2.2 mA/cm^2 at an applied potential of 0.5 V, which was higher than that of the undoped TiO_2 photoelectrode (1.5 mA/cm^2 at 0.5 V) as shown in Fig. 4B. After increasing the Fe doping concentration to 10 mM, the photocurrent density of the T-Fe10 photoelectrode increased remarkably to 2.9 mA/cm^2 at 0.5 V. The photocurrent density of the T-Fe10 photoelectrode was comparable with those of previously reported metal-doped TiO_2 photoelectrodes such as Sn-doped TiO_2 nanowires (1.85 mA/cm^2 at 0 V) [20], Fe-doped bundled TiO_2 nanowires (0.88 mA/cm^2 at 0.8 V) [11], and Ta-doped TiO_2 nanorod arrays (0.67 mA/cm^2 at 1.23 V) [21]. However, the photocurrent density of the T-Fe20 photoelectrode reduced to 1.6 mA/cm^2 at 0.5 V upon Fe doping at a concentration of 20 mM. Therefore, it is evident that Fe doping concentration has a strong impact on the PEC performance of TiO_2 photoelectrodes.

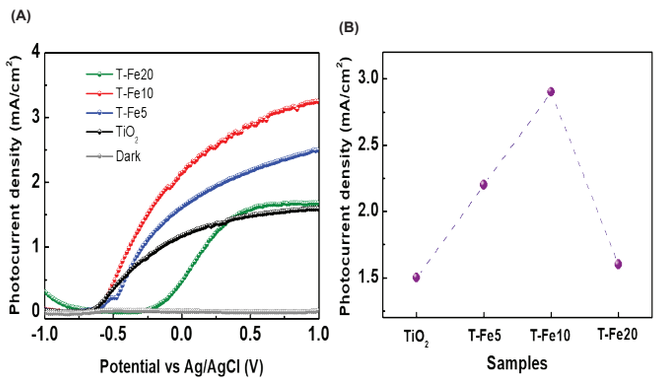

Fig. 4. (A) Photocurrent density-potential curves of undoped and Fe-doped TiO_2 nanorods with different doping concentrations; (B) Photocurrent density values of the photoelectrodes at an applied potential of 0.5 V (vs Ag/AgCl).

It is known that the PEC performance is dependent on the incident light absorption, the charge transfer and separation in the photoelectrodes, and the injection of charge from the material's surface to the electrolyte [22]. An enhancement in the PEC performance of the Fe doping photoelectrodes could be explained by considering the efficient separation and transfer of photoexcited charge. As discussed above, upon Fe doping into the TiO_2 nanorods, Ti^{4+} was substituted by Fe^{3+}. Because the energy band levels for Fe^{3+} are above the valence band level of TiO_2 (Fig. 5), Fe^{3+} can act as photogenerated hole trappers and transform into Fe^{4+} ions. Since Fe^{4+} ions are relatively unstable compared to Fe^{3+} ions, the trapped holes can be easily released from the Fe^{4+} ions and can migrate to the surface to participate in the redox reactions, which therefore enhance the PEC activity [23]. Nevertheless, Fe^{3+} may act as recombination centres for electrons and holes. Therefore, upon high doping concentration, more recombination centres are generated that compete with the redox reactions and result in a reduction of the PEC activity of the photoelectrode.

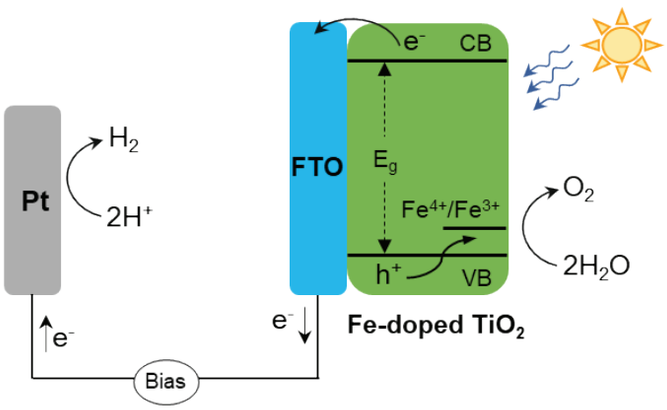

Fig. 5. Schematic of the energy level diagram for the charge transfer processes in the Fe-doped TiO_2 nanorods.

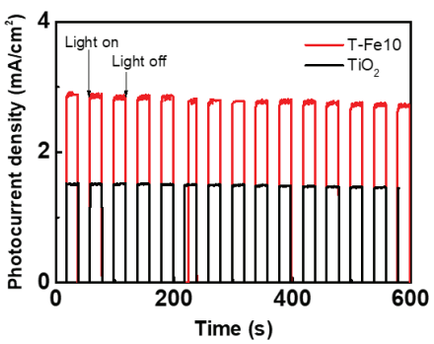

Fig. 6. Photocurrent-time scans of the undoped TiO_2 sample and Fe-doped TiO_2 sample with 10 mM Fe doping concentration (T-F10) at an applied potential of 0.5 V (vs Ag/AgCl). The duration for light on/light off is 20 s/20 s.

To evaluate the long-term stability of the PEC reaction of the Fe-doped TiO_2 nanorods, photocurrent-time (I-t) scans were recorded as shown in Fig. 6. It can be seen from the figure, these samples exhibited outstanding long-term stability. In addition, the instantaneous increase or decrease in the photocurrent at the transition from light-on to light-off indicated that the electron-hole pairs immediately generated and then separated in the TiO_2 nanorods, respectively. Thus, these results suggest effective charge separation and transfer in the TiO_2 nanorods, and a relatively long electron lifetime in the Fe-doped TiO_2 nanorods.

4. Conclusions

The *in-situ* Fe-doped TiO_2 nanorods with different Fe doping concentrations were synthesised on FTO substrates via the hydrothermal method. XRD and Raman results confirmed the success of Fe doping in which Ti^{4+} was substituted by Fe^{3+} in the crystal lattice of TiO_2. The synthesised samples showed great performance of visible light PEC activity. The Fe-doped TiO_2 nanorods with 10 mM Fe doping concentration exhibited a remarkable improvement in the photocurrent density (2.9 mA/cm^2) compared to that of the undoped TiO_2 sample (1.5 mA/cm^2). This enhanced PEC performance of the Fe-doped TiO_2 nanorod sample was ascribed to effective carrier separation and transfer due to the energy mechanism of Fe^{3+} and TiO_2. These results revealed that Fe-doped TiO_2 nanorods can serve as potential photoelectrode materials for PEC applications.

CRediT author statement

Nam Trung Tran, Thi Minh Huong Pham, Tan Lam Nguyen: Data curation, Software, Visualisation, Investigation, Writing, Methodology, Supervision.

ACKNOWLEDGEMENTS

This research is funded by Vietnam National Foundation for Science and Technology Development (NAFOSTED) under grant number 103.02-2018.329.

COMPETING INTERESTS

The authors declare that there is no conflict of interest regarding the publication of this article.

REFERENCES

[1] M.G. Walter, E.L. Warren, J.R. McKone, et al. (2010), "Solar water splitting cells", *Chemical Reviews*, **110(11)**, pp.6446-6473, DOI: 10.1021/cr1002326.

[2] K.H. Ye, H. Li, D. Huang, et al. (2019), "Enhancing photoelectrochemical water splitting by combining work function tuning and heterojunction engineering", *Nature Communications*, **10**, DOI: 10.1038/s41467-019-11586-y.

[3] L. Wang, C.Y. Lee, A. Mazare, et al. (2014), "Enhancing the water splitting efficiency of Sn-doped hematite nanoflakes by flame annealing", *Chemistry*, **20(1)**, pp.77-82, DOI: 10.1002/chem.201303427.

[4] J.S. Yoon, J.W. Lee, Y.M. Sung (2019), "Enhanced photoelectrochemical properties of Z-scheme ZnO/p-n Cu_2O PV-PEC cells", *Journal of Alloys and Compounds*, **771**, pp.869-876, DOI: 10.1016/j.jallcom.2018.09.021.

[5] J. Tian, Z. Zhao, A. Kumar, et al. (2014), "Recent progress in design, synthesis, and applications of one-dimensional TiO_2 nanostructured surface heterostructures: A review", *Chem. Soc. Rev.*, **43(20)**, pp.6920-6937, DOI: 10.1039/C4CS00180J.

[6] M. Ge, C. Cao, J. Huang, et al. (2016), "A review of one-dimensional TiO_2 nanostructured materials for environmental and energy applications", *Journal of Materials Chemistry A*, **4(18)**, pp.6772-6801, DOI: 10.1039/C5TA09323F.

[7] S. Shen, J. Chen, M. Wang, et al. (2018), "Titanium dioxide nanostructures for photoelectrochemical applications", *Progress in Materials Science*, **98**, pp.299-385, DOI: 10.1016/j.pmatsci.2018.07.006.

[8] H. Feng, M.H. Zhang, L.E. Yu (2012), "Hydrothermal synthesis and photocatalytic performance of metal-ions doped TiO_2", *Applied Catalysis A: General*, **413-414**, pp.238-244, DOI: 10.1016/j.apcata.2011.11.014.

[9] S.M. Adyani, M. Ghorbani (2018), "A comparative study of physicochemical and photocatalytic properties of visible light responsive Fe, Gd and P single and tri-doped TiO_2 nanomaterials", *Journal of Rare Earths*, **36(1)**, pp.72-85, DOI: 10.1016/j.jre.2017.06.012.

[10] J. Chen, F. Qiu, W. Xu, et al. (2015), "Recent progress in enhancing photocatalytic efficiency of TiO_2-based materials", *Applied Catalysis A: General*, **495**, pp.131-140, DOI: 10.1016/j.apcata.2015.02.013.

[11] W. Chakhari, J.B. Naceur, S.B. Taieb, et al. (2017), "Fe-doped TiO_2 nanorods with enhanced electrochemical properties as efficient photoanode materials", *Journal of Alloys and Compounds*, **708**, pp.862-870, DOI: 10.1016/j.jallcom.2016.12.181.

[12] N. Nithya, G. Bhoopathi, G. Magesh, et al. (2018), "Neodymium doped TiO_2 nanoparticles by sol-gel method for antibacterial and photocatalytic activity", *Materials Science in Semiconductor Processing*, **83**, pp.70-82, DOI: 10.1016/j.mssp.2018.04.011.

[13] J.A. Navlo, G. Colón, M. Trillas, et al. (1998), "Heterogeneous photocatalytic reactions of nitrite oxidation and Cr(VI) reduction on iron-doped titania prepared by the wet impregnation method", *Applied Catalysis B: Environmental*, **16(2)**, pp.187-196, DOI: 10.1016/S0926-3373(97)00073-8.

[14] R.D. Shannon (1976), "Revised effective ionic radii and systematic studies of interatomic distances in halides and chalcogenides", *Acta Crystallographica Section A*, **32(5)**, pp.751-767, DOI: 10.1107/S0567739476001551.

[15] J. Zhu, F. Chen, J. Zhang, et al. (2006), "Fe^{3+}-TiO_2 photocatalysts prepared by combining sol-gel method with hydrothermal treatment and their characterization", *Journal of Photochemistry and Photobiology A: Chemistry*, **180(1)**, pp.196-204, DOI: 10.1016/j.jphotochem.2005.10.017.

[16] Alamgir, W. Khan, S. Ahmad, et al. (2014), "Structural phase analysis, band gap tuning and fluorescence properties of Co doped TiO_2 nanoparticles", *Optical Materials*, **38**, pp.278-285, DOI: 10.1016/j.optmat.2014.10.054.

[17] D. Komaraiah, E. Radha, N. Kalarikkal, et al. (2019), "Structural, optical and photoluminescence studies of sol-gel synthesized pure and iron doped TiO_2 photocatalysts", *Ceramics International*, **45(18)**, pp.25060-25068, DOI: 10.1016/j.ceramint.2019.03.170.

[18] V. Swamy, B.C. Muddle, Q. Dai (2006), "Size-dependent modifications of the Raman spectrum of rutile TiO_2", *Applied Physics Letters*, **89(16)**, DOI: 10.1063/1.2364123.

[19] Y. Zhang, C.X. Harris, P. Wallenmeyer, et al. (2013), "Asymmetric lattice vibrational characteristics of rutile TiO_2 as revealed by laser power dependent Raman spectroscopy", *The Journal of Physical Chemistry C*, **117(45)**, pp.24015-24022, DOI: 10.1021/jp406948e.

[20] M. Xu, P. Da, H. Wu, et al. (2012), "Controlled Sn-doping in TiO_2 nanowire photoanodes with enhanced photoelectrochemical conversion", *Nano Letters*, **12(3)**, pp.1503-1508, DOI: 10.1021/nl2042968.

[21] S. He, Y. Meng, Y. Cao, et al. (2018), "Hierarchical Ta-doped TiO_2 nanorod arrays with improved charge separation for photoelectrochemical water oxidation under FTO side illumination", *Nanomaterials (Basel, Switzerland)*, **8(12)**, DOI: 10.3390/nano8120983.

[22] G. Wang, X. Xiao, W. Li, et al. (2015), "Significantly enhanced visible light photoelectrochemical activity in TiO_2 nanowire arrays by nitrogen implantation", *Nano Letters*, **15(7)**, pp.4692-4698, DOI: 10.1021/acs.nanolett.5b01547.

[23] J. Zhu, W. Zheng, B. He, et al. (2004), "Characterisation of Fe-TiO_2 photocatalysts synthesised by hydrothermal method and their photocatalytic reactivity for photodegradation of XRG dye diluted in water", *Journal of Molecular Catalysis A: Chemical*, **216(1)**, pp.35-43, DOI: 10.1016/j.molcata.2004.01.008.

DOI: 10.31276/VJSTE.64(2).16-20

The development of HPLC dual wavelength fluorescence detection method for the simultaneous determination of four fluoroquinolones in human plasma

Diep Thi Minh Nguyen, Tuan Anh Vu, Dien Xuan Luong, Truong Xuan Nguyen*

School of Chemical Engineering, Hanoi University of Science and Technology,
1 Dai Co Viet Street, Bach Khoa Ward, Hai Ba Trung District, Hanoi, Vietnamese

Received 31 May 2021; revised 10 July 2021; accepted 20 July 2021

Abstract:

A high-performance liquid chromatography-fluorescence detection (HPLC-FLD) method for determination of the fluoroquinolones norfloxacin (NOR), ciprofloxacin (CIP), levofloxacin (LEVO), and moxifloxacin (MOXI) in human plasma has been successfully developed. The detection was optimized with a dual wavelength excitation and emission fluorescence detector. Analytical wavelengths of $\lambda_{ex}/\lambda_{em}$ = 290/500 nm (for LEVO and MOXI) and $\lambda_{ex}/\lambda_{em}$ = 280/445 nm (for NOR and CIP) were found when measuring fluoroquinolones in the mixture. The plasma sample was pre-treated during the deproteinization step using methanol. This method was validated by linearity in the ranges of 0.05-15; 0.05-10; 0.05-15; and 0.10-10 µg ml^{-1} with limits of detection of 0.0071; 0.0080; 0.0074; and 0.0171 µg ml^{-1} for NOR, CIP, LEVO, and MOXI, respectively. Further, the HPLC-FLD method was proven to be precise and accurate with relative standard deviations lower than 6% and recoveries ranging from 92.5-105.4% for all four fluoroquinolones. Therefore, the proposed HPLC-FLD method provides an alternative approach for the simultaneous analysis of fluoroquinolones in plasma.

Keywords: **dual wavelength excitation and emission, fluoroquinolones, HPLC-FLD, plasma.**

Classification number: **2.1**

1. Introduction

Fluoroquinolones (FQs) are an important and effective class of antibacterial agents. Indeed, FQs have broad-spectrum antibacterial activity, long elimination half-lives, and good tissue penetration. To improve bactericidal activity and pharmacological properties, numerous fluoroquinolones have been developed. Currently, they are classified as second-, third-, and fourth-generation quinolones and are indicated for treatment of a large variety of infections such as respiratory, gastrointestinal, and gynaecologic, as well as sexually transmitted diseases, prostatitis, and infections of the skin, soft tissue, bone, and joints [1-3].

The appropriate use of these fluoroquinolones is an important issue that remains a difficult challenge. One approach is to continuously monitor pharmacokinetic behaviour and activity of an antibiotic in changing therapeutic environments in order to select the optimal agent, its dose, and duration of treatment so that therapeutic failure and/or the development of antibacterial resistance can be avoided [4, 5]. On the other hand, it has been thought the administration of a combination of FQs may result in a superior therapeutic outcome than that of an individual FQ. To verify this, HPLC with fluorescence detection (FLD), one the most sensitive methods for the determination of fluoroquinolones in plasma, is employed [6-8]. It is common in HPLC-FLD to fix the excitation and emission wavelengths. For example, the detection of norfloxacin, ciprofloxacin, levofloxacin, or moxifloxacin is shown in Table 1. In a similar manner, the simultaneous detection of two FQs: ciprofloxacin and moxifloxacin [9], and levofloxacin and moxifloxacin [10], or three FQs: pazufloxacin, ciprofloxacin, and levofloxacin [11], and levofloxacin, gatifloxacin, and moxifloxacin [12], or even five FQs: levofloxacin, pazufloxacin, gatifloxacin, moxifloxacin, and trovafloxacin [13] have been reported. However, the sensitivity of this method was high for certain FQs but low for others. To solve this problem, A.E. Mansilla, et al. (2005) [14] developed photo-induced fluorimetric detection and multi-emission scanning,

*Corresponding author: Email: truong.nguyenxuan@hust.edu.vn

Table 1. Fluoroquinolones determination in plasma by HPLC-FLD.

Analysed compound	Sample preparation	Mobile phase	Ex/Em wavelength	LOD/LOQ µg ml^{-1}	References
NOR	PP with acetonitrile	0.015 mol l^{-1} sodium heptanesulfonate, 0.2% triethylamine and phosphoric acid (pH 2.5)-acetonitrile-methanol 70:15:15 (v/v/v)	268/445	LOD 0.0059 LOQ 0.0195	[16]
CIP	PP with acetonitrile	phosphoric acid (0.025M)/ methanol/acetonitrile (75/13/12%, v/v/v); pH was adjusted to 3.0 by triethylamine	278/450	LOD 0.010 LLOQ 0.020	[17]
LEVO	PP with acetonitrile	acetonitrile and 0.4% triethylamine (pH 3.0) 24:76 (v/v); pH was adjusted to 3.0 by 85% phosphoric acid	295/490	LOD 0.030 LLOQ 0.150	[18]
MOXI	filtration using 0.2 µm syringe filter	acetonitrile and 0.25 mol l^{-1} Na_3PO_4 (pH 3.0) 5:95 (v/v); pH was adjusted by phosphoric acid	290/500	LOD 0.001 LOQ 0.003	[19]

PP: protein precipitation; LOD: limit of detection; LOQ: limit of quantification; LLOQ: lower limit of quantification.

which was adequate for the simultaneous determination of the four fluoroquinolones due to fixed excitation at 277 nm. As another solution, a fluorescence detector developed by J.D. Smet, et al. (2009) [15] was programmed to turn the initial excitation/emission wavelengths of 290/500 nm (for ofloxacin, moxifloxacin, sarafloxacin) into those of 279/442 nm (ciprofloxacin) between 5.8 and 8.5 min. However, this method was only suitable for FQs with retention times that were separated by enough time.

Therefore, the purpose of this study is to develop a simple and sensitive HPLC-FLD method for the simultaneous determination of fluoroquinolones in human plasma, which can be used as a model to probe pharmacokinetic behaviour and for therapeutic drug monitoring. The possibility of using dual wavelength excitation and emission allows the selection of appropriate excitation and emission wavelengths, which increases the sensitivity analysis for each FQ (norfloxacin, ciprofloxacin, levofloxacin, and moxifloxacin). To the best of our knowledge, this is the first report of an HPLC-FLD method using two couples of excitation and emission wavelengths for the simultaneous determination of four fluoroquinolones in human plasma.

2. Materials and methods

2.1. Chemicals and reagents

The fluoroquinolone standards norfloxacin (NOR, lot no. QT068050316, 99.5%), ciprofloxacin (CIP, lot no. QT012120318, 98.3%), levofloxacin (LEVO, lot no. QT165080417, 98.2%), and moxifloxacin (MOXI, lot no. QT187041117, 97.0%) were purchased from the Institute of Drug Quality Control, Ho Chi Minh city, Vietnam. Solvents were HPLC grade (Merck, Germany) and included methanol (MeOH), acetonitrile (ACN), and triethylamine (TEA). The ACS reagents of phosphoric acid (H_3PO_4) and hydrochloric acid (HCl) were purchased from Acros Organics (USA). Deionized (DI) water (18 MΩ cm^{-1}) was obtained with a Millipore Milli-Q water purification system.

2.2. Standard and sample preparation

Standard solutions: the 1000-µg ml^{-1} primary stock standards of each antibiotic, NOR, CIP, LEVO, and MOXI, were prepared in MeOH/0.1 M HCl 1:1 (v:v). Working standard solutions of 100 µg ml^{-1}, 10 µg ml^{-1}, and 1 µg ml^{-1} were prepared by appropriately diluting the stock solution with methanol. From these solutions, working standard mixtures from each antibiotic were prepared and stored at -20°C for 30 d.

Sample preparation: Blank plasma samples were collected from healthy, drug-free volunteers at a general clinic in Phu Tho province, Vietnam. The spiked sample was prepared by taking a known volume of a standard mixture solution, evaporating the solvent to collect the residue (temperature 40°C, N_2 gas), diluting the residue in the blank plasma, and vortexing it for 5 min to obtain a spiked sample of known concentration. The blank plasma and spiked samples were stored at -20°C for less than one month and were thawed immediately to room temperature before the assay treatment.

Plasma treatment: To 1 ml of thawed plasma, 4 ml of methanol was added to precipitate proteins, then the mixture was vortexed for 5 min and centrifuged for 20 min at 6000 rpm. The supernatant was filtered through 0.45 µm nylon filters before analysis [8].

2.3. Instrumentation

2.3.1. Fluorescent measurement

Fluorescent measurements were performed with a Nanolog spectrofluorometer (Horiba, USA) equipped with 450 W Xe arc lamp and double excitation monochromators. The excitation and emission spectra were recorded automatically during the measurements.

2.3.2. Chromatographic system

Chromatographic analysis was performed on an HPLC system equipped with a Sil-20AC XR automatic sampler, a CTO-20A thermostatic column box, and a RF-20A fluorescent detector (Shimadzu, Japan). The separation was achieved on a Supelco Ascentis C18 column (250×4.6 mm, 5 µm). The mobile phase was a mixture of 0.025 M phosphoric acid (pH 3, adjusted with TEA) aqueous solution (mobile phase A) and MeOH (mobile phase B). The following gradient program (with respect to mobile phase B) was used: 0-2.0 min, 15% B; 2.0-17.0 min, 15-35% B; 17.0-22.0 min, 35-80% B; and 22.0-25.0 min, 80% B. The flow rate was 1.0 ml min^{-1}. The injection volume was 10 µl. The column oven was maintained at 30°C (see Supplementary Information for optimization of the mobile phase and the gradient elution).

2.4. Method development

Detection: To develop a sensitive HPLC method using a dual wavelength excitation and emission fluorescence detector for the simultaneous quantification of the four FQs (NOR, CIP, LEVO and MOXI), the excitation spectrum of each antibiotic was recorded using the Nanolog spectrofluorimeter. Then, a test solution of the mixture was recorded using the HPLC-FLD system at two selected couples of excitation and emission wavelengths.

2.5. Method validation

Method validation was carried out according to the ICH (International Council for Harmonisation of Technical Requirements for Pharmaceuticals for Human Use) and the AOAC (Association of Official Analytical Chemists) guidelines [20, 21]. The HPLC dual wavelength fluorescence detection method was validated for selectivity, sensitivity, linearity, precision, and accuracy.

Selectivity was assessed by examining peak interference from a blank plasma sample and a spiked sample of the mixture at a concentration of 1 µg ml^{-1} of each drug.

The limit of detection (LOD) and limit of quantification (LOQ) were determined by gradually reducing the standard mixture of each drug (0.05 µg ml^{-1}) to a blank plasma sample. LOD was obtained at a concentration in which the height of the peak signal-to-noise (S/N) was equal to 3. LOQ was accepted as LOQ = 3.3×LOD. From these LOD and LOQ values, the method detection limit (MDL) and quantification limit (MQL) values were estimated by taking a dilution factor of 5 into account during the plasma sample treatment.

Linearity: The calibration samples were prepared in blank plasma over a range of 0.05-20 µg ml^{-1} (e.g., 0.05, 0.1, 0.5, 1.0, 2.5, 5.0, 10.0, 15.0, and 20.0 µg ml^{-1}). The standard calibration curve was constructed by least squares linear regression using peak areas. The linearities of the standard curves were assessed by its intercept, slope, and correlation coefficient (R^2).

Precision and accuracy: The precision and accuracy of the method were evaluated using three quality control (QC) spiked plasma samples: 1.0, 5.0, and 10.0 µg ml^{-1}. The precision was expressed as the relative standard deviation (RSD%) of the measured QC samples in sextuplicate. The accuracy was determined as a relative error bias. The results were calculated from the calibration curves by means of the external standard method. The procedure for sample preparation was the same as described above.

3. Results and discussion

3.1. Method development

Optimization of the detection: Fig. 1 shows the emission and excitation spectra of each antibiotic. The spectra were in accordance with previous studies [9-19], and the maximum excitation wavelengths of the FQs were divided into two groups: approximately 280 nm for NOR and CIP and 290 nm for LEVO and MOXI. Moreover, the fluorescent intensity of NOR or CIP was low if the antibiotic was excited at a wavelength of 290 nm. Chromatograms of the mixture recorded with dual wavelength excitation and emission fluorescence detector are presented in Fig. 2. It was quickly realized that the detection sensitivity was significantly enhanced at the excitation of 280 nm (λ_{em}=445 nm) for NOR and CIP, while the same occurred at 290 nm for LEVO and MOXI. Hence, the dual channels of the fluorescence detector were optimized at $\lambda_{ex}/\lambda_{em}$=290/500 nm (LEVO and MOXI) and $\lambda_{ex}/\lambda_{em}$=280/445 nm (NOR and CIP) for HPLC-FLD analysis of the FQs in the mixture.

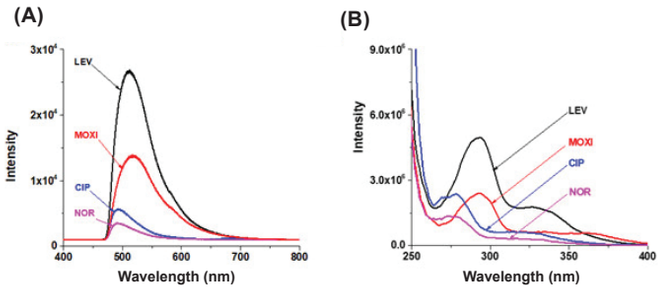

Fig. 1. (A) Emission (λ_{ex}=290 nm) and (B) excitation (λ_{em}=500 nm) spectra of each FQ at 1.0 µg ml^{-1}.

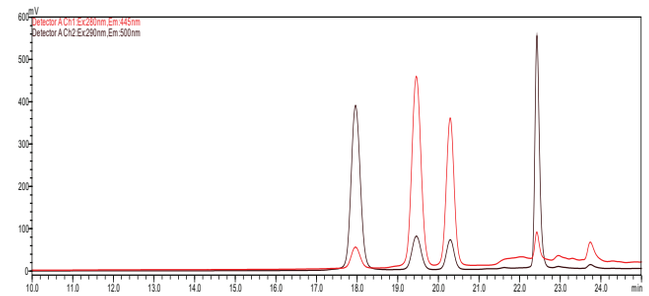

Fig. 2. Chromatograms of the FQ mixture (0.5 µg ml^{-1}) recorded with $\lambda_{ex}/\lambda_{em}$=290/500 nm (black curve) and $\lambda_{ex}/\lambda_{em}$=280/445 nm (red curve).

3.2. Method validation

Assay selectivity: Blank plasma samples were analysed and no interference was observed at the retention times of LEVO, NOR, CIP, or MOXI. Representative chromatograms of the blank plasma and spiked samples are shown in Fig. 3.

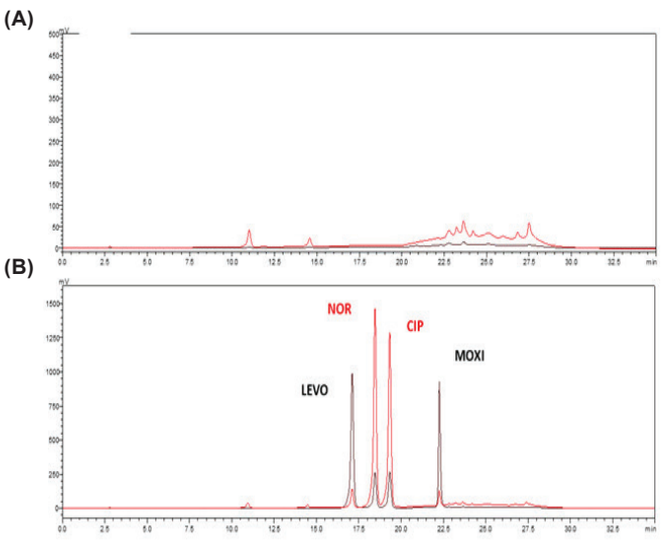

Fig. 3. Chromatograms of (A) the blank plasma sample and (B) the spiked sample (1.0 µg ml^{-1}) in plasma recorded with $\lambda_{ex}/\lambda_{em}$=290/500 nm (black curve) and $\lambda_{ex}/\lambda_{em}$=280/445 nm (red curve).

The LOD and LOQ values for the determination of the four FQs are listed in Table 2. It was found that the values for CIP determination in the simultaneous analysis by the developed method were lower than those by the reported method of which its detection ($\lambda_{ex}/\lambda_{em}$=292/525 nm) was not optimized [9]. Therefore, there is a possibility that using appropriate analytical wavelengths improved the sensitivity of the HPLC-FLD method.

Table 2. Validation parameters of the method for the analysis of fluoroquinolones in plasma.

FQs	Regression equation	R^2	Linearity (µg ml^{-1})	LOD (µg ml^{-1})	LOQ (µg ml^{-1})	MDL (µg ml^{-1})	MQL (µg ml^{-1})
NOR	$y = 1.09\times10^7x + 1.50\times10^6$	0.999	0.05-15	0.0071	0.0234	0.0355	0.1170
CIP	$y = 1.13\times10^7x + 1.40\times10^6$	0.999	0.05-10	0.0080	0.0264	0.0400	0.1320
LEVO	$y = 7.62\times10^6x + 9.70\times10^5$	0.999	0.05-15	0.0074	0.0244	0.0370	0.1220
MOXI	$y = 7.30\times10^6x + 1.25\times10^6$	0.999	0.10-10	0.0171	0.0564	0.0855	0.2820

y: peak area; x: plasma concentration of the FQ; R^2: correlation coefficient; MDL = 5×LOD; MQL = 5×LOQ.

The linearities of the four fluoroquinolones in human plasma by the proposed method were evaluated. The calibration curves were linear over the range 0.05-15 µg ml^{-1} for NOR and LEVO and 0.05-10 µg ml^{-1} for CIP and MOXI (Fig. 4). The linear regression equations with corresponding correlation coefficients of the calibration curves are indicated in Table 2.

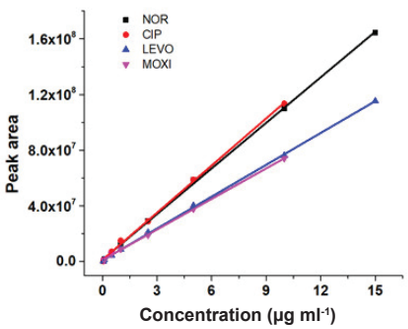

Fig. 4. Calibration curves for determination of the FQs in plasma.

Precision and accuracy: The precision and accuracy data of the analytical method are summarized in Table 3. For all four FQs, the precision was better than 6% at all three concentration levels, and the accuracies ranged from 92.5 to 105.4%. These results indicate that the proposed assay was precise and accurate.

Table 3. Precision and accuracy data of the method for the analysis of the fluoroquinolones in plasma.

FQs	Added conc. μg ml^{-1}	Found conc. μg ml^{-1}	RSD % (n=6)	Recovery % (n=6)
NOR	1.000	1.010±0.021	2.1	101.0
	5.000	5.175±0.075	1.4	103.5
	10.000	9.880±0.420	4.3	98.8
CIP	1.000	0.950±0.050	5.3	95.0
	5.000	5.040±0.072	1.4	100.8
	10.000	10.540±0.310	2.9	105.4
LEVO	1.000	1.050±0.018	1.7	105.0
	5.000	4.980±0.065	1.3	99.6
	10.000	9.965±0.171	1.7	99.7
MOXI	1.000	0.925±0.050	5.4	92.5
	5.000	4.990±0.034	0.68	99.8
	10.000	9.750±0.272	2.8	97.5

The developed method is suitable for the simultaneous determination of four FQs in human plasma because their peak plasma concentrations were in the ranges of 1.60-2.87 μg ml^{-1} for a single oral administration of norfloxacin 400 mg [22], 1.3-2.0 μg ml^{-1} for an oral administration of ciprofloxacin of 10 mg/kg every 12 h in children with severe malnutrition, 2.8 and 5.2 μg ml^{-1} for 250 and 500 mg oral administration of levofloxacin, respectively [23], and 2.60-3.79 μg ml^{-1} for 400 mg oral administration of moxifloxacin [24].

4. Conclusions

The developed and validated HPLC-FLD method is readily available for the simultaneous determination of the fluoroquinolones norfloxacin, ciprofloxacin, levofloxacin, and moxifloxacin in human plasma. The possibility of using a dual wavelength excitation and emission fluorescence detector avoids the reduced sensitivity of certain FQs in the mixture as detected by other methods. This proposed method enables simple and sensitive quantification of representative fluoroquinolones (second-, third-, and fourth-generation quinolones) in a range from 0.05 to 10 (15) μg ml^{-1} with acceptable precision and accuracy. Although the applicability of the proposed method for analysing real samples requires further investigation, this work contributes an alternative HPLC-FLD approach for therapeutic drug monitoring and pharmacokinetic study.

CRediT author statement

Diep Thi Minh Nguyen , Tuan Anh Vu, Dien Xuan Luong, Truong Xuan Nguyen: Data curation, Software, Visualisation, Investigation, Writing, Methodology, Supervision.

COMPETING INTERESTS

The authors declare that there is no conflict of interest regarding the publication of this article.

REFERENCES

[1] V.T. Andriole (2005), "The Quinolones: Past, present, and future", *Clinical Infectious Diseases*, **41(2)**, pp.113-119, DOI: 10.1086/428051.

[2] PC. Sharma, A. Jain, S. Jain (2009), "Fluoroquinolone antibacterials: A review on chemistry, microbiology and therapeutic prospects", *Acta Poloniae Pharmaceutica*, **66(6)**, pp.587-604.

[3] C. Oliphant, G.M. Green (2002), "Quinolones: A comprehensive review", *American Family Physician*, **65**, pp.455-464.

[4] A.M. Emmerson, A.M. Jones (2003), "The quinolones: Decades of development and use", *Journal of Antimicrobial Chemotherapy*, **51(1)**, pp.13-20, DOI: 10.1093/jac/dkg2083.

[5] W.M. Scheld (2003), "Maintaining fluoroquinolone class efficacy: Review of influencing factors", *Emerging Infectious Diseases*, **9(1)**, pp.1-9, DOI: 10.3201/eid0901.020277.

[6] H. Liang, M.B. Kays, K.M. Sowinski (2002), "Trovafloxacin and cinoxacin by high-performance liquid chromatography: Application to levofloxacin determination in human plasma", *Journal of Chromatography B*, **772(1)**, pp.53-63, DOI: 10.1016/s1570-0232(02)00046-6.

[7] J. Sousa, G. Alves, A. Fortuna, et al. (2012), "Analytical methods for determination of new fluoroquinolones in biological matrices and pharmaceutical formulations by liquid chromatography: A review", *Analytical and Bioanalytical Chemistry*, **403**, pp.93-129, DOI: 10.1007/s00216-011-5706-8.

[8] A. Czyrski (2017), "Analytical methods for determining third and fourth generation fluoroquinolones: A review", *Chromatographia*, **80**, pp.181-200, DOI: 10.1007/s10337-016-3224-8.

[9] N.C. Rocha, I.C. Alvarado, L.V. Cabrera, et al. (2014), "HPLC method for the simultaneous analysis of fluoroquinolones and oxazolidinones in plasma", *Journal of Chromatographic Science*, **52(10)**, pp.1281-1287, DOI: 10.1093/chromsci/bmu002.

[10] S. Schulte, T. Ackermann, N. Bertram, et al. (2006), "Determination of the newer quinolones levofloxacin and moxifloxacin in plasma by high-performance liquid chromatography with fluorescence detection", *Journal of Chromatographic Science*, **44(4)**, pp.205-208, DOI: 10.1093/chromsci/44.4.205.

[11] S. Watabe, Y. Yokoyama, K. Nakazawa, et al. (2010), "Simultaneous measurement of pazufloxacin, ciprofloxacin, and levofloxacin in human serum by high-performance liquid chromatography with fluorescence detection", *Journal of Chromatography B*, **878(19)**, pp.1555-1561, DOI: 10.1016/j.jchromb.2010.04.012.

[12] J. Grellet, J. Grellet, B.B. Ba, et al. (2004), "Simultaneous determination of levofloxacin, gati- floxacin and moxifloxacin in serum by liquid chromatography with column switching", *Journal of Chromatography B*, **810(1)**, pp.77-83, DOI: 10.1016/j.jchromb.2004.07.019.

[13] J. Sousa, G. Alves, G. Campos, et al. (2013), "First liquid chromatography method for the simultaneous determination of levofloxacin, pazufloxacin, gatifloxacin, moxifloxacin and trovafloxacin in human plasma", *Journal of Chromatography B*, **930(1)**, pp.104-111, DOI: 10.1016/j.jchromb.2013.04.036.

[14] A.E. Mansilla, A.M.D.L. Peña, D.G. Gómez, et al. (2005), "HPLC determination of enoxacin, ciprofloxacin, norfloxacin and ofloxacin with photoinduced fluorimetric (PIF) detection and multiemission scanning", *Journal of Chromatography B*, **882(1-2)**, pp.185-193, DOI: 10.1016/j.jchromb.2005.05.045.

[15] J.D. Smet, K. Boussery, K. Colpaert, et al. (2009), "Pharmacokinetics of fluoroquinolones in critical care patients: A bio-analytical HPLC method for the simultaneous quantification of ofloxacin, ciprofloxacin and moxifloxacin in human plasma", *Journal of Chromatography B*, **877(10)**, pp.961-967, DOI: 10.1016/j.jchromb.2009.02.039.

[16] T. Galaon, S. Udrescu, I. Sora, et al. (2006), "High-throughput liquid-chromatography method with fluorescence detection for reciprocal determination of furosemide or norfloxacin in human plasma", *Biomedical Chromatography*, **21(1)**, DOI: 10.1002/bmc.715.

[17] S.N. Muchohi, N. Thuo, J. Karisa, et al. (2011), "Determination of ciprofloxacin in human plasma using high-performance liquid chromatography coupled with fluorescence detection: Application to a population pharmacokinetics study in children with severe malnutrition", *Journal of Chromatography B*, **879(2)**, pp.146-152, DOI: 10.1016/j.jchromb.2010.11.032.

[18] A. Czyrski, E. Szalek (2016), "An HPLC method for levofloxacin determination and its application in biomedical analysis", *Journal of Analytical Chemistry*, **71**, pp.840-843, DOI: 10.1134/S1061934816080049.

[19] A.L. Djurdjevic, M.J. Stankov, P. Djurdjević (2006), "Optimization and validation of the direct HPLC method for the determination of moxifloxacin in plasma", *Journal of Chromatography B*, **844(1)**, pp.104-111, DOI: 10.1016/j.jchromb.2006.07.001.

[20] J. Szpylka, N. Thiex, B. Acevedo, et al. (2019), "Standard method performance requirements (SM- PRs®) 2018.001: Sugars in animal feed, pet food, and human food", *Journal of AOAC International*, **101(4)**, pp.1280-1282, DOI: 10.5740/jaoacint.SMPR2018.001.

[21] AOAC (2016), *Guidelines for Standard Method Performance Requirements*, https://www.aoac.org/wp-content/uploads/2019/08/app_f.pdf, accessed 15 January 2021.

[22] S.D. Seth, A. Beotra, S. Seth (1995), "Comparative bioavailability of two brands of norfloxacin", *Journal Association Physicians India*, **43(5)**, pp.324-326.

[23] D.N. Fish, A.T. Chow (1997), "The clinical pharmacokinetics of levofloxacin", *Clinical Pharmacokinetics*, **32**, pp.101-119, DOI: 10.2165/00003088-199732020-00002.

[24] Y.H. Xu, D. Li, X.Y. Liu, et al. (2010), "High performance liquid chromatography assay with ultraviolet detection for moxifloxacin: Validation and application to a pharmacokinetic study in chinese volunteers", *Journal of Chromatography B*, **878(32)**, pp.3437-3441, DOI: 10.1016/j.jchromb.2010.10.024.

DOI: 10.31276/VJSTE.64(2).21-27

Synthesis of acetamides bearing 3-aryl-3,4-dihydroquinazolin-4-one and 2-thioxothiazolidin-4-one moieties as novel derivatives

Tien Cong Nguyen[1*], Duc Dung Pham[1], Thi Minh Dinh Tran[2], Thi Thuy Linh Bui[3]

[1]Faculty of Chemistry, Ho Chi Minh City University of Education, 280 An Duong Vuong Street, Ward 4, District 5, Ho Chi Minh City, Vietnam
[2]Faculty of Biology, Ho Chi Minh City University of Education, 280 An Duong Vuong Street, Ward 4, District 5, Ho Chi Minh City, Vietnam
[3]Faculty of Pharmacy, Nguyen Tat Thanh University, 300A Nguyen Tat Thanh Street, Ward 13, District 4, Ho Chi Minh City, Vietnam

Received 10 September 2020; revised 12 December 2020; accepted 24 December 2020

Abstract:

In the present work, five ethyl 2-((4-oxo-3-aryl-3,4-dihydroquinazolin-2-yl)thio)acetate compounds (3a-e) were synthesized starting from anthranilic acid (1) via 2-thioxo-3-arylquinazolin-4(3H)-ones (2a-e). The reaction of (2a-e) with hydrazine hydrate to afford five 2-((4-oxo-3-aryl-3,4-dihydroquinazolin-2-yl)thio)acetohydrazide compounds (4a-e), respectively. Five new N-(4-oxo-2-thioxothiazolidin-3-yl)-2-((4-oxo-3-aryl-3,4-dihydroquinazolin-2-l)thio)acetamide compounds (5a-e) were synthesized based on the reaction of (4a-e) with thiocarbonyl-bis-thioglycolic acid and the yields of the synthesis reactions were observed to be about 58 to 72%. The chemical structure of the compounds was elucidated on the basis of IR, 1 H-NMR, 13 C-NMR and HR-MS spectral data. The reaction of anthranilic acid and appropriately substituted phenyl isothiocyanates gave five 3-aryl-2-mercaptoquinazolin-4(3H)- one compounds with good yield. In the fact, the 2a-e compounds existed in the thione form, namely 3-aryl-2-thioxo-2,3-dihydroquinazolin-4(1H)- one by tautomerization.The results investigating the biological activity of the compounds contaning 2-thioxothiazolidin-4-one heterocycle (5a-e) indicated that the combination of two scaffolds being 3-arylquinazolin-4(3H)-one and 2-thioxothiazolidin-4-one did not form the compounds with cytotoxic activity against three human cancer cells including Hep-G2 cells, LU-1 cells and HeLa cells.

Keywords: **acetamide, hydrazide, quinazolin-4(3*H*)-one, thiocarbonyl-*bis*-thioglycolic, 2-thioxothiazolidin-4-one.**

Classification number: **2.2**

1. Introduction

3-aryl-3,4-dihydroquinazolin-4-one derivatives have been of great interest in medicinal chemistry for their role as potential biological agents. These derivatives exhibit a wide range of biological effects such as antimicrobial [1-3], antifungal [1], anticonvulsant [4], antihistamine [5], an inhibitor for methionine synthase [6], and increasing HDL cholesterol [7]. Specifically, compounds containing 3-aryl-3,4-dihydroquinazolin-4-one nuclei also show promising anticancer potency [8, 9]. Besides that, the 5-arylidene-2-thioxothiazolidine-4-one scaffold is present in the molecular composition of some compounds that inhibit the hepatitis C virus (HCV) [10], human immunodeficiency virus (HIV) [11], aldose reductase [12, 13], glycogen synthase kinase-3 (GSK-3) [14], JNK-stimulating phosphatase-1 (JSP-1) [15], histone acetyltransferases (HATs) [16], and 17β-hydroxysteroid dehydrogenase type 3 [17]. A variety of biological activities like anticonvulsant [18], antimicrobial [19], anti-diabetic [20], antitumor [21, 22] and anticancer activities [23, 24], etc., have been found in compounds containing the 2-thioxothiazolidine-4-one moiety. The combination of 3-aryl-3,4-dihydroquinazolin-4-one and 2-thioxothiazolidine-4-one moieties thus promise to produce organic molecules bearing precious biological activities of both these heterocycles. This work reports the synthesis of some *N*-(4-oxo-2-thioxothiazolidin-3-yl)-2-((4-oxo-3-aryl-3,4-dihydroquinazolin-2-yl)thio) acetamide compounds. Their biological activity has been studied and is being reported soon.

2. Materials and methods

All reagents and chemicals were obtained from commercial sources and were used without purification. Melting points were recorded on a Gallenkamp melting point apparatus and were uncorrected. Fourier transform infrared (FTIR) spectra (ν, cm^{-1}) were recorded in KBr discs on a FTIR-8400S-SHIMADZU spectrometer. All the NMR spectra were recorded on a Bruker Avance III spectrometer (500 MHz for ^{1}H-NMR and 125 MHz for ^{13}C-NMR). The residual solvent DMSO-d_6 signals (δ_H 2.50, δ_C 39.52) are used as internal references. The abbreviations *s* (singlet), *d* (doublet), *dd* (doublet of doublet), *t* (triplet), *q* (quartet), and *m* (multiplet) are used to describe the splitting of the peaks. The HR-ESI-MS

*Corresponding author: Email: congnt@hcmue.edu.vn

spectra were recorded on an Agilent 6500 series Q-TOF spectrometer.

The target compounds (**5a-e**) were synthesized via a four-step pathway as illustrated in Scheme 1.

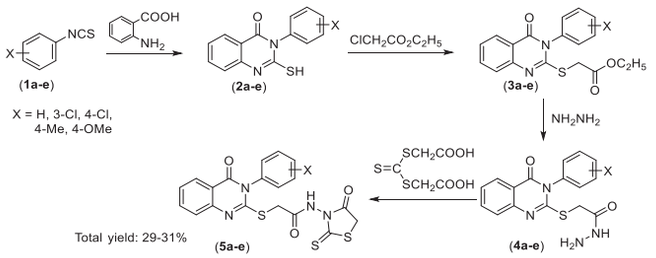

Scheme 1. The pathway for synthesis of the target compounds.

The synthesis, physical characteristics as well as spectral data of the **2a**, **3a**, **4a** and **5a** compounds were reported in our previous work [24].

2.1. General procedure for synthesis of 3-aryl-2-mercaptoquinazolin-4-one compounds (2a-e)

Anthranilic acid (13.7 g, 0.1 mol) was dissolved in absolute ethanol (200 ml), then triethylamine (3 ml) and appropriate aryl isothiocyanate (0.1 mol) were added and the reaction mixture was refluxed for 4 h. Upon completion, the reaction mixture was cooled and poured into ice-cold water. The solid was filtered and then recrystallized from a mixture of DMF and water, then washed with cold ethanol to afford crystals.

*3-(3-chlorophenyl)-2-mercaptoquinazolin-4-one (**2b**):* Yield: 78.0%. Mp. 269.5-270.7°C (lit. [7] 270°C); IR (ν, cm^{-1}): 3219, 3136 (N-H), 3030 (C-H aromatic), 1661 (C=O), 1618, 1526, 1485 (C=N, C=C aromatic), 1227 (C=S); ^{1}H-NMR (δ, ppm): 13.10 (1H, *s*, SH), 7.97 (1H, *d*, *J*=8.0 Hz, Ar-H), 7.79 (1H, J_1=J_2=7.5 Hz, Ar-H), 7.49 (4H, *m,* Ar-H), 7.36 (1H, *dd*, J_1=J_2=7.5 Hz, Ar-H), 7.31 (1H, *d*, *J*=7.0 Hz, Ar-H); ^{13}C-NMR (δ, ppm): 176.3, 160.2, 141.1, 140.1, 136.1, 133.4, 130.9, 129.8, 128.7, 128.6, 127.9, 124.9, 116.7, 116.3.

*3-(4-chlorophenyl)-2-mercaptoquinazolin-4-one (**2c**):* Yield: 81.0%. Mp. 312.4-313.6°C (lit. [7] 315°C); IR (ν, cm^{-1}): 3265, 3138 (N-H), 3032 (C-H aromatic), 1681 (C=O), 1616, 1528, 1485 (C=N, C=C aromatic), 1229 (C=S); ^{1}H-NMR (δ, ppm): 13.08 (1H, *s*, SH), 7.96 (1H, *dd*, J_1=8.0 Hz, J_2=1.0 Hz, Ar-H), 7.79 (1H, *dd*, J_1=J_2=8.0 Hz, Ar-H), 7.55 (2H, *d*, *J*=8.0 Hz, Ar-H), 7.46 (1H, *d*, *J*=8.0 Hz, Ar-H), 7.36 (3H, *m*, Ar-H); ^{13}C-NMR (δ, ppm): 176.4, 160.2, 140.1, 138.7, 136.1, 133.2, 131.5, 129.5, 127.9, 124.9, 116.7, 116.2.

*3-(4-methylphenyl)-2-mercaptoquinazolin-4-one (**2d**):* Yield: 87.0%. Mp. 300.1-301.4°C (lit. [7] 302°C); IR (ν, cm^{-1}): 3242, 3123 (N-H), 3028 (C-H aromatic), 1659 (C=O), 1620, 1522, 1485 (C=N, C=C aromatic), 1229 (C=S); ^{1}H-NMR (δ, ppm): 13.01 (1H, *s*, SH), 7.95 (1H, *dd*, J_1=8.0 Hz, J_1=1.0 Hz, Ar-H), 7.78 (1H, *ddd*, J_1=J_2=8.0 Hz, J_3=1.5 Hz, Ar-H), 7.45 (1H, *d*, *J*=7.5 Hz, Ar-H), 7.35 (1H, *dd*, J_1=J_2=7.5 Hz, Ar-H), 7.28 (2H, *d*, *J*=8.0 Hz, Ar-H), 7.14 (2H, *d*, *J*=8.0 Hz, Ar-H), 2.38 (3H, *s*, CH_3); ^{13}C-NMR (δ, ppm): 176.7, 160.3, 140.1, 137.9, 137.2, 136.0, 129.9, 129.2, 127.9, 124.8, 116.7, 116.2, 21.3.

*3-(4-methoxyphenyl)-2-mercaptoquinazolin-4-one (**2e**):* Yield: 75.0%. Mp. 272.7-273.5°C (lit. [7] 273°C); IR (ν, cm^{-1}): 3240, 3136 (N-H), 3036 (C-H aromatic), 1659 (C=O), 1618, 1528, 1485 (C=N, C=C aromatic), 1231 (C=S); ^{1}H-NMR (δ, ppm): 13.00 (1H, *s*, SH), 7.96 (1H, *d*, *J*=7.0 Hz, Ar-H), 7.78 (1H, *dd*, J_1=J_2=7.5 Hz, Ar-H), 7.45 (1H, *d*, *J*=8.0 Hz, Ar-H), 7.35 (1H, *dd*, J_1=J_2=8.0 Hz, Ar-H), 7.18 (2H, *d*, *J*=8.5 Hz, Ar-H), 7.01 (1H, *d*, *J*=8.0 Hz, Ar-H), 3.82 (3H, *s*, CH_3O); ^{13}C-NMR (δ, ppm): 177.0, 162.8, 160.4, 159.2, 140.0, 136.0, 132.4, 130.4, 127.9, 124.8, 116.7, 116.3, 114.6, 55.8.

2.2. General procedure for synthesis of ethyl 2-[(3-aryl-4-oxo-3,4-dihydroquinazolin-2-yl)thio] acetate compounds (3a-e)

After stirring the solution of a definite 3-aryl-2-mercaptoquinazolin-4-one (**2a-e**) (20 mmol) and anhydrous potassium carbonate (2.76 g, 20 mmol) in dry DMF (30 ml) for 30 min, ethyl chloroacetate (2.45 g, 20 mmol) was added and the reaction mixture was refluxed for 5 h. Upon completion, the reaction mixture was cooled and poured into ice-cold water. The white solid was filtered and recrystallized from ethanol to give pure product **3a-e**, respectively.

*Ethyl 2-[(3-(3-chlorophenyl)-4-oxo-3,4-dihydroquinazolin-2-yl)thio]acetate (**3b**):* Yield: 75.0%. Mp. 86.6-87.2°C (lit. [7]: 86.0°C); IR (ν, cm^{-1}): 3061 (C-H aromatic), 2976, 2922 (C-H aliphatic), 1732, 1690 (C=O), 1607, 1574, 1547, 1468 (C=N, C=C aromatic); ^{1}H-NMR (δ, ppm): 8.09 (1H, *dd*, J_1=8.0 Hz, J_2=1.5 Hz, Ar-H), 7.85 (1H, *ddd*, J_1=J_2=8.0 Hz, J_3=1.5 Hz, Ar-H), 7.73 (1H, *m*, Ar-H), 7.69 (1H, *m*, Ar-H), 7.65 (1H, *dd*, J_1=J_2=8.0 Hz, Ar-H), 7.51 (3H, *m*, Ar-H), 4.15 (2H, *q*, -CH_2CH_3), 4.01 (2H, *s*, -SCH_2-), 1.24 (3H, *t*, CH_3); ^{13}C-NMR (δ, ppm): 168.7, 161.0, 156.4, 147.4, 137.5, 135.6, 134.0, 131.6, 130.7, 130.0, 128.9, 127.1, 126.7, 126.4, 120.0, 61.6, 34.9, 14.6.

*Ethyl 2-[(3-(4-chlorophenyl)-4-oxo-3,4-dihydroquinazolin-2-yl)thio]acetate (**3c**):* Yield: 69.0%. Mp. 96.7-97.5°C (lit. [7]: 98.0°C); IR (ν, cm^{-1}): 3090 (C-H aromatic), 2980, 2932 (C-H aliphatic), 1732,

1684 (C=O), 1605, 1549, 1468 (C=N, C=C aromatic); ^{1}H-NMR (δ, ppm): 8.09 (1H, *d*, *J*=8.0 Hz, Ar-H), 7.85 (1H, *dd*, J_1=J_2=8.0 Hz, Ar-H), 7.69 (2H, *d*, *J*=8.0 Hz, Ar-H), 7.56 (2H, *d*, *J*=8.0 Hz, Ar-H), 7.56 (1H, *d*, *J*=8.0 Hz, Ar-H), 7.50 (1H, *dd*, J_1=J_2=8.0 Hz, Ar-H), 4.15 (2H, *q*, *J*=7.0 Hz, -CH_2CH_3), 4.01 (2H, *s*, -SCH_2-), 1.23 (3H, *t*, *J*=7.0 Hz, -CH_2CH_3); ^{13}C-NMR (δ, ppm): 168.7, 161.0, 156.6, 147.5, 135.6, 135.3, 135.1, 131.9, 130.2, 127.1, 126.7, 126.4, 120.0, 61.6, 34.9, 14.6.

Ethyl 2-[(3-(4-methylphenyl)-4-oxo-3,4-dihydroquinazolin-2-yl)thio]acetate ***(3d)****:* Yield: 73.0%. Mp. 102.6-103.7°C (lit. [7]: 102.0°C); IR (ν, cm^{-1}): 3061 (C-H aromatic), 2986, 2914 (C-H aliphatic), 1728, 1694 (C=O), 1607, 1547, 1466 (C=N, C=C aromatic); ^{1}H-NMR (δ, ppm): 8.07 (1H, *d*, *J*=8.0 Hz, Ar-H), 7.83 (1H, *dd*, J_1=J_2=7.5, Ar-H), 7.50 (1H, *d*, *J*=8.0 Hz, Ar-H), 7.47 (1H, *dd*, J_1=J_2=7.5 Hz, Ar-H), 7.40 (2H, *d*, *J*=8.0 Hz, Ar-H), 7.34 (2H, *d*, *J*=8.0 Hz, Ar-H), 4.15 (2H, *q*, *J*=7.0 Hz, -CH_2CH_3), 3.98 (2H, *s*, -SCH_2-), 2.43 (3H, s, Ar-CH_3), 1.23 (3H, *t*, *J*=7.0 Hz, -CH_2CH_3); ^{13}C-NMR (δ, ppm): 168.8, 161.1, 157.3, 147.5, 140.3, 135.4, 133.5, 130.6, 129.5, 127.1, 126.6, 126.3, 119.9, 61.5, 34.9, 21.3, 14.6.

Ethyl 2-[(3-(4-methoxyphenyl)-4-oxo-3,4-dihydroquinazolin-2-yl)thio]acetate ***(3e)****:* Yield: 77.0%. Mp. 120.8-122.1°C (lit. [7]: 122.0°C); IR (ν, cm^{-1}): 3071 (C-H aromatic), 2974, 2926 (C-H aliphatic), 1734, 1682 (C=O), 1607, 1551, 1508, 1470 (C=N, C=C aromatic); ^{1}H-NMR (δ, ppm): 8.08 (1H, *d*, *J*=8.0 Hz, Ar-H), 7.85 (1H, *dd*, J_1=J_2=8.0 Hz, Ar-H), 7.51 (1H, *d*, *J*=8.0 Hz, Ar-H), 7.49 (1H, *dd*, J_1=J_2=8.0 Hz, Ar-H), 7.39 (2H, *d*, *J*=8.0 Hz, Ar-H), 7.13 (2H, *d*, *J*=8.0 Hz, Ar-H), 4.15 (2H, *q*, *J*=7.0 Hz, -CH_2CH_3), 3.97 (2H, *s*, -SCH_2-), 3.86 (3H, *s*, OCH_3), 1.22 (3H, *t*, *J*=7.0 Hz, -CH_2CH_3); ^{13}C-NMR (δ, ppm): 168.8, 161.2, 160.7, 157.7, 147.5, 135.4, 131.1, 128.5, 127.1, 126.6, 126.3, 120.0, 115.2, 61.5, 56.0, 34.9, 14.6.

2.3. General procedure for synthesis of 2-[(3-aryl-4-oxo-3,4-dihydroquinazolin-2-yl)thio]acetohydrazide compounds (4a-e)

Refluxing a solution of ethanol (50 ml) dissolved a definite ester **3a-e** (20 mmol) and an excess of hydrazine hydrate 80% (1.5 g, 30 mmol) for 6.0 h. The reaction mixture was cooled to room temperature and the resulting solid was filtered then recrystallized from ethanol to afford crystals of **4a-e** compounds, respectively.

2-[(3-(3-chlorophenyl)-4-oxo-3,4-dihydroquinazolin-2-yl)thio]acetohydrazide ***(4b)****:* Yield: 78%. Mp: 184.7-185.6°C (lit. [7]: 186.0°C); IR (ν, cm^{-1}): 3314 (N-H), 3063 (C-H aromatic), 2986 (C-H aliphatic), 1695, 1638 (C=O), 1605, 1553, 1470 (C=N, C=C aromatic); ^{1}H-NMR (δ, ppm): 9.32 (1H, *s*, NH), 8.09 (1H, *d*, *J*=7.0 Hz, Ar-H), 7.87 (1H, *dd*, J_1=J_2=7.5 Hz, Ar-H), 7.72 (1H, *s*, Ar-H), 7.64 (1H, *dd*, J_1=J_2=8.0 Hz, Ar-H), 7.63 (2H, *m*, Ar-H), 7.50 (2H, *m*, Ar-H), 4.28 ppm (2H, *br*, -NH_2), 3.87 (2H, *s*, -SCH_2-); ^{13}C-NMR (δ, ppm): 166.5, 161.1, 156.6, 147.6, 137.6, 135.5, 134.0, 131.6, 130.6, 130.1, 129.0, 127.0, 126.6, 126.5, 120.0, 35.0.

2-[(3-(4-chlorophenyl)-4-oxo-3,4-dihydroquinazolin-2-yl)thio]acetohydrazide ***(4c)****:* Yield: 81%. Mp: 173.2-174.5°C (lit. [7]: 175.0°C); IR (ν, cm^{-1}): 3339, 3298 (N-H), 3049 (C-H aromatic), 2982 (C-H aliphatic), 1684, 1647 (C=O), 1609, 1547, 1470 (C=N, C=C aromatic); ^{1}H-NMR (δ, ppm): 9.32 (1H, *br*, NH), 8.09 (1H, *d*, *J*=8.0 Hz, Ar-H), 7.86 (1H, *dd*, J_1=J_2=8.0 Hz, Ar-H), 7.67 (2H, *d*, *J*=8.5 Hz, Ar-H), 7.63 (1H, *d*, *J*=8.0 Hz, Ar-H), 7.55 (2H, *d*, *J*=8.0 Hz, Ar-H), 7.50 (2H, *dd*, J_1=J_2=8.0 Hz, Ar-H), 4.28 (2H, *br*, -NH_2), 3.87 (2H, *s*, -SCH_2-); ^{13}C-NMR (δ, ppm): 166.5, 161.1, 156.8, 147.6, 135.4, 135.2, 135.1, 132.0, 130.1, 127.0, 126.6, 126.5, 120.0, 35.0.

2-[(3-(4-methylphenyl)-4-oxo-3,4-dihydroquinazolin-2-yl)thio]acetohydrazide ***(4d)***: Yield: 77%. Mp: 147.5-158.6°C (lit. [7]: 148.0°C); IR (ν, cm^{-1}): 3341, 3271 (N-H), 3063 (C-H aromatic), 2974 (C-H aliphatic), 1678, 1643 (C=O), 1609, 1549, 1468 (C=N, C=C aromatic); ^{1}H-NMR (δ, ppm): 9.30 (1H, *br*, NH), 8.08 (1H, *d*, *J*=8.0 Hz, Ar-H), 7.85 (1H, *dd*, J_1=J_2=8.0 Hz, Ar-H), 7.62 (1H, *d*, *J*=8.0 Hz, Ar-H), 7.49 (1H, *dd*, J_1=J_2=8.0 Hz, Ar-H), 7.39 (2H, *d*, *J*=8.0 Hz, Ar-H), 7.39 (2H, *d*, *J*=8.0 Hz, Ar-H), 4.26 (2H, *br*, -NH_2-), 3.84 (2H, *s*, -SCH_2-), 2.43 (3H, *s*, CH_3-Ar); ^{13}C-NMR (δ, ppm): 166.6, 161.2, 157.5, 147.6, 140.1, 135.3, 133.6, 130.5, 129.6, 127.0, 126.6, 126.5, 120.0, 35.0, 21.3.

2-[(3-(4-methoxyphenyl)-4-oxo-3,4-dihydroquinazolin-2-yl)thio]acetohydrazide ***(4e)****:* Yield: 82%. Mp: 154.4-155.6°C (lit. [7]: 149.0°C); IR (ν, cm^{-1}): 3335, 3294 (N-H), 3069 (C-H aromatic), 2970, 2914 (C-H aliphatic), 1686, 1645 (C=O), 1607, 1545, 1508, 1468 (C=N, C=C aromatic); ^{1}H-NMR (δ, ppm): 9.30 (1H, *s*, NH), 8.08 (1H, *d*, *J*=8.0 Hz, Ar-H), 7.84 (1H, *dd*, J_1=J_2=8.0 Hz, Ar-H), 7.62 (1H, *d*, *J*=7.5 Hz, Ar-H), 7.48 (1H, *dd*, J_1=J_2=8.0 Hz, Ar-H), 7.38 (2H, *d*, *J*=7.0 Hz, Ar-H), 7.11 (2H, *d*, *J*=8.0 Hz, Ar-H), 4.27 (2H, *br*, -NH_2-), 3.86 (3H, *s*, -OCH_3), 3.84 (2H, *s*, -SCH_2-); ^{13}C-NMR (δ,

ppm): 166.7, 161.3, 160.6, 157.9, 147.6, 135.3, 131.1, 128.6, 127.0, 126.6, 126.4, 120.0, 115.1, 56.0, 35.0.

2.4. General procedure for synthesis of N-(4-oxo-2-thioxothiazolidin-3-yl)-2-[(3-aryl-4-oxo-3,4-dihydroquinazolin-2-yl)thio]acetamide compounds (5a-e)

A definite **4a-e** compound (5 mmol) and thiocarbonyl-*bis*-thioglycolic acid (1.13 g, 5 mmol) were dissolved in absolute ethanol (15 ml) and the solution was refluxed for 8 h. The reaction mixture was cooled to room temperature and the solid separated was filtered, dried, and recrystallized from AcOH. The pure products **5a-e** were formed as a yellowish powder.

*N-(4-oxo-2-thioxothiazolidin-3-yl)-2-[(3-(3-chlorophenyl)-4-oxo-3,4-dihydroquinazolin-2-yl)thio] acetamide compounds (**5b**):* Yield: 67.0%. Mp: 223.7-224.3°C. IR (ν, cm^{-1}): 3188 (N-H), 3067 (C-H aromatic), 2974 (C-H aliphatic), 1761, 1684 (C=O), 1551, 1466 (C=C aromatic, C=N), 1242 (-N-C=S); ^{1}H-NMR (δ, ppm): 11.32 (1H, *s*, NH), 8.09 (1H, *d*, *J*=8.0 Hz, Ar-H), 7.87 (1H, *dd*, J_1=J_2=8.0 Hz, Ar-H), 7.76 (1H, *dd*, J_1=8.0 Hz, J_2=3.0 Hz, Ar-H), 7.72 (1H, *m*, Ar-H), 7.68 (1H, *dd*, J_1=J_2=8.0 Hz, Ar-H), 7.65 (1H, *dd*, J_1=J_2=8.0 Hz, Ar-H), 7.50 (2H, *m*, Ar-H), [4.44 (1H, *J*=19.0 Hz) and 4.39 (1H, *J*=19.0 Hz)] (-CH_2- in the thiazolidine ring), [4.18 (1H, *J*=20.0 Hz) and 4.13 (1H, *J*=20.0 Hz)] (-CH_2- in the -S-CH_2-CONH- group); ^{13}C-NMR (δ, ppm): 200.1 (C=S), 170.5, 165.9, 161.1 (C=O), 155.9, 147.6, 137.5, 135.3, 134.0, 131.6, 130.7, 130.1, 129.0, 127.0, 126.9, 126.7, 120.0 (C_{Ar}), 34.6 (-SCH_2-), 33.8 (-CH_2- thiazolidine ring); HR-ESI-MS *m/z* 476.9912 $(M+H)^+$ calcd. for ($C_{19}H_{14}ClN_4O_3S_3$) 476.9917.

*N-(4-oxo-2-thioxothiazolidin-3-yl)-2-[(3-(4-chlorophenyl)-4-oxo-3,4-dihydroquinazolin-2-yl)thio] acetamide compounds (**5c**):* Yield: 69.0%. Mp: 247.3-248.6°C. IR (ν, cm^{-1}): 3211 (N-H), 3086 (C-H aromatic), 2980 (C-H aliphatic), 1763, 1690 (C=O), 1549, 1466 (C=C aromatic, C=N), 1233 (-N-C=S); ^{1}H-NMR (δ, ppm): 11.31 (1H, *s*, NH), 8.09 (1H, *d*, *J*=8.0 Hz, Ar-H), 7.86 (1H, *dd*, J_1=J_2=7.0 Hz, Ar-H), 7.76 (1H, *d*, *J*=8.0 Hz, Ar-H), 7.68 (2H, *d*, *J*=9.0 Hz, Ar-H), 7.56 (2H, *m*, Ar-H), 7.50 (1H, *dd*, J_1=J_2=8.0 Hz, Ar-H), [4.43 (1H, *J*=18.5 Hz) and 4.38 (1H, *J*=18.5 Hz)] (-CH_2- in the thiazolidine ring), [4.17 (1H, *J*=15.5 Hz) and 4.12 (1H, *J*=15.5 Hz)] (-CH_2- in the -S-CH_2-CONH- group); ^{13}C-NMR (δ, ppm): 200.1 (C=S), 170.5, 165.9, 161.1 (C=O), 156.1, 147.6, 135.3, 135.1, 131.9, 130.2, 127.0, 126.9, 126.6, 120.0 (C_{Ar}), 34.6 (-SCH_2-), 33.8 (-CH_2- thiazolidine ring); HR-ESI-MS *m/z* 476.9923 $(M+H)^+$ calcd. for ($C_{19}H_{14}ClN_4O_3S_3$) 476.9917.

*N-(4-oxo-2-thioxothiazolidin-3-yl)-2-[(3-(4-methylphenyl)-4-oxo-3,4-dihydroquinazolin-2-yl)thio] acetamide compounds (**5d**):* Yield: 72.0%. Mp: 246.4-247.2°C. IR (ν, cm^{-1}): 3210 (N-H), 3093 (C-H aromatic), 2918 (C-H aliphatic), 1761, 1688 (C=O), 1609, 1549, 1466 (C=C aromatic, C=N), 1233 (-N-C=S); ^{1}H-NMR (δ, ppm): 11.29 (1H, *s*, NH), 8.08 (1H, *d*, *J*=8.0 Hz, Ar-H), 7.85 (1H, *dd*, J_1=J_2=7.5 Hz, Ar-H), 7.75 (1H, *d*, *J*=8.0 Hz, Ar-H), 7.49 (1H, *dd*, J_1=J_2=7.5 Hz, Ar-H), 7.40 (2H, *d*, *J*=8.0 Hz, Ar-H), 7.34 (2H, *d*, *J*=8.0 Hz, Ar-H), [4.43 (1H, *J*=18.5 Hz) and 4.38 (1H, *J*=18.5 Hz)] (-CH_2- in the thiazolidine ring), [4.14 (1H, *J*=16.0 Hz) and 4.09 (1H, *J*=16.0 Hz)] (-CH_2- in the -S-CH_2-CONH- group), 2.43 (3H, *s*, CH_3-Ar); ^{13}C-NMR (δ, ppm): 200.1 (C=S), 170.5, 166.0, 161.2 (C=O), 156.8, 147.6, 140.3, 135.2, 133.5, 130.5, 129.6, 126.9, 126.5, 120.0 (C_{Ar}), 34.5 (-SCH_2-), 33.8 (-CH_2- thiazolidine ring), 21.3 (CH_3-Ar); HR-ESI-MS *m/z* 479.0275 $(M+Na)^+$ calcd. for ($C_{20}H_{16}N_4NaO_3S_3$) 479.0282.

*N-(4-oxo-2-thioxothiazolidin-3-yl)-2-[(3-(4-methoxyphenyl)-4-oxo-3,4-dihydroquinazolin-2-yl)thio] acetamide compounds (**5e**):* Yield: 58.0%. Mp: 234.6-235.1°C. IR (ν, cm^{-1}): 3213 (N-H), 2978 (C-H aliphatic), 1765, 1682 (C=O), 1549, 1466 (C=C aromatic, C=N), 1231 (-N-C=S); ^{1}H-NMR (δ, ppm): 11.29 (1H, *s*, NH), 8.08 (1H, *d*, *J*=7.5 Hz, Ar-H), 7.85 (1H, *dd*, J_1=J_2=7.5 Hz, Ar-H), 7.74 (1H, *d*, *J*=8.0 Hz, Ar-H), 7.49 (1H, *dd*, J_1=J_2=7.5 Hz, Ar-H), 7.38 (2H, *d*, *J*=7.0 Hz, Ar-H), 7.13 (2H, *d*, *J*=7.0 Hz, Ar-H), [4.43 (1H, *J*=18.5 Hz) and 4.38 (1H, *J*=18.5 Hz)] (-CH_2- in the thiazolidine ring), [4.14 (1H, *J*=15.5 Hz) and 4.09 (1H, *J*=15.5 Hz)] (-CH_2- in the -S-CH_2-CONH- group), 3.86 (3H, *s*, OCH_3); ^{13}C-NMR (δ, ppm): 200.1 (C=S), 170.5, 166.0, 161.3 (C=O), 160.7, 157.2, 147.6, 135.1, 131.1, 128.5, 126.9, 126.5, 120.0, 115.2 (C_{Ar}), 56.0 (CH_3O), 34.6 (-SCH_2-), 33.8 (-CH_2- thiazolidine ring); HR-ESI-MS *m/z* 473.0402 $(M+H)^+$ calcd. for ($C_{20}H_{17}N_4O_4S_3$) 473.0412.

Cytotoxicity assay: Compounds **5a-e** were tested for cytotoxicity in three human cancer cell lines including Hep-G2 (Human hepatocellular carcinoma), LU-1 (Human lung adenocarcinoma), and HeLa (HeLa cervical cancer cells). The cell lines were cultured in vitro under standard cell culture conditions (humidified air, 5% CO_2, 37°C) according to the method of P. Skehan, et al.

(1991) [25]. The cytotoxicity assay on cancer cell lines was conducted by the Sulforhodamine B (SRB) method as described by K. Likhitwitayawuid, et al. (1993) [26]. Ellipticine was used as the positive control and dimethyl sulfoxide (DMSO) in culture media was used as the negative control. The optical density (OD) was measured by using an automated 96-well plate reader (Infinite Tecan, Switzerland) at 550 nm. The percentage of cell survival (CS%) was determined based on the absorbances of the test sample and negative control (DMSO-treated cells) as the following equation:

$$CS\% = \frac{(OD_{Sample} - OD_{day\,0})}{(OD_{DMSO} - OD_{day\,0})} * 100$$

where OD_{Sample}: optical density of sample at 550 nm; OD_{DMSO}: optical density of negative control at 550 nm; $OD_{day\,0}$: optical density of sample or DMSO at time zero (start of sample exposure).

Each sample was assayed with three replications and the result was taken as mean ± standard deviation (SD). The results are recorded in Table 1.

Table 1. The cytotoxicity of 5a-e compounds in Hep-G2, LU-1 and HeLa cell lines.

No.	Compounds	Concentration (µg/ml)	CS (%)		
			Hep-G2	*LU-1*	*HeLa*
1	DMSO	-	100	100	100
2	Ellipticine	5	2.05±1.15	3.06±1.26	2.33±1.23
3	**5a**	5	99.75±0.16	78.62±2.52	94.45±2.14
4	**5b**	5	99.26±0.66	98.74±0.90	95.52±0.63
5	**5c**	5	98.48±1.03	86.20±2.22	81.23±1.56
6	**5d**	5	95.79±0.38	66.52±2.19	65.24±1.04
7	**5e**	5	98.05±0.29	76.35±1.15	78.89±2.42

3. Results and discussion

The reaction of anthranilic acid and appropriately substituted phenyl isothiocyanates gave five 3-aryl-2-mercaptoquinazolin-4(3*H*)-one compounds with good yield. In the fact, the **2a-e** compounds existed in the thione form, namely 3-aryl-2-thioxo-2,3-dihydroquinazolin-4(1*H*)-one by tautomerization. This was confirmed not only by their IR spectra with an absorption band around 1200-1300 cm^{-1}, which was attributed to the C=S bond but also by both their ^{1}H-NMR and ^{13}C-NMR spectra. The ^{1}H-NMR spectra of the **2a-e** compounds displayed a signal at around δ 13.00, which is attributed to the N-H proton [27]. The signal appeared at high field (near 176.5 ppm) in the ^{13}C-NMR spectra of the **2a-e** compounds but was not seen in the ^{13}C-NMR spectra of the **3a-e** compounds, which must be assigned to carbon in the C=S group. However, in an alkaline environment, the **2a-e** compounds transformed into thiolate form and reacted with ethyl chloroacetate in the role of nucleophile agents to form *S*-substituted products, namely, ethyl 2-[(3-aryl-4-oxo-3,4-dihydroquinazolin-2-yl)thio]acetate. Existence of **2a-e** compounds in thione form and their transformation into *S*-substituted products were reported in our recent work [28]. The esters, in turn, reacted with hydrazine hydrate to form hydrazide compounds. The reaction sequence used to synthesize the 2-[(4-oxo-3-aryl-3,4-dihydroquinazolin-2-yl)thio] acetohydrazide compounds from anthranilic acid and aryl isothiocyanates has been reported in some works [7, 24]. However, spectral data of the synthesized compounds including both ester and hydrazide compounds, especially data on the ^{13}C-NMR spectrum, were not fully available. The formation of these compounds was confirmed by the similarity in both melting point and spectral characteristics of them with the ones of the corresponding compounds in the literature [2, 7, 24]. Furthermore, the ^{13}C-NMR spectra of the **3b-e** and **4b-e** compounds have been presented.

To form a 2-thioxothiazolidine-4-one compound, the reaction of a hydrazide with thiocarbonyl-*bis*-thioglycolic acid has been mentioned [19-24]. This method was used to prepare the *N*-(4-oxo-2-thioxothiazolidin-3-yl)-2-[(4-oxo-3-aryl-3,4-dihydroquinazolin-2-yl)thio]acetamide compounds (**5a-e**) based on the reaction of thiocarbonyl-*bis*-thioglycolic acid with appropriate hydrazides **4a-e**. Except for the **5a** compound that was synthesized and reported in our recent work [24], the **5b-e** compounds have not been found in the literature. In the IR spectra of the **5a-e** compounds, the vibration of the N-H bond appeared around 3200 cm^{-1}, which is the absorption region of the C=O bond. Besides the absorption of the lactam and amide carbonyl groups around 1690 cm^{-1}, there is an appearance of a new band around 1760 cm^{-1} assigned to the absorption of the C=O group in the 2-thioxothiazolidin-4-one ring. The pseudo-molecular ion peaks $[M+H]^+$ or $[M+Na]^+$ in the mass spectra of the products matched with theoretical calculations. In the ^{1}H-NMR spectra of the **5a-e** compounds, in addition to the signal at 4.13 ppm characterized as the -SCH_2- group bonding with quinazoline ring, there is the new signal at 4.41 ppm that was assigned to the methylene group on the thiazolidinone ring. Notably, the signals of these methylene groups did not appear in the expected *singlet* type, but both of them were split into two doublets, which is similar to what happened to the compound containing

a 2-thioxo-1,3-thiozolidin-4-one ring synthesized from 7-hydroxy-4-methylcoumarin [19]. Thus, the thiazolidine ring not only contains non-equivalent methylene protons but also makes the methylene protons of the -SCH_2CONH- group become diastereotopic protons. Protons in each of these methylene groups interact with each other and form doublet signals. Due to the proximity of chemical shifts, these signals are influenced by the roof effect and appear in the special shape as described. The signals appearing in the ^{13}C-NMR spectra of the **5a-e** compounds include 2 signals at 34.5 ppm and 33.8 ppm (2 methylene carbons), a signal at 200.1 ppm (carbon in the thioxo group), 3 signals at about 161-170 ppm (3 carbonyl carbons), and 14 signals at 120.0-156.5 ppm (unsaturated and aromatic carbons). In addition, the signals of the carbon atoms in the aromatic rings appear fully in the spectra. Particularly, the spectrum of the **5d** compound has a signal at 21.3 ppm while the spectrum of the **5e** compound has a signal at 56.0 ppm. These signals are assigned to carbon atoms in the methyl and methoxy groups in their molecules, respectively. All data showed that the structure of the **5a-e** compounds matches their desired molecular formula.

All compounds containing a 2-thioxothiazolidin-4-one ring (**5a-e**) were evaluated for their potential cytotoxicity against Hep-G2, LU-1, and HeLa cancer cell lines using Ellipticine as a positive control. The results were expressed in terms of the percentage of cell survival (CS%) (see Table 1). Disappointingly, all of the (**5a-e**) compounds possessed low toxicity against the three human cancer cell lines tested. Other biological activities of these compounds such as antimicrobial and antioxidant activities are continuing to be investigated.

4. Conclusions

In the present work, five new *N*-(4-oxo-2-thioxothiazolidin-3-yl)-2-[(4-oxo-3-aryl-3,4-dihydroquinazolin-2-yl)thio]acetamide compounds were synthesized and their structures were confirmed by IR, HR-MS, ^{1}H-NMR, and ^{13}C-NMR spectral data. However, the initial survey showed that all of these hybrid compounds based 3-aryl-2-sulfanylquinazolin-4(3*H*)-one heterocycle and 2-thioxothiazolidin-4-one heterocycle did not exhibit cytotoxic active against Hep-G2, LU-1, and HeLa cancer cell lines.

CRediT author statement

Tien Cong Nguyen: Conceptualisation, Methodology, Supervision, Resources, Writing - Review and Editing; Duc Dung Pham: Data curation, Writing original draft preparation; Thi Minh Dinh Tran: Methodology, Writing, Investigation; Thi Thuy Linh Bui: Investigation, Visualisation.

ACKNOWLEDGEMENTS

We are grateful to the Ministry of Education and Training of Vietnam for supporting this research (Grant No. B2019-SPS-02).

COMPETING INTERESTS

The authors declare that there is no conflict of interest regarding the publication of this article.

REFERENCES

[1] A.A. Monirah, A.S. Danah, E.B. Fatima (2013), "Synthesis of some-2-thioxo-3-substituted-2,3-dihydro-1H-quinazolin-4-one derivatives as potential antibacterial and antifungal agents", *Res. J. Chem. Environ.*, **17(9)**, pp.48-52.

[2] S.M.H.A. Majidi, M.G.A.A. Khuzaie (2015), "Synthesis and antimicrobial activity of some new S-substituted quinazolinones containing different heterocyclic rings", *Asian Journal of Chemistry*, **27(2)**, pp.756-762, DOI: 10.14233/ajchem.2015.18417.

[3] X. Lv, L. Yang, Z. Fan, et al. (2018), "Synthesis and antimicrobial activities of novel quinazolin-4(3*H*)-one derivatives containing a 1,2,4-triazolo[3,4-b][1,3,4]thiadiazole moiety", *Journal of Saudi Chemistry Society*, **22(1)**, pp.101-109, DOI: 10.1016/j.jscs.2017.07.008.

[4] A.S.E. Azab, S.G.A. Hamide, M.M.S. Ahmed, et al. (2013), "Novel 4(3H)-quinazolinone analogs: Synthesis and anticonvulsant activity", *Medicinal Chemistry Research*, **22(6)**, pp.2815-2827, DOI: 10.1007/s00044-012-0280-y.

[5] M. Gobinath, N. Subramanian, V. Alagarsamy (2015), "Design, synthesis and H1-antihistaminic activity of novel 1-substituted-4-(3-chlorophenyl)-[1,2,4]triazolo [4,3-a] quinazolin-5(4,H)-ones", *Journal of Saudi Chemistry Society*, **19(3)**, pp.282-286, DOI: 10.1016/j.jscs.2012.02.006.

[6] I.M. Elfekki, W.F.M. Hassan, H.E.A.E. Elshihawy, et al. (2014), "Molecular modeling studies and synthesis of novel methyl 2-(2-(4-oxo3-aryl-3,4-dihydroquinazolin-2-ylthio) acetamido) alkanoates with potential anti-cancer activity as inhibitors for methionine synthase", *Chemical and Pharmaceutical Bulletin*, **62(7)**, pp.675-694, DOI: 10.1248/cpb.c14-00158.

[7] M.B. Deshmukh, S.R. Dhongade (2004), "Synthesis and QSAR study of some HDL cholesterol increasing quinazolinone derivatives", *E-Journal of Chemistry*, **1(1)**, pp.17-31, DOI: 10.1155/2004/671567.

[8] S.E. Sayed, K. Metwally, A.A.E. Shanawani, et al. (2017), "Synthesis and anticancer activity of novel quinazolinone-based rhodanines", *Chemistry Central Journal*, **11(1)**, pp.102-111, DOI: 10.1186/s13065-017-0333-x.

[9] A. I. Khodair, M.A. Alsaf, M.S. Nafe (2019), "Synthesis, molecular modeling and anti-cancer evaluation of a series of quinazoline derivatives", *Carbohydrate Research*, **486**, DOI: 10.1016/j.carres.2019.107832.

[10] T.T. Talele, P. Arora, S.S. Kulkarni, et al. (2010), "Structure-based virtual screening, synthesis and SAR of novel inhibitors of hepatitis C virus NS5B polymerase", *Bioorganic and Medicinal Chemistry*, **18(13)**, pp.4630-4638, DOI: 10.1016/j.bmc.2010.05.030.

[11] K. Ramkumar, V.N. Yarovenko, A.S. Nikitina, et al. (2010), "Design, synthesis and structure-activity studies of rhodanine derivatives as HIV-1 integrase inhibitors", *Molecules*, **15(6)**, pp.3958-3992, DOI: 10.3390/molecules15063958.

[12] S. Jiang, S.R. Tala, H. Lu, et al. (2011), "Design, synthesis, and biological activity of novel 5-((arylfuran/1H-pyrrol-2-yl) methylene)-thioxo-3-(3-(trifluoromethyl)phenyl)thiazolidin-4-ones as HIV-1 fusion inhibitors targeting GP41", *Journal of Medicinal Chemistry*, **54(2)**, pp.572-579, DOI: 10.1021/jm101014v.

[13] M. Murata, B. Fujitani, H. Mizuta (1999), "Synthesis and aldose reductase inhibitory activity of a new series of 5-[[2-(ω-carboxyalkoxy)aryl]methylene]-4-oxo-2-thioxothiazolidine derivatives", *European Journal of Medicinal Chemistry*, **34(12)**, pp.1061-1070.

[14] S. Guiheneuf, L. Paquin, F. Carreaux, et al. (2014), "New 5-ylidene rhodanine derivatives based on the dispacamide A model", *Molecular Diversity*, **18(2)**, pp.375-388, DOI: 10.1007/s11030-014-9509-7.

[15] N.S. Cutshall, C. O'Day, M. Prezhdo (2005), "Rhodanine derivatives as inhibitors of JSP-1", *Bioorganic and Medicinal Chemistry Letters*, **15(14)**, pp.3374-3379, DOI: 10.1016/j.bmcl.2005.05.034.

[16] S.D. Furdas, S. Shekfeh, S. Kannan, et al. (2012), "Rhodanine carboxylic acids as novel inhibitors of histone acetyltransferases", *Med. Chem. Comm.*, **3**, pp.305-311, DOI: 10.1039/C2MD00211F.

[17] K. Harada, H. Kubo, J. Abe, et al. (2012), "Discovery of potent and orally bioavailable 17β-hydroxysteroid dehydrogenase type 3 inhibitors", *Bioorganic and Medicinal Chemistry*, **20(10)**, pp.3242-3254, DOI: 10.1016/j.bmc.2012.03.052.

[18] J. Gagoria, K. Singh, S.K. Jain, et al. (2008), "Synthesis and anticonvulsant study of benzylidine rhodanine derivatives", *Oriental Journal of Chemistry*, **24(2)**, pp.713-716.

[19] T.C. Nguyen, T.N. Huynh, VH. Luong, et al. (2014), "Synthesis and antibacterial activity of analogs of 5-arylidene-(4-methylcoumarin-7-yloxyacetylamino)-2-thioxo-1,3-thiazolidin-one", *Molecules*, **19(19)**, pp.13577-13586, DOI: 10.3390/molecules190913577.

[20] S.S. Alneyadi (2018), "Rhodanine as scaffold: A short review on its synthesis and anti-diabetic activities", *Heterocycles*, **96(5)**, pp.803-838, DOI: 10.3987/REV-17-878.

[21] L. Mosula, B. Zimenkovsky, D. Havrylyuk, et al. (2009), "Synthesis and antitumor activity of novel 2-thioxo-4-thiazolidinones with benzothiazole moieties", *Farmacia*, **57(3)**, pp.321-330.

[22] O. Roman, R. Lesyk (2007), "Synthesis and anticancer activity in vitro of some 2-thioxo-4-thiazolidone derivatives", *Farmacia*, **55(6)**, pp.640-648.

[23] G.N. Masoud, A.M. Youssef, M.M.A. Khalek, et al. (2013), "Design, synthesis, and biological evaluation of new 4-thiazolidinone derivatives substituted with benzimidazole ring as potential chemotherapeutic agents", *Medicinal Chemistry Research*, **22(2)**, pp.707-725, DOI: 10.1007/s00044-012-0057-3.

[24] T.C. Nguyen, T.Q. Nguyen, H.P. Dao, et al. (2019), "Synthesis and cytotoxic activity against K562 and MCF7 cell lines of some *N*-(5-arylidene-4-oxo-2-thioxothiazolidin-3-yl)-2-((4-oxo-3-phenyl-3,4-dihydroquinazoline-2-yl)thio)acetamide compounds", *Journal of Chemistry*, **2019(2b)**, pp.1-8, DOI: 10.1155/2019/1492316.

[25] P. Skehan, R. Storeng, D. Scudiero, et al. (1991), "New colorimetric cytotoxicity assay for anticancer agents", *European Journal of Cancer*, **27**, pp.1162-1168, DOI: 10.1093/jnci/82.13.1107.

[26] K. Likhitwitayawuid, C.K. Angerhofer, G.A. Cordell, et al. (1993), "Cytotoxic and antimalarial bisbenzylisoquinoline alkaloids from *Sephania evecta*", *Jounal of Natural Products*, **56(1)**, pp.30-38, DOI: 10.1021/np50091a005.

[27] M.M. Wang, G.L. Dou, D.Q. Shi (2010), "One-pot synthesis of 2,3-dihydro-2-thioxoquinazolin-4(1*H*)-ones from nitro-compounds with the aid of tin(II) chloride", *J. Heterocyclic Chem.*, **47(4)**, pp.939-943, DOI: 10.1002/jhet.392.

[28] T.C. Nguyen, T.Q. Nguyen, D.D. Pham, et al. (2020), "Synthesis and structure of ethyl 2-[(4-oxo-3phenyl-3,4-dihydroquinazolin-2-yl)sulfanyl] acetate", *Acta Cryst*., **76(5)**, pp.668-672, DOI: 10.1107/S2056989020005071.

DOI: 10.31276/VJSTE.64(2).28-33

Drying of porous media: An algorithm to determine effective parameters

Hong Thai Vu*, Trung Dung Nguyen

Department of Chemical Process Equipment, School of Chemical Technology, Hanoi University of Science and Technology, 1 Dai Co Viet Street, Bach Khoa Ward, Hai Ba Trung District, Hanoi, Vietnam

Received 16 March 2021; revised 23 May 2021; accepted 4 June 2021

Abstract:

Drying is a separation process in solid-liquid systems. The drying process plays an important role in various industries such as chemical engineering, food, agriculture, and construction. In the past decades, drying of porous media has attracted the attention of many researchers all around the world. The drying process is a complex one due to the phenomena of heat and mass transfer, which take place simultaneously. In principle, these transport processes can be modelling using continuous and discrete approaches. Following the continuous approach, porous media was simulated as continuous, and effective parameters for heat and mass transfer were employed. The system of equations governing the drying process in porous media resulting from Whitaker's model is presented and used in our numerical implementation. In this continuous model, the effective diffusivity and effective thermal conductivity parameters had strong effects on the results. The purpose of this research was to develop an algorithm to determine the effective parameters of the drying of porous media by using a continuous model.

Keywords: **continuous model, drying, effective diffusivity, numerical model.**

Classification numbers: **2.2, 2.3**

1. Introduction

Drying is a separation process in solid-liquid systems. In practice, the drying process plays an important role in various industries. In principle, these transport phenomena in porous media can be modelled by using two approaches: continuous and discrete, as mentioned by D. Michel, et al. (1987) [1]. By using the continuous model, porous media is simulated to be continuous and effective parameters for heat and mass transfer are used.

Following the continuous approach, Whitaker used a volume averaging technique to obtain a set of macroscopic transport equations from a system of basic transport laws at a microscopic level for the three phases (gas, liquid, and solid). Details of the above technique can be found in Whitaker's works [2-4]. According to Whitaker's model, porous media is assumed to be continuous, and a system of conservation equations of heat, mass, and motion is developed through the main state variables. The model developed by Whitaker has been widely applied in the study of the drying of porous media, for example, in the drying analysis of sand [5-8], glass beads [9], sandstone [10], porous insulators [11], brick [12], cellular materials [13], wood [14-17], and light concrete [18-20]. In these mentioned works, the model is usually quite successfully matched against experimental data. As a result, the above research works highlight the acceptance of the complete theory.

Among other methods, [21, 22] used a control volume finite element method (CV-FEM) [23] to solve the numerical problem. The advantage of this method is that the coupled heat and mass transfer is modelled using effective parameters, which have a physical meaning and are not lumped parameters. The model developed by Whitaker, Perré, and Turner very effectively solves the drying problem of porous media because the heat and mass transfer happen simultaneously, and these phenomena are simulated using effective parameters. However, the most difficult point when solving the problem is the determination of the model parameters as pointed out by V.T. Hong, et al. (2006) [24]. According to [25, 26], these parameters must either be experimentally determined or must be modelled from the microstructure of the material. In fact, these parameters are functions of state variables, e.g., moisture content, temperature, and pressure. These parameters should be determined with

*Corresponding author: Email: thai.vuhong@hust.edu.vn

great care concerning the microscopic material structure as they have decisive effects on simulated drying characteristics. By solving the so-called inverse problem, one can find a way to determine these parameters.

Experimental methods such as magnetic resonance imaging (MRI) have used to obtain the drying kinetics of porous materials, for example, the moisture content, X_{exp}, can be obtained as function of space and time. By using experimental data such as this, effective transport parameters such as diffusivity can be obtained by progressively modifying the transport parameters until the simulated drying kinetics (X_{sim}) match the experimental ones (X_{exp}). Therefore, the purpose of this research is to develop an algorithm to determine the effective parameters of drying of porous media by using a continuous model. However, due to the lack of experimental data, we use the forward problem to generate the data for the inverse problem by employing the control volume method and some known material parameters. Then, the algorithm of the inverse problem is presented, and numerical examples are considered to demonstrate the accuracy of the computed parameters. In this study, we consider the problem in one-dimensional space as well.

2. Governing equations

There are four equations that govern the drying process in a porous medium. The first is the conservation equation for water in liquid and gas phases. The second is the conservation equation for air in the gas phase. The third is the conservation equation of energy, and the fourth are the sets of equations of motion for the liquid phase and for the gas phase [3, 21].

The conservation equation for water in both liquid and gas phase is:

$$\frac{\partial}{\partial t}\left(\rho_w \varepsilon_w + \varepsilon_g \rho_v\right) + \nabla \cdot \left(\rho_w \mathbf{v}_w + \rho_v \mathbf{v}_g\right) = \nabla \cdot \left[\rho_g \mathrm{D}_{eff} \cdot \nabla\left(\frac{\rho_v}{\rho_g}\right)\right] \quad (1)$$

where ρ_w, ρ_v, and ρ_g are the mass density of the liquid, vapor, and gas phases, respectively, ε_w and ε_v are the volume fractions of the liquid and gas phase, respectively, v_w and v_w are the velocities of the liquid and gas phase, respectively, and D_{eff} is the effective diffusivity tensor.

The conservation equation for air in the gas phase can be formulated as:

$$\frac{\partial}{\partial t}\left(\varepsilon_g \rho_a\right) + \nabla \cdot \left(\rho_a \mathbf{v}_g\right) = \nabla \cdot \left[\rho_g \mathrm{D}_{eff} \cdot \nabla\left(\frac{\rho_a}{\rho_g}\right)\right] \quad (2)$$

The most complex one is the conservation equation of energy and it is given as:

$$\begin{aligned}&\frac{\partial}{\partial t}\left(\varepsilon_s \rho_s h_s + \varepsilon_w \rho_w h_w + \varepsilon_g \rho_v h_v + \varepsilon_g \rho_a h_a\right) + \nabla \cdot \left[\rho_w h_w \mathbf{v}_w + \left(\rho_v h_v + \rho_a h_a\right)\mathbf{v}_g\right] \\ &= \nabla \cdot \left[\rho_g h_a \mathrm{D}_{eff} \nabla\left(\frac{\rho_a}{\rho_g}\right)\right] + \nabla \cdot \left[\rho_g h_v \mathrm{D}_{eff} \nabla\left(\frac{\rho_v}{\rho_g}\right)\right] + \nabla \cdot \left(\lambda_{eff} \nabla T\right)\end{aligned} \quad (3)$$

where ε_s and ρ_s are the volume fraction and the mass density of the solid phase, respectively, h_s, h_w, h_v, and h_a are the enthalpies per unit mass of the solid, water, vapor, and air, respectively, and λ_{eff} is the effective thermal conductivity tensor.

The equation of motion for the liquid phase can be written as:

$$v_w = -\frac{Kk_w}{\eta_w}\nabla P_w \quad (4)$$

and the equations of motion for the gas phase are given as:

$$v_g = -\frac{Kk_g}{\eta_g}\nabla P_g \quad (5)$$

where K is absolute permeability tensor, k_w and k_g are the relative permeability tensors for liquid and gas phase, respectively, η_w and η_g are the dynamic viscosity of water and gas, respectively, P_w is the pressure of the liquid phase, and P_g is the pressure of the gas phase.

In addition, the boundary conditions for mass and heat transfer at the external drying surfaces of the porous medium must be specified. The gas pressures at the external drying surfaces are fixed at the pressure of the bulk drying air. Sorption isotherm, capillary pressure, ideal gas laws, and enthalpy-temperature relations will complete the set of equations (1-8) by facilitating the expression of all variables as functions of the three state variables. Finally, initial conditions are needed to close the sets of equations. These conditions can be found from the work of H.T. Vu (2006) [27].

3. Material properties

For our calculations, a light concrete reference material is considered. More information about this material can be found in these works of [21, 22]. The porosity is ψ=0.8. The solid density is $\rho_s = 2500\,\mathrm{kg.m^{-3}}$

and the heat capacity is $\overline{\rho C_p} = \varepsilon_s \rho_s (840 + 4185X)$ J.kg^{-1}.K^{-1}. The fully saturated material has a moisture content X_{sat}=1.6.

The sorption isotherm is given as:

$$\varphi(X,T) = \frac{P_v}{P_v^*(T)} = \begin{cases} 1 & , \text{ if } X > X_{irr} \\ \dfrac{X}{X_{irr}}\left(2 - \dfrac{X}{X_{irr}}\right), & \text{if } X \le X_{irr} \end{cases} \quad (6)$$

where X_{irr}=0.07, which is the irreducible content and $P_v^*(T)$ is the saturation pressure.

4. Parameters of real material and parameters to be determined

The following table presents the parameters of the real material and the parameters to be determined (Table 1). The first column is the parameters of the real material, which is light concrete in this case. Based on these values, we can derive the unknown parameters, i.e., the parameters to be determined, as functions of state variables.

Table 1. Parameters of real material and parameters to be determined.

Parameters of real material	Unknown (parameters to be determined)
$\overline{\rho C_p} = \rho_0(840 + 4185X)$ (Jkg^{-1}K^{-1})	$\overline{\rho C_p} = \rho_0(C_1 + C_2 X)$
$K_{eff} = (0.142 + 0.46X)$	$K_{eff} = (K_1 + K_2 X)$
$D_{eff} = 0.2 D_v k_{rg}$	$D_{eff} = D_1 D_v k_g$
$K_w = 2\times10^{-13}$ [m^2]	K_w
$K_g = 2\times10^{-13}$ [m^2]	K_g
$k_w = \begin{cases} 0 \; if \; X \le X_{irr} \\ S_{fw}^3 \; other \end{cases}$	$k_g = \begin{cases} 0 \; if \; X \le X_{irr} \\ 1 + (2S_{fw} - 3)S_{fw}^2 \; other \end{cases}$
$k_g = \begin{cases} 0 \; if \; X \le X_{irr} \\ 1 + (2S_{fw} - 3)S_{fw}^2 \; other \end{cases}$	$k_g = \begin{cases} 0 \; if \; X \le X_{irr} \\ k_{rg1} + (k_{rg2}S_{fw} + k_{rg3})S_{fw}^2 \; other \end{cases}$

5. The problem

The problem can be stated as follows:

1. Vector $\boldsymbol{f}_{x0}$ is the vector containing experimental data. For example, moisture content X, temperature T and pressure P at different measurement points during the drying time t_{dry}. Vector $\boldsymbol{f}_{x0}$ depends on vector $\boldsymbol{x}$, which contains the material properties.

2. We can model the drying process of porous media and calculate the vector $\boldsymbol{f}_{xc}$ that contains X, V, and P at measurement points. With different values of $\boldsymbol{x}$, we have different values of f_{xc}, respectively, so we can write: $f_{xc} = f_{xc}(x)$.

3. If we do not know the material properties x, but we have f_{x0} and find a certain vector $\hat{x}$ such that, after inserting into the model ($f_{xc}(x)$) we have a vector $f_{xc}(x)$ and vector f_{x0} that are the same (or almost the same), we can state that vector $\hat{x}$ is the vector containing the material properties we are looking for.

In practice, it is difficult to find $\hat{x}$ such that vector $f_{xc}(x)$ and vector f_{x0} are identical. Therefore, we will determine $\hat{x}$ so that the two mentioned vectors are nearly identical. This means we need to determine $\hat{x}$ such that $[f_{xc}(x) - f_{x0}]^T[f_{xc}(x) - f_{x0}]$ is a minimum, i.e., to solve the optimal problem. This problem can be summarized as follows:

$$\min r(x)$$

$$r(x) = \frac{1}{2}[f(x)]^T f(x) = \sum_{i=1}^{m} \frac{1}{2}[f_i(x)]^2 \quad (7)$$

where m is the length of vector f.

In this research, we use the Levenberg-Marquardt [28] method to solve the optimal problem. FORTRAN and MATLAB are employed to solve the equations.

6. Levenberg-Marquardt method

More details of the Levenberg-Marquardt method can be found from the research work of D.W. Marquardt [28]. The Levenberg-Marquardt steps, $\boldsymbol{s}_k$, can be defined by:

$$\min\left(\frac{1}{2}\|f'(x_k)s_k + f(x_k)\|_2^2\right) \quad (8)$$

$$subjected\ to: \|D_k s_k\|_2 \le \Delta_k$$

where: $\boldsymbol{f}'(\boldsymbol{x}_k) = \left.\dfrac{\partial \boldsymbol{f}(\boldsymbol{x})}{\boldsymbol{x}}\right|_{x=x_k}$, vector Δ_k is a given vector, and D_k is a matrix.

Note that x_k is the value of vector x_k at step k and s_k is a vector of the same length as x_k. The length of $\boldsymbol{x}$ is the number of parameters. For example, if we need to determine one parameter (d_{v1}), the length of $\boldsymbol{x}$ is 1 and the length of Δ_k is 1 as well. The size of the matrix D_k is 1x1, but the length of $f(x)$ is $3n$, where n is the number of measurement points. In our model, we have 3 elements, so then there are 3 measurement points. Then, the length of $f(x)$ is 9 and, similarly, the length of $f'(x_k)$ is 9.

We have $\|a\|_2$ as the norm matrix of vector a, which can be calculated as: $\|a\|_2 = \sqrt{a^T a}$ In addition, we have $\|a\|_2^2 = a^T a$. For example:

$$\|f'(x_k)s_k + f(x_k)\|_2 = \sqrt{[f'(x_k)s_k + f(x_k)]^T [f'(x_k)s_k + f(x_k)]}$$
$$\|f'(x_k)s_k + f(x_k)\|_2^2 = [f'(x_k)s_k + f(x_k)]^T [f'(x_k)s_k + f(x_k)]. \quad (9)$$

The trust region changes between the number of iterations corresponding to the real value and the assumed value of the target function. Then, we have:

$$\rho_k = \frac{r(x_k) - r(x_k + s_k)}{r(x_k) - \frac{1}{2}\|f'(x_k)s_k + f(x_k)\|_2^2} \quad (10)$$

This value must be greater than an extremely small positive number (normally 0.0001). In case the loop is not satisfied, we must reduce the trust region and repeat the iteration. When the ratio is close to 1, we can proceed to the next steps.

In the Levenberg-Marquardt algorithm, the condition of Eq. (8) must be satisfied with

$$\left[f'(x_k)^T f'(x_k) + \lambda_k D_k^T D_k\right] s_k = -f'(x_k)^T f(x_k) \quad (11)$$

where $\lambda_k \geq 0$.

7. Algorithm to determine the effective parameters

An algorithm to determine the effective parameters is presented in Fig. 1.

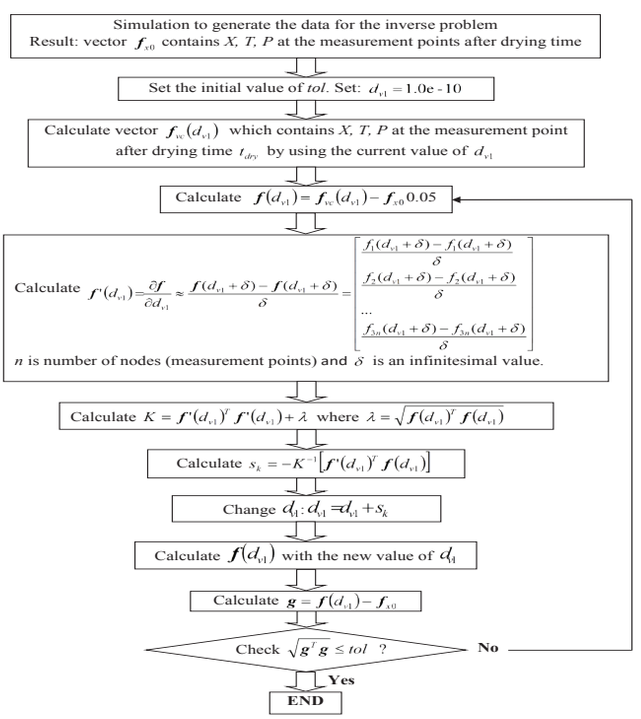

Fig. 1. Algorithm to determine the effective diffusivity.

8. Results and discussion

The convergence of the inverse problem is illustrated in Fig. 2. From this figure, we can see that after four iterations, the problem is converged. This result also shows that d_{v1} from the calculation is very consistent with the initial assumption value of d_{v1}. This result is very important because it determines the convergence of the inverse problem and also confirms the correctness of the algorithm.

Furthermore, we will apply this algorithm to determine the effective diffusivity. This parameter is calculated as follows:

$$D_{eff} = 0.2 \cdot \delta_{va} \cdot k_g \quad (12)$$

where δ_{va} [m^2s^{-1}] is the binary diffusivity of vapor in air, and

$$\delta_{va}(T,P) = D_{v1} \cdot \left(\frac{T}{T_R}\right)^{D_{v2}} \frac{P_R}{P_g} \quad (13)$$

where D_{v1}=2.26.01^{-5}, D_{v2}=1.81, and k_g is the relative permeability of gas.

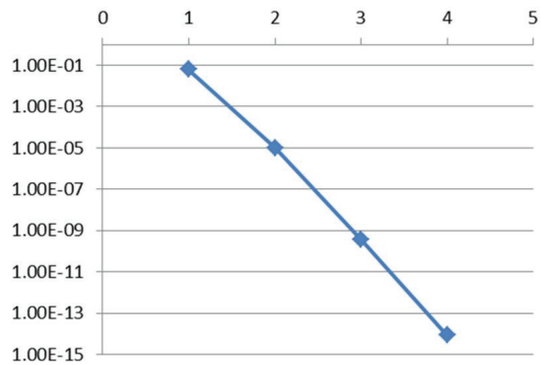

Fig. 2. Illustration of the convergence of the inverse problem.

In the inverse problem, we assume that both material parameters D_{v1} and D_{v2} are unknown. The inverse problem is then to retrieve the values D_{v1}= 2.26.10^{-5} and D_{v2}=1.81 given above. We then use the Levenberg-Marquardt algorithm first by assigning D_{v1} and D_{v2} to some initial values D_{v1}=D_{v1}^0 and D_{v2}=D_{v2}^0. After that, we solve the inverse problem to determine the computed parameters, which are denoted by D_{v1}^C and D_{v2}^C. In our calculation, we use a 20-node mesh (*N=20*) and 51 sampling points (*S=51*) for the forward problem. In the inverse problem, we choose the initial values D_{v1}^0=3.0.10^{-5} and D_{v2}^0=3.0. By solving the inverse problem, we get D_{v1}^C=2.26.10^{-5} and

D_{v2}^{C}=1.81. These values are very close to the value of D_{v1} and D_{v2} above.

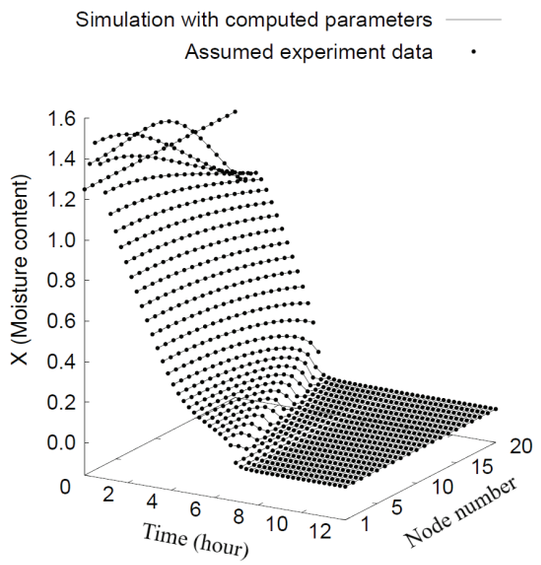

Fig. 3. Simulation of drying using data computed from solving the inverse problem *(N=20, S=51).*

The use of these two computed parameters in the forward problem is presented in Fig. 3. In this figure, the result of the inverse problem is shown, and the assumed input is presented by dotted lines (assumed experimental data) taken from a spherical specimen. From these data, the inverse problem is solved by iteratively changing the material parameters D_{v1} and D_{v2}. With each new set of material parameters, a simulation is done, and the moisture profiles (solid lines) are computed and compared with the assumed input data. The process is repeated until the simulated result (solid lines) matches the input data (dotted lines). In Fig. 3, the solid lines are the simulation result computed with the final values of material parameters D_{v1} and D_{v2}. It shows that, in this case, the drying kinetics are computed with good accuracy.

9. Conclusions

In this research, an algorithm to determine the effective parameters of the drying of porous media is presented. By solving the inverse problem, we obtained very reasonable results. However, more numerical tests should be realized to understand and improve the solution of the inverse problem. In the next step of our research, the model will be extended into two- and three-dimensional space. In addition, the use of real experimental data to evaluate the model will also be within the scope of our future research.

CRediT author statements

Hong Thai Vu: Methodology, Software, Resources, Writing - Review and Editing; Trung Dung Nguyen: Data curation, Software, Writing original draft preparation.

COMPETING INTERESTS

The authors declare that there is no conflict of interest regarding the publication of this article.

REFERENCES

[1] D. Michel, M. Quintard, J.R. Puiggali (1987), "Experimental and numerical study of pine wood drying at low temperature", *Drying Technology*, **87**, pp.185-193.

[2] S. Whitaker (1999), *The Method of Volume Averaging,* Kluwer Academic Publishers, 218pp.

[3] S. Whitaker (1977), "Simultaneous heat, mass, and momentum transfer in porous media: A theory of drying", *Advances in Heat Transfer*, **13**, pp.119-203, DOI: 10.1016/S0065-2717(08)70223-5.

[4] S. Whitaker (1998), "Coupled transport in multiphase systems: A theory of drying", *Advances in Heat Transfer*, **31**, pp.1-104, DOI:10.1016/S0065-2717(08)70240-5.

[5] S. Whitaker, W.T.H. Chou (2007), "Drying granular porous media - theory and experiment", *Drying Technology*, **1(1)**, pp.3-33, DOI: 10.1080/07373938308916768.

[6] G.R. Hadley (1985), "Numerical modeling of the drying of porous materials", *Proceedings of The 4th International Symposium on Drying, Drying'85*, pp.135-142, DOI: 10.1007/978-3-662-21830-3_15.

[7] A.C. Oliveira, E.O. Fernandes (1986), "Simulation of the convective drying of capillary-porous materials", *Proceedings of The 5th International Symposium on Drying, Drying'86*, pp.65-70.

[8] J.R. Puiggali, M. Quintard, S. Whitaker (1988), "Drying granular porous media: Gravitational effects in the isenthalpic regime and the role of diffusion models", *Drying Technology*, **6(4)**, pp.601-629, DOI: 10.1080/07373938808916401.

[9] M. Quintard, J.R. Puiggali (1986), "Numerical modelling of transport processes during the drying of a granular porous medium", *Heat and Technology*, **4(2)**, pp.37-57.

[10] C.K. Wei, H.T. Davis, E.A. Davis, et al. (1985), "Heat and mass transfer in waterladen sandstone: Convective heating", *AIChE Journal*, **31(8)**, pp.1338-1348, DOI: 10.1002/aic.690310813.

[11] H.C. Tien, K. Vafai (1990), "A synthesis of infiltration effects on an insulation matrix", *International Journal of Heat and Mass Transfer*, **33(6)**, pp.1263-280, DOI: 10.1016/0017-9310(90)90256-T.

[12] N. Boukadida, S.B. Nasrallah, P. Perre (2000), "Mechanism of two-dimensional heat and mass transfer during convective drying of porous media under different drying conditions", *Drying Technology*, **18(7)**, pp.1367-1388, DOI: 10.1080/07373930008917783.

[13] G.H. Crapiste, S. Whitaker, E. Rotstein (1988), "Drying of cellular material - I. A mass transfer theory", *Chemical Engineering Science*, **43**(**11**), pp.2919-2928, DOI: 10.1016/0009-2509(88)80045-9.

[14] P. Perre (1997), "Image analysis, homogenization, numerical simulation and experiment as complementary tools to enlighten the relationship between wood anatomy and drying behaviour", *Drying Technology*, **15**(**9**), pp.2211-2238, DOI: 10.1080/07373939708917359.

[15] G.A. Spolek, O.A. Plumb (1980), "A numerical model of heat and mass transport in wood during drying", *Proceedings of The 2nd International Symposium on Drying, Drying'80*, pp.84-92.

[16] S. Truscott (2004), *A Heterogenous Three-Dimensional Computational Model for Wood Drying*, PhD Thesis, University of Queensland.

[17] S.L. Truscott, I.W. Turner (2005), "A heterogeneous threedimensional computational model for wood drying", *Applied Mathematical Modelling*, **29**(**4**), pp.381-410, DOI: 10.1016/j.apm.2004.09.008.

[18] A.A. Moghaddam, A. Kharaghani, E. Tsotsas, et al. (2017), "Kinematics in a slowly drying porous medium: Reconciliation of pore network simulations and continuum modelling", *Physics of Fluids*, **29**(**2**), DOI: 10.1063/1.4975985.

[19] V.H. Thai, T. Metzger, E. Tsotsas (2018), "A comparison between the use of continuous and pore network approach in the simulation of the drying process of porous media with different pore size distributions", *Vietnam Journal of Chemistry*, **56**(**5**), pp.564-569, DOI: 10.1002/vjch.201800048.

[20] T. Metzger, T.H. Vu, A. Irawan, et al. (2008), "Pore-scale modelling of transport phenomena in drying", *Micro-Macro-Interactions in Structured Media and Particle Systems*, Springer, DOI: 10.1007/978-3-540- 85715-0_15.

[21] P. Perre, I.W. Turner (1999), "A 3-D version of transport: A comprehensive heat and mass transfer computational model for simulating the drying of porous media", *International Journal of Heat and Mass Transfer*, **42**, pp.4501-4521, DOI: 10.1016/S0017-9310(99)00098-8.

[22] P. Perre, I.W. Turner (2002), "A heterogeneous wood drying computational model that accounts for material property variation across growth rings", *Chemical Engineering Journal*, **86(1-2)**, pp.117-131, DOI: 10.1016/S1385-8947(01)00270-4.

[23] S.V. Patankar (1980), *Numerical Heat Transfer and Fluid Flow*, Hemisphere Co., 200pp.

[24] V.T. Hong (2006), "Influence of pore size distribution via effective parameters in a continuous drying model", *Proceedings of The 15th International Drying Symposium (IDS 2006)*, **A**, pp.554-561.

[25] H.T. Vu, E. Tsotsas (2018), "Mass and heat transport models for analysis of the drying process in porous media: A review and numerical implementation", *International Journal of Chemical Engineering*, **2019**, DOI: 10.1155/2018/9456418.

[26] H.T. Vu, E. Tsotsas (2019), "A framework and numerical solution of the drying process in porous media by using a continuous model", *International Journal of Chemical Engineering*, DOI: 10.1155/2019/9043670.

[27] H.T. Vu (2006), *Influence of Pore Size Distribution on Drying Behaviour of Porous Media by A Continuous Model*, PhD Thesis, Otto-von-Guericke-Universitat Magdeburg.

[28] D.W. Marquardt (1963), "An algorithm for the least-squares estimation of nonlinear parameters", *SIAM Journal of Applied Mathematics*, **11**, pp.431-441.

DOI: 10.31276/VJSTE.64(2).34-41

V.I.E.T.N.A.M. by 4D printing of composites

Suong V. Hoa[1*], Daniel I. Rosca[2]

[1]Concordia Center for Composites (CONCOM), Department of Mechanical, Industrial and Aerospace Engineering, Concordia University, 1455 Blvd. De Maisonneuve Ouest, Montreal, Quebec H3G 1M8, Canada
[2]Center for Research on High Performance Polymers and Composites (CREPEC), 817 rue Sherbrooke Ouest, Montreal, Quebec, Canada

Received 5 September 2021; revised 20 September 2021; accepted 26 October 2021

Abstract:

4D printing is a well-known manufacturing technique with widespread applications among many areas of the society. This paper presents an application of 4D printing of composites (4DPC) to make composite structures of complex geometries without the need for complex moulds. This application is illustrated through the formations of the letters V, i, e, t, n, a, and m, which form the word Vietnam. In the procedure, laminates made of carbon/epoxy prepregs are laid on a flat mould. The deposition of the prepregs on the flat mould is done using an automated fibre placement machine (AFP), which can be considered as a large size 3D printer. For a smaller structure, the prepreg deposition can be accomplished using an AFP machine or by hand lay-up. Upon curing and cooling to room temperature, the laminate transforms itself from a flat configuration to the shape of the intended letter, except for the letter V. The mechanism that enables this transformation relies on the anisotropy of the laminate. This method has many potential applications, particularly in the delivery of bulky three-dimensional structures to remote locations.

Keywords: **alphabet letters, anisotropy, 4D printing of composites.**

Classification number: **2.3**

1. Introduction

1.1. 3D printing and 4D printing

3D printing is a well-known manufacturing technique with widespread applications among many areas of society. One of the many 3D printing techniques is fused deposition modelling (FDM). In this technique, melted materials are squeezed through a nozzle of small diameter (fractions of a millimetre). The nozzle is moved by a robotic arm controlled by a computer program. The combination of the motion of the arm, together with controlling of the deposition of the material, provides the ability to produce structures of complex geometries without the need for a complex mould.

In normal 3D printing, the materials remain the same throughout the whole structure. 4D printing is an extension of 3D printing in which the material properties may vary along spatial coordinates [1-4]. Fig. 1 illustrates the concept of 4D printing. For comparison, the figure on the left shows the process of 3D printing where layers of material are deposited to make up a structure. The mandrel used for this deposition is just a simple flat plate. For 4D printing, the materials vary from point to point within the structure. This can be done by changing the materials during the course of the deposition. In Fig. 1, the black colour represents one material and the red colour represents another. Because these materials have different properties, they have different reactions to external stimuli such as the application of heat, electricity, moisture, or light, etc. After a flat stack of material has been deposited, as shown in the left figure, the stack of material is subjected to an external stimulus and this exposure will make the structure change its shape. This process is called self-reconfiguration as shown in the figure on the right. By properly controlling the type of materials and their positions, predetermined complex structures can be obtained.

Corresponding author: Email: hoasuon@alcor.concordia.ca

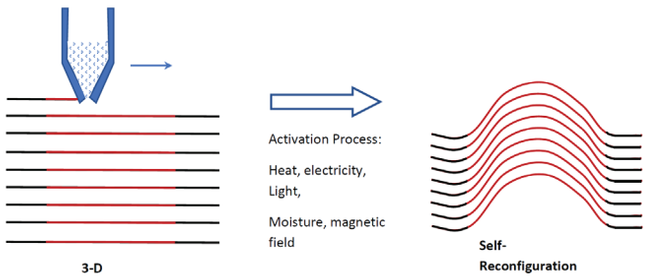

Fig. 1. Concept of regular 4D printing.

1.2. 4D printing of composites (4DPC)

The 4D printing method described above is usually operated with isotropic materials, such as elastomers and polymers. They have low stiffness (about 1 GPa) and strength (about 10 MPa). Indeed, 4DPC is a method that attempts to utilize long, continuous fibre-reinforced composite materials that have high stiffness (about 180 GPa) and strength (about 100 MPa) along the fibre direction. These materials have been used to construct major engineering structures such as the body of airplanes, automobiles, wind turbine blades, etc. Actually, these are not exotic materials only available in a lab, but are available commercially.

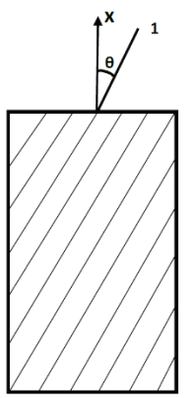

Fig. 2: A typical layer; the fibre direction can be along the length (x direction) of the layer (when θ=0) or off-axis (when θ is different from 0).

The basic element of a laminate is an individual layer (Fig. 2). Each layer has a thickness of about 0.125 mm. For comparison, a hair has a thickness of 0.100 mm. Within each layer, there are many fibres that are made of either carbon or glass. The diameter of each fibre is about 0.007 mm (carbon) or 0.010 mm (glass). The fibres are bonded together with an adhesive that is usually made of epoxy. One way to visualize a layer of composite material is like a piece of tape, except that there are strong, stiff fibres within the tape and that it is sticky on both sides.

The presence of the fibres gives the layer anisotropic behaviour, i.e. the material's properties depend on the direction. For example, the layer is very strong along the fibre direction but relatively weak transverse to the fibre direction. Engineering structures such as airplanes, automobiles, and wind turbine blades are usually subjected to loadings along many directions at the same time. As such, the use of a single layer does not satisfy all loading conditions. In order to address this, a laminate made of multiple layers is usually required. Within a laminate, layers of different orientations are stacked together. One example of a laminate is shown in Fig. 3 where it is made of up of layers at 0^o, 90^o, 45^o and -45^o. The lay-up sequence shown in this figure constitutes a symmetric laminate. What this means is that the laminate has a plane of symmetry at mid thickness as there are identical materials and fibre orientations and at equal distances from the mid plane. The use of symmetric laminates avoids distortion of the laminate due to manufacturing and it simplifies the understanding and design behaviour of the laminates. Symmetric laminates have been used almost exclusively by the worldwide composites community for more than seven decades.

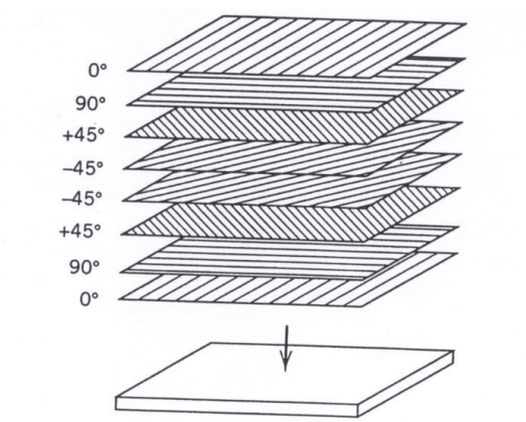

Fig. 3. A laminate made of 0^o, 90^o, 45^o, and -45^o.

The method of 4DPC uses asymmetric laminates, which is not the normal way. Indeed, for most applications of composites so far, asymmetry and anisotropy have been considered as a liability. However, asymmetric laminates are the main mechanism behind 4DPC and this is due to the complex behaviour of the laminate. Actually, asymmetry is considered an asset because it gives rise to the fourth dimension, i.e., the self-reconfiguration of the structure when subjected to the change in temperature. To understand and predict the change in shape of a structure,

it is necessary to utilize some theory. M.L. Dano and M.W. Hyer (2002) [5] and a few other researchers [6, 7] have examined the behaviour of asymmetric laminates upon cooling from cure temperature. It was shown that these laminates can exhibit different shapes at different temperatures and geometrical configurations. Some can take a saddle shape and some can take the shape of circular cylinders. It has also been shown that for plates at room temperature where the length over thickness ratio is significantly large, the radius of curvature obtained using the energy approach by Dano, Hyer and others approximate that obtained using laminate theory. As such, for a situation where the shape at room temperature is concerned, and for thin plates with large length over thickness ratios, the use of laminate theory is sufficient for the prediction of the shape. A few salient features of laminate theory are presented below.

1.3. Laminate theory [8]

The main purpose of laminate theory is to obtain the properties of the laminate, which is a stack of individual layers (laminas) each with a specific material, thickness, and fibre orientation, from the properties of the individual layers.

From the lamina's properties, the properties of the laminate, which consists of a number of laminae with a certain stacking sequence, can be obtained as:

$$4_{ij} = \int \overline{Q_{ij}} dz \qquad B_{ij} = \int \overline{Q_{ij}} z dz \qquad D_{ij} = \int \overline{Q_{ij}} z^2 dz \tag{1}$$

where i, j = 1, 2, 6, and z are the structural coordinates along the thickness of the laminate and:

$$\begin{aligned}
\overline{Q_{11}} &= Q_{11}\cos^4\theta + 2(Q_{12}+2Q_{66})\cos^2\theta\sin\theta + Q_{22}\sin^4\theta \\
\overline{Q_{12}} &= (Q_{11}+Q_{22}-4Q_{66})\cos^2\theta\sin^2\theta + Q_{12}(\cos^4\theta+\sin^4\theta) \\
\overline{Q_{16}} &= (Q_{11}-Q_{12}-2Q_{66})\cos^3\theta\sin\theta + (Q_{12}-Q_{22}+2Q_{66})\cos\theta\sin^3\theta \\
\overline{Q_{22}} &= Q_{11}\sin^4\theta + 2(Q_{12}+2Q_{66})\sin^2\theta\cos^2\theta + Q_{22}\cos^4\theta \\
\overline{Q_{26}} &= (Q_{11}-Q_{12}-2Q_{66})\cos\theta\sin^3\theta + (Q_{12}-Q_{22}+2Q_{66})\cos^3\theta\sin\theta \\
\overline{Q_{66}} &= (Q_{11}+Q_{22}-2Q_{12}-2Q_{66})\sin^2\theta\cos\theta + Q_{66}(\cos^4\theta+\sin^4\theta)
\end{aligned} \tag{2}$$

with

$$\begin{aligned}
Q_{11} &= \frac{E_1}{1-\nu_{12}\nu_{21}} \\
Q_{12} &= \frac{\nu_{12}E_2}{1-\nu_{12}\nu_{21}} = \frac{\nu_{21}E_1}{1-\nu_{12}\nu_{21}} \\
Q_{22} &= \frac{E_2}{1-\nu_{12}\nu_{21}} \\
Q_{66} &= G_{12}
\end{aligned} \tag{3}$$

where, θ is the angle between the fibre direction in a layer relative to the x coordinate of the laminate, as shown in Fig. 2, E_1 is modulus along the fibre direction, E_2 is modulus transverse to the fibre direction, G_{12} is in-plane shear modulus, ν_{12} is major Poisson ratio, and ν_{21} is minor Poisson ratio with the relation $E_1\nu_{21}=E_2\nu_{12}$. Typical properties of a carbon/epoxy material are shown in Table 1.

Table 1. Properties of a typical carbon/epoxy unidirectional composite material [8].

Modulus along fibre direction E_1 (GPa)	155 (22.48 msi)
Modulus transverse to fibre direction E_2 (GPa)	12.10 (1.75 msi)
In plane shear modulus G_{12} (GPa)	3.20 (0.464 msi)
Major Poisson ratio ν_{12}	0.248
Coefficient of thermal expansion along fibre direction, α_1 (10^{-6}/°C)	-0.018 (-0.01x10^{-6}/°F)
Coefficient of thermal expansion transverse to fibre direction, α_2 (10^{-6}/°C)	24.3 (13.5 x 10^{-6}/°F)
Moisture expansion coefficient along fibre direction, β_1 (%/%M)	146
Moisture expansion coefficient transverse to the fibre direction, β_2 (%/%M)	4770

For the case of a laminate subjected to a temperature change ΔT, the relations for the strains and curvatures in terms of the stress and moment resultants are given as:

$$\begin{bmatrix} \varepsilon_x^o \\ \varepsilon_y^o \\ \gamma_{xy}^o \\ \kappa_x^o \\ \kappa_y^o \\ \kappa_{xy}^o \end{bmatrix} = \begin{bmatrix} a_{11} & a_{12} & a_{16} & b_{11} & b_{12} & b_{16} \\ a_{12} & a_{22} & a_{26} & b_{21} & b_{22} & b_{26} \\ a_{16} & a_{26} & a_{66} & b_{61} & b_{62} & b_{66} \\ b_{11} & b_{21} & b_{61} & d_{11} & d_{12} & d_{16} \\ b_{12} & b_{22} & b_{62} & d_{12} & d_{22} & d_{26} \\ b_{16} & b_{26} & b_{66} & d_{16} & d_{26} & d_{66} \end{bmatrix} \begin{bmatrix} N_x^T \\ N_y^T \\ N_{xy}^T \\ M_x^T \\ M_y^T \\ M_{xy}^T \end{bmatrix} \tag{4}$$

where, the column on the left-hand side represents the in-plane strains and curvatures at the mid plane of the laminate, the square matrix represents components of the compliance, and the column on the right-hand side represents the thermal stress resultants and thermal moment resultants, respectively.

The inverse of the relations in Eq. (4) is:

$$\begin{bmatrix} N_x^T \\ N_y^T \\ N_{xy}^T \\ M_x^T \\ M_y^T \\ M_{xy}^T \end{bmatrix} = \begin{bmatrix} A_{11} & A_{12} & A_{16} & B_{11} & B_{12} & B_{16} \\ A_{12} & A_{22} & A_{26} & B_{12} & B_{22} & B_{26} \\ A_{16} & A_{26} & A_{66} & B_{16} & B_{26} & B_{66} \\ B_{11} & B_{12} & B_{16} & D_{11} & D_{12} & D_{16} \\ B_{12} & B_{22} & B_{26} & D_{12} & D_{22} & D_{26} \\ B_{16} & B_{26} & B_{66} & D_{16} & D_{26} & D_{66} \end{bmatrix} \begin{bmatrix} \varepsilon_x^o \\ \varepsilon_y^o \\ \gamma_{xy}^o \\ \kappa_x \\ \kappa_y \\ \kappa_{xy} \end{bmatrix} \tag{5}$$

where the A_{ij}, B_{ij}, D_{ij} are given by Eq. (1).

The thermal stress resultants and thermal moment resultants are given as:

$$N_x^T = \int_{-\frac{H}{2}}^{\frac{H}{2}} (\overline{Q_{11}}\alpha_x^T + \overline{Q_{12}}\alpha_y^T + \overline{Q_{16}}\alpha_{xy}^T)\Delta T\, dz \tag{6A}$$

$$N_y^T = \int_{-\frac{H}{2}}^{\frac{H}{2}} (\overline{Q_{12}}\alpha_x^T + \overline{Q_{22}}\alpha_y^T + \overline{Q_{26}}\alpha_{xy}^T)\Delta T\, dz \quad (6B)$$

$$N_{xy}^T = \int_{-\frac{H}{2}}^{\frac{H}{2}} (\overline{Q_{16}}\alpha_x^T + \overline{Q_{26}}\alpha_y^T + \overline{Q_{66}}\alpha_{xy}^T)\Delta T\, dz \quad (6C)$$

$$M_x^T = \int_{-\frac{H}{2}}^{\frac{H}{2}} (\overline{Q_{11}}\alpha_x^T + \overline{Q_{12}}\alpha_y^T + \overline{Q_{16}}\alpha_{xy}^T)\Delta T z\, dz \quad (6D)$$

$$M_y^T = \int_{-\frac{H}{2}}^{\frac{H}{2}} (\overline{Q_{12}}\alpha_x^T + \overline{Q_{22}}\alpha_y^T + \overline{Q_{26}}\alpha_{xy}^T)\Delta T z\, dz \quad (6E)$$

$$M_{xy}^T = \int_{-\frac{H}{2}}^{\frac{H}{2}} (\overline{Q_{16}}\alpha_x^T + \overline{Q_{26}}\alpha_y^T + \overline{Q_{66}}\alpha_{xy}^T)\Delta T z\, dz \quad (6F)$$

where the α terms are the off-axis coefficients of thermal expansion and are given as:

$$\alpha_x = \alpha_1 m^2 + \alpha_2 n^2;\ \alpha_y = \alpha_1 n^2 + \alpha_2 m^2;\ \alpha_{xy} = 2(\alpha_1 - \alpha_2)mn \quad (7)$$

and α_1 and α_2 are the on-axis coefficients of thermal expansion of a particular layer, as given in Table 1.

The strains and curvatures due to the effect of cooling can be written as:

$$\begin{Bmatrix} \varepsilon_x^o \\ \varepsilon_y^o \\ \gamma_{xy}^o \\ \kappa_x^o \\ \kappa_y^o \\ \kappa_{xy}^o \end{Bmatrix} = \begin{bmatrix} a_{11} & a_{12} & a_{16} & b_{11} & b_{12} & b_{16} \\ a_{12} & a_{22} & a_{26} & b_{21} & b_{22} & b_{26} \\ a_{16} & a_{26} & a_{66} & b_{61} & b_{62} & b_{66} \\ b_{11} & b_{21} & b_{61} & d_{11} & d_{12} & d_{16} \\ b_{12} & b_{22} & b_{62} & d_{12} & d_{22} & d_{26} \\ b_{16} & b_{26} & b_{66} & d_{16} & d_{26} & d_{66} \end{bmatrix} \begin{bmatrix} N_x^T \\ N_y^T \\ N_{xy}^T \\ M_x^T \\ M_y^T \\ M_{xy}^T \end{bmatrix} \quad (8)$$

By obtaining the strains and curvatures as shown in the relations of Eq. (8), the deformation of the laminate due to cooling from either the curing temperature or processing temperature can be obtained.

1.4. 3D printer for composites

A normal 3D printer is usually small and can sit on a desktop. For the case of long, continuous fibre composites, an automated fibre placement (AFP) machine is used [9]. Actually, AFP machines have been designed to make large structures such as an airplane's body or wings. As such, these machines are huge and costly. The initial intention is not for 3D printing. However, this manufacturing technique is additive and has all features of a 3D printer. Laminates used in 4DPC can be made either by hand lay-up or by the use of an AFP machine.

2. Potential applications of 4D printing of composites

4DPC have many potential applications and they are given in the following subsections.

2.1. Manufacturing of composite structures of complex shape using only a simple flat mould

One example is the manufacturing of an "S" shape structure as shown in Fig. 4 [10]. If one were to use the conventional method of composite manufacturing, S-shaped moulds would need to be made, and this involves time and money.

Another application is the case of a composite flower as shown in Fig. 5. For this structure, 4DPC is the only technique that can accomplish the manufacturing. Indeed, normal composite manufacturing methods cannot make this structure.

Fig. 4. Composite "S" shape made by 4DPC [10].

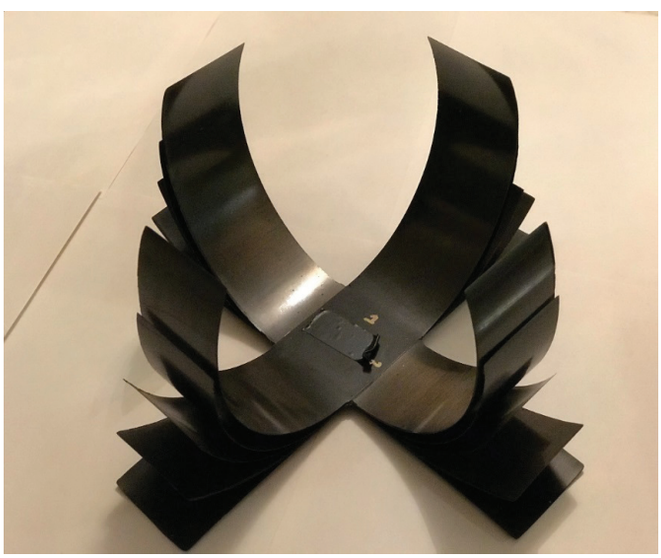

Fig. 5. Composite flower made by 4DPC.

Another potential application of 4DPC is the manufacturing of composite leaf springs as shown in Fig. 6 [11]. This spring has an elastic constant of 486 N/cm and it was subjected to more than 1 million cycles (from curved to completely flat and back) without any sign of degradation.

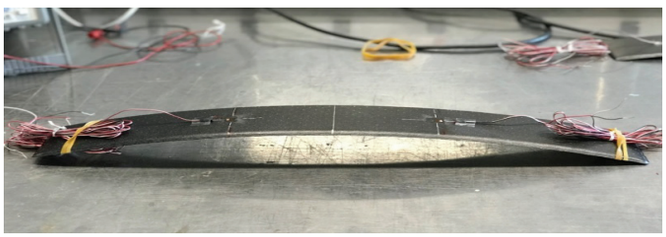

Fig. 6. Composite leaf spring made by 4DPC [11].

2.2. Manufacturing of corrugated core for flexible wings

The efficiency of aircraft wings can be significantly improved by changing their shape during flight. This is called "morphing" [12]. Morphing can be accomplished by adjusting the angle between the trailing edge relative to the body of the wing as shown in Fig. 7 (left). By making the core of the trailing edge in the form of corrugation the movement of the trailing edge is facilitated [13]. The use of 4DPC enables efficient and low-cost manufacturing of the corrugated composites.

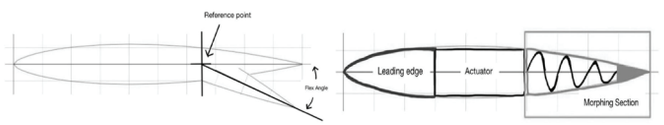

Fig. 7. Morphing of aircraft wings (left: shape changing and right: corrugated composite core).

2.3. Efficient packaging

Another potential application of 4DPC is efficient packaging for transportation. In a situation where some structure, such as housing, needs to be installed at a remote location such as outer space or the North or South poles, where access to manufacturing facilities are scarce, the use of 4DPC can offer a solution. The complex structure can be transported in the form of simple flat structures. Upon arrival, the application of the external stimulus can be imposed thereby transforming the flat structure in to a complex 3D structure.

Along the lines of the ability to transform a flat stack of layers into a three-dimensional structure, the idea of trying out the concept on forming letters of the English alphabet were attempted. Indeed, each letter in the English alphabet has different degrees of curvature and complexity. Hopefully, the experience learned during these exercises can be useful for real structures.

3. Illustrations of capacity of the technique through letters of the alphabet

In an effort to examine the ability of 4D printing of composites, the concept of 4DPC can be examined to see if it can be used to make structures of complex geometries. One example would be for the case of letters of the alphabet. The formation of the letters that make up the word CONCORDIA was made [14]. In this paper, the lay-up sequences for the letters V, e, t, m are developed. These letters, together with the letters already made for the word CONCORDIA can be put together to make up the word Vietnam.

4. Principles of the procedure

There are basically four guidelines to form complex geometries from flat laminates for the technique of 4DPC. These are:

4.1. Symmetric laminates remain flat in both the initial and final configurations

In symmetric laminates such as those with lay-up sequences [0/90]s or [0n/90n]s, the laminate does not change its configuration when its temperature is reduced from curing temperature to room temperature. This reduces complexity in the design of structures using composite materials. As such these laminates have been used for many years in making many engineering structures such as airplane and automotive structures. These types of laminates are used to serve as the base for many letters in this paper.

4.2. Unidirectional laminates are flat

Unidirectional laminates are those that contain only fibres along one direction, such laminates with lay-up sequence $[0]_1$, $[0]_3$ etc. A combination of these laminates such as $[0]_1+[0]_3=[0]_4$ is also a unidirectional laminate. Upon cooling from cure temperature to room temperature, this laminate remains flat.

4.3. Un-symmetric cross ply laminates show curvature

Un-symmetric cross-ply laminates are those consisting of layers at 0^o orientation and 90^o orientation, and are not

symmetric. The laminate sequence has the form $[0_m/90_n]$ where m and n are integers. For example, for the letter "a", there are regions where the laminate has the lay-up sequence $[0/90_3]$, where m=1 and n=3. Upon curing and cooling to room temperature, this laminate will change its shape from flat to curved where the 90° layers are on the concave side.

4.4. Use of non-stick separator to prevent bonding

In order to facilitate the transformation from flat configuration to curved configuration, it is necessary for some surfaces not to stick together. There are regions in some of the letters that should be separated after curing and cooling. Consider the case of the letter "a" in Fig. 14. The red line shows a non-stick caul plate. Its function is to prevent bonding between the base and the laminate above. At the beginning during the deposition of the layers, all layers are flat and are on top of each other. Since the prepregs are adhesive, they need to be separated such that when they cure and solidify, the layers should not bond to each other. This allows the rise of the majority of the "a" letter above the base plate.

Using the above 4 mechanisms, the lay-up sequences for the letters making up the word VIETNAM are presented below.

4.5. Letter V

In the 7 letters making up the word Vietnam, the letter V is the exception where the 4DPC does not work well. The reason is due to the limit of the minimum curvature that can be made using current commercially available composite materials. Using the material properties in Table 1 and the procedure given in equation (1) to (8), the radius of curvature for a [0/90] laminate is 5 cm [10]. Using the lay-up sequence as shown in Fig. 8 would give a structure looking similar to the letter U. This represents the lower limit of the radius of curvature at a corner.

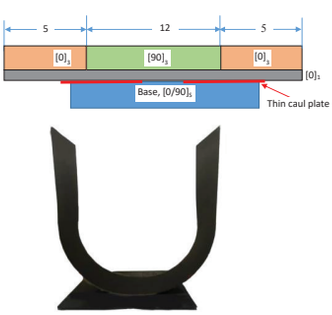

Fig. 8. Lay-up sequence and the letter U.

In order to obtain a sharp corner for the letter V, an alternate procedure (not 4DPC) is used as shown in Fig. 9. In this procedure, two symmetric laminates of lay-up sequence [0/90/0] are bonded onto a thin aluminum piece. The aluminum piece is then bent to the desired radius.

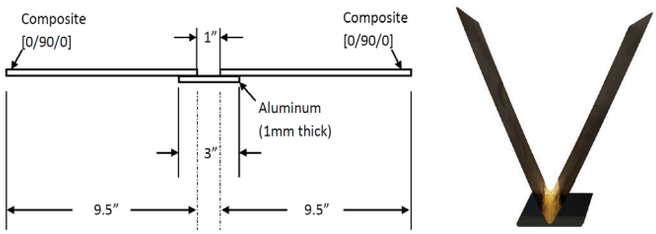

Fig. 9. Lay-up arrangement and letter V.

4.6. Letter "i"

The lay-up sequence for the letter "i" was already presented in [14]. It is included here for completeness of the presentation. The lay-up configuration for the letter "i" is shown in Fig. 10.

- First a base laminate of symmetric lay-up [0/90]s is made (blue part).
- A thin layer of metal (7 inch long) is placed from the right side of the base plate (red line). This shim is used to prevent bonding of the upper to the lower part.
- A layer of unidirectional composite [0], with length of 12 inch is laid over.
- From the left side, a laminate of three layers of $[0]_3$ of length 2 inch is laid. This is followed by a laminate of $[90]_3$ of length 6 inch, and finally by another laminate of $[0]_3$ with 4 inch length.

After curing and cooling to room temperature, the assembly changes its shape to a curved shape of the letter "i" as shown in the bottom figure of Fig. 10.

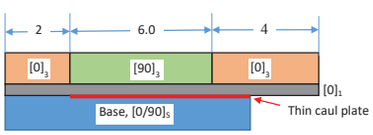

Fig. 10. Lay-up sequence and the letter "i".

4.7. Letter e

The lay-up sequence for the letter e is shown in Fig. 11. The letter e can be considered as a double letter "c". Note that there two shim locations (red line) in order to separate the two parts from each other.

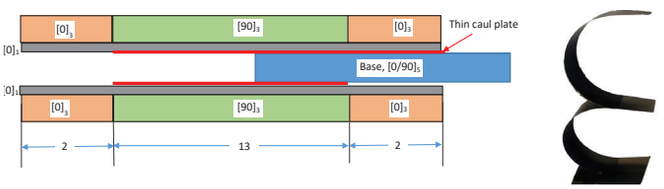

Fig. 11. Lay-up sequence and the letter "e".

4.8. Letter t

The lay-up sequence for the letter "t" is as shown in Fig. 12. Note that the red shims are broken at strategic locations in order to allow for bonded regions and non-bonded regions.

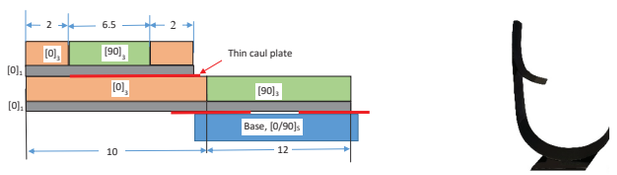

Fig. 12. Lay-up sequence and the letter "t"

4.9. Letter n

The lay-up sequence for the letter "n" was already presented in [14]. It is included here for completeness of the presentation.

The configuration of letter "n" is shown in Fig. 13. The configuration looks like a fork with the upper side and lower side separated by a middle portion.

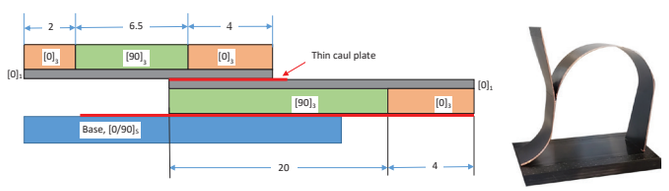

Fig. 13. Lay-up sequence and the letter "n".

Figure 13 (bottom) shows a photograph of the letter "n" after manufacturing. The bond at the lower left side of the letter "n" in Fig. 13 (bottom) corresponds to the bond on the left side in Fig. 13 (top). The right portion of the upper fork in bottom figure corresponds to the right portion of the upper fork in the top figure. It separates from curved portion of the letter "n" due to the non-stick layer as shown by the red line in top figure. The middle part in top figure corresponds to the right portion of the letter "n" in bottom figure.

4.10. Letter "a"

The lay-up sequence for the letter "a" was already presented in [14]. It is included here for completeness of the presentation.

The lay-up arrangement for the letter "a" is as shown in Fig. 14. The top figure shows the intended fibre orientations before the lay-up process, which shows an apparent gap between the right sides of the upper fork and lower fork. The middle figure shows the lay-up arrangement after the lay-up process, which shows a bonding region between the right sides of the upper fork and lower fork. Note that in the top figure, the gap between the upper fork and lower fork is exaggerated, since the thickness of 4 layers of 0° would be only 0.6 mm.

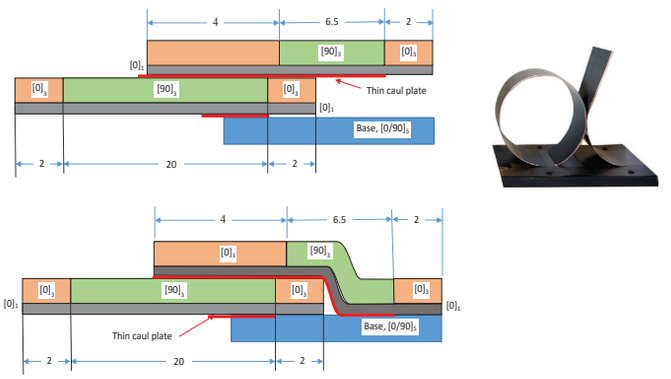

Fig. 14. Lay-up sequence and the letter "a".

The bottom figure 14 shows a photograph of the letter "a" after manufacturing.

4.11. Letter m

Figure 15 shows the lay-up sequence and the final letter "m". Note that the bonding between the base plate and the actual letter is over 2 inch of the $[0]_3$ laminate on the right hand side.

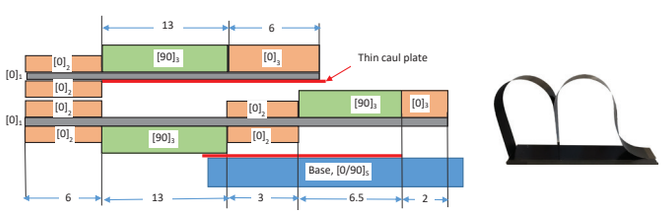

Fig. 15. Lay-up sequence and the letter "m".

4.12. The final word "Vietnam"

The above letters were placed together to make the word Vietnam as shown in Fig. 16.

Fig. 16. Final configuration of the word "Vietnam".

5. Conclusions

In this paper, the lay-up arrangements for the letters "V, i, e, t, n, a, m" have been presented. The principle of 4D printing of composites (4DPC) was used such that no special moulds of complex geometries were required. Instead, the anisotropies of the lay-up sequences allow only flat layers that are laid on flat moulds to begin with. After curing and cooling to room temperature, the flat layers curl up and make the different letter configurations. The principle of 4DPC can be extended to manufacture composite structures of complex geometries without the need for complex moulds and is the basis of the concept of mouldless composite manufacturing. The procedure developed during these exercises can be used to manufacture engineering structures of complex shapes.

CRediT author statement

Suong V. Hoa: Data analysis and Interpretation, Writing and Manuscript revising; Daniel I. Rosca: Method, Data analysis and Writing.

COMPETING INTERESTS

The authors declare that there is no conflict of interest regarding the publication of this article.

REFERENCES

[1] S. Tibbits (2013), "The emergence of 4D printing", TED conference, https://www.ted.com/talks/skylar_tibbits_the_emergence_of_4d_printing, accessed 8 August 2021.

[2] M. Farhang, M.S.H. Hassani, L. Xun, et al. (2017), "A review of 4D printing", *Materials and Design*, **122**, pp.42-79, DOI: 10.1016/j.matdes.2017.02.068.

[3] M. Rafiee, R.D. Farahani, D. Theriault (2020), "Multi-material 3D and 4D printing", *Advanced Science*, **7**, DOI: 10.1002/advs.201902307.

[4] M.Q. Zafar, H. Zhao (2020), "4D printing: Future insight in additive manufacturing", *Metals and Materials International*, **26**, pp.564-585, DOI: 10.1007/s12540-019-00441-w.

[5] M.L. Dano, M.W. Hyer (2002), "Snap through behavior of unsymmetric fibre reinforced composite laminates", *International journal of Solids and Structures*, **39(1)**, pp.175-198, DOI: 10.1016/S0020-7683(01)00074-9.

[6] M. Schlecht, K. Schulte (1999), "Advanced calculations of the room temperature shapes of unsymmetric laminates", *J. Composite Materials*, **33(16)**, DOI: 10.1177/002199839903301601.

[7] A. Hamamoto, M.W. Hyer (1987), "Non-linear temperature-curvature relationships for unsymmetric graphite-epoxy laminates", *Int. Journal of Solids and Structures*, **23(7)**, pp. 919-935, DOI: 10.1016/0020-7683(87)90087-4.

[8] M. Hyer (2008), *Introduction To the Principles of Composite Materials*, Destech.

[9] V.S. Hoa (2018), "Automated composites manufacturing", *Vietnam Journal of Science, Engineering and Technology*, **60(1)**, pp.28-37 (in Vietnamese).

[10] H.S. Van (2017), "Factors affecting the properties of composites made by 4D printing (mouldless composites manufacturing), *Advanced Manufacturing: Polymers and Composites Science*, **3(3)**, pp.101-109, DOI: 10.1080/20550340.2017.1355519.

[11] H.S. Van (2019), "Development of composite springs using 4D printing method", *Composite Structures*, **210**, pp.869-876, DOI: 10.1016/j.compstruct.2018.12.003.

[12] T. Yokozeki, S. Takeda, T. Osagawara, et al. (2006), "Mechanical properties of corrugated composites for candidate materials of flexible wing structures", *Composites Part A: Applied Science and Manufacturing*, **37(10)**, pp.1578-1586, DOI: 10.1016/j.compositesa.2005.10.015.

[13] D.T. Filipovic, G.R. Kress (2019), "Manufacturing method for high-amplitude corrugated thin- walled laminates", *Composite Structures*, **222**, DOI: 10.1016/j.compstruct.2019.110925.

[14] H.S. Van, D. Rosca (2020), "Formation of letters of the alphabet using 4d printing of composites", *Materials Today Communications*, **25**, DOI: 10.1016/j.mtcomm.2020.101115.

DOI: 10.31276/VJSTE.64(2).42-49

The influence of fly ash and foam contents on the properties of lightweight foamed concrete

Ngo Si Huy*, Mai Thi Hong

Department of Engineering and Technology, Hong Duc University, 565 Quang Trung Street, Dong Ve Ward, Thanh Hoa City, Thanh Hoa, Vietnam

Received 23 February 2022; revised 10 March 2022; accepted 4 May 2022

Abstract:

Due to rapid industrialization and modernization, a large number of both fly ash (FA) and ground granulated blast furnace slag (GGBFS), both by-products from thermal power plants and steel factories, are increasing day by day. Thus, recycling these industrial wastes to produce lightweight foamed concrete (LFC) was investigated in this study. Eight LFC mixtures were designed with different FA content and foam content to investigate their effect on the properties of LFC. Test results indicate that both FA and foam contents had a significant influence on the properties of LFC. The quality of LFC decreased with increasing foam content while the presence of FA improved its properties. The properties of LFC and its dry unit weight had a close relationship, and the correlation between them was described by linear regression. For example, high foam content resulted in more void volumes inside the LFC thus reducing its properties. Meanwhile, the presence of FA minimized the void volume and enhanced the LFC's properties. All LFCs in this investigation showed good quality, which were classified as grade M3.5-12.5 based on TCVN 9029:2017, which means they can be used as unburnt bricks with significantly low unit weight and thermal conductivity.

Keywords: **fly ash, foam content, GGBFS, lightweight foamed concrete.**

Classification number: **2.3**

1. Introduction

In recent years, the demand for electricity as well as steel during industrialization and modernization has been increasing rapidly in Vietnam. Many thermal power plants, iron factories, and steel factories have been built, which release a large amount of industrial waste. As estimated in 2019, about 16.4 million tons of FA and bottom ash were emitted from thermal power plants and a small part of which has been used to replace cement and fine aggregate in the production of concrete and unfired bricks [1]. However, the vast majority of these ashes are landfilled in a storage yard. The risk of overcapacity storage yards and leaks of these wastes are tremendous and can cause environmental pollution. On the other hand, approximately 1.12 million tons of GGBFS were generated in 2021 [2] and a part of which was used to partially replace cement for several important domestic construction projects. However, there are still huge amounts of FA and GGBFS that need to be recycled instead of being buried in storage yards. Moreover, the use of FA and GGBFS in the construction industry has been studied by many researchers around the world. Previous studies have proved that FA and GGBFS can be used as alternative binder materials in soil stabilization [3-6] residual granitic soil (RGS, controlled low strength materials [7, 8] coal ash, gypsum, red mud, paste and mortar [9, 10], and LFC [11-13]. Recycling FA and GGBFS in construction materials contributes to reducing the use of cement and minimizing their negative effects on the environment.

Foamed concrete was first described in 1923 as possessing outstanding advantages such as light weight and good sound and thermal insulation [14]. With its lighter weight, the use of LFC contributes to reducing static loads on a structure and thus reduces the sizes of structures and foundations. Using foamed concrete also conserves materials and reduces production, transportation, and construction costs. Therefore, LFC has received a lot of attention from researchers around the world in recent years. However, some studies have indicated that the biggest challenge to the widespread use of LFC is that its compressive strength is too low, so its application is still limited [15, 16] high workability (flowing and self-compacting). Currently, it has only been used as insulating walls, heat resistant roofs, and lightweight brick instead of unburnt bricks. In recent years, several studies have investigated the use of industrial wastes such as FA and GGBFS in producing

*Corresponding author: Email: ngosihuy@hdu.edu.vn

LFC [11-13]. However, either FA or GGBFS alone were used in these previous studies and works on the combination of both FA and GGBFS in the production of LFC are lacking.

The quality of LFC is affected by many factors such as curing conditions, quality of original composition materials, mixture proportion, and its dry density [17]. Among these factors, dry density has the most impact on LFC's properties [17-19]. However, most previous studies have only focused on the effect of dry density on the compressive strength of LFC and its effect on other properties still needs to be investigated. Therefore, in this study, both FA and GGBFS were used to replace 40-60% of cement in producing LFC. The effect of foam and FA contents on the engineering properties of LFC such as compressive strength, ultrasonic pulse velocity (UPV), water absorption, and thermal conductivity were investigated. The correlation between LFC's properties and its dry unit weight were established. The microstructure of LFC was also investigated using scanning electron microscopy (SEM).

2. Materials and experimental programs

2.1. Materials

A blend of cement, FA, and GGBFS was used as the binder in this study and their properties are given in Table 1. The specific gravity of cement is the highest, followed by GGBFS and FA. Cement type PCB40 was sourced from Nghi Son Company, while FA and GGBFS were taken from the Nghi Son Coal Power Plant and Hoa Phat Steel Factory, respectively. The main compositions of cement and GGBFS are SiO_2 and CaO, meanwhile, the main compositions of FA are SiO_2 and Al_2O_3. Fly ash with a summation of SiO_2, Al_2O_3, and Fe_2O_3 above 70% is classified as type-F based on TCVN 10302:2014 [20]. The natural appearance and morphology of cement, FA, and GGBFS observed by SEM are shown in Fig. 1. According to Fig. 1, the cement particle size is the largest among the three binder materials. While cement and GGBFS have irregular shapes, FA is spherical.

Table 1. Properties of binder materials.

Categories		Cement	FA	GGBFS
Physical properties	*Specific gravity*	3.12	2.16	2.84
	Loss on ignition (%)	0.5	6.9	0.4
Chemical composition (wt.%)	SiO_2	22.3	55.7	36.9
	Al_2O_3	6.7	21.7	12.4
	Fe_2O_3	4.7	6.6	-
	CaO	55.5	1.1	30.7
	MgO	2.4	2.2	14.8
	SO_3	1.3	-	0.4
	Na_2O	0.6	0.2	0.3
	K_2O	0.7	2.1	0.9
	TiO_2	0.7	0.7	0.4

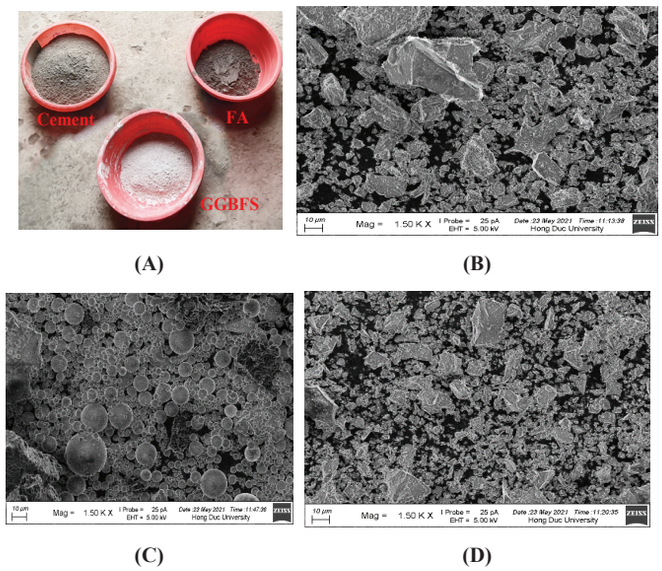

Fig. 1. (A) Natural appearance of binder materials and SEM micrographs of (B) cement, (C) FA, and (D) GGBFS.

Other compositions of LFC are river sand, tape water, superplasticizer (SP), and foam. The sand had particle sizes ranging from 0.15 to 0.63 mm and a density of 2680 kg/m^3 was used as the fine aggregate. SP, with a density of 1.05±0.2 kg/m^3 was utilized to reduce the water content and ensure the flowability of fresh concrete. A foaming agent named EABASSOC was used with water in a ratio of 1/40. Foam was created by using a foam generator as shown in Fig. 2.

Fig. 2. Foam generation.

2.2. Mix proportions

Eight LFC mixtures were designed with the proportions presented in Table 2. The GGBFS content was equal to 30% of the total binder by weight, while the FA contents are 10 and 30% in M10 and M30 mixtures, respectively. Previous studies have indicated that increasing the sand content results in a reduction of the compressive strength of LFC [21, 22]. Thus, the amount of sand in this investigation was taken as 0.25 times the total binder content (cement, FA,

Table 2. Mixture proportions.

No.	Mixture	W/B	Ingredient proportions (kg/m^3)						Foam (m^3)
			Cement	*FA*	*GGBFS*	*Sand*	*Water*	*SP*	
1	M10-1	0.22	571.7	95.3	285.9	238.2	211.8	1.5	0.37
2	M10-2		533.8	89.0	266.9	222.4	197.7	1.4	0.41
3	M10-3		469.0	78.2	234.5	195.4	173.7	1.3	0.48
4	M10-4		456.4	76.1	228.2	190.2	169.0	1.2	0.50
5	M30-1	0.2	402.1	301.5	301.5	251.3	201.0	1.4	0.33
6	M30-2		380.9	285.7	285.7	238.0	190.4	1.3	0.37
7	M30-3		334.0	250.5	250.5	208.8	167.0	1.2	0.44
8	M30-4		315.3	236.5	236.5	197.0	157.6	1.1	0.47

and GGBFS). The SP content and ratio of water to binder were selected so that the concrete mixtures had sufficient workability. It is noticed that the workability of the paste (mixture of binder, sand, water, and SP) is very important to the successful fabrication of the samples. If the paste is too dry or too wet, the samples will be segregated or have high-volume shrinkage after casting. Based on the extensive experiment, the paste has suitable workability as determined by a flow diameter of around 18±2 cm as measured in accordance with TCVN 3121:2003 [23].

The first group included four mixtures (from M10-1 to M10-4) and was designed with a FA content of 10%, a water-to-binder (W/B) ratio of 0.22, and an SP content equal to 0.16% of the total binder. The second group consisted of four mixtures (from M30-1 to M30-4), which was designed with an FA content equal to 30% of the total binder. As mentioned above, the spherical particles of FA will yield an increase in paste workability [24] tentatively named Fa-RmLG, was made from fly ash (Fa, thus the W/B ratio and SP content in these mixtures were, respectively, reduced to 0.20 and 0.14%. Mixtures M10 and M30 denote those with 10 and 30% FA, respectively. The numbers after M10 and M30, from 1 to 4, denote the mixture numbers, which were designed with varying foam content. The objective of this study is to examine the effect of foam and FA contents on the engineering properties of LFC. The correlations between the properties of LFC and its unit weight are also established.

2.3. Sample preparation and test methods

All dry materials were mixed first, then water and SP were added and mixed until a homogeneous paste was obtained. The flow diameter of the paste was immediately checked after mixing. If a flow diameter of 18±2 cm was achieved, the foam was added and mixed until the mixture was homogeneous. If the flow diameter was not satisfied, SP was used to adjust the flowability of the paste. It was noticed that the foam content used in practice was higher than the presented value in Table 2 because the foam bubbles were broken during the experiment. The steel mould, with a dimension of 100×100×100 mm, was used for sample casting. The samples were de-moulded 24 hours after casting and stored under ambient air conditions until testing day.

The unit weight of fresh concrete was checked immediately after mixing, while the dry unit weight of hardened concrete was measured under TCVN 9030:2017 [25] at 28 days. Compressive strength and water absorption of LFC were also tested based on TCVN 9030:2017 [25], while the UPV test was conducted in compliance with TCVN 9357:2012 [26]. Thermal conductivity was directly measured using ISOMET-2014 equipment. The compressive strength and UPV were measured at 7, 14, and 28 days, while the water absorption and thermal conductivity were measured at 28 days. The reported value herein is the average value of at least three measurements. After breaking from compression testing at 28 days, several pieces from the samples were collected for microstructure examination using SEM. The compressive strength, UPV, and thermal conductivity tests of LFC are illustrated in Fig. 3.

3. Results and discussion

3.1. Unit weight

The fresh and dry unit weight of the LFC mixtures are presented in Table 3. The FA content and foam volume are also given in Table 3 for comparison and discussion. In general, the dry unit weight of LFC was found to be 86-92% of its fresh unit weight. The loss of unit weight in

(A) (B) (C)

Fig. 3. (A) Compression, (B) UPV, (C) thermal conductivity test equipment.

Table 3. Unit weight of LFC.

No.	Mixture	FA content (%)	Foam (m^3)	Fresh unit weight (kg/m^3)	Dry unit weight (kg/m^3)	Classification based on TCVN 9029:2017
1	M10-1	10	0.37	1404	1278	D1300
2	M10-2		0.41	1311	1169	D1200
3	M10-3		0.48	1152	1063	D1100
4	M10-4		0.50	1121	1030	D1000
5	M30-1	30	0.33	1459	1313	D1300
6	M30-2		0.37	1382	1223	D1200
7	M30-3		0.44	1212	1103	D1100
8	M30-4		0.47	1144	986	D1000

the dry condition is due to the evaporation of water that existed in fresh concrete. In each group, the unit weight of LFC decreased with increasing foam content. For the M10 group, the dry unit weight reduced from 1278 to 1121 kg/m^3 while the foam volume increased from 0.37 to 0.50 m^3. Similarly, a reduction in the dry unit weight of the M30 group, from 1313 to 986 kg/m^3, corresponded to the foam content increasing from 0.33 to 0.47 m^3. Notably, the mixtures in the two groups M10 and M30 were designed with a similar dry unit weight, which was identified with the same classification as in TCVN 9029:2017 [27]. For those with similar unit weights, for example M10-1 and M30-1, the foam volume of M30-1 was lower than that of M10-1. It was noticed that the proportion of FA in the M10 and M30 mixtures were, respectively, 10 and 30% of the total binder. The specific gravity of FA was significantly lower than that of cement (Table 1). With the same content, the volume of FA was larger than that of cement. Thus, as increasing the FA content yields a reduction in the void volume of LFC, and the foam volume is consequently reduced.

3.2. Compressive strength

The compressive strength developments of the M10 and M30 mixtures versus curing time are plotted in Figs. 4A, 4B, respectively. In each group, the compressive strength increased with a reduction in foam content and increasing curing time. As the hydration products continuously form over time; consequently, the compressive strength of concrete also increases with time. On the other hand, a high foam volume results in a high void volume and high porosity of the concrete sample, which causes a reduction in compressive strength. This finding is in line with reports from previous studies [17-19]. The compressive strength of the M10 mixtures reduced from 16.3 to 8.4 MPa, meanwhile, those of the M30 mixtures dropped from 21.4 to 6.4 MPa. With a similar dry unit weight, the compressive strength of an

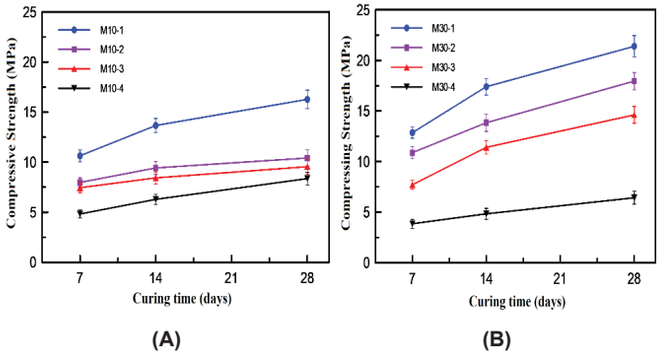

Fig. 4. Compressive strength of the (A) M10 and (B) M30 mixtures.

M30 mixture is higher than that of the corresponding M10 mixture, except for mixture M30-4. Notably, even M10 and M30 mixtures have a similar unit weight, but the foam contents of the M30 mixtures are lower than that in corresponding M10 mixtures. The high FA content in M30 mixtures is associated with the low foam volume used in M30 mixtures as mentioned previously because of the lower specific gravity of FA compared to that of cement. Consequently, the void volumes in the M30 mixtures are lower than that of their corresponding M10 mixtures, which results in higher compressive strength. However, M30-4 had a lower compressive strength than M10-4 because the dry unit weight of M30-4 is actually lower than that of M10-4. It is noted that the dry unit weight is the main factor affecting the properties of LFC [17-19]. Therefore, a correlation between the 28-day compressive strength and dry unit weight of LFC is established as shown in Fig. 5. Regardless of water-to-binder ratio and foam and FA contents, the correlation between compressive strength and dry unit weight can be described by linear regression with a high coefficient of determination ($R^2 = 0.82$).

With a 28-day compressive strength of above 15 MPa, mixtures M10-1, M10-2, and M30-1 can be used for semi-structure in practice, while other mixtures can be used as non-structure such as lightweight bricks instead

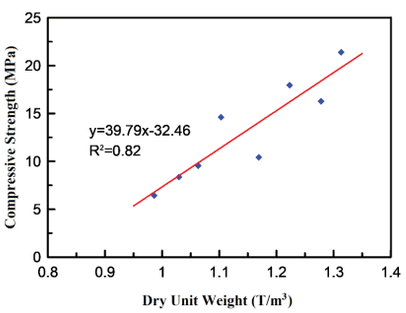

Fig. 5. The correlation between compressive strength and dry unit weight.

of unfired bricks. Based on TCVN 9029:2017 [27], with compressive strength ranging from 6.4 to 21.4 MPa, the LFC in this investigation is classified as grades M3.5 to M12.5, which is indicated as a high grade of LFC. It is also noticed that most popular cement and fired clay bricks used in practice have a compressive strength of around 5 to 7.5 MPa and a unit weight of around 1800 to 2500 kg/m^3. All LFCs in this study have similar or even better compressive strength than that of conventional cement and fired clay bricks, but a significantly lower unit weight. Therefore, the LFCs in this study show a huge potential to be utilized as unfired bricks in practice.

3.3. Ultrasonic pulse velocity

Figures 6A and 6B show the UPV values of the M10 and M30 mixtures, respectively. Similar to compressive strength, the UPV values of LFC increased with curing time and reduced with increasing foam content. It has been established that the UPV value and density of concrete have a close relationship [28]. Furthermore, the UPV value is also related to the compressive strength value [29]. As hydration products were generated during the curing time, the resulting product had high density, high compressive strength as well as high UPV value. In each group, the UPV value of LFC samples reduced with increasing foam content. The 28-day UPV value of the M10 mixtures decreased from 3145 to 2715 m/s when the foam content increased from 0.37 to 0.50 m^3. Similarly, those values of the M30 mixtures decreased from 3531 to 2602 m/s as the foam content changed from 0.33 to 0.47 m^3.

In general, with higher FA content, the M30 mixtures showed a higher UPV value than the corresponding M10 mixtures, except for M30-4. As mentioned above, the presence of FA had a positive effect of decreasing the void volume inside LFC, thus improving the UPV value. It was noticed that the dry unit weight of M10-4 was higher than that of M30-4 (as seen in Table 3). Both FA and foam contents are related to the dry unit weight of LFC, thus affecting the UPV value. With higher dry unit weight, M30-1, M30-2, and M30-3 showed higher UPV than M10-1, M10-2, and M10-3, respectively. This means that the UPV value of LFC strongly depends on its dry unit weight, which is in agreement with a previous study [28]. The correlation between UPV and dry unit weight of LFC can be described by linear regression as shown in Fig. 7A. Although UPV tests have been used to evaluate the relative quality of normal concrete [18, 19], it is rarely applied to LFCs in the literature. Most of the LFC in this study can be used as unburnt bricks with significantly low unit weight as mentioned earlier. Based on previous studies [30, 31], most unburnt bricks had a UPV value ranging from 1700 to 2920 m/s. Indeed, with UPV values ranging from 2602 to 3531 m/s, which are higher than previously reported values [30, 31], all of the LFCs in this investigation can be classified as good quality. The correlation between the compressive strength and UPV of LFC is also presented in Fig. 7B, which helps to predict the compressive strength of LFC when compression tests are not allowed.

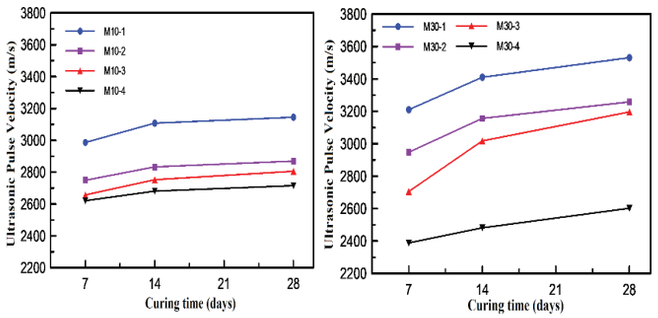

Fig. 6. Ultrasonic pulse velocity of the (A) M10 and (B) M30 mixtures.

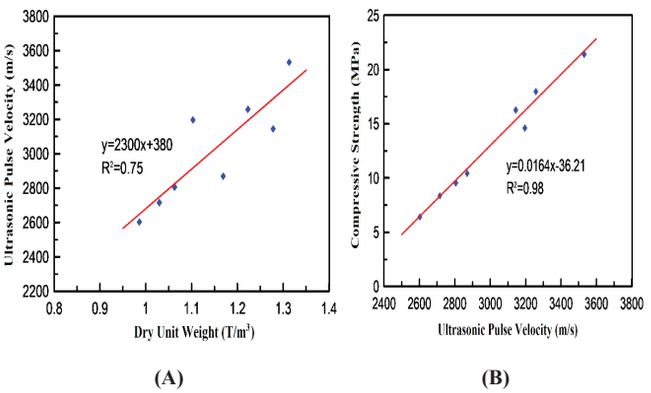

Fig. 7. The correlation between (A) UPV and dry unit weight and (B) compressive strength and UPV.

3.4. Water absorption

Water absorption of the M10 and M30 mixtures at 28 days are shown in Figs. 8A and 8B, respectively. In each group, the mixture with high foam content showed a high water absorption capacity. The water absorption of the M10 mixtures increased from 6.7 to 10.1% when foam content was increased from 0.37 to 0.50 m^3. For the M30 mixtures, the water absorption increased from 5.7 to 10.2% as the foam content increased from 0.33 to 0.47 m^3. Generally, the water absorption of the M30 mixture was slightly lower than that of the corresponding M10 mixture because the former had a lower foam content than the latter. The high FA content in the M30 mixtures also helped to reduce water absorption, except for M30-4. Again, it is noted that M30-4 had a lower dry unit weight than M10-4 (as shown in Table 3). A linear

equation is used to illustrate the relationship between the water absorption of LFC and its dry unit weight as shown in Fig. 9. For cement-sand-based LFC produced by A.M. Abd et al. (2016) [18], the concrete samples with a unit weight of 1200 kg/m^3 had a water absorption of about 26%, which was significantly higher than those values of LFC produced in the present study. The use of FA in the present study contributes to reducing the void volume inside of concrete, thus, the water absorption value in comparison to reported values studied by A.M. Abd, et al. (2016) [18] was lower. It is also noticed that all LFCs in the present study have a water absorption of below 16%, which satisfies a requirement for them to be used as unburnt bricks [32].

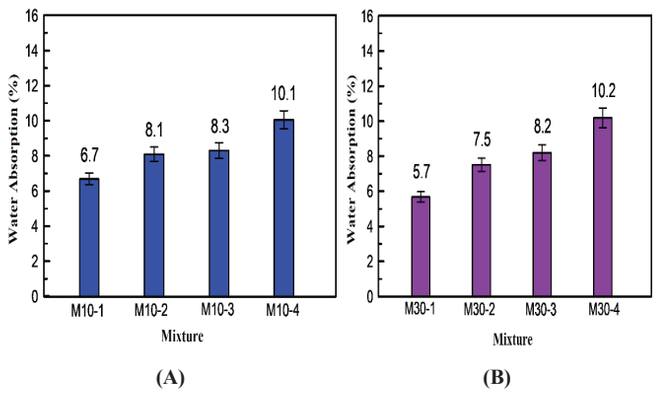

Fig. 8. Water absorption of the (A) M10 and (B) M30 mixtures.

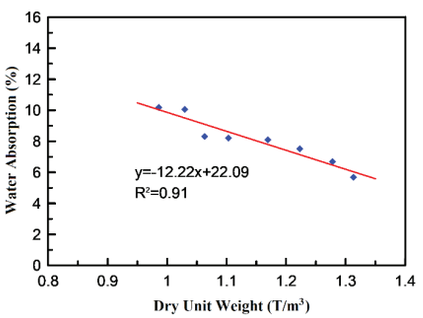

Fig. 9. The correlation between water absorption and dry unit weight.

3.5. Thermal conductivity

The thermal insulation ability of LFC is expressed through the thermal conductivity value, which is plotted in Fig. 10. For the M10 and M30 mixtures, the thermal conductivity ranged from 0.401-0.644 W/mK and 0.387-0.899 W/mK, respectively. According to Fig. 10, the thermal conductivity decreased with increasing foam content. In general, the M30 mixture had a higher thermal conductivity value than the corresponding M10 mixture, except for M30-4. This phenomenon is due to the higher FA content used in the M30 mixtures than that used in the M10 mixtures. H. Uysal, et al. (2004) [33] indicated that the density of concrete has a strong effect on its thermal conductivity. The higher the density, the lower the thermal conductivity. Regardless of FA and foam contents, a mixture with higher dry unit weight yielded a higher thermal conductivity. The effect of the dry unit weight of LFC on its thermal conductivity in this study can be described by linear regression as shown in Fig. 11. On the other hand, the thermal conductivity of normal concrete is around 1.2-1.5 W/mK [33], which is significantly higher than that of LFC in this investigation. Therefore, with low thermal conductivity, all the LFCs in this study can be used as thermal insulation materials.

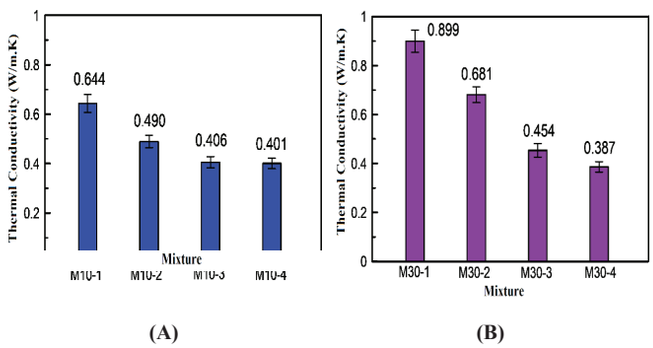

Fig. 10. Thermal conductivity of the (A) M10 and (B) M30 mixtures.

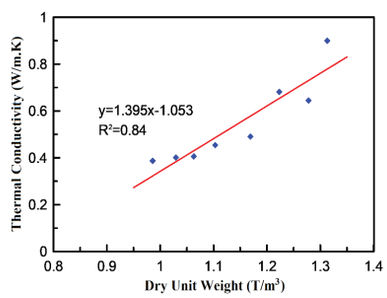

Fig. 11. The correlation between thermal conductivity and dry unit weight.

3.6. SEM observation

Figures 12 and 13 show changes in the microstructure morphology of the M10 and M30 mixtures, respectively. When foam content was increased, more spherical shapes were observed. These spherical bubbles increased the void volume inside the LFC, thus, they have a negative effect on LFC properties such as unit weight, compressive strength, UPV, water absorption, and thermal conductivity as mentioned earlier. On the other hand, the bubbles in Fig. 13 are smaller than those in Fig. 12. It should be noted that the M10 and M30 mixtures were designed with FA contents equal to 10 and 30% of the

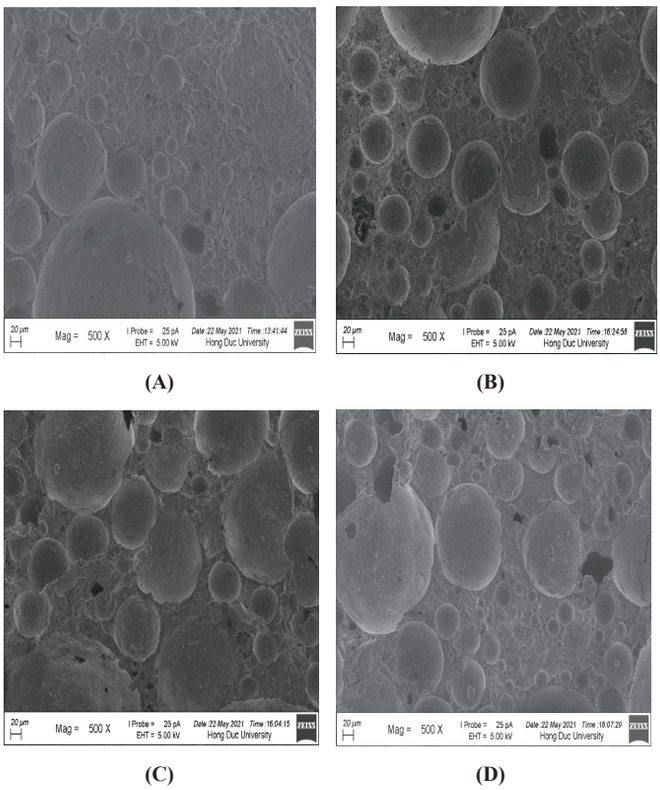

Fig. 12. SEM observation of (A) M10-1, (B) M10-2, (C) M10-3, and (D) M10-4.

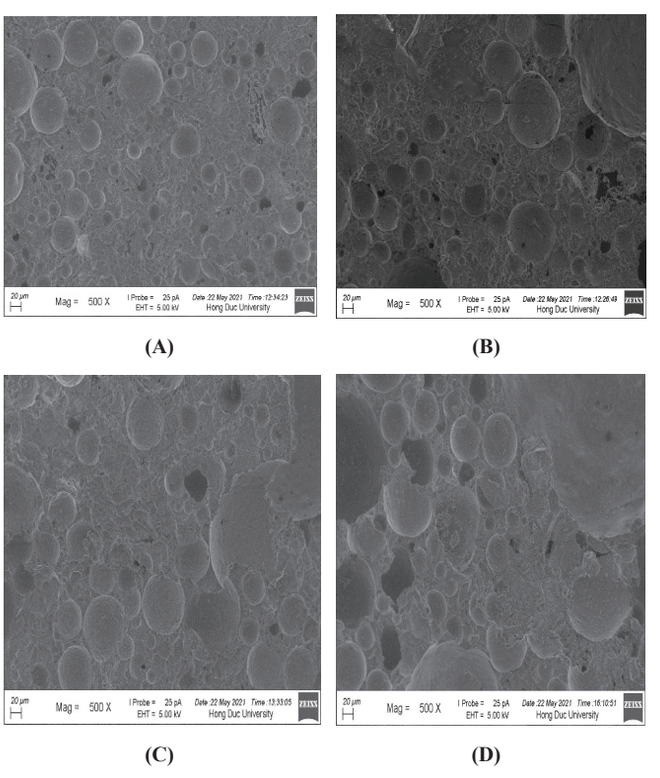

Fig. 13. SEM observation of (A) M30-1, (B) M30-2, (C) M30-3, and (D) M30-4.

total binder materials (as shown in Table 2). With a low specific gravity, FA has many more particles than cement. These FA particles will minimize the void volume inside the LFC, thus the sizes of bubbles in M30 mixtures are smaller than that in M10-mixtures. Consequently, if the void is reduced, the properties of LFC will increase. These findings prove that both foam and FA contents have a significant influence on the properties of LFC.

4. Conclusions

In this study, eight LFC mixtures were designed with various FA and foam contents. The influence of both FA and foam contents on the LFC's properties were investigated. Some main conclusions may be drawn based on the above experimental program, as follows:

(1) Dry unit weight, compressive strength, UPV, and thermal conductivity of LFC decreased, while its water absorption capacity increased with increasing foam content.

(2) The presence of FA contributed to reducing void volume inside the LFC, thus improving its properties.

(3) The dry unit weight of LFC was significantly impacted by both foam and FA contents. Meanwhile, LFC's properties strongly depended on its dry unit weight. Thus, the correlation between the properties of LFC and its dry unit weight were established.

(4) Under SEM observation, high foam content resulted in more bubbles that reduced the properties of the LFCs. Meanwhile, the use of high FA content minimized the size of the bubbles, which improved the properties of LFC.

(5) All LFCs in this investigation were classified as grade M3.5-12.5 based on TCVN 9029:2017 indicating a good, lightweight foamed concrete. These LFCs can be used instead of unfired bricks with significantly low unit weight and thermal conductivity.

CRediT author statement

Ngo Si Huy: Data analysis and interpretation, Writing and Manuscript revising; Mai Thi Hong: Method, Data analysis and Writing.

COMPETING INTERESTS

The authors declare that there is no conflict of interest regarding the publication of this article.

REFERENCES

[1] S.H. Ngo, T.P. Huynh, T.T.T. Le (2020), "Effects of NaOH concentrations on properties of the thermal power plant ashes-bricks by alkaline activation", *Journal of Wuhan University of Technology - Matter. Sci. Edit*, **35**, pp.131-139, DOI: 10.1007/s11595-020-2236-2.

[2] S.H. Ngo, T.P. Huynh (2022), "Effect of paste content on long-term strength and durability performance of green mortars", *Journal of Science and Technology in Civil Engineering (STCE) - HUCE*, **16(1)**, pp.113-125, DOI: 10.31814/stce.huce(nuce)2022-16(1)-10.

[3] Y. Kim, T.Q. Tran, G. Kang, T.M. Do (2019), "Stabilization of a residual granitic soil using various new green binders", *Construction and Building Materials,* **223**, pp.724-735, DOI: 10.1016/j.conbuildmat.2019.07.019 .

[4] T.Q. Tran, Y. Kim, G. Kang, et al. (2019), "Feasibility of reusing marine dredged clay stabilized by a combination of by-products in coastal road construction", *Transportation Research Record*, **2673**, pp.519-528, DOI: 10.1177/0361198119868196.

[5] A.S. Brand, P. Singhvi, E.O. Fanijo, et al. (2020), "Stabilization of a clayey soil with ladle metallurgy furnace slag fines", *Materials*, **13(19)**, DOI: 10.3390/ma13194251.

[6] T.T. Le, S.S. Park, J.C. Lee, et al. (2021), "Strength characteristics of spent coffee grounds and oyster shells cemented with GGBS-based alkaline-activated materials", *Construction and Building Materials*, **267**, DOI: 10.1016/j.conbuildmat.2020.120986.

[7] T.M. Do, Y.S. Kim, G.O. Kang, et al. (2018), "Thermal conductivity of controlled low strength material (CLSM) made entirely from by-products", *Key Engineering Materials*, **773**, pp.244-248.

[8] Y. Kim, B.H. Dinh, T.M. Do, et al. (2020), "Development of thermally enhanced controlled low-strength material incorporating different types of steel-making slag for ground-source heat pump system", *Renewable Energy*, **150**, pp.116-127, DOI: 10.1016/j.renene.2019.12.129.

[9] N.T. Dung, T.P. Chang, C.T. Chen (2014), "Engineering and sulfate resistance properties of slag-CFBC fly ash paste and mortar", *Construction and Building Materials*, **63**, pp.40-48, DOI: 10.1016/j.conbuildmat.2014.04.009.

[10] N.T. Dung, T.P. Chang, T.R. Yang (2014), "Performance evaluation of an eco-binder made with slag and CFBC fly ash", *Journal of Materials in Civil Engineering*, **26(12)**, DOI: 10.1061/(ASCE)MT.1943-5533.0001019.

[11] E.P. Kearsley, P.J. Wainwright (2001), "The effect of high fly ash content on the compressive strength of foamed concrete", *Cement and Concrete Research*, **31(1)**, pp.105-112, DOI: 10.1016/S0008-8846(00)00430-0.

[12] A.O. Richard, M. Ramli (2013), "Experimental production of sustainable lightweight foamed concrete", *Current Journal of Applied Science and Technology*, **3**, pp.994-1005, DOI: 10.9734/BJAST/2013/4242.

[13] T.H. Wee, D.S. Babu, T. Tamilselvan, et al. (2006), "Air-void system of foamed concrete and its effect on mechanical properties", *ACI Materials Journal*, **103(1)**, pp.45-52, .

[14] R.C. Valore (1954), "Cellular concretes part 1 composition and methods of preparation", *ACI Journal Proceedings*, **50(5)**, pp.773-796, DOI: 10.14359/11794.

[15] M.R. Jones, A. McCarthy (2005), "Preliminary views on the potential of foamed concrete as a structural material", *Magazine of Concrete Research*, **57(1)**, pp.21-31.

[16] C. Krämer, M. Schauerte, T.L. Kowald, et al. (2015), "Three-phase-foams for foam concrete application", *Materials Characterization*, **102**, pp.173-179, DOI: 10.1680/macr.2005.57.1.21.

[17] D. Falliano, D. De Domenico, G. Ricciardi, et al. (2018), "Experimental investigation on the compressive strength of foamed concrete: Effect of curing conditions, cement type, foaming agent and dry density", *Construction and Building Materials*, **165**, pp.735-749, DOI: 10.1016/j.conbuildmat.2017.12.241.

[18] A.M. Abd, D.S. Jarullah (2016), "Producing lightweight foam concrete building units using local resources", *Civil and Environmental Research*, **8(10)**, pp.54-63.

[19] M. Kozłowski, M. Kadela (2018), "Mechanical characterization of lightweight foamed concrete", *Advances in Materials Science and Engineering*, DOI: 10.1155/2018/6801258.

[20] Vietnamese National Standard, TCVN 10302:2014 (2014), *Activity Admixture - Fly Ash for Concrete, Mortar and Cement*.

[21] M.S. Hamidah, I. Azmi, M.R.A. Ruslan, et al. (2015), "Optimisation of foamed concrete mix of different sand-cement ratio and curing conditions", *Proceeding: Use of Foamed Concrete in Construction*, Thomas Telford Publishing, pp.37-44.

[22] Z. Abdollahnejad, Z. Zhang, H. Wang, et al. (2018), "Comparative study on the drying shrinkage and mechanical properties of geopolymer foam concrete incorporating different dosages of fiber, sand and foam agents", *Proceeding: High Tech Concrete - Where Technology and Engineering Meet*, Springer International Publishing, pp.42-48, DOI: 10.1007/978-3-319-59471-2_6.

[23] Vietnamese National Standard, TCVN 3121:2003 (2003), *Mortar for Masonry - Test Methods, Part 3: Determination of Consistence of Fresh Mortar (by Flow Table)*.

[24] T. Manh Do, G.O. Kang, Y. Kim (2019), "Development of a new cementless binder for controlled low strength material (CLSM) using entirely by-products", *Construction and Building Materials*, **206**, pp.576-589, DOI: 10.1016/j.conbuildmat.2019.02.088.

[25] Vietnamese National Standard, TCVN 9030:2017 (2017), *Lightweight Concrete - Test Methods*.

[26] Vietnamese National Standard, TCVN 9357:2012 (2012), *Normal Concrete - Nondestructive methods - Assessment of Concrete Quality using Ultrasonic Pulse Velocity*.

[27] Vietnamese National Standard, TCVN 9029:2017 (2017), *Lightweight Concrete - Foam Concrete and Non-Autoclaved Concrete Products - Specification*.

[28] J.A. Bogas, M.G. Gomes, A. Gomes (2013), "Compressive strength evaluation of structural lightweight concrete by non-destructive ultrasonic pulse velocity method", *Ultrasonics*, **53(5)**, pp.962-972, DOI: 10.1016/j.ultras.2012.12.012.

[29] R. Solís-Carcaño, E.I. Moreno (2008), "Evaluation of concrete made with crushed limestone aggregate based on ultrasonic pulse velocity", *Construction and Building Materials*, **22(6)**, pp.1225-1231, DOI: 10.1016/j.conbuildmat.2007.01.014.

[30] P. Turgut (2010), "Masonry composite material made of limestone powder and fly ash", *Powder Technology*, **204(1)**, pp.42-47, DOI: 10.1016/j.powtec.2010.07.004.

[31] S. Naganathan, N. Subramaniam, K.N. Mustapha (2012), "Development of brick using thermal power plant bottom ash and fly ash", *Asian Journal of Civil Engineering*, **13**, pp.275-287.

[32] Vietnamese National Standard, TCVN 6477:2016 (2016), *Concrete Bricks*.

[33] H. Uysal, R. Demirboğa, R. Şahin, et al. (2004), "The effects of different cement dosages, slumps, and pumice aggregate ratios on the thermal conductivity and density of concrete", *Cement and Concrete Research*, **34(5)**, pp.845-848, DOI: 10.1016/j.cemconres.2003.09.018.

DOI: 10.31276/VJSTE.64(2).50-53

Experimental investigations on the rheological properties of the proposed 3D printing mortar

Thi Loan Pham[1*], Xiao Jian Zhuang[1], Thi Hoai Thu Nguyen[2], Phan Anh Nguyen[2], Duy Thanh Trinh[2]

[1]Department of Structural Engineering, Tongji University, 1239 Siping Road, Shanghai, PR China
[2]Department of Civil Engineering, Haiphong University, 171 Phan Dang Luu, Kien An District, Hai Phong City, Vietnam

Received 7 May 2021; revised 3 June 2021; accepted 23 July 2021

Abstract:

In order to explore the full potential that 3D technology can bring to the construction industry, considerable amounts of research have been carried out all over the world. However, compared to traditional construction, research related to the application of 3D printing in the construction industry is still in its infancy. Publications related to applying 3D printers in the construction fi eld has become a hot trend in recent decades. Even after nearly three decades of global exploration into numerous projects, the complete potential of 3D printing technology in the construction industry remains unrealized. Numerous challenges impede the effective application of 3D printing in construction, with the formulation of the concrete mixture being a critical factor. This study specifically addresses mix proportion design approaches and tests, focusing on assessing the rheological properties of fresh mortar. In consideration of their practicality and relevance in construction, materials like cement, fly ash, and natural sand were chosen for the mix proportion analysis. The study employed slump-flow tests, V-funnel tests, and buildability tests to evaluate the properties of the fresh mortar. This initial exploration into mixture proportion and the methodology for assessing rheological properties in 3D printing mortar serves as a valuable reference and guide, laying the groundwork for the development of 3D printing technology in Vietnam.

Keywords: **buildability test, fresh properties, mortar, slump-flow test, V-funnel test, 3D printing.**

Classification number: **2.3**

1. Introduction

In order to explore the full potential that 3D technology can bring to the construction industry, considerable amounts of research have been carried out all over the world. However, compared to traditional construction, research related to the application of 3D printing in the construction industry is still in its infancy. Publications related to applying 3D printers in the construction field has become a hot trend in recent decades.

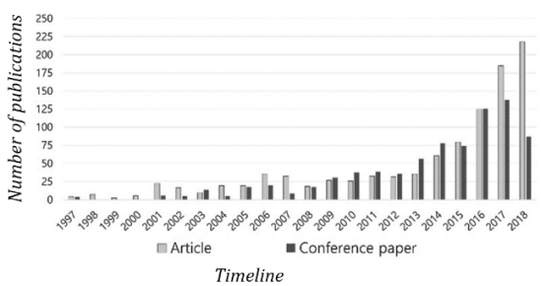

Fig. 1. Trend of publication output from 1997 to 2018 [1].

As shown in Fig. 1, since 2014 publications related to 3D printing technology has significantly increased. Many well-known buildings, bridges, as well as architectural icons, have been constructed on-site with applying 3D printing technology [2-6]. These achievements offer insights into the full potential that 3D printing technology can bring to the construction industry.

Along with these highlighted opportunities, there have been many challenges to applying 3D printing technology on-site such as mixture proportion design, printing of large-scale components, reinforcement, etc. [7]. Among these challenges, the mixture proportion design is crucial for the preparation of 3D printing concrete. Cement-based materials are the most common ingredient and has been applied in civil structures for centuries and maintain a significant role in modern buildings as well. Moreover, successful attempts to design appropriate printing approaches for cement-based materials have been investigated by many researchers as well [8-14]. In this study, the authors employed the mixture approach by C. Zhang, et al. (2019) [15] to design the mix proportion of the mortar.

Because they are highly practical and convenient in construction, the main constituents of the mixtures mentioned here are cement, sand, and fly ash, which have been selected by many other authors [15-17]. The reason for this is to support the application of 3D printing to

[*]Corresponding author: Email: loanpt297@gmail.com

large-scale and on-site buildings while strictly regarding extrudability, buildability, workability, and open-time as the key requirements for 3D-printable concretes [8]. To respond to those mentioned requirements, concrete used for 3D printing technology must be as fluid as possible to be easily transported through printing system components such as pipes, nozzles, and extrusion through the printer head. Meanwhile, the concrete must be stable to prevent disunity or jamming during the flow. The fluid characteristics, setting behaviours, and viscosity performances are considered to be the most useful critical features that specify the printability and stability of concrete for 3D printing. Each behaviour can be detected and evaluated by one or more experimental methods. The slump-flow test, V-funnel test, and buildability test are simple and relatively reliable tests that are widely used [18]. Therefore, these three tests were employed in this study to evaluate the printability of the mortar.

In summary, this study suggested a mix proportion design approach and tests that access some rheological properties of the fresh mortar with highly practical applications.

2. Material preparation

In this research, ordinary Portland cement (OPC) by Chinfon and fly ash (FA) by Haiphong Thermal Power Plant were used to form the binder component. Table 1 illustrates the chemical composition of OPC and FA. According to ASTM C618, fly ash by Haiphong Thermal Power Plant is categorised as class F [19].

Table 1. Chemical composition of fly ash and ordinary Portland cement [20].

Chemical composition	Weight percentage (%)	
	Fly ash	*Cement*
SiO_2	45.56	22.45
Al_2O_3	23.04	5.42
Fe_2O_3	5.34	3.6
TiO_2	0.1	-
$K_2O + Na_2O$	7.44	1.1
CaO	1.08	61.75
MgO	1.29	1.15
P_2O_5	0.2	-
SO_3	-	2.18
MnO	0.1	-

A commercially available manufactured sand with nominal maximum aggregate size of 1.00 mm was used. The sand was quickly dried and stored in a closed plastic bag. Hence, the sand was considered as dry meaning the water content of the mixture does not contribute to the total water amount.

Superplasticizer SikaPlast®-398 SF (SP) was used to adjust the workability of the fresh mortar and its physical characteristics are given in Table 2.

Table 2. SikaPlast®-398 SF physical characteristics (SP) [21].

Physical characteristics	Test method	Test result	Specification
Specific gravity @20°C	SK-TM002	1.095	1.085-1.105
pH value @25°C	SK-TM003	5.610	4.500-6.500
Solid content @105°C	SK-TM004	30.600	29.500-31.500

Materials used for mixing mortar in this research is presented in Fig. 2.

(A) Cement (B) Fly ash (C) Sand (D) Superplasticizer

Fig. 2. Materials used for mixing mortar.

According to the successful investigations by previous authors, the authors take the water to binder ratio by weight to be 0.45. Cement and fly ash are considered as the binder. Then, the authors employed the formula of [15] to determine the amount of sand:

$$S = 4.22F + 351 \quad (1)$$

where: S is the amount of sand (gram/liter); F is the flowability of cement paste (mm); and fine sand is from natural sand by 1.00 mm square hole sieve.

The mixture proportion given in the Table 3 was prepared and then evaluated by the following tests.

Table 3. Mortar mix ratio.

Cement	Fly ash	Sand	Water	SP
0.5	0.5	2.58	0.42	0.12

Note: ratio by weight and to binder.

3. Results and discussion

3.1. Flowability test

The flowability of the binder is a critical parameter in this research. The flowability value, F, of cement paste is calculated using the sand content in Eq. 1 by C. Zhang, et al. (2019) [15].

According to the Chinese standard GB/T 8077-2012, the flowability of the binder is tested as described below [22]. Five-hundred grams of binder is prepared, and the total mixing time was five minutes. The mixing steps includes three steps as follows. Firstly, with a velocity of 140±5 r/min, the binder is dry mixed for 1 min. Next, mixing is continued for 1.5 min after adding water and

superplasticizer. Finally, the binder is mixed for 2.5 min at high velocity of 285±10 r/min. After the mixing, the ready-mixed binder is poured into a truncated cone. Then, the cone is vertically lifted and the flowability of the cement binder is measured immediately. The inner diameters of the top and bottom rims and the height of the cone are 36, 60, and 60 mm, respectively. The result of the flowability of the binder was 220 mm as captured in Fig. 3. The value of the flowability can range between 130 and 240 mm [15]. This value was taken to account for the amount of sand based on Eq. 1 and the result is presented in Table 3.

Fig. 3. Flowability of the tested binder.

3.2. V-funnel test

The viscosity and the deformability of fresh concrete is evaluated with the V-funnel test. The configuration of the V-shaped funnel used in this test is shown in Fig. 4. Firstly, the V-funnel is filled up with fresh mortar. Then, the funnel is lifted and the elapsed time between opening the bottom outlet and the complete emptying of the funnel without significant segregation and jamming through the narrow opening is defined as the V-funnel flow time (V_t). The mixing steps were like that of the paste for the flowability test.

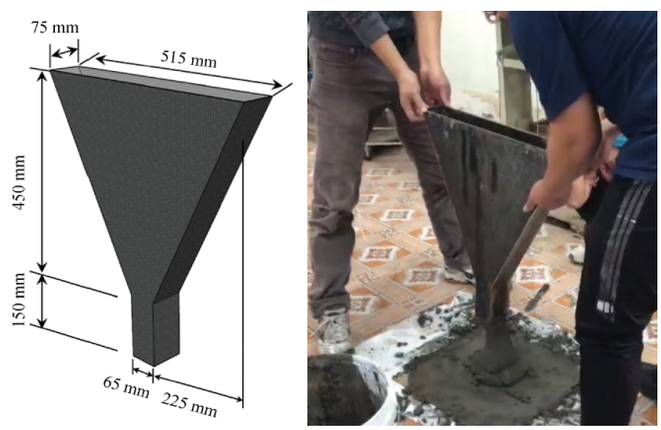

Fig. 4. Description of V-funnel test.

After filling the V-funnel with the prepared fresh mortar, it was lifted up and the mortar passed through the opening well with no segregation or jamming. The time (V_t) it took to completely empty out the mortar was 15 sec. According to previous research, this value of V_t falls within the typical ranges of 9 to 25 sec [18].

3.3. Buildability test

The remaining height of the slumped mortar cylinder under the action of gravity can be used to evaluate the yield stress and the buildability of the tested mortar. The height and diameter of the cylinder mould were 80 mm with reference to the previous experimental experience of the authors [15]. According to this reference, the buildability test procedure is as follows: initially, the cylinder mould is filled with mortar by three layers, where each layer is compacted by rodding 15 times. Then, the mould is vertically lifted, and buildability is assessed by the shape and the remaining height of the cylinder sample. If significant deformation is not observed after lifting the mould away, it can be concluded that the mortar has appropriate buildability. The mixing steps were like that of the paste for the flowability test.

Fig. 5. The slump of the sample in the buildability test.

The height of the mortar cylinder remained about 72 mm and the specimen did not deform after lifting the mould away as shown in Fig. 5. This means that the mortar has a solid ability but not enough viscosity.

Based on the slump-flow test, V-funnel test, and buildability test results, the mix proportion can be practically designed and initially evaluated by the proposed method in this study.

4. Conclusions

Based on the test results with the first analysis on mixture proportion design approach and the test used to evaluate rheological properties for the 3D printing mortar in Vietnam, some conclusions and suggestions are given:

(1) Applying 3D printing technology in construction has inevitable trends in the near future.

(2) The mixture proportion design approach presented herein is appropriate and reliable.

(3) Slump-flow test, V-funnel test, and buildability test employed in this study are highly practical for designing and initially evaluating mortar used for 3D printing technology in the construction field.

CRediT author statement

Thi Loan Pham: Data analysis and interpretation, Writing and manuscript revising; Xiao Jian Zhuang: Method, Data analysis and Writing, Thi Hoai Thu Nguyen: Method, Data analysis and Writing, Phan Anh Nguyen: Method, Data analysis and Writing, Duy Thanh Trinh: Method, Data analysis and Writing.

ACKNOWLEDGEMENTS

The authors would like to acknowledge the financial support from the National Natural Science Foundation of China (51950410599), the material support from Thanh Hung Concrete Joint Venture Company and the laboratory support at Haiphong University, Vietnam. The authors specially thank to Mr. Vu Hong Luan at VIDPOL Joint Stock Company for creating the experimental equipment.

COMPETING INTERESTS

The authors declare that there is no conflict of interest regarding the publication of this article.

REFERENCES

[1] D. Lee, H. Kim, J. Sim, et al. (2019), "Trends in 3D printing technology for construction automation using text mining", *Int. J. Precis. Eng. Manuf.*, **20(5)**, pp.871-882, DOI: 10.1007/s12541-019-00117-w.

[2] L. Stinson (2019), "World's largest 3D-printed building completed in Dubai", https://3dprint.com/207936/3d-printed-yhnova-house-done/archive.curbed.com/2019/12/30/21035765/world-largest-3d-printed-building-dubai-apis-cor, accessed 5 May 2020

[3] L. Alter (2018), "3D printed house displayed at Milan Design Week", https://3dprint.com/207936/3d-printed-yhnova-house-done/treehugger.com/green-architecture/3d-printed-house-displayed-milan-design-week.html, accessed 5 May 2020.

[4] 3dsourced (2020), https://3dsourced.com/guides/3d-printed-house-2/#4_ICON, accessed 5 May 2020.

[5] S. Saunders (2018), "Robotic 3D printed YHNOVA house officially inaugurated, tenants to move in soon", https://3dprint.com/207936/3d-printed-yhnova-house-done/, accessed 5 May 2020.

[6] A. Frearson (2014), "Chinese company 3D prints 10 buildings in a day using construction waste", https://www.dezeen.com/2014/04/24/chinese-company-3d-prints-buildings-construction-waste/, accessed 5 May 2020.

[7] F. Hamidi, F. Aslani (2019), "Additive manufacturing of cementitious composites: Materials, methods, potentials, and challenges", *Constr. Build. Mater.*, **218**, pp.582-609, DOI: 10.1016/j.conbuildmat.2019.05.140.

[8] B. Zhu, J. Pan, B. Nematollahi,et al. (2019), "Development of 3D printable engineered cementitious composites with ultra-high tensile ductility for digital construction", *Mater. Des.*, **181**, DOI: 10.1016/j.matdes.2019.108088.

[9] B. Lu, Y. Weng, M. Li, et al. (2019), "A systematical review of 3D printable cementitious materials", *Constr. Build. Mater.*, **207**, pp.477-490, DOI: 10.1016/j.conbuildmat.2019.02.144.

[10] A. Kazemian, X. Yuan, E. Cochran, et al. (2017), "Cementitious materials for construction-scale 3D printing: Laboratory testing of fresh printing mixture", *Constr. Build. Mater.*, **145**, pp.639-647, DOI: 10.1016/j.conbuildmat.2017.04.015.

[11] G. Ma, Z. Li, L. Wang (2018), "Printable properties of cementitious material containing copper tailings for extrusion based 3D printing", *Constr. Build. Mater.*, **162**, pp.613-627, DOI: 10.1016/j.conbuildmat.2017.12.051.

[12] S.J. Lee, J.P. Won (2016), "Shrinkage characteristics of structural nano-synthetic fibre-reinforced cementitious composites", *Compos. Struct.*, **157**, pp.236-243, DOI: 10.1016/j.compstruct.2016.09.001.

[13] G.W. Ma, L. Wang, Y. Ju (2018), "State-of-the-art of 3D printing technology of cementitious material - an emerging technique for construction", *Sci. China Technol. Sci.*, **61(4)**, pp.475-495, DOI: 10.1007/s11431-016-9077-7.

[14] M. Moini, J. Olek, J.P. Youngblood, et al. (2018), "Additive manufacturing and performance of architectured cement-based materials", *Adv. Mater.*, **30(43)**, DOI: 10.1002/adma.201802123.

[15] C. Zhang, Z. Hou, C. Chen, et al. (2019), "Design of 3D printable concrete based on the relationship between flowability of cement paste and optimum aggregate content", *Cem. Concr. Compos.*, **104**, DOI: 10.1016/j.cemconcomp.2019.103406.

[16] Z. Liu, M. Li, Y. Weng, et al. (2019), "Mixture design approach to optimize the rheological properties of the material used in 3D cementitious material printing", *Constr. Build. Mater.*, **198**, pp.245-255, DOI: 10.1016/j.conbuildmat.2018.11.252.

[17] T.T. Le, S.A. Austin, S. Lim, et al. (2012), "Mix design and fresh properties for high-performance printing concrete", *Mater. Struct.*, **45(8)**, pp.1221-1232, DOI: 10.1617/s11527-012-9828-z.

[18] G. Ma, L. Wang, "A critical review of preparation design and workability measurement of concrete material for largescale 3D printing", *Front. Struct. Civ. Eng.*, **12(3)**, pp.382-400, DOI: 10.1007/s11709-017-0430-x.

[19] ATSM (2020), Standard Specification for Coal Ash and Raw or Calcined Natural Pozzolan for Use in Concrete, https://astm.org/Standards/C618.htm., accesses 5 May 2020.

[20] P.T. Duc (2019), *Research on Using Fly Ash from Hai Phong Thermal Power Plant as a Mineral Additive to Improve the Properties of Bulk Concrete*, City-level science and technology research project, Haiphong Department of Science and Technology (in Vietnamese).

[21] Sika Vietnam (2020), "SikaPlast®-398 SF", https:// vnm.sika.com/vi/xay-d-ng/ph-gia-be-tong/be-tong-th-ng-phm/ph-gia-sieu-d-o/sikaplast-398-sf.html, accesses 5 May 2020.

[22] General Administration of Quality Supervision (2012), *GB/T 8077-2012 Methods for Testing Uniformity of Concrete Admixture*, Inspection and Quarantine of the People's Republic of China, Standardization Administration of the People's Republic of China.

DOI: 10.31276/VJSTE.64(2).54-58

Growing and laying performances of two varieties of Noi chickens raised in an intensive farming system

Vu Hoa Dang[1*], Van Diep Duong[2], Thi Huong Nguyen[2], Ngoc Khanh Do[2], Thi Hue Le[2], Minh Hieu Nguyen[2], Thi Ut Tran[2], Hoang Nguyen Nguyen[2], Thuy Nhung Dang[3]

[1]National Institute of Animal Sciences, 9 Tan Phong Street, Thuy Phuong Commune, Bac Tu Liem District, Hanoi, Vietnam
[2]Dabaco Breeding Chicken Company Ltd, Ho Ve Village, Lac Ve Commune, Tien Du District, Bac Ninh Province, Vietnam
[3]Vietnam National University of Agriculture, Trau Quy Commune, Gia Lam District, Hanoi, Vietnam

Received 19 July 2021; revised 10 August 2021; accepted 14 October 2021

Abstract:

This study was conducted to compare the black and dark brown varieties of Noi purebred chickens raised in an intensive farming system. A total of 600 black and 600 dark brown Noi chickens were observed starting from 1 day after hatching. At 20 weeks of age, 30 black Noi cocks and 300 black Noi hens, as well as 30 dark brown Noi cocks and 300 dark brown Noi hens, were studied until the beginning of reproduction. All roosters and hens were kept in individual cages and mating was accomplished artificially. At 24 weeks of age, the black and dark brown Noi cocks had average weights of 2555 and 2600 g, respectively, and 1796 and 1830 g for hens, respectively. There was no difference in body weight between the two varieties. The first egg-laying ages of both varieties were relatively late. From the age of 25 weeks up to 50 weeks, the egg yields of the black and dark brown Noi hens were 74.33 and 77.98 eggs/hen, respectively, with average egg weights of 48.3 and 49.7 g, respectively. Embryonic egg rates were low at 80.3 and 81.9% for the black and dark brown varieties, respectively, and the rate of chick/incubated eggs was 73.4 and 77.0%, respectively. The Noi chickens, especially the dark brown variety, reached a relatively high egg yield in an intensive farming system, which creates great potential for the exploitation and development of this genetic source.

Keywords: **growth performance, laying performance, native hen, Noi chicken.**

Classification number: **3.1**

1. Introduction

Vietnam is a diverse country in terms of chicken genetic resources with 37 native chicken breeds listed. Noi chickens are also known as fighting cocks [1]. These native chickens have been recognised in Vietnam for a long time and are raised in many areas. Its main uses are for fighting games, a hobby of the local people, and for food as their firm and crispy skin are a specialty that Vietnamese people love. In recent years, there have been a few studies on the biological characteristics and genetic diversity of the Noi chicken in the southern provinces of Vietnam [2, 3]. In order to satisfy the Vietnamese preference for chicken meat, several studies on the hybridization between the Noi cock and some coloured-feather breeds have been conducted in recent years [4]. Indeed, hybrid Noi chicken farming has brought about high and sustainable incomes for households in many regions of Vietnam. Therefore, purebred cocks are now a demand of many breeders. However, the ability to propagate and develop pure Noi chickens has been very limited. The reason for this is the vast majority of Noi chickens raised in backyards only begin to lay eggs at 1 year of age with only 5-8 eggs per clutch and 4-5 clutches per year [5].

Surveys in the Binh Dinh province of the south-central region - one of the largest Noi chicken breeding areas in Vietnam showed that, based on feather colour, two Noi chicken varieties can be distinguished, namely, the black Noi and dark brown Noi chickens. Within the framework of the Dabaco research program, which is a large group in the field of feed and livestock that aims to develop genetic resources of Vietnam's indigenous chickens, two varieties of Noi were collected, purebred, and raised in an intensive farming system at Dabaco

[*]Corresponding author: Email: hoadangvu@gmail.com

Breeding Chicken Company, Vietnam, in 2019 and 2020. This study was conducted to evaluate growth and egg-laying performances, and to show the potential for the exploitation and development of native chicken genetic sources.

2. Materials and methods

A total of 600 black and 600 dark brown Noi experimental chickens were included in this study at 1 day old. The number of chickens selected to enter the laying stage at 20 weeks of age included 30 black cocks, 300 black hens, 30 dark brown cocks, and 300 dark brown hens, and they were kept until 50 weeks of age. All chickens were raised in an intensive farming system in a closed house. From 1 day old until 10 weeks of age, the chickens were kept on the floor with rice husks. From 11 to 50 weeks of age, the chickens were kept individually in cages with a length × width × height of 39×28×36 cm.

The lighting regime was as follows: for chickens under 4 weeks of age, 23 hours per day at 40-60 lux, then at 20-30 lux; for chickens 4-20 weeks old, 18 hours per day at 10 lux; for laying hens, 12-16 hours per day at 40-60 lux.

Table 1. Chemical composition of complete feed and diets.

Chemical composition	Growing periods (age of week)			Laying period
	0-4	5-10	11-20	
Nutrient value of feed				
Metabolic energy (Kcal/kg)	2800	2700	2600	2650
Crude protein (%)	19.0	17.0	14.5	16.0
Crude fibre (%)	6.0	6.0	6.0	6.0
Calcium (%)	0.5-1.5	0.5-1.5	0.5-1.5	1.5-5.0
Total phosphorus (%)	0.2-1.0	0.2-1.0	0.2-1.0	0.2-1.0
Lysine (%)	1.00	0.90	0.65	0.73
Met. + Cys. (%)	0.75	0.68	0.55	0.62
Diets				
Male	Ad libitum	40-74*	80-115*	119-127*
Female	Ad libitum	38-69*	75-98*	97-124*

*: g/head/day

The chemical composition of complete feed and diet for different life stages are shown in Table 1.

Some major vaccines included those for Marek, infectious bronchitis, Gumboro, Newcastle, and CRD. Common veterinary drugs were also used according to the company's technical regulations.

Chickens were numbered at 1 day old. Every week, 30 males and 30 females were randomly sampled and weighed. During the laying stage, the eggs were collected daily and recorded for each hen, and then they were weighed weekly. Artificial insemination was used with a 1:10 ratio of male-to-female and mated every 3-4 days per one. Incubation eggs were collected from 34 weeks of age and incubated in an automatic industrial system with trays to monitor the chicks of each mother hen.

Data were collected and analysed using Excel 2010 and Minitab 16 software. Statistical comparisons were made using the T-test and Chi-squared test.

3. Results

The two varieties of black and dark brown Noi chickens could be easily distinguished through a number of key features of their appearances (see Table 2 and Fig. 1).

Table 2. Physical appearance characteristics of two Noi chicken varieties.

Physical appearance	Black Noi		Dark brown Noi	
Main details	*Male*	*Female*	*Male*	*Female*
Body shape	Small front, gradually bigger back	Big front, gradually smaller back	Small front, gradually bigger back	
Feather colour	All black		Red neck, brown and black body	Dark brown with yellow lines body
Skin	Yellow, pink, and red colours			
Beak	Black and yellow colours			
Leg	Black and yellow colours			
Comb	Red colour, pea and strawberry shape			
Wattles	Red colours			
Toe	Smooth scale and stand in line			

Fig. 1. Black Noi chickens (left) and dark brown Noi chickens (right).

Table 3. Body weight at different periods of two Noi chicken varieties (g).

Age	Black Noi (Mean±SE)		Dark brown Noi (Mean±SE)	
Weeks	*Male (n=30)*	*Female (n=30)*	*Male (n=30)*	*Female (n=30)*
1	65.0±0.6	66.1±0.7	74.2±1.9	78.1±2.1
4	220.2±2.0	221.3±2.1	222.4±2.3	227.1±2.4
10	930.3^{a}±6.8	863.2^{b}±4.5	933.3^{a}±6.7	805.4^{b}±4.3
20	2150.4^{a}±25.5	1575.3^{b}±20.8	2170.4^{a}±24.9	1590.2^{b}±20.6
24	2555.4^{a}±22.6	1796.3^{b}±7.9	2600.2^{a}±23.1	1830.1^{b}±8.2

$^{a, b}$: means in the same row and same varieties without common letter are different at $p<0.05$

In general, there was no difference in body weight between the black and dark brown varieties. At 10 weeks of age, there was a marked difference in body weight between males and females for both black and dark brown varieties. At 20 and 24 weeks of age, this difference was 35 and 42%, respectively (Table 3 and Fig. 2).

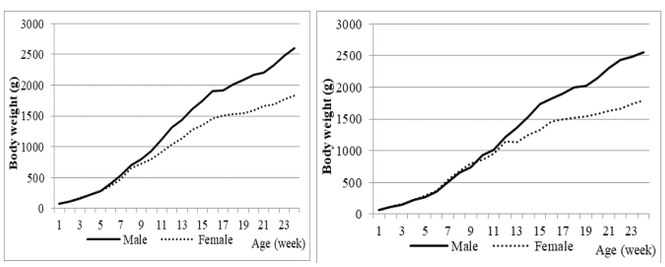

Fig. 2. Body weight at different ages for the black Noi chicken (left) and for the dark brown Noi chicken (right).

Table 4. Hen egg production and cumulated eggs curve for two Noi chicken varieties.

Hen egg production	Black Noi (n=296)	Dark brown Noi (n=500)
Age to first egg (week)	23	24
Age to 5% hen-day production (week)	25	26
Age to 30% hen-day production (week)	28	28
Age to 50% hen-day production (week)	30	30
Age at peak hen-day production (week)	35	35
Egg production at peak (%)	58.78	65.83
Cumulated eggs per hen up to 50 age of week	74.33^{b}±1.73	77.98^{a}±1.13
Average egg weight (g)	48.34±0.57	49.65±0.62

$^{a, b}$: means in the same row without common letter are different at $p<0.05$.

The egg production, yield, and egg weight of the two types are shown in Table 4 and Fig. 3. There was not much difference in the evolution of the egg production as well as the egg weight between the two Noi chicken varieties. However, the dark brown hens had higher laying rates at the peak given that the cumulated egg per hen up to 50 weeks of age was significantly higher than that of the black Noi.

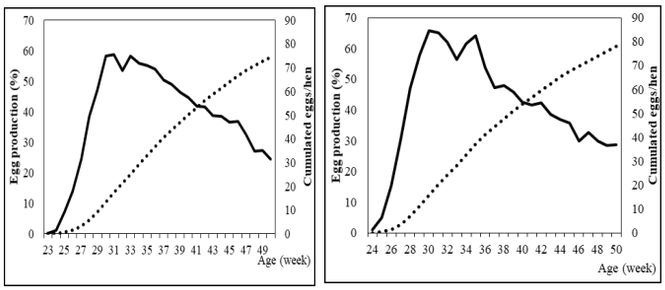

Fig. 3. Curves of egg production (lines) and cumulated eggs (points) for black Noi chicken (left) and for dark brown Noi chicken (right).

Table 5. Egg incubation results for the two Noi chicken varieties.

Egg incubation	Black Noi	Dark brown Noi	p
Number of incubated eggs	3488	8435	
Rate of embryonated egg (%)	80.3	81.9	0.038
Rate of chick/embryonated egg (%)	91.4	94.0	0.001
Rate of chick/incubated egg (%)	73.4	77.0	0.001

There was a clear difference between the black and dark brown varieties in terms of the embryonated egg proportion and hatching rates (Table 5).

4. Discussion

Recently, the exploitation and development of livestock gene resources have become important research directions for developing countries-especially Vietnam-as it is a country with many local chicken breeds. However, low growth and egg laying performances are the main challenges to farming these chicken breeds. Research results and production practices in many countries like Vietnam have indicated that crossing local chickens with exotic, high-yielding breeds may be an effective solution. Therefore, the use of an intensive farming system in a closed house with a complete feed, suitable lighting regime, and veterinary care in the present experiment could be an effective solution to improve local chicken farming performance. In agreement with our hypothesis, research already done on native chickens in Bangladesh showed that changes in traditional management practices could improve the performance of native chicken farming and thus contribute to household incomes per year [6]. Indeed, the low production performance of native breeds of chickens can be improved through enhancements to husbandry practices, better health care, and supplementary feeds during the lean season [7].

The appearance characteristics of 815 Noi chickens raised in the households of six Mekong delta provinces were evaluated, and the results showed that Noi chickens with brown feathers accounted for 38.9%, while those with black feathers accounted for 11.7%, and the remainder were other colours [3]. This study focused on the black and dark brown Noi chicken varieties. The differences in colour can

be clearly seen in Fig. 1, and the most obvious difference between these two varieties is their feather colour as shown in Table 1.

There was no difference in the observed body weights between the black and dark brown Noi chicken varieties at all ages, and they are some of the largest statured native chicken breeds in Vietnam alongside Dong Tao, Ho, and Mia chickens. The body weight of the cock at first laying weeks (24 weeks of age) was equivalent to that of Dong Tao and Ho chickens but greater than that of Mia chickens. Dong Tao chickens raised in a semi-intensive system at 24 weeks of age had a weight of 2585 g for cocks and 2189 g for hens [8]. In intensive farming, at 20 weeks of age, Ho chickens had a weight of 2147 g for cocks and 1886 g for hens, while Mia chickens were 1843 g for cocks and 1647 g for hens [9].

The body weights of the other native chicken breeds of Vietnam with medium or small statures were lower than that of the Noi chickens. For example, Ri chickens at 19 weeks of age were 1838 g for cocks and 1286 g for hens [10]. The H'Mong chickens at 38 weeks of age were 2.02 kg for cocks and 1.56 kg for hens [11]. Native breeds in some countries also had smaller body weights than Noi chickens like the Hon Chu chickens of the People's Democratic Republic of Lao raised in extensive farming at 20 weeks of age reached only 780 g for cocks and 670 g for hens [12]. However, in a semi-intensive system, they had weights at 24 weeks of age of 2174 g for cocks and 1858 g for hens [12]. The body weights of native chickens in Tanzania were 1948 g for males and 1348 g for females, respectively [13]. The native chickens in Jordan were mature at 22-30 weeks of age, and cock and hen body weights reached 1890 and 1240 g, respectively [14].

The age Noi chickens first began to lay eggs were 161-168 days old and the laying ages of 5% were 25-26 weeks (Table 4). This data was equivalent to the result of Southern Noi chickens over two selective generations [15]. When raised in the backyard, but some other native chicken breeds in Vietnam such as Ri chicken began to lay at 130 days old [16] or 144-151 days old for Tau Vang chicken [17]. Age of initiation egg laying of local chickens in Bangladesh was 152-159 days old [18], and in Ethiopia was 6.89-6.97 months [19]. This proved that late egg-laying was one main characteristic of both Noi chicken varieties.

The cumulated eggs up to 50 weeks of age of the black and dark brown Noi chickens reached 74 and 78 eggs per hen, respectively (Table 4). Meanwhile, the egg yield/hen/year over the two selective generations of Noi chickens in the Southern provinces were only 67.7 and 71.5 eggs, respectively [15], or 94.5 eggs [3]. Raised by backyard farming, the Noi's egg yield was only 48 eggs/hen/year [20]. Ho chickens in backyard farming laid 13 eggs per clutch, 5.2 clutches per year and the egg yield was 66 eggs/hens/year [21]. The egg number of hens per clutch in Ethiopia was 14.9-15.7, and the highest was 17.7 eggs [19].

Thus, an intensive farming system using the mixed feed, keeping chickens in individual cages, and under proper lighting were all important factors to achieve the relatively high egg yield in this experiment for both Noi chicken varieties. Similarly, Indonesian Kampung chickens raised in extensive, semi-intensive, and intensive farming conditions had 3, 6, and 7 clutches per year, respectively, and achieved egg yields of 47, 59, and 146 eggs/hen/year, respectively. Hence, the egg production in intensive systems tripled that of extensive systems [22].

The average egg weights observed from the first laying week until 50 weeks of age for both Noi chicken varieties were about 48-50 g (Table 4). The egg weight of the Noi chickens was 45.4 g [3], and at 38-40 weeks of age were 46.3-46.5 g [15]. The chickens with a larger stature had egg weights greater than that of chickens with smaller stature. For example, the egg weight of Ri chickens was only 38.8 g at 40 weeks of age and 45.2 g at 60 weeks of age [10]. However, the egg weight of Noi chickens were lower than that of Ho chickens [21]. Similarly, five local Indonesian breeds with small statures had small egg weights from 39.2 to 47.5 g [22].

Through the two selected generations, the rates of embryonated eggs of the Noi chickens ranged between 94.5-95.2%, and the rates of chick/incubated eggs were between 77.7-77.8% [15]. Meanwhile, the rate of embryonated Noi chicken eggs was 83.3%, and the hatching rate/embryonated egg rate was 85.3% [3]. These percentages of embryonated eggs were all higher than those obtained in Table 4. It could be possible that artificial insemination was the cause of this lower incidence. However, the percentage of embryonated eggs of Ho chickens raised by backyard farming were even lower with 82.83 [23] and 61.99% [24].

5. Conclusions

The two varieties of black and dark brown Noi chickens in this research had an easily distinguishable appearance through their feather colour.

There was no difference in body weight between these two varieties.

Both varieties of Noi chickens laid late. The black and dark brown Noi reached egg yields of 74 and 78 eggs/hen/26 laying weeks, respectively, and had average egg weights of 48.3 g and 49.7 g, respectively.

In an intensive farming system, Noi chickens, especially the dark brown variety, reached a relatively high egg yield, which has created great potential for the exploitation and development of this genetic source.

CRediT author statement

Vu Hoa Dang: Data analysis and Interpretation, Writing and Manuscript revising; Van Diep Duong, Thi Huong Nguyen, Ngoc Khanh Do, Thi Hue Le, Minh Hieu Nguyen, Thi Ut Tran, Hoang Nguyen Nguyen, Thuy Nhung Dang: Method, Data analysis and Writing.

ACKNOWLEDGEMENTS

The authors are thankful to the managers of the Dabaco Breeding Chicken Company for creating favourable conditions to execute this research.

COMPETING INTERESTS

The authors declare that there is no conflict of interest regarding the publication of this article.

REFERENCES

[1] T.N. Lan Phuong, K.D.T. Dong Xuan, I. Szalay (2015), "Traditions and local use of native Vietnamese chicken breeds in sustainable rural farming", *World's Poultry Science Journal*, **71**, pp.385-396, DOI: 10.1017/S0043933915000380.

[2] N.T. Ngu, et al. (2016), "Appearance characteristics of Noi chickens raised in the Mekong Delta", *Can Tho University Journal of Science*, **203**, pp.7-14 (in Vietnamese).

[3] C.T. Vu (2018), *Conformation, Characteristics, Genetic Diversity and the Application of Molecular Indicator in Selection Improving Reproductive Performance of Noi Chicken*, Doctoral Thesis in Agriculture, Can Tho University, Vietnam (in Vietnamese).

[4] N.Q. Khiem, L.T.T. Hien, P.V. Canh (2015), "Production capacity of the Choi x LV hybrid complex raised at Thuy Phuong Poultry Research Center", *Journal of Agriculture and Rural Development*, **18(273)**, pp.93-98 (in Vietnamese).

[5] Ministry of Agriculture and Rural Development (2004[a]), Fighting-cock, Atlas of livestock breeds in Vietnam: 53 (in Vietnamese).

[6] K. Sarkar, M. Golam (2009), "A move from subsistence to semi-commercial family poultry farming with local chickens; effective strategies for family poultry in Bangladesh", *World's Poultry Science Journal*, **65(2)**, pp.251-259, DOI: 10.1017/S004393390900021X.

[7] M.K. Padhi (2016), *Importance of Indigenous Breeds of Chicken for Rural Economy and Their Improvements for Higher Production Performance*, Hindawi Publishing Corporation Scientifica, **2016**, 9pp.

[8] L.T. Tham, et al. (2016), "Growth, carcass yield and meat quality of Dong Tao chickens", *Vietnam Journal of Agriculture Sciences*, **14(11)**, pp.1716-1725 (in Vietnamese).

[9] N.C. Thanh, et al. (2009), "Biological characteristics, performances of three local chicken breeds: Ho, Dong Tao and Mia", *Animal Husbandry Scientific and Technical Journal*, **4(122)**, pp.2-10 (in Vietnamese).

[10] N. Moula, P.K. Dang, F. Farnir, et al. (2011), "The Ri chicken breed and livelihoods in north Vietnam: Characterisation and prospects", *Journal of Agriculture and Rural Development in the Tropics and Subtropics*, **112(1)**, pp.57-69.

[11] P.C. Thieu, V.V. Su, H.L. Son (2008), *Research Results on Conservation and Development of H'Mong Chickens over 3 Generations Rearing at National Institute of Animal Sciences*, Report on the Conference on Livestock Genetic Resources Conservation 1990-2004, pp.145-153 (in Vietnamese).

[12] S. Souksanith, D.V. Binh (2018), "Conformational and performance characteristics of Hon Chu chicken", *Vietnam Journal of Agriculture Sciences*, **16(12)**, pp.1039-1048 (in Vietnamese).

[13] N.A. Mwalusanya, A.M. Katule, S.K. Mutayoba, et al. (2002), "Productivity of local chickens under village management conditions", *Tropical Animal Health and Production*, **34(5)**, pp.405-416, DOI: 10.1023/A:1020048327158.

[14] A. Abdelqader, C.B.A. Wollny, M. Gauly (2008), "On-farm investigation of local chicken biodiversity and performance potentials in rural areas of Jordan", *Animal Genetic Resources Information*, **43**, pp.49-57, DOI: 10.1017/S1014233900002728.

[15] B.T. Phuong, D.S. Hung, N.T. Hiep, et al. (2019), "Selection enhancing productivity of southern Noi chickens through three generations", *Journal of Agriculture*, **245**, pp.8-12 (in Vietnamese).

[16] Ministry of Agriculture and Rural Development (2004[b]). Ri chickens, Atlas of livestock breeds in Vietnam: 44 (in Vietnamese).

[17] T.V. Tinh, et al. (2012), "Selection and purebred breeding of Tau Vang chickens over four generations", *Journal of Agriculture and Rural Development*, **6**, pp.119-124 (in Vietnamese).

[18] S. Faruque, M.S. Islam, M.A. Afroz, et al. (2013), "Evaluation of the performance of native chicken and estimation of heritability for body weight", *Journal of Bangladesh Academy of Sciences*, **37(1)**, pp.93-101.

[19] C. Chebo, H. Nigussie (2016), "Performances, breeding practices and trait preferences of local chicken ecotypes in southern zone of Tigray, northern Ethiopia", *Asian Journal of Poultry Science*, **10**, pp.158-164, DOI:10.3923/ajpsaj.2016.158.164.

[20] N.V. Quyen, V.V. Son (2008), "Research results on reproductive characteristics of Noi chickens raised in the backyard in the Mekong delta provinces", *Journal of Agriculture and Rural Development*, **3**, pp.46-48 (in Vietnamese).

[21] N.V. Duy, D.D.Luc, P.K.Dang, et al. (2015), "Ho chicken in Bac Ninh province (Vietnam): From an indigenous chicken to local poultry breed", *International Journal of Poultry Science*, **14(9)**, pp.521-528, DOI:10.3923/ijps.2015.521.528.

[22] T. Sartika, R.R. Noor (2005), "Production performance of some local chicken genotypes in Indonesia: An overview", https://www.researchgate.net/publication/237682408Production_performance_of_some_local_chicken_genotypes_in_Indonesia_An_overview, accessed 5 May 2020.

[23] B.H. Doan, N.V. Luu (2006), "A survey on distribution, conformation, growth and productivity of Ho chicken", *Journal of Agricultural Science and Technology*, **4(4 and 5)**, pp.95-99 (in Vietnamese).

[24] N.V. Duy, N. Moula, E. Moyse, et al. (2020), "Productive performance and egg and meat quality of two indigenous poultry breeds in Vietnam, Ho and Dong Tao, fed on commercial feed", *Animals*, **10(3)**, DOI: 10.3390/ani10030408.

DOI: 10.31276/VJSTE.64(2).59-64

Eosinophilic gastroenteritis with ascites at Children's Hospital No.2: A case report and review of the literature

Van Thieu Ha[1, 2*], Huu Tung Trinh[2]

[1]*Department of Pediatrics, Pham Ngoc Thach University of Medicine, 12 Quang Trung Street, 12 Ward, 10 District, Ho Chi Minh City, Vietnam*
[2]*Department of Gastroenterology, Children's Hospital No.2, 14 Ly Tu Trong Street, Ben Nghe Ward, 1 District, Ho Chi Minh City, Vietnam*

Received 7 September 2021; revised 20 September 2021; accepted 30 November 2021

Abstract:

EGE is a rare disorder presenting with a cluster of gastrointestinal symptoms associated with eosinophils histological infiltration. This disease was first described by Kaiser in 1937. The prevalence of EGE in the United States is estimated to be 22 to 28 per 100,000 persons. EGE usually occurs between 20 and 50 years of age, but recently it has been shown to manifest in children. EGE can affect the entire digestive tract from the stomach to the colon. The clinical features of EGE are related to the affected gastrointestinal tract segment and the degree of eosinophil infiltration. Pathogenesis of the disorder is still unclear. It is hypothesised that there is a role for IgE-mediated immunity and T-lymphocyte (Th2)-mediated immunity. Eosinophilic gastroenteritis (EGE) is a digestive disorder marked by eosinophilic infiltration in the stomach and intestine, affecting both children and adults. It is categorized into mucosal, muscularis, and subserosa types based on the dominant layer of infiltration. The subserosa type often manifests with ascites, accompanied by symptoms resembling intestinal obstruction. Ascites in EGE is characterized by significant eosinophilia in ascitic fluid. While EGE with ascites mimicking appendicitis and peritonitis is uncommon in pediatric patients, this publication seeks to present a case series detailing EGE's clinical features, treatment responses, and a review of current management strategies for eosinophilic ascites. Understanding the diverse presentations and responses to treatment is crucial for improving diagnostic accuracy and enhancing therapeutic approaches in EGE cases with ascites, contributing valuable insights to the medical community's knowledge base.

Keywords: **endoscopic biopsy, eosinophilia in children, eosinophilic ascites, gastrointestinal.**

Classification number: **3.2**

1. Introduction

EGE is a rare disorder presenting with a cluster of gastrointestinal symptoms associated with eosinophils histological infiltration. This disease was first described by Kaiser in 1937. The prevalence of EGE in the United States is estimated to be 22 to 28 per 100,000 persons. EGE usually occurs between 20 and 50 years of age, but recently it has been shown to manifest in children [1]. EGE can affect the entire digestive tract from the stomach to the colon. The clinical features of EGE are related to the affected gastrointestinal tract segment and the degree of eosinophil infiltration. Pathogenesis of the disorder is still unclear. It is hypothesised that there is a role for IgE-mediated immunity and T-lymphocyte (Th2)-mediated immunity.

The presentation of EGE is usually nonspecific gastrointestinal symptoms, and ascites is rarely seen [1, 2]. About 75% of cases have elevated eosinophil in blood. While no gold standard of diagnosis has yet been established, diagnoses are mainly based on the history and presence of eosinophils in tissue biopsy after excluding other conditions including peripheral eosinophilia [1]. Currently, there is no consensus of diagnosis nor are there specific treatment guidelines, for example, on the dosage, administration, and duration period of therapeutic steroids. Some drugs such as Cromolyn, Ketotifen, Montelukast, and Omalizumab can be used in some cases, but are not recommended.

From 2018 to 2020, we recorded 5 cases of ascites due to EGE admitted to the Department of Gastroenterology at Children's Hospital No.2. The process of establishing the diagnosis included a long period of monitoring clinical presences and laboratory findings. Although our clinical cases have similar GI symptoms, each case still has its own characteristics.

2. Case series

2.1. Case 1

A 14-year-old female patient came to us with a chief complaint of intermittent epigastric pain for 4 months. During this admission, the patient had epigastric pain continuously for 3 days. She had no febrile or other GI symptoms except for a little vomiting. Personal and family history had no documented tuberculosis or allergies. Physical examination revealed soft abdomen, mild distention, right iliac fossa pain, positive Blumberg sign, and unclear abdominal wall resistance. Laboratory results are detailed in Table 1 below. The accumulation of abdomen fluid in ultrasound and the elevation of eosinophils count in blood as well as the presence of inflammatory cells clusters, mainly eosinophils, in the intestinal wall were prominent in these findings (Fig. 1).

*Corresponding author: Email: thieuhv@pnt.edu.vn

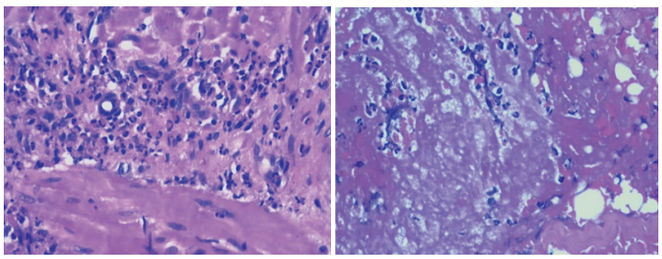

Fig. 1. Eosinophilic infiltration of the muscular layer of the intestinal wall and peritoneum biopsy sample of case 1 (Hematoxylin-Eosin staining×100).

Table 1. Clinical features and laboratory results of case reports 1, 2, and 3.

Case presentation	Case 1	Case 2	Case 3
Symptoms	Epigastric abdominal pain, vomiting, no diarrhoea, no weight loss	Periumbilical pain, vomiting, loose stools, weight loss	Periumbilical pain, increasing ascites, vomiting
Clinical examination	Mild abdominal distension, right iliac fossa pain, rebound tenderness (+/-), non- significant guarding sign.	Ascites, muscular resistance (-)	Ascites, tenderness around the umbilicus, no guarding sign, moist rales, bilateral alveolar hypoechoic, no oedema of limbs, face
Initial diagnosis	Acute appendicitis, enteritis	Unexplained peritoneal effusion, enteritis	Multi-membrane effusion of unknown causes-Pneumonia-follow-up eosinophilic enteritis or malignancy
Complete blood count	WBC: 16.7 K/Ul Neu: 10.6 K/ul Eo: 1.44 K/ul Hb: 11.8 g/d PLT: 448 K/Ul	WBC: 12 K/ul Neu: 6.9 K/ul Eos: 1.9 K/ul Hb: 18.4 g/dl PLT: 382 K/Ul	WBC: 12.9K/Ul Neu: 6.62 K/ul Eos: 1.16K/Ul Hb: 12.4 g/dl PLT: 428 K/ul
Immunoassay	ANA-8 (-) profiles (anti-dsDNA, anti-cardiolipin, antiphospholipid, anti-Sm, anti Jo-1, anti SS-A, anti SS-B)* Normal protein electrophoresis Normal C3, C4; Normal IgA, IgG, IgM		
Parasitic serology	Fasciola (+) Strongyloides stercoralis (+)	(-)	(-)
Peritoneocentesis	Exudate, neutrophil predominance, PCR of common agents (-), normal ADA	Exudate eosinophil predominance, normal ADA	Exudate, inflammatory cell diversity, no foreign cells recorded
Tuberculosis test	ADA peritoneal fluid* (-); VS* (-), Sputum BK* (-), Stool BK (-)		
Ultrasound	Abundant abdominal fluid, intestinal wall thickened ileocecum	Abundant abdominal fluid, thickened small intestinal wall	Large amount of abdominal fluid, no hepatosplenomegaly, not found abdominal lymph nodes
Abdominal CT scan	Abdominal free fluid, thickened small bowel wall, no abnormal dilation of intestinal loops	Enlarged liver, normality in liver tissue density Abdominal free fluid, thickened and oedematous wall of small intestine and ascending cecum, no enlarged abdominal lymph nodes.	Large amount of ascites. Thickened of the pericardium and momentum, no enlarged mesenteric and retroperitoneal lymph nodes. Pneumonia
Upper gastrointestinal endoscopy	Nodular gastritis	Congestive gastritis	Active chronic gastritis *H. pylori* test (+)
Lower gastrointestinal endoscopy	Did not perform	Inflammation of the ileum	Ulcerative ileocecal ulcer
Pathology	Clusters of inflammatory cells mainly eosinophils within intestinal wall; infiltration of fatty and fibres in connective tissue.	Active chronic proliferative ileitis, with clusters of inflammatory cells mainly eosinophils	Considerable infiltration eosinophils within all intestinal submucosal

*ANA: antinuclear antibody; anti-ds-DNA: anti-double stranded DNA; anti-Sm: anti-Smith; anti Jo-1: histidyl tRNA synthetase; anti SS-A: anti-Sjögren syndrome A; anti-SS-B: anti-Sjögren syndrome B); *C3, C4: complement 3 and 4; *BK: bacille de Koch; *VS: erythrocyte sedimentation rate; *ADA: adenosine deaminase, (+): positive, (-): negative.

Treatment progress: the patient was initially treated with intravenous antibiotics and parasite eradication (Ivermectin and Albendazole) along with exploratory laparoscopic surgery. The protocol recorded that abdomen was filled with yellow-brown fluid and the entire small intestine was inflamed, thickened, and congested. Similar condition with appendix. Stomach, colon, uterus, and appendages were normal. Appendix removal and abdominal fluid aspiration were performed. After the surgery, our patient remained with abdominal pain and increasing distention in addition to bilious vomiting. She had no fever and no hepatosplenomegaly or abnormal lymph nodes. Since the biopsy results proposed enteritis caused by increased eosinophils, we started to use intravenous corticosteroids therapy (2 mg/kg/day) and continued parenteral nutrition. After 5 days, distention state was greatly improved, eosinophils returned to normal range, and abdominal ultrasound showed a reduction of ascites. Treatment was to gradually reduce the dose of corticosteroids, switching to an oral route, and applying a diet towards avoiding allergies. There was a significant recovery and the patient was discharged from the hospital.

2.2. Case 2

A 16-year-old male patient was admitted to the hospital because of abdominal distention. He had abdominal pain mainly in the periumbilical area for 1 month and gradually distention along with nausea, vomiting, and loose stool 5-6 times/day, which was not accompanied by fever or weight loss. Physical examination recorded a soft belly, ascites, slight tenderness around navel, no resistance in abdominal wall and no enlarged liver and spleen. Personal history: enteritis, peritoneal infection, hospitalised for 21 days. Significant laboratory results: WBC 12 K/ul, eosinophil 1.9 K/ul, normal range for high sensitivity C-reactive protein as well as hepatic and renal function. Immunoassay: negative. Serological diagnosis of parasites: negative. Abdominal CT scan: hepatomegaly (#170 mm), normal density of liver tissue, large amount of intra-abdominal fluid. Thick oedematous wall of small intestine and ascending cecum, no enlarged abdominal lymph nodes. Peritoneal fluid: exudate, cellblock: eosinophil predominance 60%, ADA: 4.41 U/l. Tuberculosis test: negative. Endoscopy: congestive gastritis, ileitis. Pathology images of intestinal wall tissue biopsied: inflammatory proliferative chronic ileal mucosal activity, with clusters of inflammatory cells mainly eosinophils (see Fig. 2). Diagnosis: EGE, eosinophilic peritoneal effusion. The patient was treated with steroids therapy and an allergenic diet restriction.

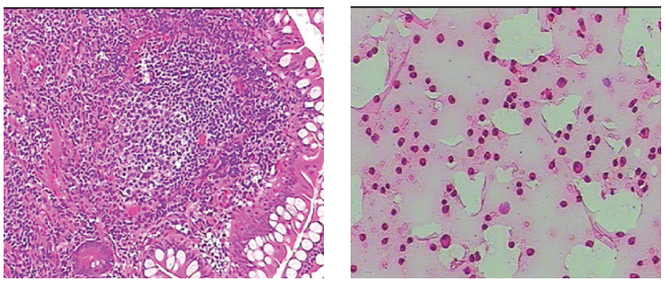

Fig. 2. Left: eosinophilic infiltration of the peritoneum in a biopsy sample of case 2 (Papanicolaou×100 method), right: histology of proliferative ileal mucosa, with clusters of inflammatory cells predominantly eosinophils of case 2 (Hematoxylin-Eosin staining×100).

2.3. Case 3

A 7-year-old female patient was hospitalised with multi-membrane effusion and malnutrition. She had gradually increased abdominal pain around the umbilicus for 1 month with ascites accumulation. Besides that, she had a phlegm cough without pyrexia. Clinical examination: significant ascites with soft abdomen, hepatosplenomegaly, slight tenderness around the umbilicus with no guarding, abdominal wall resistance, or signs of mucosal bleeding. She also had some moist rales in addition. Personal history announced the malignancy monitoring diagnosis due to multi-membrane effusion because of intra abdomen para vascular nodes findings. The patient was scheduled for exploratory surgery but, unexpectedly, the operation was not performed due to her absence with the reason being that ascites had improved according to parents' consideration. Abdominal CT scan at previous admission: massive abdominal effusion, mainly localised in front of stomach and liver; slightly inflammation of the intestinal wall, associated at the beginning of the ileum; oedematous condition of the mesentery and the great omentum; small lymph nodes (d#12 mm) adjacent to the abdominal aorta. At this admission period: large amount of ascites with high density, mostly localised in the epigastrium; thickened of the pericardium and momentum (d#15 mm). There are no enlarged mesenteric and retroperitoneal lymph nodes. Moreover, inflammation images related to the middle lobe of the lung. Endoscopy showed several scattered superficial ulcers effected along the first region of the right colon. The cecum had oedematous inflammation and numerous superficial ulcers too. Through the ileocecal valve for 10 cm, the ileal mucosa finding was similar to the under-gut disorder (see Fig. 3). Pathology had demonstrated the numerous presences of eosinophils in the intestinal submucosa, active chronic gastritis with positive *H. pylori* test. Other laboratory investigations are summarised in Table 1. For management, we also combined corticosteroids and parenteral feeding intervention, then continued by a hypoallergenic diet and oral medications. The patient responded well and left the hospital.

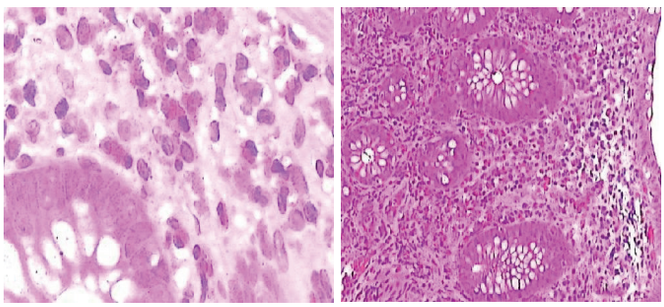

Fig. 3. Histology of infiltration of eosinophils in the intestinal submucosa (Hematoxylin eosin).

2.4. Case 4

A 14-year-old female patient was hospitalised due to a 10-day history of dull epigastric and periumbilical pain. She had other nonspecific GI symptoms like little vomiting after having meal, anorexia, and weight loss. We found a soft abdomen and no warning signs on clinical examination. Laboratory results showed the peripheral eosinophilia and a massive peritoneal effusion together with a diffusely thickened ileal wall in abdominal ultrasound demonstration. Therefore, we performed both upper and lower gastrointestinal endoscopy, exploratory laparoscopy along with tissue biopsied, and peritoneal fluid analysis to confirm the ailment. Upper gastrointestinal endoscopy showed nodular gastritis together with *H. pylori* infection, which was determined by CLO test and microbiological culture. Regarding the lower gastrointestinal endoscopy, we only found a polyp near the edge of the anus. On laparoscopy we recorded clear yellow abdominal fluid with medium volume accumulation, especially at the beginning region of the jejunum, which showed as thickened, inflamed, and speckled with white. Histopathological images revealed that the ileal tissue sample has considerable infiltration of eosinophils in the muscle layer and serosa (>200 Eos/HPF), and fewer in the mucosal layer (>50 Eos/HPF). Other clinical features and laboratory testing on admission are presented in Table 2. Intravenous corticosteroids combined with gastritis medicines were the main treatment during the hospitalised period.

Table 2. Clinical features and laboratory results of case reports 4 and 5.

Case presentation	Case 4	Case 5
Symptoms	Epigastric and dull periumbilical pain, anorexia, little vomiting after meal, constipation, weigh loss	Cystitis unresponsive to conventional treatment, Gradually increase abdominal pain, vomiting after meal
Clinical examination	Soft abdomen, no significant guarding signs	
Initial diagnosis	Following gastroenteritis	Cystitis Gastroenteritis
Complete blood count	Elevated eosinophils	
Immunoassay	Normal	IgE elevation
Parasitic serology	(-)	Toxocara (+)
Peritoneocentesis	Exudative, predominant neutrophils, PCR common agents (-)	
Tuberculosis test	ADA peritoneal fluid* (-); VS* (-), Sputum BK* (-), Stool BK (-)	Did not perform
Ultrasound	Massive ascites volume. Diffusely thickened intestinal wall (duodenum jejunum and the first region of ileum)	Ascites Thickened inflammation of stomach, antrum, pylorus, and duodenum Cystitis
Abdominal CT scan	Did not perform	Lymphoma (-)
Upper gastrointestinal endoscopy	Nodular gastritis *H. pylori* test (+)	Congestive oedema inflammation related the entire lining of the oesophagus, stomach, duodenum
Pathology	Eosinophil infiltration in the muscle layer and serosa, fewer in the mucosal layer of the ileum	Eosinophil infiltration in all tissue samples of oesophagus, stomach and duodenum

*BK: bacille de Koch; *VS: erythrocyte sedimentation rate; *ADA: adenosine deaminase.

2.5. Case 5

A 4-year-old male was admitted to hospital with a chief complaint of abdominal pain after 18 days of illness. Firstly, he had dribbling disorder and hypogastric burning pain condition when urinating. The patient was concluded cystitis syndrome at local hospital and was treated with 10 days of oral medicines (unknown type) but there still no relief of abdominal pain and urinary frequency.

After that, he had constant dull abdominal pain, vomiting 10 times per day after eating, and a slight headache in the forehead and temples. During the period of the illness, he had no fever, no blood vomiting, or other GI symptoms. Personal history recorded a mild dull periumbilical pain 2 times a week for 4 months prior to this admission. For the current presentations, the abdomen was soft, and the pain was continuous for 10 days. Some major laboratory findings included peripheral and central eosinophilia, positive Toxocarids antibody, IgE elevation and the abdominal ultrasound demonstrated an inflamed disorder mainly related to the stomach, antrum, the pylorus, specifically the thickness of duodenum wall with the diameter of 6 mm, and cystitis ailment in addition. Endoscopy: congestive oedematous inflammation related the entire lining of the oesophagus, stomach, duodenum. Pathology images: inflammatory cell infiltration with eosinophil predominance in all tissue samples of oesophagus, stomach and duodenum. We showed other clinical data and significant paraclinical testing in Table 2. Although antibiotic (Amoxicillin/Clavulanic acid) for ten days and parasite eradication (Albendazole) were used for initial treatment, the child still had abdominal pain and little vomiting about 3 times a day. When EGE was confirmed by the combination of physical examination and histology-proved biopsy, we used intravenous corticosteroids (Methyl prednisone) continually for 7 days with 2 mg/kg/day dosage for management. As a result, the patient had an obvious improvement of his abdominal pain and vomiting and was discharged after 23 days of hospitalisation.

3. Discussion

3.1. Clinical features and diagnosis

In the first case, the process of diagnosis was difficult because the patient had no specific or suggested symptoms nor an allergy history that would explain the ascites presence. Following the algorithm of peritoneal effusion, we performed clinical and paraclinical examinations to investigate appropriate causes such as peritoneal tuberculosis, liver disease (cirrhosis, portal hypertension), cardiovascular disease (heart failure, pericardial disease), kidney disease (nephrotic syndrome, chronic kidney disease), malignancy, parasite infection... [3] and none of these causes were involved in this patient.

According to the literature, EGE with the status of ascites includes 3 types: mucosal, muscular, and serosal types based on the depth of the lesion. The serosal type is the least common, ranging from 4.5 to 9% in Japan and 13% in the United States. Its mechanism can be the irritation of the peritoneum leading to ascites, along with peripheral elevation of eosinophil while peritonitis and perforation may occur in severe cases [2]. In comparison with other studies, we noted serosal ascites, exudative ascites, and predominant inflammatory cells, mainly eosinophils [4, 5].

Occasionally, EGE is associated with reflux esophagitis, dysphagia, and other vague symptoms such as abdominal pain, nausea, vomiting, diarrhoea, and weight loss, making it difficult to perform early diagnosis. In a case series in Australia, EGE was initially misdiagnosed as functional dyspepsia because the clinical presentation depends on the location, extent, and depth of the lesion in the gastrointestinal tract [6]. Furthermore, due to the characteristics of right iliac fossa pain and Blumberg sign

(+), we consulted with the surgeon about the appendicitis and peritonitis condition. As a result, our staff decided to perform emergency appendectomy and exploration.

A positive diagnostic serologic test for *Fasciola hepatica* and *Strongyloidiasis* may explain the eosinophil increases in the WBC, and fascioliasis may also cause multi-membrane effusions [7]. However, when treating these agents by anthelmintic, the clinical signs did not improve.

In the second case, peritoneal effusion was the initial presentation at hospital admission and many related diseases were investigated. However, based on the increase of eosinophil in the blood and the histological infiltration, we established the diagnosis earlier.

In the third case, the clinical features were similar to the second one with multi-membrane effusion. However, in the previous hospital admission, CT scan results had noticed para vascular nodes, so that made it impossible for us to rule out malignancy despite the recording of peripheral eosinophilic and peritoneocentesis. Therefore, the indication for exploratory surgery with lymph node biopsy that had been set at that time was completely appropriate. However, the follow-up process for that episode was interrupted because the family did not bring the child back to the hospital as scheduled (seeing that the ascites had improved). In this admission, with the suggestion of elevated eosinophils, multi-membrane effusion, and after excluding other causes, especially screening for cancer markers, along with peritoneal fluid test and pathology results, we confirmed the diagnosis with EGE. A considerable amount of literature suggests that 70% of cases have elevated eosinophils in blood especially in serosa type which has the higher risk of recurrence later [8].

Regarding the endoscopic features of the gastrointestinal tract, we recorded nodular gastritis in cases 1 and 4, congestive gastritis in case 2, and active chronic gastritis in case 3, which was accompanied with *H. pylori* infection. There was a distinctive characteristic in case 5 with congestive oedematous inflammation related the entire lining of the oesophagus, stomach, and duodenum. Meanwhile, when conducting lower gastrointestinal endoscopy on clinical cases 2 and 3, we recorded an ulcerative ileocecal ulcer and case 2 showed damage to both the upper and lower gastrointestinal tract.

Among our EGE with ascites patients, *H. pylori* presence was determined in two cases. Here, we explored the similar findings with a recent study in Japan that the rate of *H. pylori* infection was significantly lower in EGE, and Eosinophilic Esophagitis patients compared with controls, and this may explain the imbalance between Th1/Th2 in the aetiology of these disorders [8]. Countries with low hygienic environments and low socioeconomic conditions (overcrowding, low income, etc.) have higher infection rates and lower allergy-related diseases, such as asthma, eczema, allergic rhinitis, and others. The association between EGE and *H. pylori* infection has not been adequately considered in the literature. Additionally, prospective studies in children are needed to further investigate this association.

In terms of histopathological images, all cases of intestinal biopsies were infiltrated with many clusters of inflammatory cells, mainly eosinophils.

3.2. Treatment

Due to the diversity of clinical manifestations as well as the low morbidity rate, there have not been many studies on the disease progression, which makes it difficult to develop a treatment regimen for the disease. Many therapeutic options have been suggested including dietary considerations and medicinal remedies such as steroids, leukotrienes inhibitors, and mast cells stabilizers but no conclusive evidence has been published to describe the efficacies of these treatments. The therapeutic role of steroids in the treatment of EGE is not established. The recommendation dose for prednisone is 1-2 mg/kg/day for 7-10 days and then discontinuation after 4 months may be considered [9].

Dietary strategy means eliminating foods that are likely to cause allergies such as beef, cow's milk, eggs, soybeans, peanuts, etc. A series of paediatric EGE patients showed remission of symptoms in 40% of cases after dietary treatment, which consisted of an elemental diet in children under 6 months and hypoallergenic feeding in older children [10].

A similar case to ours was described by G. Ming, et al. (2015) [5] with an 11-year-old male patient admitted to the hospital because of abdominal pain for 7 days. The patient had a history of allergy to eggs. Clinical examination noted ascites and other organs were normal; eosinophil test increased, accounting for 31% of total white blood cells; ascites exudate with white blood cells increased, along with mainly eosinophils accounting for 91%. Endoscopy revealed oedema, congestion, and haemorrhagic spots of the antrum and duodenum and pathology revealed eosinophil infiltration into the mucosa. The patient was treated with corticosteroids and cetirizine, clinical and laboratory symptoms improved rapidly within 2 weeks.

In fact, our patient due to clinical conditions of vomiting, abdominal distension, and abdominal pain, the treatment was combined with intravenous feeding and corticosteroids at the dose of 2 mg/kg/day. After 1 week, the patient improved clinically and eosinophil counts in the blood returned to normal. As a result, the patient was discharged after two weeks starting EGE treatment.

Therefore, clinical physicians should have a high suspicion of EGE when children have nonspecific gastrointestinal symptoms such as nausea, vomiting, weight loss, bloating, abdominal discomfort, abdominal pain, diarrhoea, ascites, or oedema along with peripheral eosinophilia. Additionally, histological biopsy should be performed to obtain findings the infiltration of eosinophils into the submucosa, eosinophils within the epithelium of the crypts or villi or crypt hyperplasia, etc., which is helpful to confirm the diagnosis.

Recently, no therapeutic treatment available has been proven to have a specific efficacy on the disease. Instead, the treatment is based on the hypothesis of pathophysiology including the mechanism of allergy and inflammatory response, thereby diet remedy and anti-inflammatory medicines such as corticosteroids have been suggested [11]. Indications for surgical treatment are suggested when there are complications of perforation, intussusception, or intestinal obstruction [12].

4. Prognosis

C. Reed, et al. (2015) [13] conducted a follow-up for 26 months to evaluate the progression of the disease based on clinical symptoms, endoscopic images, and pathology. The results showed 60% clinical response, 51% improvement in endoscopic lesions and 69% histological recovery; in which there is 27% improvement in all 3 criteria above. The follow-up process is not effective due to the invasive means of monitoring [13, 14]. In fact, our patients continue to be monitored clinically and will have endoscopic examination when necessary.

5. Conclusions

EGE is a rare disease and collaboration between clinicians, endoscopists, and histopathologists can reduce missed diagnoses. Diagnosis is based on findings of dense eosinophilic infiltrates in the stomach and/or intestine combined with the clinical setting.

In terms of treatment and long-term follow-up, more clinical trials with larger sample sizes are sorely needed to compare the effectiveness of each remedy option as well as to establish the most optimal therapeutic method and appropriate duration of maintenance treatment.

CRediT author statement

Van Thieu Ha: Data analysis and interpretation, Writing and Manuscript revising; Huu Tung Trinh: Method, Data analysis and Writing.

Ethical approval

The need for institutional ethics approval for this case report was waived. All patients provided informed consent for their case details and images to be published.

COMPETING INTERESTS

The authors declare that there is no conflict of interest regarding the publication of this article.

REFERENCES

[1] D.Y.M. Leung, C.A. Akdis, L.B. Bacharier, et al. (2016), "Allergic and eosinophilic gastrointestinal disease", *Pediatric Allergy*, Elsevier, 568pp.

[2] S. Tagore, P. Rawla, K.S. Yarlagadda, et al. (2019), "EGE: Diagnosis and clinical perspectives", *Clin. Exp. Gastroenterol.*, **12**, pp.239-253.

[3] A. Bavdekar, N. Thakur (2016), "Ascites in children", *Indian J. Pediatr.*, **83(11)**, pp.1334-1340, DOI:10.1007/s12098-016-2168-1.

[4] S.M. Belkhir, R. Khentache, L. Andre-Ledun, et al. (2018), "Eosinophilic ascites, a challenging diagnosis", *Int. Arch. Intern. Med.*, **2(1)**, DOI: 10.23937/iaim-2017/1710009.

[5] G. Ming, Y. Bo, Y.L. Ping (2015), "EGE with ascites in a child", *Indian Pediatr.*, **52(8)**, pp.707-708.

[6] M.M. Walker, M. Potter, N.J. Talley, et al. (2018), "EGE and other eosinophilic gut diseases distal to the oesophagus", *Lancet Gastroenterol. Hepatol.*, **3**, pp.271-280, DOI:10.1016/S2468-1253(18)30005-0.

[7] S. Montembault, L. Serfaty, J.L. Poirot, et al. (1997), "Hemorrhagic ascites disclosing massive *Fasciola hepatica* infectio", *Gastroenterol. Clin. Biol.*, **21(10)**, pp.785-788.

[8] S. Ishiharaa, Y. Kinoshitaa, A. Schoepfer (2016), "Eosinophilic esophagitis, EGE, and eosinophilic colitis: Common mechanisms and differences between east and west", *Inflamm. Intest. Dis.*, **1(2)**, pp.63-69, DOI:10.1159/000445131.

[9] F.M. Tien, J.F. Wu, Y.M. Yeng, et al. (2011), "Clinical features and treatment responses of children with EGE", *Pediatr. Neonatol.*, **52(5)**, pp.272-278, DOI:10.1016/j.pedneo.2011.06.006.

[10] V.B. Busoni, C. Lifschitz, S. Christiansen, et al. (2011), "Eosinophilic gastroenteropathy: A pediatric series", *Arch. Argent. Pediatr.*, **109(1)**, pp.68-73, DOI:10.1590/s0325-00752011000100019.

[11] A.J. Lucendo, A. Arias (2012), "EGE: An update", *Expert Rev. Gastroenterol. Hepatol.*, **6(5)**, pp.591-601, DOI:10.1586/egh.12.42.

[12] R.A. Abou, H.W. El (2016), "EGE: Approach to diagnosis and management", *World J. Gastrointest. Pharmacol. Ther.*, **7(4)**, pp.513-523, DOI: 10.4292/wjgpt.v7.i4.513.

[13] C. Reed, J.T. Woosley, E.S. Dellon (2015), "Clinical characteristics, treatment outcomes, and resource utilization in children and adults with EGE", *Dig. Liver Dis.*, **47(3)**, pp.197-201, DOI:10.1016/j.dld.2014.11.009.

[14] E. Cavalli, A. Brusaferro, E.S. Pieri, et al. (2019), "Eosinophilic esophagitis in children: Doubts and future perspective", *J. Transl. Med.*, **17**, DOI: 10.1186/s12967-019-2014-0.

DOI: 10.31276/VJSTE.64(2).65-68

Association of *CFAP65* rs56411706 with male infertility in 393 Vietnamese individuals

Thuy Duong Nguyen[1, 2*], Thi Khanh Ly Nguyen[1], Thi Thu Ha Duong[1]

[1]*Institute of Genome Research, Vietnam Academy of Science and Technology, 18 Hoang Quoc Viet Street, Nghia Do Ward, Cau Giay District, Hanoi, Vietnam*
[2]*Graduate University Science and Technology, Vietnam Academy of Science and Technology, 18 Hoang Quoc Viet Street, Nghia Do Ward, Cau Giay District, Hanoi, Vietnam*

Received 12 October 2021; revised 15 November 2021; accepted 1 December 2021

Abstract:

Approximately two thousand genes have been found to be involved in spermatogenesis and their mutations have been reportedly associated with male infertility. Recent studies have shown that *CFAP65* was crucial for spermatogenesis, and several mutations in this gene could result in male infertility. However, the association of polymorphisms in *CFAP65* with male infertility remains unknown. In this study, the relationship between *CFAP65* rs56411706 and male infertility was assessed in a Vietnamese population by 171 male infertility patients who had been diagnosed with non-obstructive azoospermia (NOA), oligozoospermia, or asthenozoospermia while 222 healthy controls were genotyped using polymerase chain reaction-restriction fragment length polymorphism (PCR-RFLP). Statistical analysis demonstrated that the allele frequencies of *CFAP65* rs56411706 followed Hardy-Weinberg equilibrium (HWE) ($p>0.05$). The Chi-square test revealed no correlation between the polymorphism and male infertility in this study ($p>0.05$). This is the first study on the association between a single nucleotide polymorphism in the *CFAP65* gene and male infertility in a Vietnamese population. The results of this study would help enrich the knowledge about the effects of *CFAP65* polymorphisms on male infertility in the Vietnamese population.

Keywords: ***CFAP65*, male infertility, PCR-RFLP, rs5611706, spermatogenic qualitative defects.**

Classification number: **3.2**

1. Introduction

Qualitative spermatogenesis defects are one of four major etiological categories of male infertility [1]. It is characterised by sperm motility, morphology, and functional parameters such as DNA and chromatin integrity [2]. Various clinical classifications for qualitative defects of spermatogenesis include "teratozoospermia" (reduced percentage of sperm with normal morphology) [3], "oligozoospermia" (reduced sperm count) [4], and "asthenozoospermia" (reduced sperm motility) [2]. However, to describe more than one abnormality within the semen parameters, other terms such as oligoteratozoospermia, oligoasthenozoospermia, and asthenoteratozoospermia are also used [2].

Asthenozoospermia, a type of asthenoteratozoospermia, is characterised by the presence of sperm flagellar anomalies that occur at the end of spermatogenesis and concurrently with head compaction and reshaping [5]. Over 80% of male infertility cases exhibit some alterations of sperm motility. The multiple morphological abnormalities of asthenozoospermia phenotypes include (1) morphological abnormalities such as short-coiled, absent, bent, and/or irregular-calibre flagella associated with dramatically declined motility or (2) ultrastructural flagellar defects, e.g., absent central pair (CP), disorganised double microtubules (DMT), dysplasia of fibrous sheath (FS), or absence of dynein arms [2]. Several genes have so far been identified as having an association with multiple morphological abnormalities of sperm flagella phenotypes [2, 6] leading to an absence of inner dynein arm (IDA), disorganized 9+2, absent CP, disorganised FS, or DMT [2]. Abnormalities of *CFAP* genes, which have been found to be involved in spermatogenesis, could cause fertility impairment in males [7-11]. Notably, *CFAP65* has been recognised

*Corresponding author: Email: tdnguyen@igr.ac.vn

as a new gene candidate for fertility impairment due to its functions regarding sperm flagellar morphology and paraflagellar rod synthesis [12, 13].

The *CFAP65* encodes cilia- and flagella-associated protein 65, which is highly expressed in testis during spermatogenesis. Several mutations on *CFAP65* have been reported to cause male infertility [8, 12, 14]. Consequently, the association between single nucleotide polymorphisms on this gene and the risk of male fertility is expected to be a good consideration. The polymorphism of rs56411706 occurring in the coding region of the *CFAP65* gene was analysed *in silico* using SIFT. This software predicts the effect of an amino acid substitution on protein function based on sequence homology among different species and physical properties. The obtained score of 0.09 suggested that rs56411706 is a promising candidate for an association study. Therefore, in this study, we conducted the PCR-RFLP experiment to investigate the relationship between *CFAP65* rs56411706 and the risk of male infertility in a Vietnamese population.

2. Materials and methods

2.1. Subjects

Our research subjects consisted of 171 men diagnosed with NOA caused by either oligo/azoospermia or asthenozoospermia and 222 healthy men with normal semen who had conceived at least one child. Unfertilised men with normal male reproductive organs and hormone balances were screened for semen and checked for microdeletion of the AZF region or other major abnormalities in the Y chromosome. The study was approved by the Ethical Review Committee of the Institute of Genomics Research (No: 9-2019/NCHG-HĐĐĐ). Prior to the commencement of the study, all participating individuals gave written informed consent.

2.2. Genotype determination

The total DNA of 393 individuals was extracted from peripheral blood samples using the GeneJet Whole Blood Genomic DNA Purification (Thermo Fisher). Quantity of genomic DNA was analysed by electrophoresis on 1% agarose, and DNA was quantified using NanoDropTM One spectrometer, Thermo Fisher. The gene fragment containing polymorphism *CFAP65* rs56411706 was amplified by PCR with a specific pair of primers sequenced F: 5'-CATTCTGCAAGGCGGTGATT-3' and R: 5'-AGGCTAAATTTTCCC TGGGGC-3'. The 10-µl PCR reaction mixture contained 1 µl of 10X PCR buffer; 100 µM dNTPs; 0.15 µM of forward and reverse PCR primer each; 0.1 U *Taq* DNA polymerase (Thermo Fisher); 10 ng genomic DNA; and H_2O. The PCR protocol consisted of denaturation at 95°C for 5 min followed by 35 cycles of 95°C for 30 s, 60°C for 30 s, and 72°C for 30 s, and the final extension for 7 min at 72°C. Electrophoresis on a 1% agarose gel was performed using 3 µl of the PCR product for each sample. Products of PCR reaction were subjected to 5 h digestion by *Hha*I at 37°C. Digested products were separated by electrophoresis on 2% agarose gel. The number and size of DNA fragments used to determine the genotype of *CFAP65* rs56411706 are presented in Table 1.

Table 1. The number and size of DNA fragments of *CFAP65* rs56411706 genotypes.

Genotype	DNA fragments	DNA length (bp)
CC	2	215, 112
CA	3	215, 112, 327
AA	1	327

2.3. Statistical analysis

Statistical analyses were conducted with the statistical software R version 3.6.1 [15]. HWE equilibrium was tested using HWE exact [16, 17]. Logistic regression was used to estimate a 95% (CI) and odds ratio (OR) for binary variables, with a p-value less than 0.05 considered significant. A total of three genetic patterns were investigated: dominant, recessive, and additive. The allele composition, genotype of polymorphism *CFAP65* rs56411706, and the association between single nucleotide polymorphism and infertility risk were examined. SNPassoc [18] was used to perform association analyses.

3. Results

3.1. Genotyping CFAP65 rs56411706

The specific PCR products were processed with the restricted enzyme *Hha*I. The genotypes of *CFAP65* rs56411706 were determined based on the size and number of DNA bands of the restricted product (Table 1, Fig. 1).

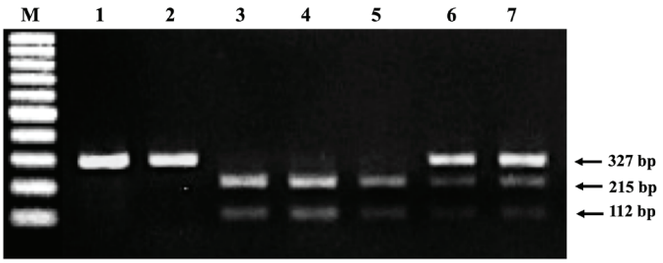

Fig. 1. Restriction enzyme-digested PCR products on agarose gel 2%.

Note: M: marker 100 bp; 1: uncut PCR product; 2: homozygous AA (1 band of 327 bp); 3-5: wildtype with the homozygous CC (2 bands of 112 and 215 bp); 6, 7: heterozygous CA (3 bands of 112, 215, and 327 bp).

Statistical analyses showed no differences in genotype composition and allele frequency between the case and control groups (Table 2). The distribution of this polymorphism was examined across two groups and as a whole by using the Chi-square test. The population followed HWE equilibrium (p>0.05) with CC/CA/AA genotype compositions of 0.72, 0.24, and 0.04, respectively (Table 2).

Table 2. Genotype composition and allele frequency of polymorphism *CFAP65* rs56411706.

Group	Genotype			Allele frequency (%)		p	HWE
	CC	*CA*	*AA*	*C*	*A*		
Control (n=222)	123 (0.72)	42 (0.24)	6 (0.04)	0.84	0.16	0.99	+
Case (n=171)	160 (0.72)	55 (0.24)	7 (0.04)	0.84	0.16	0.70	+
Total (n=393)	283 (0.72)	97 (0.24)	13 (0.04)	0.84	0.16	0.99	+

Note: HWE: Hardy-Weinberg equilibrium; +: follow the Hardy-Weinberg equilibrium.

Table 3. Association between *CFAP65* rs56411706 and male infertility.

Model	Control (n=222)	Case (n=171)	OR	95% CI	p
Additive					0.296
CC	160(72.07%)	123 (71.93%)	1.00		
CA	55 (24.77%)	42 (24.56%)	1.006	0.631-1.609	0.977
AA	7 (3.16%)	6 (3.51%)	0.894	0.283-2.909	0.848
Dominant					
CA+CC	215 (96.84%)	165 (96.49%)	1.00		
AA	7 (3.16%)	6 (3.51%)	0.89	0.28-2.86	0.84
Recessive					
AA+AC	160 (72.07%)	123 (71.93%)	1.00		
CC	62 (27.93%)	48 (28.07%)	0.99	0.636-1.553	0.975

Note: n: number of individuals; OR: odds ratio; 95% CI: 95% confidence interval; p: measured using Chi-square test.

3.2. Association analysis of CFAP65 rs56411706 with risk of male infertility

Chi-square testing on all three dominant, recessive, and additive models showed no association between this polymorphism and the risk of male infertility with a p-value greater than the significance level of 0.05 (Table 3).

4. Discussion

The gene *CFAP65* is evolutionarily conserved in several species [8]. The putative homolog of *CFAP65* is abundantly expressed in adult male mice, according to the murine testicular transcriptome analysis [8, 19]. Similarly, in Chlamydomonas, *CFAP65* is highly activated during flagellar regeneration [20]. The disruption of sperm motility caused by *CFAP65* was first discovered in Rose comb chickens [21]. A 2 bp frameshift mutation later confirmed the pathogenicity of *CFAP65* mutation in male mice [8]. Remarkably, phenotypes of mutated mice with *CFAP65*-frameshift-caring mutation were consistent with human asthenozoospermia [8].

In humans, *CFAP65*, comprising 13 transcripts, is found on 2q35. The cilia and flagella-associated protein 65, which is encoded by this gene, is highly and preferentially expressed in the testis according to the ENCODE [22], FANTOM [23], and GTEx databases [24]. Furthermore, proteomic analyses have found *CFAP65* in the centrioles of human spermatozoa [19]. In a study by W. Wang, et al. (2019) [14], *CFAP65* was identified as the causative gene for completely immotile spermatozoa. According to the proteomic analysis, in the absence of *CFAP65* during manchette organization, both mitochondrial sheath (MS) assembly and acrosome formation were unable to function properly [8]. Importantly, endogenous immunoprecipitation and immunostaining experiments revealed that *CFAP65* might form a cytoplasmic protein network with *MNS1, ZPBP1, RSPH1, TPPP2*, and *SPACA1* [13] in which the perturbations to the *CFAP65*-centered proteostasis network caused a series of defects in sperm head and flagella leading to severe asthenoteratospermia [13]. A homozygous nonsense mutation (p.Glu1781*) in *CFAP65* was identified in a consanguineous Chinese family with an abnormal flagella patient [19], and a biallelic mutation in *CFAP65* was also identified to cause asthenozoospermia.

In *CFAP65* rs56411706 polymorphism, a nucleotide was substituted at NM_194302.4:c.1024G>T. This substitution altered alanine to serine at position 342. Although the *CFAP65* rs56411706 polymorphism did

not show any association with male infertility in the Vietnamese population, our findings provide insights into *CFAP65* single nucleotide polymorphisms of male infertility.

4. Conclusions

In this study, the *CFAP65* rs56411706 polymorphism was analysed among 393 studied subjects. Results revealed the frequencies of genotypes CC/CA/CC to be 0.72/0.24/0.04, respectively. Their distribution all followed HWE. However, no relationship was established between *CFAP65* rs56411706 and male infertility ($p>0.05$). To gain more insight into this association, examinations of other polymorphisms in the *CFAP65* need to be considered.

CRediT author statement

Thuy Duong Nguyen: Data analysis and Interpretation, Writing and Manuscript revising; Thi Khanh Ly Nguyen, Thi Thu Ha Duong: Method, Data analysis and Writing.

ACKNOWLEDGEMENTS

We thank all sample donors for contributing to this research. This research was funded by the Ministry of Science and Technology, Vietnam (60/19-ĐTDL.CN-XNT).

COMPETING INTERESTS

The authors declare that there is no conflict of interest regarding the publication of this article.

REFERENCES

[1] H. Tournaye, C. Krausz, R.D. Oates (2017), "Novel concepts in the aetiology of male reproductive impairment", *Lancet Diabetes Endocrinol.*, **5(7)**, pp.544-553, DOI: 10.1016/S2213-8587(16)30040-7.

[2] D.V.S. Sudhakar, R. Shah, R.K. Gajbhiye (2021), "Genetics of male infertility - Present and future: A narrative review," *Journal of Human Reproductive Sciences*, **14(3)**, pp.217-227, DOI: 10.4103/jhrs.jhrs_115_21.

[3] M. De Braekeleer, M.H. Nguyen, F. Morel, et al. (2015), "Genetic aspects of monomorphic teratozoospermia: A review", *J. Assist. Reprod. Genet.*, **32(4)**, pp.615-623, DOI: 10.1007/s10815-015-0433-2.

[4] N. Kumar, A. Singh (2015), "Trends of male factor infertility, an important cause of infertility: A review of literature", *Journal of Human Reproductive Sciences*, **8(4)**, pp.191-196, DOI: 10.4103/0974-1208.170370.

[5] J.F.N. Mbango, C. Coutton, C. Arnoult, et al. (2019), "Genetic causes of male infertility: Snapshot on morphological abnormalities of the sperm flagellum", *Basic Clin. Androl.*, **29**, DOI: 10.1186/s12610-019-0083-9.

[6] E. Casas, M.E. Kehrli (2016), "A review of selected genes with known effects on performance and health of cattle", *Frontiers in Veterinary Science*, **3**, DOI: 10.3389/fvets.2016.00113.

[7] L. Li, F. Feng, Y. Wang, et al. (2020), "Mutational effect of human *CFAP43* splice-site variant causing multiple morphological abnormalities of the sperm flagella", *Andrologia*, **52(6)**, DOI: 10.1111/and.13575.

[8] W. Li, H. Wu, F. Li, et al. (2020), "Biallelic mutations in *CFAP65* cause male infertility with multiple morphological abnormalities of the sperm flagella in humans and mice", *J. Med. Genet.*, **57(2)**, pp.89-95, DOI: 10.1136/jmedgenet-2019-106344.

[9] Y.W. Sha, X. Wang, Z.Y. Su, et al. (2019), "Patients with multiple morphological abnormalities of the sperm flagella harbouring *CFAP44* or *CFAP43* mutations have a good pregnancy outcome following intracytoplasmic sperm injection", *Andrologia*, **51(1)**, pp.10-13, DOI: 10.1111/and.13151.

[10] X. He, C. Liu, X. Yang, et al. (2020), "Bi-allelic loss-of-function variants in *CFAP58* cause flagellar axoneme and mitochondrial sheath defects and asthenoteratozoospermia in humans and mice", *Am. J. Hum. Genet.*, **107(3)**, pp.514-526, DOI: 10.1016/j.ajhg.2020.07.010..

[11] W. Li, X. He, S. Yang, et al. (2019), "Biallelic mutations of *CFAP251* cause sperm flagellar defects and human male infertility", *J. Hum. Genet.*, **64(1)**, pp.49-54, DOI: 10.1038/s10038-018-0520-1.

[12] V.M.S. Torres, H.L.G. Blanco, R.A.S. Torres, et al. (2020), "Whole exome sequencing identifies multiple novel candidate genes in familial gastroschisis", *Mol. Genet. Genomic Med.*, **8(5)**, DOI: 10.1002/mgg3.1176.

[13] W. Wang, S. Tian, H. Nie, et al. (2021), "*CFAP65* is required in the acrosome biogenesis and mitochondrial sheath assembly during spermiogenesis", *Hum. Mol. Genet.*, **30(23)**, pp.2240-2254, DOI: 10.1093/hmg/ddab185.

[14] W. Wang, C. Tu, H. Nie, et al. (2019), "Biallelic mutations in *CFAP65* lead to severe asthenoteratospermia due to acrosome hypoplasia and flagellum malformations", *J. Med. Genet.*, **56(11)**, pp.750-757, DOI: 10.1136/jmedgenet-2019-106031.

[15] The R Project for Statistical Computing (2020), https://www.R-project.org/, accessed 5 May 2020.

[16] J.E. Wigginton, D.J. Cutler, G.R. Abecasis (2005), "A note on exact tests of Hardy-Weinberg equilibrium", *Am. J. Hum. Genet.*, **76(5)**, pp.887-893.

[17] D.J. Schaid, A.J. Batzler, G.D. Jenkins, et al. (2006), "Exact tests of Hardy-Weinberg equilibrium and homogeneity of disequilibrium across strata", *Am. J. Hum. Genet.*, **79(6)**, pp.1071-1080.

[18] J.R. González, L. Armengol, X. Solé, et al. (2007), "SNPassoc: An R package to perform whole genome association studies", *Bioinformatics*, **23(5)**, pp.644-645, DOI: 10.1093/bioinformatics/btm025.

[19] S. Tang, X. Wang, W. Li, et al. (2017), "Biallelic mutations in *CFAP43* and *CFAP44* cause male infertility with multiple morphological abnormalities of the sperm flagella", *Am. J. Hum. Genet.*, **100(6)**, pp.854-864, DOI: 10.1016/j.ajhg.2017.04.012.

[20] G.J. Pazour, N. Agrin, J. Leszyk, et al. (2005), "Proteomic analysis of a eukaryotic cilium", *J. Cell Biol.*, **170(1)**, pp.103-113, DOI: 10.1083/jcb.200504008.

[21] F. Imsland, C. Feng, H. Boije, et al. (2012), "The Rose-comb mutation in chickens constitutes a structural rearrangement causing both altered comb morphology and defective sperm motility", *PLOS Genet.*, **8(6)**, DOI: 10.1371/journal.pgen.1002775.

[22] F. Abascal, R. Acosta, J. Adrian, et al. (2020), "Perspectives on ENCODE", *Nature*, **583(7818)**, pp.693-698, DOI:10.1038/s41586-020-2449-8.

[23] I. Abugessaisa, J.A. Ramilowski, M. Lizio, et al. (2021), "FANTOM enters 20th year: Expansion of transcriptomic atlases and functional annotation of non-coding RNAs", *Nucleic Acids Res.*, **49(D1)**, pp.892-898, DOI: 10.1093/nar/gkaa1054.

[24] Genotype-Tissue Expression (2020), https://www.gtexportal.org/home/, accessed 5 May 2020.

DOI: 10.31276/VJSTE.64(2).69-75

In silico screening of chalcones and their derivatives as potential inhibitors of spike proteins and ACE2 enzymes for SARS-CoV-2 treatment

Thi Thu Hang Ta, Bao Kim Nguyen, Thi Hong Khanh Do, Thanh Tung Bui*

University of Medicine and Pharmacy, Vietnam National University - Hanoi, 144 Xuan Thuy Street, Dich Vong Hau Ward, Cau Giay District, Hanoi, Vietnam

Received 1 August 2021; revised 31 August 2021; accepted 10 November 2021

Abstract:

The COVID-19 pandemic causing acute respiratory syndrome is a significant public health problem. Drugs that can treat this disease are currently a high priority. The SARS-CoV-2 spike protein and human ACE2 enzyme receptor, which both play important roles in virus entry into the host cell, are promising therapeutic targets for inhibiting viral infection. This research evaluates the potential of chalcone compounds to inhibit the spike proteins and ACE2 enzymes through molecular docking *in silico* approaches. Based on the ChemFaces database, we collected 92 chalcone compounds. These compounds were further docked to target the active sites of spike protein and human ACE2. After comparing the binding energies of the 92 compounds to artemisinin, ribavirin, and lopinavir, which have inhibitory activity to these protein targets of SARS-CoV-2, we chose 20 out of the 92 compounds that had a higher ability to inhibit the protein targets than the reference inhibitors. Next, five phytochemical compounds with the best binding energy were selected, which included flavanomarein, sarcandrone B, sarcandrone A, calyxin H, and sieboldin. Then, Lipinski's 5 rule was used to evaluate the drug-like properties of these compounds. Predictive ADME/tox filtering tests were also applied to the top docked compounds. The results suggest that sarcandrone B has good pharmacokinetic properties, which should be further explored as an anti-SARS-CoV-2. To confirm these findings, experimental studies are recommended.

Keywords: **chalcones, human ACE2, *in silico*, molecular docking, SARS-CoV-2, spike protein.**

Classification number: **3.3**

1. Introduction

Coronaviruses are a broad group of viruses that may cause moderate to severe respiratory illnesses in humans and also may infect many different species. Since the novel coronavirus designated as SARS-CoV-2 was first discovered in Wuhan city, Hubei province, China, the scientific community as well as the human race have had to confront the extraordinary task of finding a cure to this disease. This new coronavirus illness has spread rapidly around the world as it is highly transmissible. As of 20 August, 2021, there have been 209,558,900 reported cases and 4,398,234 deaths globally. In Vietnam, 312,611 cases and 7,150 deaths have been reported [1]. One of the biggest concerns is that the symptoms of the disease are often very diverse and can manifest differently in each patient. Clinical symptoms are usually noticed 5 to 6 days after infection, but the incubation period can be up to 14 days [2]. Those who are infected with SARS-CoV-2 have signs of viral pneumonia such as fever, cough, and chest pain as well as dyspnoea and bilateral infiltration in severe situations, which is similar to SARS and MERS patients.

SARS-CoV-2 has a 29.9 kb-size positive-sense RNA genome. It is composed of 14 open reading frames (ORFs), which encodes for a total of 27 proteins divided into structural and non-structural proteins (NSPs) [3]. Covering the surface of SARS-CoV-2, spike proteins are an important protein to viral entering because SARS-CoV-2 employs the receptor binding domain (RBD) of its glycosylated S protein to engage the cell-specific surface receptors and trigger membrane fusion [4]. This includes binding to the human Angiotensin Conversion enzyme

*Corresponding author: Email: tungasia82@gmail.com

(hACE2) followed by human protease proteolytic activation [5]. Owing to the roles of the spike protein and ACE2 enzyme in the mechanism of SARS-CoV-2 cell entry, considerable attention has been paid to these major targets for medications and vaccines treating COVID-19 [5].

Due to the few side effects and great health advantages of phytochemicals, anti-infection treatments based on plants have attracted health researchers throughout the world [6]. Indeed, the development of plant-based medicines for their antibacterial, antivirus, anticancer, and antioxidant properties are being continually explored [7, 8]. Chalcones are a group of polyphenolic compounds derived from plants that belong to the flavonoid family. Many studies indicated that some chalcones have a variety of antioxidant, antimicrobial, antimycobacterial, and antileishmanial properties [9-11]. Chalcones also exhibit inhibitory activity against the tobacco mosaic virus, HIV, herpes simplex virus, and dengue virus [11-13]. In that context, there is some existing evidence about the anti-SARS-CoV-2 potential of chalcones and their derivatives [14, 15]. Our research focuses on the virtual screening of chalcones and their derivatives against SARS-CoV-2-related spike protein viruses and human ACE2 enzymes. The structures were all collected from ChemFaces database, which is a professional high purity natural products manufacturer.

2. Materials and methods

2.1. Ligands preparation

The ligand structures were collected from ChemFaces for the SARS-CoV-2 spike protein and the human ACE2 target involved 92 bioactive compounds. The structures were downloaded from PubChem in .sdf format and then converted into 3D structures in PDB format using MOE software. Structure Data Format (SDF) structures of the reference inhibitors (artemisinin, ribavirin, lopinavir) were retrieved from the PubChem database. After that, they were optimised by Avogadro software using Conjugate Gradients and converted to .pdbqt format using Autodock Tools software.

2.2. Retrieval and preparation of protein structure

Three-dimensional images of the SARS-CoV-2 spike protein (PDB ID: 6VSB) and human ACE2 (PDB ID: 1R4L) were retrieved from the Protein Data Bank RCSB [16, 17]. The co-crystal ligand XX5 in the structure of human ACE2 was used to evaluate and optimize the docking model. All water molecules and co-crystals were removed from the protein molecule using Discovery Studio Visualizer 4.0 software, while missing hydrogen atoms were added using Autodock Vina before regenerating the active site using MGL Autodock Tools 1.5.6 software. The active site of the SARS-CoV-2 spike protein and human ACE2 were identified as (x, y, z) = (40.003, 6.069, 28.538) (grid box size 12 Å×10 Å×13 Å); (x, y, z) = (204.457, 199.799, 246.898) (grid box size = 50 Å×50 Å×50 Å). The protein was saved in .pdbqt format to prepare for the docking program.

2.3. Lipinski's rule of five

Lipinski's rule of five helps to compare drug-like and non-drug-like molecules [18]. Lipinski's rule of five is popularly used to evaluate the potential molecular to become a therapeutic drug. This rule acts as a filter to screen promising compounds with particular pharmacological drugs.

We used the online tool to evaluate Lipinski's rule of five [19]. The chemical structures were downloaded from the PubChem database and set at pH 7.0.

2.4. Molecular docking study

AutoDock Vina performed an initial simulated screening of 92 bioactive compounds against SARS-CoV-2 spike protein and human ACE2. The molecular interactions between compounds that have good free binding energies and molecular targets were viewed using Discovery Studio Visualizer 2020.

2.5. Prediction of ADMET by computational analysis

The physicochemical efficiencies of the compounds were analysed by *in silico* ADMET profiling. An ADMET profile involves five parameters: absorption, distribution, metabolism, excretion, and toxicity, which all play a significant role to demonstrate the likelihood of success of turning a compound into a drug. Drug absorption depends on many factors including membrane permeability, intestinal absorption, levels of skin permeability, substrate, or inhibitor of P-glycoprotein. Drug distribution is influenced by variables such as CNS permeability, the blood-brain barrier (logBB), and the volume of distribution (VDss). Based on the CYP models for substrate or inhibition (CYP2D6, CYP3A4, CYP1A2, CYP2C19, CYP2C9, CYP2D6, and CYP3A4), metabolism is expected. Based on the total clearance model and the renal OCT2 substrate, excretion is expected. Based on AMES toxicity, hepatotoxicity, and skin sensitization, the toxicity of drugs is expected. These criteria have been determined and their standard ranges have been tested for compliance. ADMET profiling was predicted using the pkCSM tool [20]. The canonical SMILES molecular structures of collected compounds were retrieved from PubChem [21].

3. Results

3.1. Evaluation of the docking model

Before screening compounds, the docking model needs to be evaluated for its accuracy. The results after docking the co-crystal ligand produced an RMSD value of 0.777 Å. This value satisfies the condition that RMSD is less than 1.5 Å, indicating that the results of molecular docking on the target are reliable. The results of re-docking and the interaction between the co-crystallised ligand with the human ACE2 are shown as shown in Figs. 1 and 2.

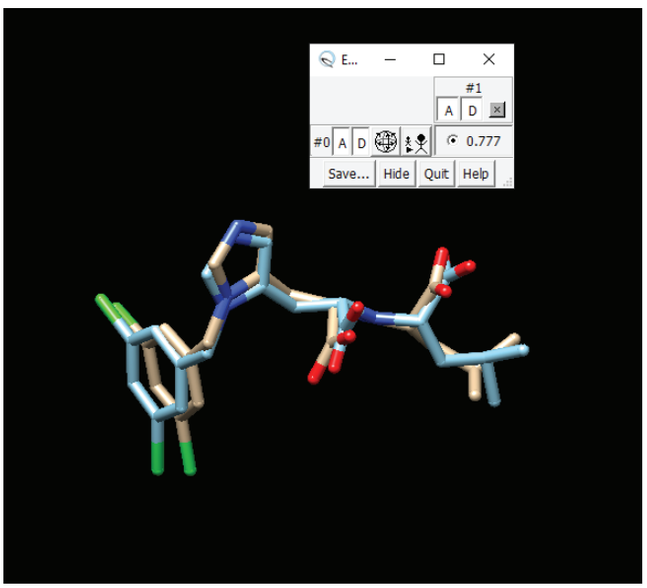

Fig. 1. Co-crystallised ligand re-dock results of 1R4L.

3.2. Molecular docking of compounds with the target protein

We docked 92 bioactive compounds retrieved with SARS-CoV-2 spike protein and human ACE2. To evaluate the compounds' abilities to inhibit target proteins, we compared the docking scores of the ligands with artemisinin, ribavirin, and lopinavir. Artemisinin has also been demonstrated by M. Sehailia, et al. (2020) [22] to act as a spike protein inhibitor. Recently, the effectiveness of lopinavir, an inhibitor of the proteases, and ribavirin, a nucleoside analogue to eliminate the removal of SARS-

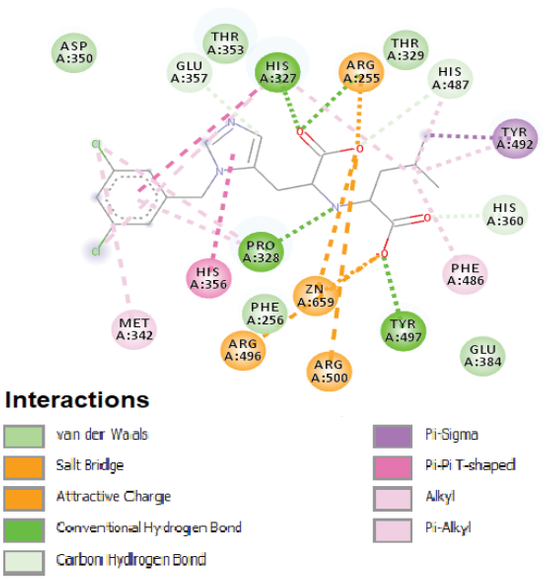

Fig. 2. 2D representation of the interaction of co-crystallised ligand XX5 with human ACE2.

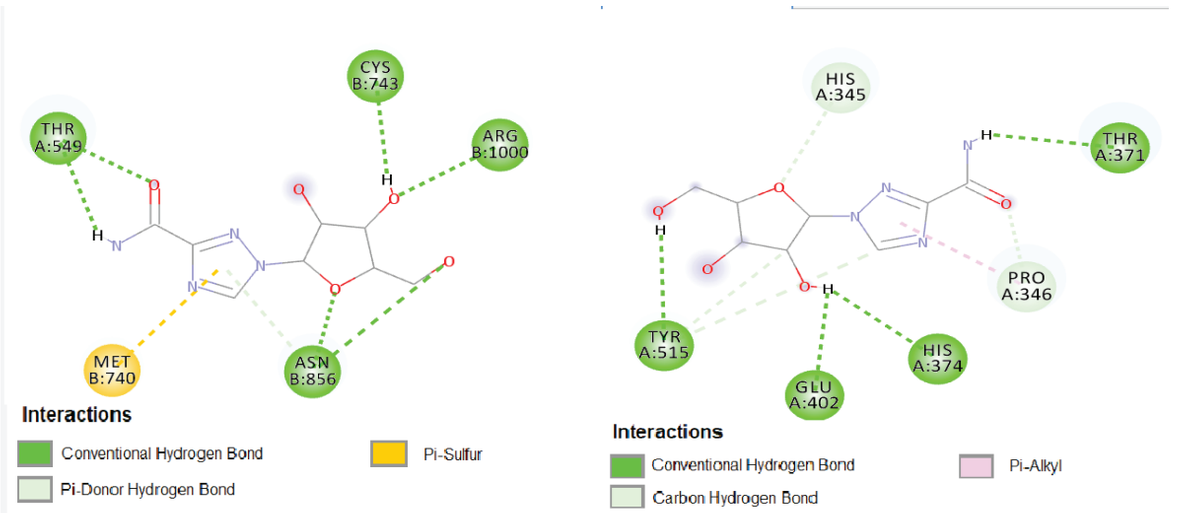

(A) (B)

Fig. 3. Interactions between (A) ribavirin and spike protein and (B) ribavirin and human ACE2.

CoV-2, has been documented [23-26]. Artemisinin had binding affinities of -7.3 kcal/mol for the spike protein. The binding energies of lopinavir and ribavirin were found to be -6.3 and -5.7 kcal/mol, respectively, when docked in the spike protein and -6.7 and -7.6 kcal/mol when docked in the human ACE2. Figure 3 shows the interaction between the reference inhibitors and targets.

A hit list of 20 bioactive compounds was defined based on the negative and low value of ΔG and compared with the reference inhibitors (Table 1).

Table 1. The docking results of 20 hit phytochemicals and reference compounds with spike protein and human ACE2.

No.	Name	Binding energy with spike protein (kcal/mol)	Binding energy with human ACE2 (kcal/mol)	No.	Name	Binding energy with spike protein (kcal/mol)	Binding energy with human ACE2 (kcal/mol)
1	Isoliquiritin	-8.3	-8.4	13	Phlorizin dihydrate	-8.1	-7.8
2	Flavanomarein	-8.9	-9.4	14	Isodorsmanin A	-8	-8.5
3	Sarcandrone B	-9.4	-10.3	15	Calyxin H	-9	-6.2
4	Sarcandrone A	-9.8	-3.4	16	Isoliquiritoside	-8.1	-8.7
5	Trilobatin	-8	-8.4	17	Xanthohumol I	-8.2	-8.3
6	Morachalcone A	-7.9	-8.2	18	Xanthohumol L	-8.1	-8.3
7	Trilobatin 2"-acetate	-8.8	-8.3	19	Xanthohumol B	-7.9	-8.1
8	Nothofagin	-8.3	-8.7	20	Sieboldin	-8.4	-8.8
9	Bavachromene	-8.2	-8.1	**R1**	**XX5**		**-7.5**
10	Kuraridine	-8.2	-7.8	**R2**	**Artemisinin**	**-7.9**	
11	Marein	-8.5	-8.6	**R3**	**Ribavirin**	**-6.3**	**-6.7**
12	Neoisoliquiritin	-8.6	-8.5	**R4**	**Lopinavir**	**-5.7**	**-7.6**

From these, the top five bioactive compounds with the most negative binding energies were chosen, which were flavanomarein, sarcandrone B, sarcandrone A, calyxin H, and sieboldin. It was observed that all these compounds were the topmost docked compound to the spike protein as well as human ACE2. The results show that the ligands majorly interacted with the residues through hydrogen bonds and π-anion bonds.

3.3. Lipinski's rule of five

Lipinski's rule of five helps to distinguish between drug-like and non-drug-like molecules. It predicts with high probability the drug-like effectiveness or failure of molecules complying with 2 or more of the following rules: molecular mass (MW) below 500 Dalton; high lipophilicity (LogP does not exceed 5); no more than 5 donors of hydrogen bonds (HBD); no more than 10 acceptors of hydrogen bonds (HBA1); and molar refractivity (MR) should be between 40-130. The top five bioactive compounds are listed in Table 2. These compounds satisfy more than 2 criteria. Next, we focus on analysing the pharmacokinetic properties of these drugs including absorption, distribution, metabolism, excretion, and toxicity.

Table 2. The result of Lipinski's rule of five.

No.	Name	Molecular weight	HBD	HBA1	logP	MR	Drug-likeness
1	Flavanomarein	450	7	11	-0.3114	104.59	Yes
2	Sarcandrone B	554	3	8	6.381006	153.61203	Yes
3	Sarcandrone A	554	3	8	6.381006	153.61203	Yes
4	Calyxin H	566	5	7	6.485604	162.271667	Yes
5	Sieboldin	452	8	11	-0.4968	106.589844	Yes

3.4. Prediction of absorption, distribution, metabolism, excretion, and toxicity (ADMET) profile.

The prediction of absorption, distribution, metabolism, excretion, and toxicity profile of the five selected drugs are shown in Table 3.

Table 3. The result of the ADMET profile.

Properties	Flavanomarein	Sarcandrone B	Sarcandrone A	Calyxin H	Sieboldin
Absorption					
Water solubility (log mol/l)	-3.082	-3.608	-3.447	-2.912	-2.777
Caco-2 permeability (log P_{app} in 10^{-6} cm/s)	0.487	-0.323	-0.343	-0.877	-1.175
Intestinal absorption (human) (%)	40.359	100	100	78.977	22.15
Distribution					
VDss (human) (log l/kg)	0.915	-2.186	-2.199	-1.682	1.154
BBB permeability (log BB)	-1.428	-1.235	-1.287	-1.235	-1.567
CNS permeability (log PS)	-4.267	-3.039	-2.969	-2.742	-4.178
Metabolism					
CYP2D6 substrate	No	No	No	No	No
CYP3A4 substrate	No	Yes	Yes	Yes	No
CYP1A2 inhibitor	No	No	No	No	No
CYP2C19 inhibitor	No	Yes	Yes	Yes	No
CYP2C9 inhibitor	No	Yes	Yes	Yes	No
CYP2D6 inhibitor	No	No	No	No	No
CYP3A4 inhibitor	No	Yes	Yes	Yes	No
Excretion					
Total clearance (log ml/min/kg)	0.011	0.34	0.322	0.202	-0.158
Renal OCT2 substrate	No	No	No	No	No
Toxicity					
AMES toxicity	Yes	No	No	No	No
Hepatotoxicity	No	No	No	No	No
Skin sensitisation	No	No	No	No	No
Minnow toxicity (log mM)	5.937	-0.18	-2.32	-0.349	6.787

The first property is the absorption process in which human intestinal absorption (HIA) and human colon adenocarcinoma-2 cell line (Caco-2) are two important parameters that determine the absorption of the drug. A substance is considered poorly absorbed if the percentage absorbed in the human intestine is less than 30% [20]. The results show that sieboldin was poorly absorbed with an absorbance of 30%. Three compounds, sarcandrone B, sarcandrone A, and calyxin H, are well absorbed in the intestine especially sarcandrone A and B, which have a maximum absorption percentage of 100%. The Caco-2 cell line consists of human colon adenocarcinoma cells. A compound has high Caco-2 permeability if it has P_{app}>8×10^{-6} cm/s, i.e., logPapp>0.9 [20]. The results of all five compounds had a Caco-2 permeability less than 0.9.

Secondly, the distribution of a substance is expressed through several parameters including lipid-solubility, concentration, as well as the binding capability to plasma proteins, transfer proteins, and lipid-solubility. The steady-state volume of distribution (VDss) is the theoretical volume to which the total dose of a drug should be uniformly distributed to obtain the same plasma concentrations [20]. The higher the VDss, the more the drug is distributed in tissue rather than plasma. Compounds were said to be well distributed to tissues if logVDss>0.45 and poorly distributed if logVDss<-0.15 [20]. The two compounds flavanomarein and sieboldin distributed well to tissues with logVDss values of 0.915 and 1.154, respectively. The remaining three compounds were poorly distributed. The capability of a drug to cross into the brain is a factor to consider to help reduce toxicities and side effects or to improve the effectiveness of drugs whose pharmacological activity is within the brain [20]. The blood-brain barrier ability of all compounds was poor because their logBB values were all less than -1. Compounds are considered to enter the central nervous system (CNS) in the presence of logPS>-2 [20]. The results showed that all five compounds failed to enter the CNS because their logPS values were less than -2.

Cytochrome P450 plays an important role in the metabolism of many drugs. P450 inhibitors can significantly alter the pharmacokinetics of these drugs. The results showed that the two flavanomarein compounds and sieboldin, are not substrates of CYP2D6, CYP3A4 and are not inhibitors of CYP1A2, CYP2C19, CYP2C9, CYP2D6, and CYP3A4. The compounds sarcandrone A, B, and calyxin H are substrates of CYP2D6, CYP3A4 and are inhibitors of CYP2C19, CYP2C9, and CYP3A4.

Regarding elimination, we predicted total clearance and likelihood as a renal OCT2 substrate. The resulting total clearance is shown in Table 3. Organic Cation Transporter 2 (OCT2) is a renal absorption transporter that plays an important role in renal processing and clearance of drugs and endogenous compounds [20]. All substances are not OCT2 substrates.

The toxicity prediction results for the five compounds showed that only flavanomarein caused AMES toxicity (mutagenicity). The remaining compounds are not hepatotoxic, mutagenic, and have no skin toxicity.

4. Discussion

In this study, we screened 92 chalcones compounds on the spike protein and ACE2 targets of the SARS-CoV-2 virus. The results obtained 5 compounds with the most negative free binding energy including sarcandrone A and B, flavanomarein, calyxin H, and sieboldin.

Sarcandrone A and sarcandrone B are flavan-chalcone dimers isolated from *Sarcandra hainanensis*. From the results of evaluating the HIV-1 inhibitory ability of C.M. Cao, et al. (2009) [27] obtained IC_{50} values of sarcandrone A and B at 18.05 and 25.27 mM, respectively. In our study, the docking results showed that sarcandrone A and sarcandrone B are the two compounds with the most negative free binding energy on the SARS-CoV-2 spike target. Sarcandrone A has a free binding energy of -9.8 kcal/mol and -3.4 kcal/mol corresponding to the two targets of SARS-CoV-2 spike protein and human ACE2 enzyme. Meanwhile, sarcandrone B inhibits these two targets with good free binding energies of -9.4 and -10.3 kcal/mol, respectively, to the spike protein and ACE2 enzyme. These two compounds have similar structures that differ mainly in the position of the -OH and -OCH_3 groups on the (D) ring. This may be the reason for sarcandrone A's poor ability to inhibit the ACE2 target with a free binding energy of -3.4 kcal/mol. In addition, ADMET results for both compounds were quite positive with 100% intestinal absorption without hepatotoxicity, skin toxicity, or AMES toxicity. Therefore, these are two potential natural compounds for the treatment of COVID-19.

Calyxin H is isolated from *Alpinia katsumadai* and *Alpinia blepharocalyx* [28, 29]. Our research results show that calyxin H strongly inhibits SARS-CoV-2 spike proteins with a free binding energy of -9.0 kcal/mol, which is much more negative than the positive controls artemisinin, ribavirin, and lopinavir. The pharmacokinetic prediction also shows that the compound is well soluble in water, does not cross the blood-brain barrier, does not penetrate the central nervous system, and has little toxicity. Therefore, we can see the great potential of calyxin H in inhibiting the spike protein of SARS-CoV-2.

Flavanomarein is the main compound in *Coreopsis tinctoria*, which has been shown to have good antioxidant, antidiabetic, antihyperlipidemic, and antihypertensive effects [30-33]. However, the antiviral effects of flavanomarein have not been studied. The docking results of flavanomarein on the spike protein of SARS-CoV-2 and the human ACE2 enzyme gave good results. Specifically, flavanomarein inhibited the spike protein and ACE2 receptor with binding energies of -8.9 and -9.4 kcal/mol, respectively. However, the intestinal absorption of this compound is not high at a little more than 40%. Flavanomarein has no skin toxicity and no hepatotoxicity but causes AMES toxicity.

Sieboldin is a dihydrochalcone compound present in several species of *Malus*. Sieboldin exhibits cytotoxicity to cancer cell lines and an antioxidant capacity [34]. This compound also showed inhibitory potential on both important targets of SARS-CoV-2 with binding energies of -8.4 and -8.8 kcal/mol for the spike protein and ACE2 enzyme, respectively. In addition, sieboldin is well distributed to tissues, is not metabolised in the liver, and has little toxicity. However, the absorption of sieboldin in the human intestine is poor at only 22.15%.

As soon as SARS-CoV-2 appeared, scientists began aggressively searching for drugs to treat COVID-19. The *in silico* approach was chosen to screen a large number of substances for potential compounds in a short time. As a result, many compounds with the ability to inhibit SARS-CoV-2 have been found such as amentoflavone, epigallocatechin gallate, and kaempferol [35-37]. However, the five potential compounds that we screened are relatively new and unpublished compounds with the ability to inhibit two targets: ACE2 and spike protein of the SARS-CoV-2 virus. The *in silico* method has high reliability, but it also inevitably leads to the discovery of the failure of non-potential compounds. Therefore, *in vivo* and *in vitro* studies should be conducted.

5. Conclusions

In this study, we found five natural chalcone compounds, flavanomarein, sarcandrone B, sarcandrone A, calyxin H, and sieboldin, that strongly inhibited the spike protein and ACE2 receptor of the SARS-CoV-2 virus. Among them, sarcandrone B has the most potential due to its strong inhibition of these 2 targets, its drug-like properties, good pharmacokinetic parameters, and low toxicity. Therefore, further tests on the ability of sarcandrone B to inhibit SARS-CoV-2 need to be conducted.

CRediT author statement

Thi Thu Hang Ta, Bao Kim Nguyen, Thi Hong Khanh Do: Methodology, Data analysis and Writing; Thanh Tung Bui: Data analysis and Interpretation, Writing - Reviewing and Editing.

COMPETING INTERESTS

The authors declare that there is no conflict of interest regarding the publication of this article.

REFERENCES

[1] T. Binh (2022), "Agreement to move COVID-19 from group A infectious disease to group B", *Vietnam Ministry of Health Information Portal on COVID-19 Pandemic*, https://ncov.moh.gov.vn, accessed 5 May 2021 (in Vietnamese).

[2] N. Chams, S. Chams, R. Badran, et al. (2020), "COVID-19: A multidisciplinary review", *Frontiers in Public Health*, **8**, DOI: 10.3389/fpubh.2020.00383.

[3] A. Wu, Y. Peng, B. Huang, et al. (2020), "Genome composition and divergence of the novel coronavirus (2019-nCoV) originating in China", *Cell Host & Microbe*, **27(3)**, pp.325-328, DOI: 10.1016/j.chom.2020.02.001.

[4] Y. Huang, C. Yang, X. Xu, et al. (2020), "Structural and functional properties of SARS-CoV-2 spike protein: Potential antivirus drug development for COVID-19", *Acta Pharmacologica Sinica*, **41(9)**, pp.1141-1149, DOI: 10.1038/s41401-020-0485-4.

[5] A.C. Papageorgiou, I. Mohsin (2020), "The SARS-CoV-2 spike glycoprotein as a drug and vaccine target: Structural insights into its complexes with ACE2 and antibodies", *Cells*, **9(11)**, DOI: 10.3390/cells9112343.

[6] R. Ghildiyal, V. Prakash, V.K. Chaudhary, et al. (2020), "Phytochemicals as antiviral agents: Recent updates", *Plant-Derived Bioactives*, Springer Nature, DOI: 10.1007/978-981-15-1761-7_12.

[7] D. Biswas, S. Nandy, A. Mukherjee, et al. (2020), "*Moringa oleifera* Lam. and derived phytochemicals as promising antiviral agents: A review", *South African Journal of Botany*, **129**, pp.272-282, DOI: 10.1016/j.sajb.2019.07.049.

[8] H. Lillehoj, Y. Liu, S. Calsamiglia, et al. (2018), "Phytochemicals as antibiotic alternatives to promote growth and enhance host health", *Vet. Res.*, **49(1)**, DOI: 10.1186/s13567-018-0562-6.

[9] S. Burmaoglu, O. Algul, A. Gobek, et al. (2017), "Design of potent fluoro-substituted chalcones as antimicrobial agents", *Journal of Enzyme Inhibition and Medicinal Chemistry*, **32(1)**, pp.490-495, DOI: 10.1080/14756366.2016.1265517.

[10] L.D. Chiaradia, P.G.A. Martins, M.N.S. Cordeiro, et al. (2012), "Synthesis, biological evaluation, and molecular modeling of chalcone derivatives as potent inhibitors of *Mycobacterium tuberculosis* protein tyrosine phosphatases (PtpA and PtpB)", *J. Med. Chem.*, **55(1)**, pp.390-402, DOI: 10.1021/jm2012062.

[11] M.V.P. Mello, T.F.S. Domingos, C.R. Rodrigues, et al. (2018), "A comprehensive review of chalcone derivatives as antileishmanial agents", *Eur. J. Med. Chem.*, **150**, pp.920-929, DOI: 10.1016/j.ejmech.2018.03.047.

[12] S.T. Hassan, R. Masarčíková, K. Berchová (2015), "Bioactive natural products with anti-herpes simplex virus properties", *J. Pharm. Pharmacol.*, **67(10)**, pp.1325-1336, DOI: 10.1111/jphp.12436.

[13] J.H. Wu, X.H. Wang, Y.H. Yi, et al. (2003), "Anti-AIDS agents 54. A potent anti-HIV chalcone and flavonoids from genus *Desmos*", *Bioorg. Med. Chem. Lett.*, **13(10)**, pp.1813-1815, DOI: 10.1016/S0960-894X(03)00197-5.

[14] S. Verma, D. Twilley, T. Esmear, et al. (2020), "Anti-SARS-CoV natural products with the potential to inhibit SARS-CoV-2 (COVID-19)", *Frontiers in Pharmacology*, **11**, DOI: 10.3389/fphar.2020.561334.

[15] N. Duran, M.F. Polat, D.A. Aktas, et al. (2021), "New chalcone derivatives as effective anti-SARS-CoV-2 agents", *International Journal of Clinical Practice*, **75(12)**, DOI: 10.1111/ijcp.14846.

[16] P. Towler, B. Staker, S.G. Prasad, et al. (2004), "ACE2 X-ray structures reveal a large hinge-bending motion important for inhibitor binding and catalysis", *J. Biol. Chem.*, **279(17)**, pp.17996-18007, DOI: 10.1074/jbc.M311191200.

[17] D. Wrapp, N. Wang, K.S. Corbett, et al. (2020), "Cryo-EM structure of the 2019-nCoV spike in the prefusion conformation", *Science*, **367(6483)**, pp.1260-1263, DOI: 10.1126/science.abb2507.

[18] C.A. Lipinski (2004), "Lead- and drug-like compounds: The rule-of-five revolution", *Drug Discovery Today: Technologies*, **1(4)**, pp.337-341, DOI: 10.1016/j.ddtec.2004.11.007.

[19] B. Jayaram, T. Singh, G. Mukherjee, et al. (2012), "Sanjeevini: A freely accessible web-server for target directed lead molecule discovery", *BMC Bioinformatics*, **13(17)**, DOI: 10.1186/1471-2105-13-S17-S7.

[20] D.E. Pires, T.L. Blundell, D.B. Ascher (2015), "pkCSM: Predicting small-molecule pharmacokinetic and toxicity properties using graph-based signatures", *J. Med. Chem.*, **58(9)**, pp.4066-4072, DOI: 10.1021/acs.jmedchem.5b00104.

[21] S. Kim, J. Chen, T. Cheng, et al. (2021), "PubChem in 2021: New data content and improved web interfaces", *Nucleic Acids Research*, **49(D1)**, pp.D1388-D1395, DOI: 10.1093/nar/gkaa971.

[22] M. Sehailia, S. Chemat (2020), "Antimalarial-agent artemisinin and derivatives portray more potent binding to Lys353 and Lys31-binding hotspots of SARS-CoV-2 spike protein than hydroxychloroquine: Potential repurposing of artenimol for COVID-19", *Journal of Biomolecular Structure and Dynamics*, **39(16)**, DOI: 10.1080/07391102.2020.1796809.

[23] J. Lim, S. Jeon, H.Y. Shin, et al. (2020), "Case of the index patient who caused tertiary transmission of COVID-19 infection in Korea: The application of Lopinavir/Ritonavir for the treatment of COVID-19 infected pneumonia monitored by quantitative RT-PCR", *J. Korean Med. Sci.*, **35(6)**, DOI: 10.3346/jkms.2020.35.e79.

[24] I.F.N. Hung, K.C. Lung, E.Y.K. Tso, et al. (2020), "Triple combination of interferon beta-1b, lopinavir-ritonavir, and ribavirin in the treatment of patients admitted to hospital with COVID-19: An open-label, randomised, phase 2 trial", *The Lancet*, **395(10238)**, pp.1695-1704, DOI: 10.1016/S0140-6736(20)31042-4.

[25] S. Tong, Y. Su, Y. Yu, et al. (2020), "Ribavirin therapy for severe COVID-19: A retrospective cohort study", *International Journal of Antimicrobial Agents*, **56(3)**, DOI: 10.1016/j.ijantimicag.2020.106114.

[26] M.A. Unal, C.V. Bitirim, G.Y. Summak, et al. (2021), "Ribavirin shows antiviral activity against SARS-CoV-2 and downregulates the activity of TMPRSS2 and the expression of ACE2 *in vitro*", *Canadian Journal of Physiology and Pharmacology*, **99(5)**, pp.449-460, DOI: 10.1139/cjpp-2020-0734.

[27] C.M. Cao, Y. Peng, L.J. Xu, et al. (2009), "Two flavonoid dimers from *Sarcandra hainanensis* (PEI) SWAMY *et* BAILEY", *Chemical and Pharmaceutical Bulletin*, **57(7)**, pp.743-746, DOI: 10.1248/cpb.57.743.

[28] J.W. Nam, G.Y. Kang, A.R. Han, et al. (2011), "Diarylheptanoids from the seeds of *Alpinia katsumadai* as heat shock factor 1 inducers", *J. Nat. Prod.*, **74(10)**, pp.2109-2115, DOI: 10.1021/np200355n.

[29] J.K. Prasain, J.X. Li, Y. Tezuka, et al. (1998), "Calyxin H, epicalyxin H, and blepharocalyxins A and B, novel diarylheptanoids from the seeds of *Alpinia blepharocalyx*", *Journal of Natural Products*, **61(2)**, pp.212-216, DOI: 10.1021/np970404d.

[30] L. Chen, D.J. Hu, S.C. Lam, et al. (2016), "Comparison of antioxidant activities of different parts from snow chrysanthemum (*Coreopsis tinctoria* Nutt.) and identification of their natural antioxidants using high performance liquid chromatography coupled with diode array detection and mass spectrometry and 2, 2′-azinobis (3-ethylbenzthiazoline-sulfonic acid) diammonium salt-based assay", *Journal of Chromatography A*, **1428**, pp.134-142, DOI: 10.1016/j.chroma.2015.10.037.

[31] S.C. Lam, S.F. Lam, J. Zhao, et al. (2016), "Rapid identification and comparison of compounds with antioxidant activity in *Coreopsis tinctoria* herbal tea by high-performance thin-layer chromatography coupled with DPPH bioautography and densitometry", *Journal of Food Science*, **81(9)**, pp.C2218-C2223, DOI: 10.1111/1750-3841.13402.

[32] J. Wang, G. Aierken, X. Li, et al. (2016), "Testing the absorption of the extracts of *Coreopsis tinctoria* Nutt. in the intestinal canal in rats using an Ussing chamber", *Journal of Ethnopharmacology*, **186**, pp.73-83, DOI: 10.1016/j.jep.2016.03.061.

[33] M. Wolniak, M. Tomczykowa, M. Tomczyk, et al. (2007), "Antioxidant activity of extracts and flavonoids from *Bidens tripartita*", *Acta. Pol. Pharm.*, **64(5)**, pp.441-447.

[34] Z. Xiao, Y. Zhang, X. Chen, et al. (2017), "Extraction, identification, and antioxidant and anticancer tests of seven dihydrochalcones from *Malus* 'Red Splendor' fruit", *Food Chem.*, **231**, pp.324-331, DOI: 10.1016/j.foodchem.2017.03.111.

[35] M.T. Islam, C. Sarkar, D.M. El-Kersh, et al. (2020), "Natural products and their derivatives against coronavirus: A review of the non-clinical and pre-clinical data", *Phytotherapy Research*, **34(10)**, pp.2471-2492, DOI: 10.1002/ptr.6700.

[36] S. Khaerunnisa, H. Kurniawan, R. Awaluddin, et al. (2020), "Potential inhibitor of COVID-19 main protease (M^{pro}) from several medicinal plant compounds by molecular docking study", *Preprints*, DOI: 10.20944/preprints202003.0226.v1, https://www.preprints.org/manuscript/202003.0226/v1, accessed 5 May 2021.

[37] S. Adem, V. Eyupoglu, I. Sarfraz, et al. (2020), "Identification of potent COVID-19 main protease (M^{pro}) inhibitors from natural polyphenols: An *in silico* strategy unveils a hope against corona", *Preprints*, DOI: 10.20944/preprints202003.0333.v1, https://www.preprints.org/manuscript/202003.0333/v1, accessed 5 May 2021.

DOI: 10.31276/VJSTE.64(2).76-81

Evaluating the protective effects of *Panax bipinnatifidus* Seem. extracts on hypoxia/reoxygenation-subjected cardiomyocytes

Vu Thi Thu*, Ngo Thi Hai Yen

VNU University of Science, Vietnam National University, 144 Xuan Thuy Street, Dich Vong Hau Ward, Cau Giay District, Hanoi, Vietnam

Received 4 April 2022; revised 20 April 2022; accepted 24 May 2022

Abstract:

The search for new products to treat ischemic heart diseases has interested scientists for years as it is the main cause of cardiovascular disease mortality. In this study, we evaluated the protective effects of *Panax bipinnatifidus* Seem. extracts (PSE) on hypoxia/reoxygenation (HR)-treated rat H9C2 cardiomyocytes. Rat H9C2 cardiomyocytes were either grown under normal condition or subjected to HR conditions. NecroX-5 (10 µM) was used as positive control for cardiac protective effect. The PSE (5-500 µg/ml) was employed to culture media at the onset of reoxygenation. Cell viability and mitochondrial function were tested using a Cell Counting Kit-8 and suitable fluorescence kits. The obtained data shows that HR conditions dramatically induced H9C2 cell death ($p<0.05$). Treatment of PSE (5-62.5 µg/ml) effectively reduced HR injuries in a dose-dependent manner. Similar to the NecroX-5 group, ginseng extract-treated cells had higher viability levels compared to that of the HR-subjected cells ($p<0.05$). In addition, supplementing PSE at the onset of reoxygenation strongly prevented the collapse of mitochondrial membrane potential and reduced mitochondrial oxidative stress ($p<0.05$). This study suggested the total saponin extracts from *Panax bipinnatifidus* Seem. exerts cardioprotective properties against HR damage.

Keywords: **hypoxia/reoxygenation, H9C2, NecroX-5, oxidative stress.**

Classification numbers: **3.3, 3.5**

1. Introduction

Myocardial infarction is the main cause of death from cardiovascular disease [1]. The timing of revascularization in combination with anti-oxidants and anti-platelet agents are decisive factors for an effective treatment of patients [2]. The search for natural products to develop new anti-ischemic drugs has been of intense interest of scientists due to ischemic heart disease being the main cause of cardiovascular disease mortality [3, 4]. Experimental data have shown that drugs used in the treatment of myocardial infarction have mechanisms related to mitochondrial preservation [5-8].

Ginseng is a precious medicinal herb that is widely used in traditional medicine and pharmaceutical industries in many countries. Many naturally growing ginseng species such as Vietnamese Ginseng, *Panax bipinnatifidus* Seem., Radix Angelicae Sinensis, and Salvia miltiorrhiza Bunge have been recognized and widely used in traditional remedies for anti-fibrotic treatment, anti-infarction, increasing nerve function, reducing the risk of cancer, and maintaining a healthy immune system or blood sugar stability [9-11]. For ischemic diseases, the efficacy of the antioxidant property of ginseng and its ginsenosides on stroke outcomes has been described [12-14]. Also, ginseng extracts have been shown to possess beneficial effects in the treatment of myocardial infarction [15-17]. Of these extracts, *Panax bipinnatifidus* Seem. has anti-platelet activity with its major saponin components like stipuleanoside R2 and araloside A methyl ester [10, 18, 19]. However, experimental analysis of the role of total saponin extract of *Panax bipinnatifidus* Seem. in modulating cardiomyocytes and mitochondrial function during the revascularization phase is still lacking. Therefore, this study was carried out to evaluate the potential role of *Panax bipinnatifidus* Seem. extract in an ischemic heart model using H9C2 cardiomyocytes.

*Corresponding author: Email: vtthu2015@gmail.com

2. Materials and methods

2.1. Samples

H9C2 cardiomyocytes (ATCC©-USA) were provided by the Cardiovascular and Metabolic Disease Centre, Inje University and *Panax bipinnatifidus* Seem. extract [10, 18] was provided by Phenikaa University. The study was performed at Life Science Research Centre, Faculty of Biology, University of Science, Vietnam National University, Hanoi.

2.2. Materials

Dulbecco's Modified Eagle Medium 4.5 g/l glucose (DMEM, Gibco, USA); Penicillin-Streptomycin (PS, Gibco, USA); Fetal Bovine Serum (FBS, Gibco, USA); Phosphate Buffered Saline (PBS, Gibco, USA); Cobalt Chloride ($CoCl_2$, Sigma, USA); Dimethyl Sulfoxide (DMSO, Sigma, USA); Cell Counting Kit-8 (CCK-8, Dojindo, Japan); 2′,7′-Dichlorodihydrofluorescein-diacetate (CM-H_2DCFDA, Invitrogen, USA); Tetramethyl Rhodamine Ethyl Ester (TMRE, Invitrogen, USA); Inverted microscopy Axiovert (S100, Carl Zeiss, Germany); Culture dishes, 96-well black, glass bottom plates, CO_2 incubator (Shellab, USA); Microreader plate (Tristar, USA).

2.3. Methods

Cell culture, hypoxia-reoxygenation (HR) in vitro model and treatments:

H9C2 cells were maintained in DMEM supplemented with 100 µg/ml of PS and 10% FBS at 37°C and 5% CO_2. The cells were grown in a 96-well black plate with glass bottom at a density of 5×10^3 cells/well. Cells were cultured under normal conditions and supplied with *Panax bipinnatifidus* Seem. extract (0-1000 µg/ml) to evaluate the toxicity as well as to determine the optimal dose of PSE. For a $CoCl_2$-stimulated HR model, after 24 h, the cells were subjected to $CoCl_2$ (300 µM) at 37°C and 5% CO_2 for 24 h (simulating the hypoxia stage) as described in the previous publication [20]. Then, the medium containing $CoCl_2$ was removed and the cells were continuously grown for 24 h in new media containing either DMSO (HR, HR-$CoCl_2$+DMSO) or DMSO plus PSE (PSE, HR-$CoCl_2$+DMSO+ PSE). Cells were cultured under normal conditions (DMEM, 10% FBS, 1% PS, 37°C and 5% CO_2) for 54 h without any treatment, which served as a control group. The optimal dose of PSE was chosen to assess its cardioprotective effects against HR via cell viability and mitochondrial indexes. Experiments were performed at least in triplicate.

The HR model was also created by alternating the O_2 levels of the culture conditions. H9C2 cells were cultured in normal media at 37°C with 5% CO_2 for 18 h. For hypoxic cultures, the cells were then cultured in serum-free low-glucose DMEM at 37°C, 95% N_2, 5% CO_2, and 2% O_2. For reoxygenated culture, cells were grown under normal conditions following the hypoxic condition. After incubating under hypoxic condition for 6 h, H9C2 cells were then transferred to reoxygenation for 24 h. At the time of reoxygenation, H9C2 cells were separately treated with either PSE or NecroX-5 (10 µM, serving as positive drug control). The stocks of NecroX-5 and PSE were prepared in DMSO. The final concentration of DMSO in cultured medium was 0.1%. The difference was expressed as a percentage value relative to the HR group.

Cell viability assay:

Cell viability was assessed by using a CCK-8 kit as described in the last study [21]. H9C2 cells were seeded in triplicate into 96-well culture plates at a density of 5×10^3 cells per well. At the end of the experiment, the cell groups were further incubated with CCK-8 solution for 1-4 h. The absorbance value, indicating cell viability, was measured at 450 nm using the microplate reader. The number of alive cells was expressed as a value relative to the normal control or HR. The cell images were also captured by using an Axiovert inverted microscope. Experiments were repeated at least 3 times.

Measurement of mitochondrial membrane potential:

At the end of experiment, the cell groups were stained with 0.1 µM TMRE (ex/em: 535/570 nm) for 30 min at room temperature. After washing twice with PBS, fluorescence intensities were measured using the microplate reader. The TMRE intensity was expressed as a percentage value relative to the HR. Experiments were performed in triplicate.

Measurement of hydroperoxide production:

At the end of experiment, the cell groups were stained with 5 µM CM-H_2DCFDA (ex/em: 485/525 nm) at 37°C for 30 min to detect changes in hydroperoxide

(H_2O_2) levels. After washing, the fluorescence intensity was measured using the microplate reader. The total fluorescence intensity in each well was expressed as a percentage value relative to the control or HR or NecroX-5. Experiments were repeated in triplicate.

Statistical analysis:

Data are presented as mean ± standard error of the mean (SEM) using Origin 8.5. Differences between the two groups were evaluated by one-way analysis of variance (ANOVA) and Tukey's test. Differences with a $p \leq 0.05$ were considered significant.

3. Results and discussion

3.1. PSE reduced H9C2 cell death under $CoCl_2$-stimulated HR injury in a dose-dependent manner

H9C2 cells were cultured in DMEM supplemented with 10% FBS, 100 µg/ml of PS, and 5% CO_2 at 37°C for 24 h and were then treated with PSE (0-1000 µg/ml) for the next 48 h. The cell viability of PSE was determined using the CCK-8 kit as described in the previous study [21]. The 48-h EC_{50} of PSE was determined to be 199.41 (µg/ml) using Origin 8.5 (Fig 1). The results indicate that PSE showed less toxicity to the H9C2 cells under normal conditions.

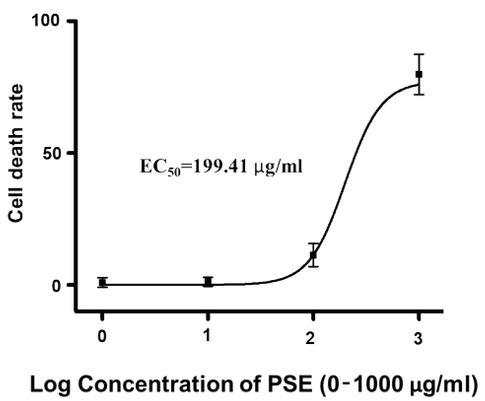

Fig. 1. EC_{50} value of *Panax bipinnatifidus* Seem. extract.

Consistent with the previous study [20], the results showed that viabilities were dramatically reduced in the $CoCl_2$-exposed H9C2 cells compared to normal cells (Fig. 2, $p<0.05$). PSE at doses of 5, 10, 31.25, and 62.5 µg/ml strongly prevented cell death from HR. In contrast, PSE at doses of 125, 250, and 500 µg/ml showed toxicity to cardiomyocytes under HR conditions.

Interestingly, among the $CoCl_2$-exposed groups, the high percentages of H9C2 viability were presented in PSE treatments at doses of 31.25 and 62.5 µg/ml. Treatment of PSE at doses of 31.25 µg/ml and 62.5 µg/ml dramatically increased the cell viability up to 81.63±2.01% and 81.88±0.96%, respectively (where 100% is for the normal control). Though PSE showed less toxicity to H9C2 cells under normal conditions (Fig. 1), the viability of the PSE-treated groups with the higher doses (125, 250, and 500 µg/ml) was lower than that of the $CoCl_2$-stimulated HR. The results indicated that PSE exerted cardioprotective effects on cardiomyocytes under $CoCl_2$-stimulated HR were in a dose-dependent manner. Cell morphology and cell count are shown in Fig. 2C, which portrays less alive cells with PSE doses at 125, 250, and 500 µg/ml. It was reported that PSE has anti-platelet activity with its major saponin component, araloside A methyl ester [10, 18, 19]. Another research had screened the bioactive role of crude PSE and reported its weak inhibitory effect on markedly nitric oxide production in lipopolysaccharide-treated RAW 264.7 cells [22]. The current results further document the bioactivity of PSE with different effects on cell viability that depend on HR treatments. These findings showed that the effective doses of PSE against HR damage were about 31.25 and 62.5 µg/ml. In this study, a PSE post-hypoxic treatment at a dose of 31.25 µg/ml was chosen for further evaluation.

3.2. PSE protected cardiomyocytes via preserving mitochondria function against HR damage

The data showed the cardioprotective effects of PSE against HR injury via elevating cell viability (Fig. 3B), enhancing mitochondrial membrane potential ($\Delta\Psi m$), and reducing oxidative stress levels (Fig. 4). The experiment designed for HR model is depicted in Fig. 3A. In this model, NecroX-5, the positive control, showed its efficacy in protecting the cells against HR as mentioned in the previous study [7]. As described, H9C2 cells were subjected to different conditions and the cell survival rates were measured using the CCK-8 kit (Fig. 3). Post-hypoxic treatment of either NecroX-5 or PSE significantly increased the cell viability compared to HR condition ($p<0.05$). Among HR-exposed groups, the highest H9C2 viability was shown in the PSE-treated cells (231.34±12.38, % vs. HR). Though the cell viability

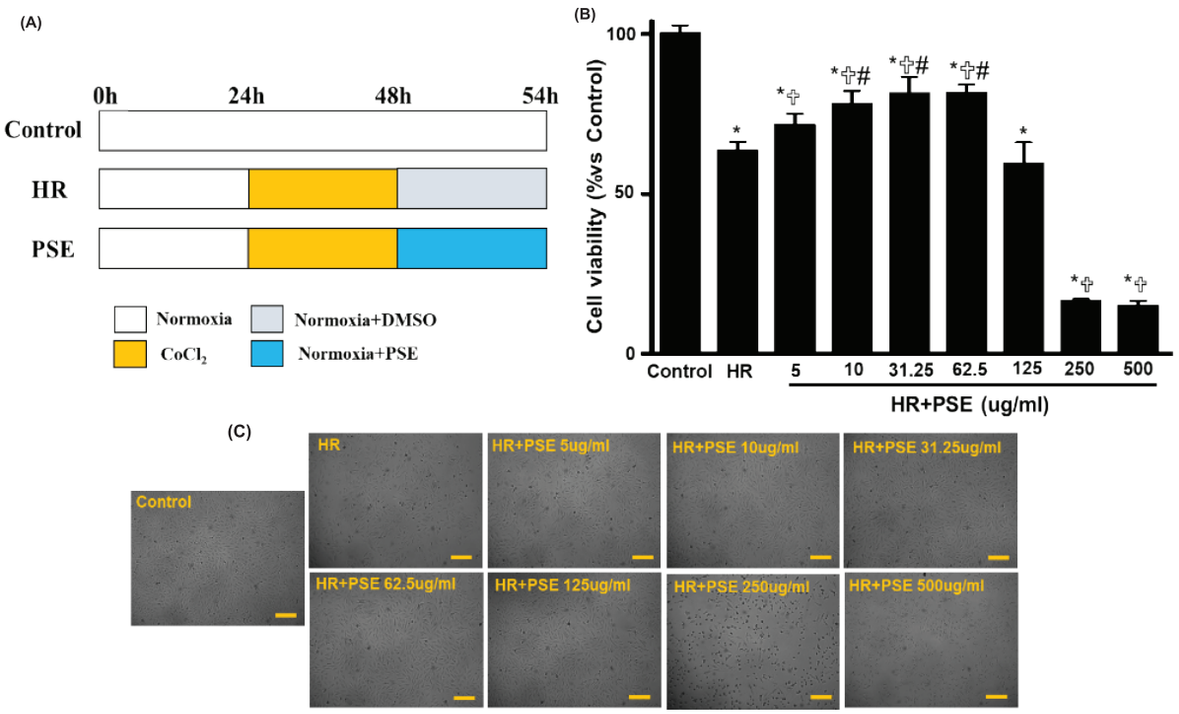

Fig. 2. **Experimental design and cell viability assay**. **(A)** $CoCl_2$-stimulated HR model and *Panax bipinnatifidus* Seem. extract treatment. **(B)** The graph indicates H9C2 cell viability under different conditions and treatments. **(C)** H9C2 cell images captured under different conditions and treatments. HR: $CoCl_2$-stimulated condition; PSE: HR+PSE; *p<0.05 vs. Control; +p<0.05 vs. HR; #p<0.05 vs. PSE at dose of 5 µg/ml; scale bar=100 µm; 10x of magnification; n=3-4 for each group.

of the PSE-treated group (at dose of 31.25 µg/ml) was higher than another PSE-treated group (i.e., at dose of 62.5 µg/ml, 213.14±10.98, % vs. HR), there was no significant difference between these two groups. Moreover, the use of DMSO (0.1%) showed no significant effect on the life of H9C2 cells under HR conditions as mentioned in a previous study [23]. These results further confirmed the effective role of PSE in protecting H9C2 cardiomyocytes against HR damage (Fig. 2) and the protective effects of the other products of ginseng [16]. The data suggests that different protective levels could be dependent on the concentration and components of the tested extracts.

In this study, TMRE was used to evaluate the role of PSE on the mitochondrial function according to the manufacturer's instructions. The values of TMRE intensity in HR, DMSO, NecroX-5 and PSE groups were 61.24±0.05%, 61.23±0.13%, 81.30±1.37%, and 69.10±0.26%, respectively (100% of normal control, Fig. 4A). Thus, consistent with a previous report [16], PSE significantly protected mitochondrial function against HR. Post-hypoxic treatment of NecroX-5 and PSE significantly increased the ΔΨm compared to non-treated HR condition (Fig. 4A, p<0.05). There was no significant difference in TMRE intensity between NecroX-5 and PSE groups (p>0.05). Thus, the results indicate that intervention methods could be varied by changing ginseng species and/or saponin components. Moreover, the loss of ΔΨm during HR was prevented by pre-treating with the triterpenoid saponin clematichinenoside [24] or post-hypoxic treatment of majonoside-R2 [16].

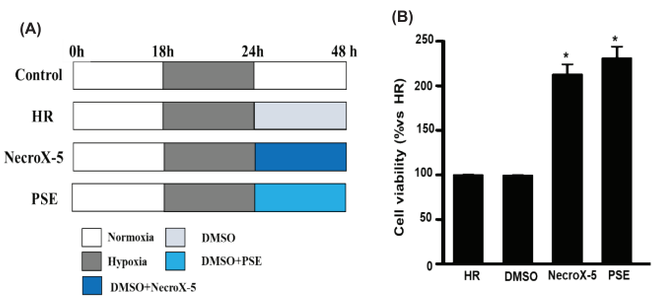

Fig 3. Experimental design and the H9C2 cell viability under conditions. **(A)** Hypoxia/reoxygenation (HR) model and treatments. **(B)** The graph indicates H9C2 cell viability under different treatments. NecroX-5: HR+NecroX-5 (10 µM); PSE: HR+PSE (*Panax bipinnatifidus* Seem. extract, 31.25 µg/ml); *p<0.05 vs. HR; n=3 for each group.

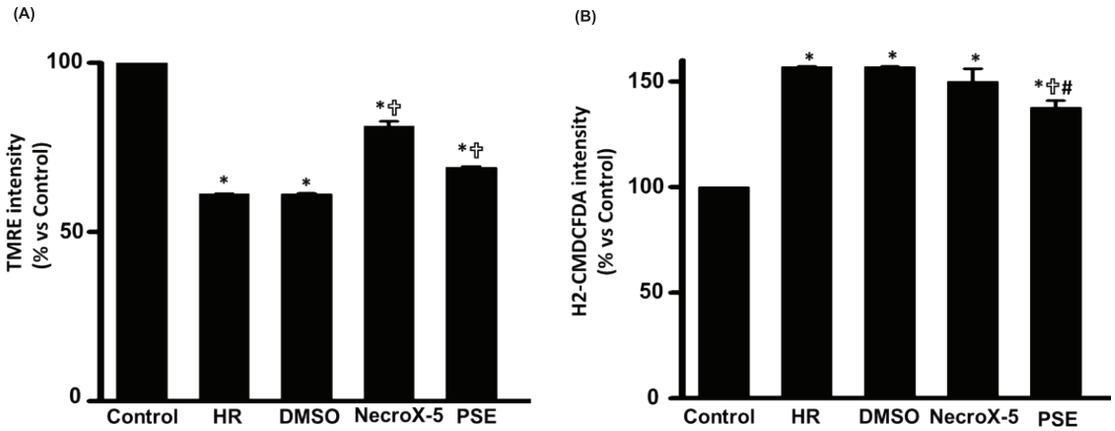

Fig. 4. Mitochondrial function. The graphs present mitochondrial alterations in H9C2 cells subjected to different treatments. **(A)** Mitochondrial membrane potential (TMRE intensity) and **(B)** H_2O_2 production (CM-H_2DCFDA intensity). HR: hypoxia/reoxygenation; NecroX-5: HR + NecroX-5 (10 μM); PSE: HR+PSE (31.25 μg/ml); *p<0.05 vs. Control; ✞p<0.05 vs. HR; #p<0.05 vs. NecroX-5; n=3 for each group.

Besides, the ability of PSE to preserve mitochondrial function can be further demonstrated by H_2O_2 production. Indeed, the H_2O_2 levels in H9C2 determined by using CM-H_2DCFDA were minimized in the NecroX-5- and PSE-treated groups as compared to the non-treated HR group (Fig. 4B). CM-H_2DCFDA intensity values evaluated in HR, DMSO, NecroX-5, and PSE were 157.01±0.16%, 156.83±0.24%, 149.98±6.01%, and 137.64±3.21%, respectively (where 100% is the normal control). Interestingly, there was a significant difference between NecroX-5 and PSE groups ($p<0.05$). This finding provides more evidence for the antioxidant properties of ginseng products under HR damage [16, 25]. Most likely this phenomenon is a result of the saponin components [26] and extraction solvents [27]. The efficacy in maintaining mitochondrial function of ginseng products against HR damage has been previously described [17, 25, 28]. However, more studies should be done to clarify the exact mechanism action of PSE on cardiomyocytes under HR injuries.

4. Conclusions

To the best of our knowledge, this is the pilot study investigating the protective effects of *Panax bipinnatifidus* Seem. extract against HR damage via protecting cardiomyocytes as well as preserving mitochondrial function.

CRediT author statement

Vu Thi Thu: Data analysis and interpretation, Writing and Manuscript revising; Ngo Thi Hai Yen: Method, Data analysis and Writing.

ACKNOWLEDGEMENTS

We thank Prof. Han Jin, Assoc. Prof. Nguyen Lai Thanh, Assoc. Prof. Nguyen Huu Tung, Prof. Vu Thi Thom, Dr. To Thanh Thuy, Dr. Pham Thi Bich for their help and supports. This research has been done under the research project QG.22.03 of Vietnam National University, Hanoi.

COMPETING INTERESTS

The authors declare that there is no conflict of interest regarding the publication of this article.

REFERENCES

[1] D. Mozaffarian, E.J. Benjamin, A.S. Go, et al. (2016), "Heart disease and stroke statistics - 2016 update: A report from the American heart association", *Circulation*, **133(4)**, DOI: 10.1161/CIR.0000000000000350.

[2] S.M. Picker (2013), "Platelet function in ischemic heart disease", *Journal of Cardiovascular Pharmacology*, **61(2)**, DOI: 10.1097/FJC.0b013e318279b78a.

[3] J.P.S. Han, S.J. Park, V.T. Thu, et al. (2013), "Effects of the novel angiotensin II receptor type I antagonist, fimasartan on myocardial ischemia/reperfusion injury", *International Journal of Cardiology*, **168(3)**, pp.2851-2859, DOI: 10.1016/j.ijcard.2013.03.151.

[4] S.M. Zhang, Z.P. Xie, M.L. Xu, et al. (2015), "Cardioprotective effects of fucoidan against hypoxia-induced apoptosis in H9C2 cardiomyoblast cells", *Pharmaceutical Biology,* **53(9)**, pp1352-1357, DOI: 10.3109/13880209.2014.982298.

[5] J.S. Armstrong (2008), "Mitochondria-directed therapeutics", *Antioxid Redox Signal*, **10(3)**, pp575-578, DOI: 10.1089/ars.2007.1929.

[6] A. Heller, G. Brockhoff, A. Goepferich (2012), "Targeting drugs to mitochondria", *Eur. J. Pharm. Biopharm.,* **82(1)**, pp.1-18, DOI: 10.1016/j.ejpb.2012.05.014.

[7] V.T. Thu, H.K. Kim, L.T. Long, et al. (2012), "NecroX-5 prevents hypoxia/reoxygenation injury by inhibiting the mitochondrial calcium uniporter", *Cardiovasc. Res*., **94(2)**, pp.342-350, DOI: 10.1093/cvr/cvs122.

[8] A.M. Walters, G.A. Porter, P.S. Brookes (2012), "Mitochondria as a drug target in ischemic heart disease and cardiomyopathy", *Circulation Research*, **111(9)**, pp.1222-1236, DOI: 10.1161/CIRCRESAHA.112.265660.

[9] I.D. Peña, H.J. Kim, C.J. Botanas, et al. (2016), "The psychopharmacological activities of Vietnamese ginseng in mice: Characterization of its psychomotor, sedative-hypnotic, antistress, anxiolytic, and cognitive effects", *Journal of Ginseng Research*, **41**, pp.201-208, DOI: 10.1016/j.jgr.2016.03.005.

[10] V.T. Thom, N.H. Tung, D.V. Diep, et al. (2018), "Antithrombotic activity and saponin composition of the roots of Panax bipinnatifidus Seem. growing in Vietnam", *Pharmacognosy Research*, **10(4)**, pp.333-338, DOI:10.4103/pr.pr_58_18.

[11] M.M. Hafez, S.S. Hamed, S.D. Alsharari, et al. (2017), "Effect of ginseng extract on the TGF-β1 signaling pathway in CCl(4)-induced liver fibrosis in rats", *BMC Complement Altern. Med.*, **17(1)**, DOI: 10.1186/s12906-016-1507-0.

[12] L. Liu, G.A. Anderson, T.G. Fernandez, et al. (2019), "Efficacy and mechanism of Panax ginseng in experimental stroke", *Front. Neurosci.*, **13**, DOI: 10.3389/fnins.2019.00294.

[13] X.T. Gan, M. Karmazyn (2018), "Cardioprotection by ginseng: Experimental and clinical evidence and underlying mechanisms", *Can. J. Physiol. Pharmacol.*, **96(9)**, pp.859-868, DOI: 10.1139/cjpp-2018-0192.

[14] P. Luo, G. Dong, L. Liu, et al. (2015), "The long-term consumption of Ginseng extract reduces the susceptibility of intermediate-aged hearts to acute ischemia reperfusion injury", *PLOS One*, **10(12)**, DOI: 10.1371/journal.pone.0144733.

[15] Y. Luo, Y. Jiang, Y. He, et al. (2020), "Vina-Ginsenoside R4 from Panax ginseng leaves alleviates 6-OHDA-induced neurotoxicity in PC12 cells via the PI3K/Akt/GSK-3β signaling pathway", *J. Agric. Food Chem.*, **68(51)**, pp.15239-15248, DOI: 10.1021/acs.jafc.0c06474.

[16] V.T. Thu, N.T.H. Yen, N.H. Tung, et al. (2021), "Majonoside-R2 extracted from Vietnamese ginseng protects H9C2 cells against hypoxia/reoxygenation injury via modulating mitochondrial function and biogenesis", *Bioorg. Med. Chem. Lett.*, **36**, DOI: 10.1016/j.bmcl.2021.127814.

[17] V.T. Thu, N.T.H. Yen, P.T. Bich (2021), "Studying the protective effects of Vietnamese ginseng extract on H9C2 cardiomyocytes in hypoxia-reoxygenation model *in vitro*", *Vietnam Journal of Physiology*, **25(1)**, pp.47-56 (in Vietnamese).

[18] H.D. Van, T.H. Nguyen, T.T.T. Nguyen, et al., (2017), "Study on chemical constituents from the roots of Panax bipinnatifidus Seem. collected in Sapa, Laocai", *VNU Journal of Science: Medical and Pharmaceutical Sciences*, **33**, DOI:10.25073/2588-1132/vnumps.4079.

[19] V.T. Thom, N.T.T. Giang, N.H. Ngan, et al., (2019), "*In vitro* anti-coagulation activity of Panax bipinnatifidus Seem. and Panax stipuleanatus H.T. Tsai et K. M. Feng saponin enriched extracts", *Asian Journal of Pharmacognosy*, **3(2)**, pp13-17.

[20] N.T.H. Yen (2019), "Designing and evaluating the effectiveness of hypoxia chamber applied in myocardial hypoxia-reoxygenation model *in vitro*", *Vietnam Journal of Physiology*, **23(3)**, pp.1-8.

[21] V.T. Thu, H.K. Kim, T.T. Thuy, et al. (2016), "NecroX-5 exerts anti-inflammatory and anti-fibrotic effects via modulation of the TNFα/Dcn/TGFβ1/Smad2 pathway in hypoxia/reoxygenation-treated rat hearts", *Korean J. Physiol. Pharmacol.*, **20(3)**, pp.305-314, http://dx.doi.org/10.4196/kjpp.2016.20.3.305.

[22] H.A.T. Nguyen, et al. (2021), "Bioactive saponins from panax bipinnatifidus seem. growing in Vietnam", *Vietnam Journal of Science and Technology*, **58(6A)**, pp.228-235 (in Vietnamese).

[23] V.T. Thu, P.T. Bich, N.T.H. Yen (2021), "Evaluating the affect of dimethyl sulfoxide on the viability of H9C2 cardiomyocytes", *Vietnam Journal of Physiology,* **25(2)**, pp.13-23 (in Vietnamese).

[24] H. Ding, R. Han, X. Chen, et al. (2016), "Clematichinenoside (AR) attenuates hypoxia/reoxygenation-induced H9C2 cardiomyocyte apoptosis via a mitochondria-mediated signaling pathway", *Molecules*, **21(6)**, DOI: 10.3390/molecules21060683.

[25] Y.H. Zuo, Q.B. Han, G.T. Dong, et al. (2018), "Panax ginseng polysaccharide protected H9C2 cardiomyocyte from hypoxia/reoxygenation injury through regulating mitochondrial metabolism and RISK pathway", *Front. Physiol*., **9**, DOI: 10.3389/fphys.2018.00699.

[26] Q. Duong, P.T.V. Nguyen, H.T.T. Nguyen, et al. (2016), "Effects of ocotillol-type saponins majonoside-R1 and vina-ginsenoside-R2 on abrogating depression and neuronal oxidative stress in socially isolated depression mouse model", *Int. J. Appl. Res. Nat. Prod.*, **9**, pp.27-32.

[27] Y. Huang, P. Yao, H. Wang, et al. (2019), "Ginseng extracts modulate mitochondrial bioenergetics of live cardiomyoblasts: A functional comparison of different extraction solvents", *J. Ginseng. Res.*, **43(4)**, pp.517-526, DOI: 10.1016/j.jgr.2018.02.002.

[28] Y. Yu, G. Sun, Y. Luo, et al. (2016), "Cardioprotective effects of Notoginsenoside R1 against ischemia/reperfusion injuries by regulating oxidative stress- and endoplasmic reticulum stress-related signaling pathways", *Scientific Reports*, **6(1)**, DOI: 10.1038/srep21730.

DOI: 10.31276/VJSTE.64(2).82-85

A new species of the genus Macrosemia from Vietnam

Yen Hoang Luu[1, 2], Thai Hong Pham[3*], Hong Minh Bui[4], Jérôme Constant[5]

[1]*Vietnam Forest Museum, Forest Investigation and Planning Institute, Km 12+300 Ngoc Hoi. Vinh Quynh Ward, Thanh Tri District, Hanoi, Vietnam*
[2]*Mientrung Institute for Scientific Research, VAST, 18 Hoang Quoc Viet Street, Nghia Do Ward, Cau Giay District, Hanoi, Vietnam*
[3]*Vietnam National Museum of Nature & Graduate School of Science and Technology, VAST, 18 Hoang Quoc Viet Street, Nghia Do Ward, Cau Giay District, Hanoi, Vietnam*
[4]*Department of Biology, Hanoi National University of Education, 136 Xuan Thuy Street, Dich Vong Hau Ward, Cau Giay District, Hanoi, Vietnam*
[5]*Royal Belgian Institute of Natural Sciences,29 Vautierstreet,1000 Brussels, Belgium*

Received 2 June 2021; revised 15 August 2021; accepted 20 December 2021

Abstract:

Conducting a taxonomic examination of the Macrosemia genus in Vietnam, this study introduces a novel species, Macrosemia sapaensis sp. nov., discovered in Lao Cai Province in northern Vietnam. The research encompasses details on the species' distribution, accompanied by adult photographs and illustrations of male genitalia. A key to the Macrosemia genus in Vietnam is presented, primarily based on male characteristics, aiding in the identification of species within the genus. The study contributes to the broader understanding of the biodiversity of cicadas in Vietnam, specifically within the Macrosemia genus, and serves as a valuable resource for researchers and enthusiasts interested in the taxonomy and diversity of these fascinating insects in the region. The new species differs from all species of the genus *Macrosemia* from Vietnam (exclude in the species *M. lamdongensis*) in the markings of forewings that are widely spread or roundish infuscation on each apical portion of veins RA2, RP, M1, M2, M3, M4, and CuA1, which form a series along the subapical margin of the forewing. Meanwhile, the rest have forewings without widely spread or roundish infuscation on each apical portion of veins RA2, RP, M1, M2, M3, M4, and CuA1 forming a series along the subapical margin of the forewing.

Keywords: **Auchenorrhyncha, cicadini, Hoang Lien National Park, morphology, taxonomy.**

Classification number: **3.4**

1. Introduction

The cicada genus *Macrosemia*, erected by M. Kato (1925) [1], contains eighteen species and is mainly distributed in the Oriental Region. It belongs to the tribe Cicadini of the subfamily Cicadinae with *Platylomia hopponis* Kato, 1925 as the type species [2]. Two additional species, *Platylomia kareisana* (Matsumura, 1907) and *Platylomia matsumurai* Kato, 1928, were transferred to *Macrosemia* by Matsumura (1930) [3] and Kato (1931) [4], respectively. Later, Kato (1932) [5] considered *Macrosemia hopponis* to be only a form of *Platylomia kareisana*. Two other species were later described in the genus: *Macrosemia kiangsuensis* Kato, 1938, and *Macrosemia anhweiensis* Ouchi, 1938. The uncertainty about the exact classification of *Macrosemia* and its close relationship with *Platylomia* was also illustrated by Duffels & Van der Laan's (1985) treatment of the two genera. They listed three species of *Macrosemia*: *M. anhweiensis* Hua 2000, *M. kiangsuensis* Hua 2000 (including the variety virescens Liu, 1940), and *M. matsumurai* (Kato, 1928). Oddly enough, the type species of *Macrosemia*, *Platylomia hopponis*, was listed as a synonym of *Platylomia kareisana* under *Platylomia* [6]. The species was placed in *Platylomia* following Hayashi (1979) [7]. Five species: *Platylomia divergens* (Distant, 1917), *Platylomia assamensis* Distant, 1905, *Platylomia diana* Distant, 1905, *Platylomia saturate* (Walker, 1858), and *Platylomia pieli* Kato, 1938 were transferred to *Macrosemia* Kato, 1925 by Y. Lee (2008) [8]. P. Thai, et al. (2016) [4] described one new species, *Macrosemia lamdongensis*, from Lam Dong province, Tay Nguyen area, Vietnam and removed two species *Macrosemia assamensis* (Distant, 1905) and *Macrosemia divergens* (Distant, 1917) from the Vietnam cicada fauna. Here, we describe one new species, *Macrosemia sapaensis* sp. nov., from Lao Cai province, north Vietnam. It is the sixth species of *Macrosemia* found and is described here as a new species from Vietnam.

2. Materials and methods

Two males of the new species *Macrosemia* were collected from Sa Pa, Hoang Lien National Park, Lao Cai province, north Vietnam, and the type specimen of this new species was deposited in the Vietnam National

*Corresponding author: phthai@misr.vast.vn

Museum of Nature, Vietnam (VNMN), and Naturalis Biodiversity Centre, Leiden, The Netherlands (NCB).

Morphological terminology follows that of Moulds (2005) [9]. The male genitalia of the holotype were examined and photographed using a dissecting microscope (Leica MZ12 5). A distribution map and photos of habitus are provided.

Specimens examined are listed by province.

3. Results and discussion

3.1. Taxonomy

Family Cicadidae Latreille, 1802

Subfamily Cicadinae Latreille, 1802

Tribe Cicadini Latreille, 1802

Genus Macrosemia Kato, 1925 Macrosemia Kato, 1925b: 57.

Type species: Platylomia hopponis Kato, 1925 (Kato 1925a) (Formosa = Taiwan).

3.2. Remarks

According to Y. Lee et al. (2003) [10] and Y. Lee (2008) [8], Genus Macrosemia Kato, 1925 is different from Platylomia Stål, 1870 by the following characteristics: robust and thick body; eyes not prominent laterally; head including eyes about as wide as or narrower than base of mesonotum; postclypeus a little prominent anteriorly, shorter than vertex in mid-dorsal length in dorsal view; ventral side of postclypeus, in many species, with distinct fuscous or black longitudinal central band which diverges at anterior end; pronotal collar well developed and broad; mid lateral tooth of pronotal collar produced laterally or posterolaterally, not anterolaterally; male operculum long with comparatively acute apex and swollen at about posterior 2/3; forewing slender with sharp tip, its length longer than 3.2 times its width [11].

3.3. Key to the genus Macrosemia in Vietnam

1) Uncal lobes protruding obliquely and distinctly curved laterad, forming a V-shape with a right angle in ventral view……..*M. sapaensis* sp. nov.

- Uncal lobes not so……2

2) Fore wing with widely spread or roundish infuscation on each apical portion of veins RA2, RP, M1, M2, M3, M4, and CuA1….....3

- Fore wing without widely spread or roundish infuscation on each apical portion of veins RA2, RP, M1, M2, M3, M4, and CuA1…….....…4

3) Tergite 3 with a transverse dense white hair fascia along anterior margin……..……..*M. lamdongensis*

- Tergite 3 without a transverse dense white hair fascia along anterior margin…….....*M. saturata*

4) Fore and hind wings with basal cell blackish-brown; operculum with a black streak around.....…*M. tonkiniana*

- Fore and hind wings without basal cell blackish-brown; operculum without a black streak around.....5

5) Male dull ochraceous; operculum reaching sternite VI, entirely ochraceous except extreme margins and apex, posteriorly globosely convex……*M. diana*

- Male greenish ochraceous; operculum large and long reaching centre of sternite VII, widely apart from each other and occupying lateral abdominal areas, strongly sinuate on each side of base and suddenly convex on disk of posterior two-third, narrowed and a little rounded posteriorly……*M. pieli*

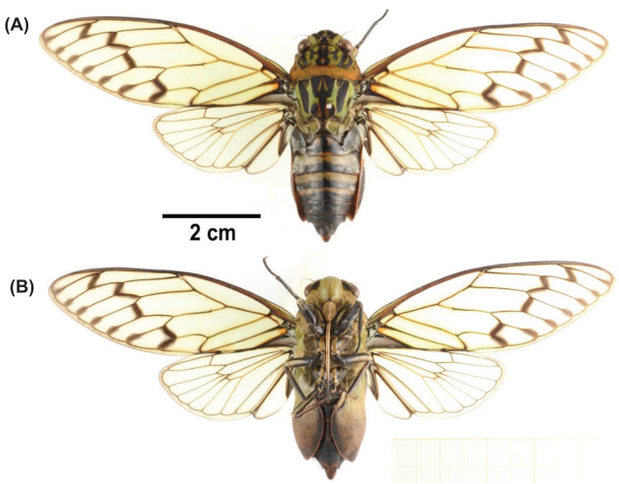

Fig. 1. *Macrosemia* sapaensis sp. nov.: A: dorsal view of male, B: ventral view of male.

Etymology: the species epithet refers to the locality of origin of the specimens: Sapa, Hoang Lien National Park, Lao Cai province in north Vietnam (Fig. 1).

Material examined: Holotype ♂: Hoang Lien National Park, Sapa, Lao Cai, 24.ix.2013, 1,900 m; coll. Pham Hong Thai (VNMN).

Paratype ♂: [Lao Cai province, Vietnam, 15 km W of Sapa, Tram Ton Pass, 1,900 m, 22.22N 103.50E, 15-

19.X.1999, light trap, VN99-1, coll. R. de Jong,] (NBC).

Head: head including eyes slightly narrower than base of mesonotum; vertex pale green, with a large irregular marking at ocellar area, a broad pair of oblique spots between eyes and anterior arm of epicranial, two small fascia oblique against anterior margin of pronotum, fascia on posterior margin eyes against anterior margin of pronotum black; eyes brown-black, ocelli red; frons black with marking on posterior margin pale green; supra-antennal pale yellow-brown; antennae black; gena yellowish opalescent with large black marking around base antennae; lorum black; posclypeus greenish opalescent with transverse groove pale brown, margin against anteclypeus black; anteclypeus yellowish opalescent; rostrum yellowish opalescent, reaching pass posterior coxae, longitudinal lines centre darker, apical rostrum brown-black (Fig. 2).

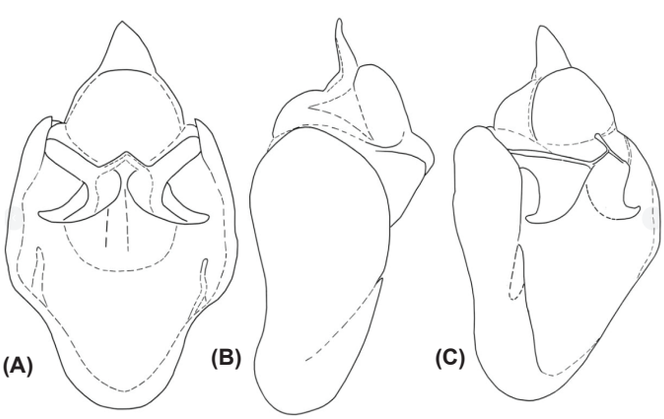

Fig. 2. ***Macrosemia sapaensis*** **sp. nov.: (A)** male genitalia in ventral view, **(B)** male genitalia in lateroventral view, **(C)** male genitalia in lateral view.

Thorax: pronotum pale green, with a surrounding line black, a pair of central longitudinal stripes, broadened both anteriorly and posteriorly, markings along furrows of inner area, and two spots at each posterolateral part of outer dilatation, black; pronotal collar pale green, margin and marking on lateral part of pronotal collar black, with dentate projection but not cute, apex brown-black; mesonotum pale green, with five black broad fasciae, a median fascia reaching from anterior margin of mesonotum to cruciform elevation, and ending in a black triangle on cruciform elevation, posterior half 1.5-3 times as wide as anterior part, paramedian suture extending to just beyond half-length of mesonotum, 1.5-5 times as wide as anterior part of median fascia, and about as broad as or somewhat broader than distance between paramedian and median fasciae, pair of round black spots in front of anterior angles of cruciform elevation, lateral fasciae continuous from anterior to posterior margin of mesonotum and about as broad as distance between lateral and paramedian fasciae; two pair of small black triangles at anterior mesonotal margin between paramedian and lateral fasciae, cruciform elevation greenish opalescent with margin of posterior angles black, wing groove black; thorax greenish opalescent in ventral view, with episternum 2,3 black (Fig. 2).

Wings: fore and hind wings hyaline, fore wing venation pale yellow-brown basally and brown-black apically; fore wings slightly tinged and spotted with infuscations on r, r-m, m-cu, and CuA2, on RA, RP, M1, M2, M3, M4, CuA1, CuA2, on M3+4, CuP+1A, and on node, basal cell and clavus pale brown (Fig. 2).

Legs: foreleg with markings as follows: coxae brown-black with apex opalescent, femur brown-black with a longitudinal fasciae opalescent in lateroventral view, primary spine larger than secondary spine, tibia brown-black, tarsus black; middle leg, with coxae black with half inner and a longitudinal fasciae oblique yellowish opalescent, trochanter black, femur brown-black with apex and longitudinal fascia oblique yellowish opalescent, tibia with half brown-black at base and black at apex, tarsus black; hind leg, with coxae black with half inner and a longitudinal fasciae oblique yellowish opalescent, trochanter with half brown-black at base and yellowish opalescent at apex, femur brown with apex and a longitudinal yellowish opalescent in lateroventral view, tibia pale brown with marking brown-black at base and apex, tarsus brown (Fig. 2).

Abdomen: longer than distance from head to cruciform elevation, black in dorsal view, tergite 3 with a transverse fascia of dense white hairs along the anterior margin, with the fascia enlarged at the lateral margins; tergites 4-6 with edges of lateral margins pale brown; timbal cover black, distinctly covering timbal; pale yellow-brown in ventral view, posterior margin of sternite II and anterior margin of sternite III black, posterior margin of sternite IV-VI and sternite VII dark brown, area close to posterior margin of sternite VII with brownish black X-shaped marking, apex of sternites VIII brownish black (Fig. 2).

Operculum: elongate, fairly broad, and reaching to posterior margin of segment 7; length about as 1.5X width. Pale yellow-brown, with one fifth of length from

base black, rim along operculum margin pale yellow-brown except basal part of outer margin black; lateral margin slightly concavely sinuates on basal third, medial margin slightly concave on basal part and convex apically (Fig. 2).

Genitalia ♂: basal pygofer lobes angular, well separated from lateral margin of pygofer. Basal part of uncus globose, broad and almost semi-circular. Uncus bifurcated, castaneous, with uncal lobes protruding obliquely and distinctly curved laterad, forming a V-shape with a right angle in ventral view, and quarter round in lateral view.

Measurements of one male (in mm): body length: 40.2; fore wing length: 51.1; fore wing width: 17; head width: 12.2; pronotum width: 16.6; mesonotum width: 13.3.

Remarks: this species was collected by light trapping at high mountain (1,900 m).

Distribution: north Vietnam (Lao Cai province)

4. Conclusions

The new species differs from all species of the genus *Macrosemia* from Vietnam (exclude in the species *M. lamdongensis*) in the markings of forewings that are widely spread or roundish infuscation on each apical portion of veins RA2, RP, M1, M2, M3, M4, and CuA1, which form a series along the subapical margin of the forewing. Meanwhile, the rest have forewings without widely spread or roundish infuscation on each apical portion of veins RA2, RP, M1, M2, M3, M4, and CuA1 forming a series along the subapical margin of the forewing. *Macrosemia sapaensis*, is distinguishable from *M. lamdongensis* by the markings on the third abdominal tergite, with a transverse fascia densely covered with white hair along anterior margin in *M. sapaensis*, and without such fascia along anterior margin in *M. lamdongensis*; *M. sapaensis*, with uncal lobes protruding obliquely and very curved laterad and uncus lobe on ventral (outer) surface.

CRediT author statement

Thai Hong Pham: Data analysis and Interpretation, Writing and Manuscript revising; Hong Minh Bui, Yen Hoang Luu, Jérôme Constant: Method, Data analysis and Writing.

ACKNOWLEDGEMENTS

The present study was supported by Vietnam Academy of Science and Technology, under the grant number (QTBY01.08/22-23 and QTKR01.02/22-23).

COMPETING INTERESTS

The authors declare that there is no conflict of interest regarding the publication of this article.

REFERENCES

[1] M. Kato (1925), "The Japanese Cicadidae, with descriptions of some new species and genera", *Transactions of the Natural History Society of Formosa*, **15(1)**, pp.1-47.

[2] M. Yang, C. Wei (2013), "On the cicada genus Nipponosemia Kato, with description of one new species from China (Hemiptera, Cicadidae)", *Zookeys*, **1(1)**, DOI: 10.3897/zookeys.293.464649.

[3] FLOW (2020) https://hemiptera-databases.org/cool/database.php?db=cool&lang=Zh&card=publication&id=2118, accessed 5 May 2020.

[4] P. Thai, J. Constant (2016), "The cicada genus Macrosemia Kato, 1925 (Hemiptera: Cicadidae) from Vietnam, with the description of a new species and key to species", **38(3)**, DOI:10.15625/0866-7160/v38n3.6632.

[5] Y.J. Lee, M. Hayashi (2004), "Taxonomic review of Cicadidae (Hemiptera, Auchenorrhyncha) from Taiwan, part 3. Dundubiini (two other genera of Cicadina), Moganiini, and Huechysini with a new genus and two new species", *Journal of Asia-Pacific Entomology*, **7(1)**, pp.45-72, DOI: 10.1016/S1226-8615(08)60200-9.

[6] J. Duffels, J.P. Laan (2013), "Catalogue of the Cicadoidea (Homoptera, Auchenorhyncha), 1956-1980", *Food and Agriculture Organization of the United Nations*, **34(1)**, pp.333-388.

[7] Y. Lee, M. Hayashi (2004), "Taxonomic review of cicadidae (Hemiptera, Auchenorrhyncha) from Taiwan, part 3. Dundubiini (two other genera of cicadina), moganiini, and huechysini with a new genus and two new species", *Journal of Asia-Pacific Entomology*, **7(1)**, pp.45-72, DOI: 10.1016/S1226-8615(08)60200-9.

[8] Y. Lee (2008), "A checklist of Cicadidae (Insecta: Hemiptera) from Vietnam, with some taxonomic remarks", *Zootaxa*, **1787(1-9)**, pp.1-27, DOI: 10.11646/zootaxa.1787.1.1.

[9] M. Moulds (2005), "An appraisal of the higher classification of cicadas (Hemiptera: Cicadidae) with special reference to the Australian fauna", *Records of the Australian Museum*, **57(3)**, pp.375-446.

[10] Y. Lee, M. Hayashi (2003), "Taxonomic review of cicadidae (Hemiptera, Auchenorrhyncha) from Taiwan, part 1. Platypluerini, Tibicenini, Polyneurini, and Dundubiini (Dundubiina)", *Insecta Koreana*, **20(3-4)**, pp.149-185.

[11] G. Liu (1940), "New oriental cicadidae in the museum of comparative zölogy". *Bulletin of the Museum of Comparative Zoölogy*, **87(1)**, pp.73-117.

DOI: 10.31276/VJSTE.64(2).86-94

Fabrication of electrospinner for producing tube-shaped artificial blood vessels toward treatment applications in cardiovascular diseases

Binh Thanh Vu[1, 2], Thai Minh Do[1, 2], Hiep Thi Nguyen[1, 2*]

[1]*School of Biomedical Engineering, International University, Quarter 6, Linh Trung Ward, Thu Duc City, Ho Chi Minh City, Vietnam*
[2]*Vietnam National University - Ho Chi Minh City, Linh Trung Ward, Thu Duc City, Ho Chi Minh City, Vietnam*

Received 5 April 2022; revised 5 May 2022; accepted 27 May 2022

Abstract:

Cardiovascular disease stands as a leading cause of high mortality rates in Vietnam and globally. Addressing this, there's an increasing demand for artificial blood vessels to replace damaged ones in cardiovascular patients. Tissue engineering offers the prospect of replacing damaged blood vessels. Recent advances in science have shown that it is possible to successfully replace human blood vessels. For example, cells can be grown into sheets of tissue to form a layer of vascular cells with impressive strength. Recognizing this need, our team designed a specialized electrospinner machine for crafting artificial blood vessel models. The electrospinner comprises crucial components: a high-power supply source, collectors with tubular structures, and a syringe pump system. This study aimed to (i) construct the electrospinner machine and (ii) assess its operation. Through experimentation, we identified key parameters influencing vascular formation, including DC high voltage source, needle-tip-to-collector distance, needle tip diameter, syringe pump speed, and ambient temperature/ humidity. The results demonstrated the machine's stability and user safety. Optimizing the conditions for vascular fabrication opens avenues for more effective production of artificial blood vessels, potentially revolutionizing cardiovascular treatments and addressing a critical health concern in Vietnam and beyond.

Keywords: **artificial blood vessel, cardiovascular diseases, electrospinner.**

Classification number: **3.6**

1. Introduction

Cardiovascular disease, including coronary artery disease and peripheral vascular disease, is the leading cause of death in Vietnam and other countries around the world. Therefore, the development of artificial blood vessels [1] to replace aging conduits in cardiovascular patients is becoming increasingly urgent, especially in bypass surgeries and other revascularization procedures. Tissue engineering offers the prospect of replacing damaged blood vessels. Recent advances in science have shown that it is possible to successfully replace human blood vessels. For example, cells can be grown into sheets of tissue to form a layer of vascular cells with impressive strength.

In recent years, electrospinning has revolutionized material science [2]. By this method, a solution (obtained by the melting or dissolution of one or a mixture of materials) is ejected into fibres ranging in size from micrometres to nanometres. A basic electrospinning device consists of three main parts: (i) a high voltage DC power supply that generates a steady voltage of several tens of kilovolts, (ii) a pump that controls the injection rate of the mentioned solution, and (iii) a grounded fibre collector [3]. The operation principle of electrospinning begins with using the force of an electric field to produce extremely thin fibres from a viscous solution, for example, a solution of polymers such as polycaprolactone [4], chitosan, polyvinyl alcohol, etc. These thin fibres follow the direction of the electric field force to the fibre collector and attach to it. When applying high voltage to the nozzle and grounding the fibre collector, there will be a large electric field between the nozzle and the collector. A very small current is generated, which electrifies the nozzle. Therefore, the solution passing through this nozzle is also electrified and the charged particles are accelerated by the electric field thereby ejecting the solution moving in the direction of the above electric field. As a result, the solution is uniformly accelerated and forms a thin filament with a radius as small as a few nanometres [5]. Currently, electrospinning is widely used on an industrial scale in various fields including electronics, semiconductors,

*Corresponding author: Email: nthiep@hcmiu.edu.vn

environment, fashion, chemistry, and medicine and for diverse applications as light-emitting diodes, kidney filters, and air filters [6].

With advancements in science and technology, electrospinning has also made great contributions to biomedical research in the manufacture of medical devices, especially in the fabrication of tissue scaffolds and controlled drug release systems [7]. Researchers around the world have been applying this method in their research to find innovative solutions for medical treatment. In Vietnam, the concept of electrospinning is quite new and has only been studied for the last five years. Currently in Vietnam there are only two research facilities that own (manufacture) electrospinning equipment: Hue University of Science and University of Technology, Vietnam National University, Ho Chi Minh city. Current market prices of electrospinning devices, including the cost to import to Vietnam, are about $20,000-500,000. Despite their excessive cost, the application ranges of the above devices are limited, especially in the context of artificial tissue manufacturing where interest in products used in the treatment of artificial skin and blood vessels continues to increase among domestic scientists.

The main components of an electrospinner include the high-voltage power supply, the syringe pump system, and the collector system as shown in Fig. 1. In the electrospinner, the machine's high voltage power supply is the core of the operation. This is a DC source that ranges from 5 to 30 kV. These power supplies on the market are expensive and are not suitable for our application. Therefore, we designed our own high voltage power supply. In addition, we designed a syringe pump system with a pumping speed of 1-20 ml/hour and plastic preformed structures for insulation purposes. The design of the fibre collector system is necessary to actively fabricate scaffolds of different shapes for applications in tissue engineering. The fibre collector was designed in the form of a hub to achieve a tubular structure. Then, we operated and assessed the electrospinner by fabricating tubular scaffolds and evaluating their surface structure.

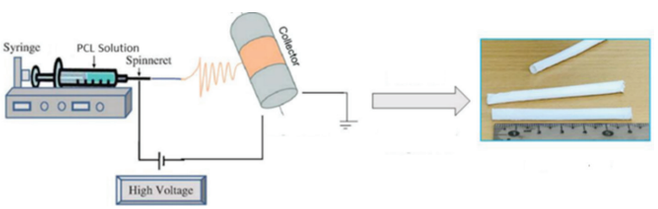

Fig. 1. Overview of the fabrication of polycaprolactone (PCL) tubes.

2. Materials and methods

2.1. Materials

Frozen bovine artery endothelial cells (BAECs) were provided by the School of Biomedical Engineering, International University, Vietnam National University, Ho Chi Minh city. BAECs were thawed and cultured in nutrient medium (DMEM, 10% foetal bovine serum, 1% antibiotics, Gibco) at 37°C, 5% CO_2 until 70-80% coverage of the culture dish was reached. Then, the BAECs were detached with Trypsin/EDTA 0.25% (Gibco) and seeded on PCL scaffolds to perform further evaluations.

2.2. Methods

Design of high voltage DC power supply:

From the 220 VAC main, the power source was rectified directly to a DC voltage of about 277 VDC via the use of a full power rectifier circuit. This high voltage DC source is then used as the power source for the DRIVER MOSFET, which opens and closes the FET at a very high frequency in the primary part of the flyback transformer. As a result, the output of the flyback transformer will be pushed to a very high DC voltage. This process is illustrated in Fig. 2.

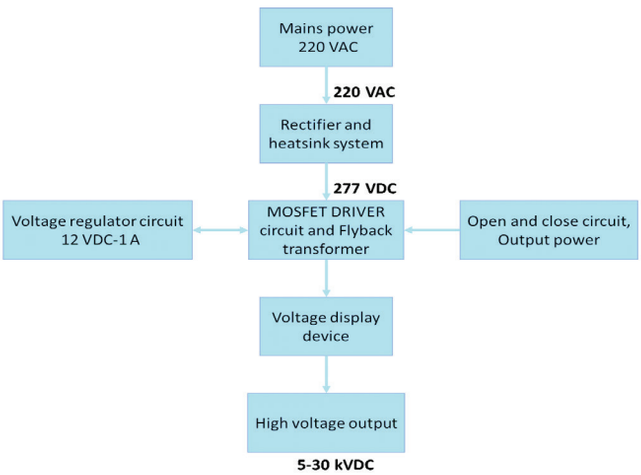

Fig. 2. High voltage DC power supply circuit block diagram.

The principle of operation of our designed electrical circuit is easy to understand and is also capable of solving interference problems. The circuit was designed on ORCAD software, which is a powerful software that supports electronic circuit design tasks. To simplify the circuit, the component pins are specifically labelled and marked with the power terminals, which helps engineers read and trace the design. The designed circuit is depicted in Fig. 3.

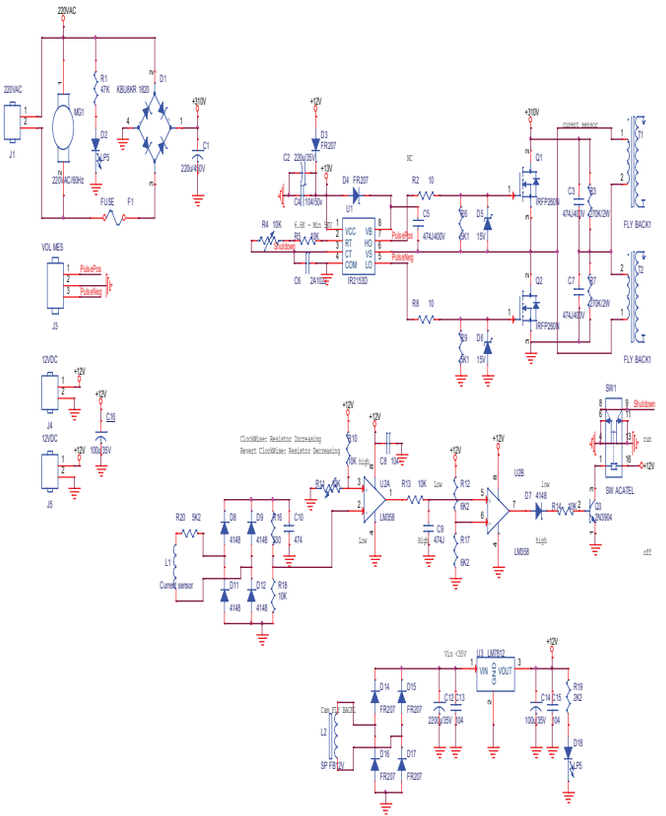

Fig. 3. The principal circuits of the high voltage source.

Design of fibre collector system:

The fibre collector system consists of one aluminium foil spool and one drum, which is a monolithic billet that is turned in a cylindrical shape. The system is rotated by a moving belt, which transmits the force from the motor to the shaft of the drum. The drum rotation is monitored by a microcontroller system.

The electronic circuit acts as the central processing task for the collector system. This circuit is designed with the central microcontroller ST32F407 with a core clock speed of 168 MHz, and support for processing 32-bit numbers. Therefore, it is suitable for motor control applications by PID algorithms. In addition, we also use specialized drivers for brushless motors to make control more convenient.

In this project, brushless motors are selected and used for its characteristics of large rotational power and low vibration at high speed as it is necessary to control and align the membranes (Fig. 4).

ZM-6405E brushless motor driver bridge: the DC motor driver ZM-6405E allows a large current supply, control over the brushless motor with a maximum power of 200 W and can accept PWM Analog signal voltage to control motor speed.

Brushless motor: the brushless motor BL75S10-230TF9 has a maximum power of 100 W at 3000 rpm and a force of 0.32 N.

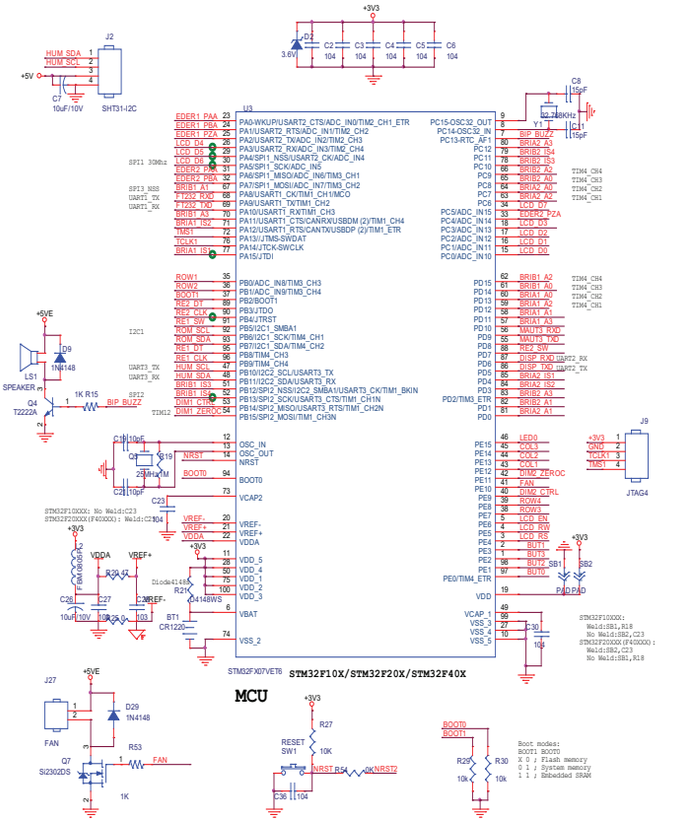

Fig. 4. Central control circuit of the collector system.

Design of syringe pump system:

The syringe pump and slider system are controlled by the MCU slaver SMT32F030F4P6 as illustrated in Fig. 5. The main purpose of the master and slaver method is to stabilize the injection rate of the syringe pump in the range 0.1 to 20 ml/h with the cylinder sizes available on the Vietnamese market. Meanwhile, the slider system also needs to be controlled to move the syringe pump system back and forth.

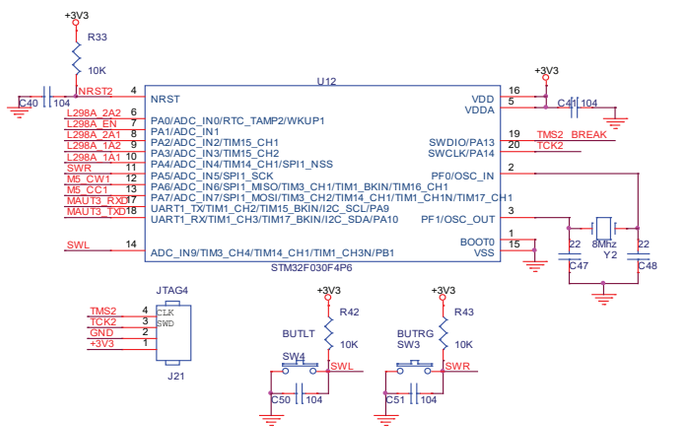

Fig. 5. The central control circuit of the syringe pump.

The needle and syringe system consists of two main components: a fixed frame (including two front shields to help hold the cylinder, two rear shields connecting the stepper motor, a 20x80-mm support frame made of fixed aluminium) and the moving part (including centre thrust plate, lead screw, nut and two-phase stepper motor). We use a screw mechanism to convert the circular motion of the stepper motor into the reciprocating motion of the cylinder. To limit the pushing speed to the maximum amount, we choose the lowest step screw bar of 1 mm combined with two round sliders mounted in parallel to support and balance the push cycle. Two linear bearings and screw nuts are rigidly fixed on the central thrust plate, which plays the role of fixing and transmitting the movement of the motor (Fig. 6).

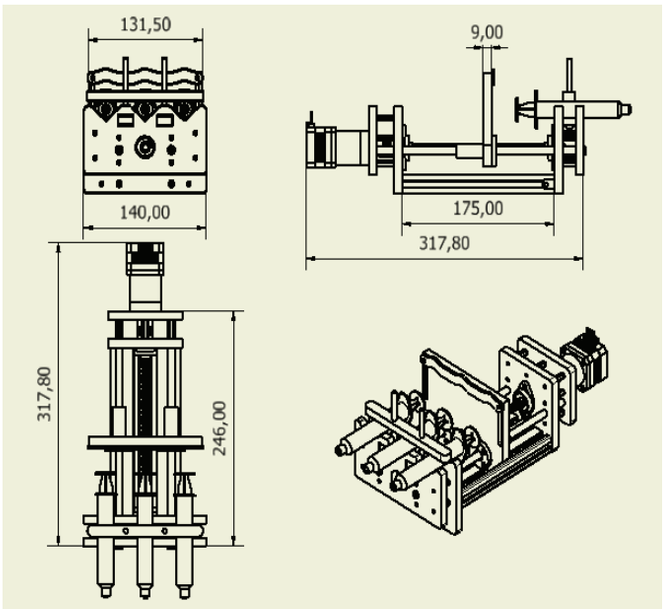

Fig. 6. Syringe pump system on Solidworks software.

PCL tubular fabrication:

The PCL tube is fabricated based on a long metal mould (4 cm length and 2, 3, or 4 mm diameter corresponding to the diameter of the tubular fibre collector) by electrospinning whose details are given below.

The electrospinning system consists of 1-3 piston(s) containing PCL solution and the nozzle is connected to the anode of the high voltage power source. On the other hand, the piston(s) is placed in a pump system with a pumping rate of 0.2 ml/h.

The collector is a metal mould shaft (4 cm length and 2, 3, or 4 mm diameter). The metal mould is connected to the cathode of the power supply and is stabilized in a rotating system with a speed of 750-800 rpm.

The procedure was carried out based on our previous study [8] and 15% PCL solution was prepared previously in acetone solvent.

- 5 ml of the solution is placed into the piston. The distance from the needle tip to the collector is set to 10 cm.

- The pumping system is set up with a pump rate of 0.2 ml/h.

- The high voltage power supply is 15-18 kV, and the collector has a rotation of 750-800 rpm.

- Electrospinning is done within 3-4 h to obtain a PCL tube.

Evaluate surface structure of PCL scaffold through Scanning electron microscope (SEM):

Scanning electron microscopy (SEM) can produce high-resolution images of a specimen by using a narrow beam of electrons scanning the surface of a specimen, which is followed by the recording and analysis of the radiation emitted from the interaction of the electron beams with the sample surface to obtain an image of the specimen with high magnification.

Evaluate BAEC adhesion and proliferation on PCL scaffold through SEM:

- Use a 1-ml needle to transfer the BAEC suspension onto the PCL scaffolds in a 96-well plate, which was then supplemented with culture medium and placed in the humidified incubator.

- After defined time intervals, samples were washed three times (1-2 ml each time) with phosphate-buffered saline (PBS).

- The sample was then soaked in 2.5% glutaraldehyde at 4^{o}C for 2 h.

- Remove excess glutaraldehyde solution, wash with PBS 2-3 times.

- Samples are soaked in alcohol at 30^{o}, 50^{o}, 75^{o} and 96^{o}, respectively, for 20 min each time. The sample was then allowed to dry at room temperature.

- Conduct SEM.

3. Results and discussion

3.1. Design of high voltage DC power supply

In this study, we designed an 11x15-cm PCB board using FR4 material with two layout layers. This printed circuit was designed with multiple lines with a large width to ensure the power of the power supply is operated efficiently. This motherboard is shown in Fig. 7. In addition, we also designed a display PCB main that indirectly measures high voltage from the primary source signals as illustrated in Fig. 8.

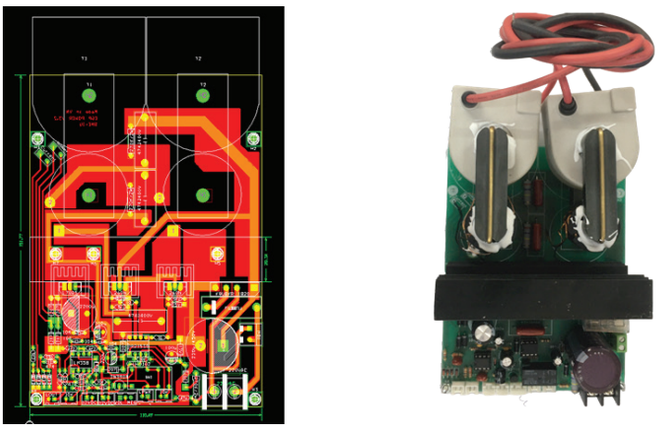

Fig. 7. Layout of the high voltage power supply circuit.

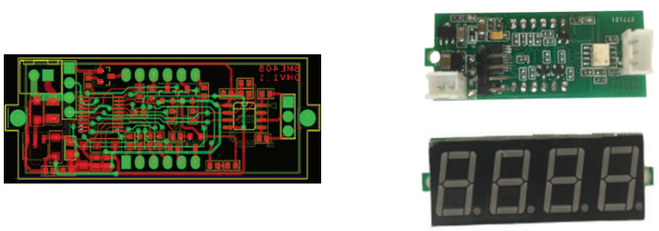

Fig. 8. High voltage display circuit.

To prevent electromagnetic interference in a high voltage field, the power supply was completed with aluminium housing. We reviewed several power supplies on the market and produced an optimal solution that makes the high-voltage power supply easy to use and safe. It was designed with a power switch, display of the output voltage status, and a single knob to adjust the output voltage. In addition, it also has a built-in display of current and voltage. The completed power supply is shown in Fig. 9.

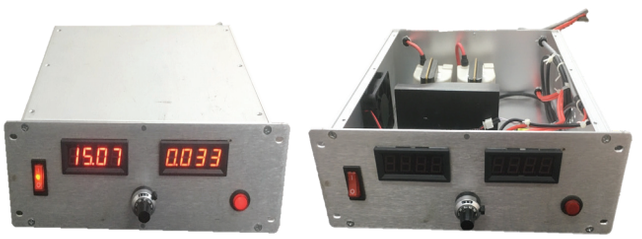

Fig. 9. DC high voltage power supply after being successfully built.

A crucial factor when researching, manufacturing, and operating high voltage power supplies is safety assurance. To avoid fatal injuries caused by high voltage, the grounding part of the high voltage system should be managed with care. Do not operate a high voltage power supply system without grounded wiring. The user needs to ensure a minimum distance from the high voltage electrodes. When voltage is being supplied, a retention distance of at least ½ inch per kV is recommended [9]. In addition, it is necessary to maintain dry conditions and provide insulating boots to the user if necessary. Several distances are calculated as follows:

100 kV → 100 x (2.54/2) = 100 x 1.27 = 127 cm = 1.27 m

50 kV → 0.635 m

30 kV → 38.1 cm

3.2. Design of fibre collector system

We used ORCAD Layout software to design the PCB. The central processor STM32F407 was designed in the middle of the main, while other power components such as the H-bridge and the source are mounted with heat sinks and placed on the outside to reduce temperature during operation. The PCB layout circuit is illustrated in Fig. 10.

The MCU enters the corresponding task segments to increase or decrease the target value, and thanks to the PID algorithm, the actual rotation speed asymptotically follows the desired value.

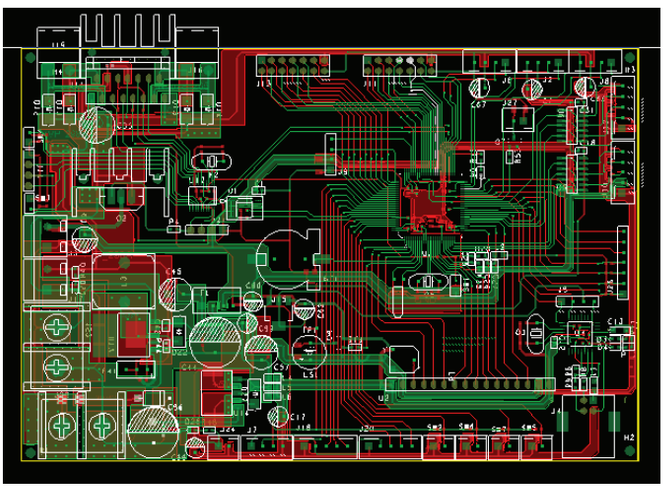

Fig. 10. PCB main control of the collector system.

Upon entering the program, the microcontroller initializes peripherals such as H-bridge, EEPROM, and LCD display by sending data frames to the display device. Next, the central controller loads the default values for these peripherals set in the EEPROM. PID, timer, and H-bridge parameters are initialized. This motor control process is based on a PID algorithm with pulse feedback inputs read from the encoder to record the round(s) per minute. The actual rotation speed approaches the desired value thanks to the control algorithm. The interplay between two microcontrollers on the main, MCU Master STM32F407, and MCU slave for slider and syringe pump function uses UART interrupts.

The collector control system was installed in an aluminium box to prevent electromagnetic interference

from the external high-voltage field (Fig. 11). The LCD used is a 20x4 type that can display not only collector control information but also other information such as infrared light, syringe pump, humidity, and temperature. Interactions with user will be via 3 x 4 matrix pushbuttons and knob encoder.

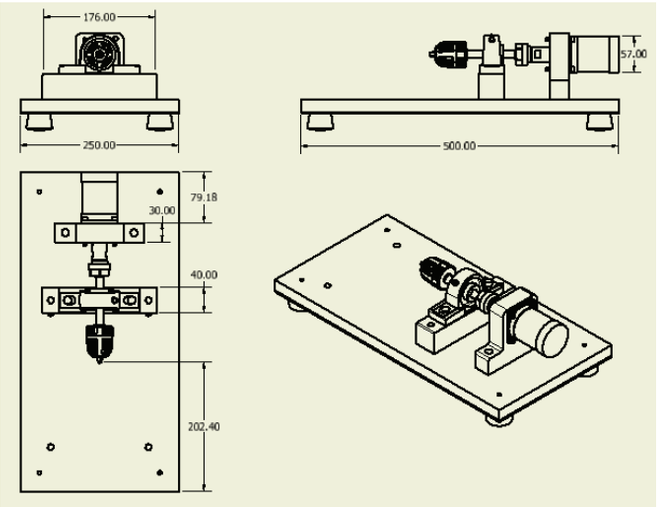

Fig. 11. Design of the mandrel collector system.

3.3. Syringe pump system design

The TB6600 stepper motor driver circuit uses the IC TB6600HQ/HG is used for stepper motors 42/57/86 that is either 2-phase or 4-wire with load current of 4A/42VDC, which is commonly applied in machines such as CNC, laser, or other automatic machines (Fig. 12). Measure is a dedicated control bridge for the stepper motor, which will make the syringe pump control easier and more accurate.

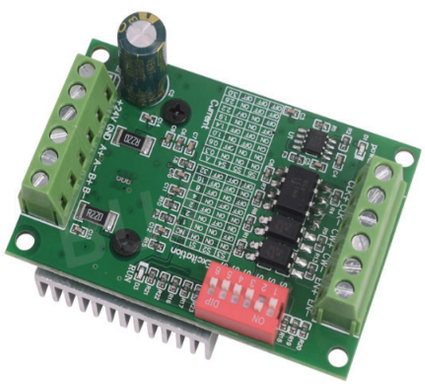

Fig. 12. Stepper motor driver bridge TB6600.

When the system starts, the master microcontroller will send a command to the slaver processor of the syringe pump system to initiate the command according to the parameters set in the ROM. The slaver processor will initiate the pump speed and move the slider.

In the main processing loop, the slaver processor will wait for a command from the master processor. If an instruction is received via the UART interrupt, the processor immediately executes that instruction. When complete, the processor will stop pumping and move the slider back to its original position.

Calculation of pump speed, travel speed, and slider movement range are also performed in by program in the slaver MCU.

With the need to create greater polymer coverage on the mandrel, we use a slider system driven by a 4-phase stepper motor that combines with the syringe pump system. The system is programmed to generate a cyclic motion over a fixed distance through the lead screw system and the slider. On the slider, there are several available positions to fix the needle pump, which makes it easy to adjust the distance between the needle and collector (Fig. 13). The system will automatically align the distance on the slider thanks to a travel switch placed in the original position of the coordinates.

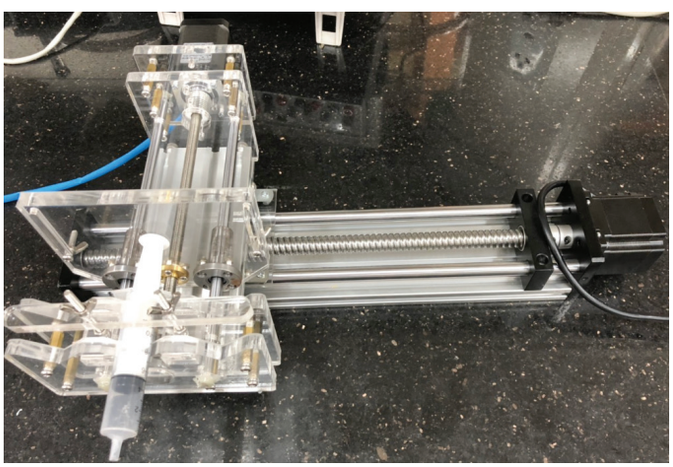

Fig. 13. Syringe pump system installed on the slider.

3.4. Fabrication of tubular Polycaprolactone (PCL) scaffold

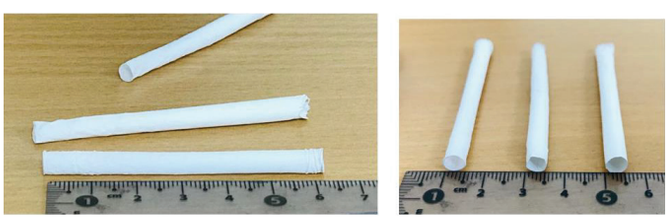

Fig. 14. Macroscopic structure of PCL tubes.

Figure 14 shows the macroscopic structure of the PCL tube obtained after being fabricated by electrospinning i.e., ejecting the polycaprolactone solution in a high-

voltage electric field). After using this method, the obtained scaffold has an average length of 4-5 cm and diameter of 2, 3, or 4 mm based on the shape of the collector mould.

3.5. Surface structure of PCL scaffold

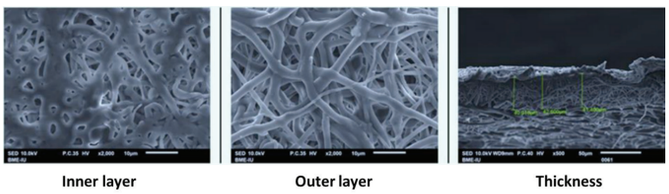

Fig. 15. The microstructure of the PCL tube fabricated by electrospinning. The measured thicknesses are 40.018, 42.000, and 41.400 µm, respectively.

After using electrospinning to obtain a tubular structure similar to blood vessel, the microstructure was observed by SEM as depicted in Fig. 15. Under high magnification (x2000), the structure of the PCL scaffold is made up of micrometre-sized filaments on both the inner and outer surfaces. However, the shapes of the inner and outer surfaces of the PCL tube are different. The inner fibres have more of a flat shape than the outer fibres. This is explained by the fact that the inner surface is in direct contact with the collector during electrospinning and the charged fibres/particles of the PCL solution move from the needle tip to the collector at a certain speed. Finally, the fibres/particles hit the collector, which causes the polymer fibres in the innermost layer (inner surface) to have a flat shape compared to the outer surface.

According to the descriptions of the structural types of blood vessels, the diameter varies depending on vascular classifications along with other factors such as anticoagulation capacity, mechanical durability, etc. Of which, the ability to prevent blood clotting is one of the most important prerequisite properties of blood vessels in general. This ability, according to previous studies, comes from secreted proteins of the monolayer of endothelial cells in the lumen of the vessel.

A dense structure of PCL fibres stacked and interlaced form a small pore structure that makes it difficult for cells to penetrate deep into the inner structure of the PCL tubule. This structure readily forms monolayers of endothelial cells.

In addition, in Fig 15, the thickness of the PCL tube was recorded at high magnification, which was found to be around 40-42 µm. This thickness, along with the physical properties of PCL, creates a conduit structure bearing the appropriate properties as well as a certain elasticity. This data has been published in our previous studies that show suitability for making artificial blood vessels.

Thus, this study has fabricated PCL scaffolds with basic characteristics of small vascular tubes: diameters of 2, 3, or 4 mm, physical-mechanical strength, and a structure that facilitates a monolayer of endothelial cells established within the lumen of the vessel.

3.6. Spreading ability of BAECs on PCL tubes

After determining the stable BAEC cell line through subcultures, cells were examined for their ability to spread on the PCL structure. Fig. 16 depicts the interaction of BAECs on PCL scaffolds based on images of the cell shape and extracellular matrix (ECM) region, which were taken on day five of culture.

In the absence of cells (Fig. 16A), the inner surface of the tube is composed of a structure of randomly arranged and stacked micrometre-sized fibres (a consequence of the electric field due to electrospinning) followed by a very small pore structure of irregular shape. In general, the scaffold structure is uneven but still has stability in fibre size, structure, and pore size fluctuations of about 1-3 µm. Because it is composed of microfibers, the surface of the scaffold structure has a relative roughness, which is one of the factors that facilitates cells adherence to the PCL substrate.

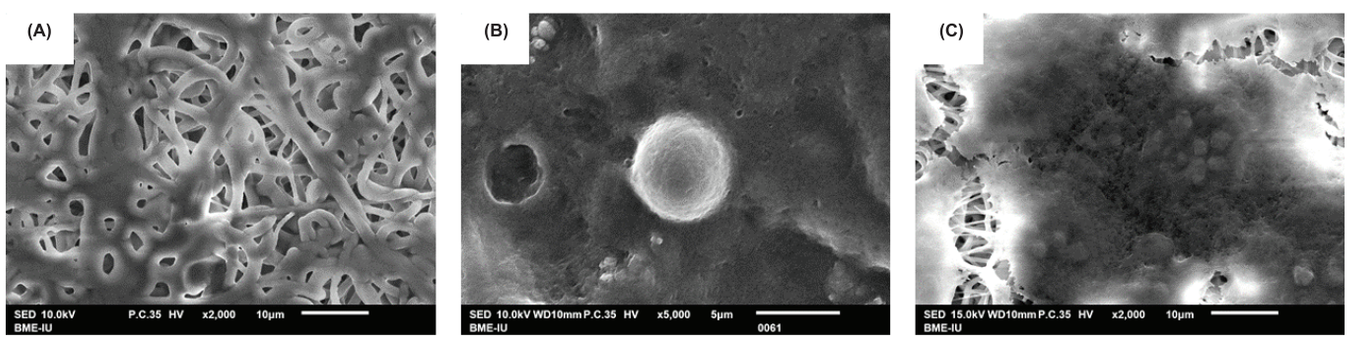

Fig. 16. Interaction of BAECs on PCL scaffolds. (A) The inner surface of the PCL matrix is devoid of cells. **(B)** BAECs at day five of culture on PCL scaffold. **(C)** The extracellular matrix region of BAECs at day five of culture on PCL scaffold.

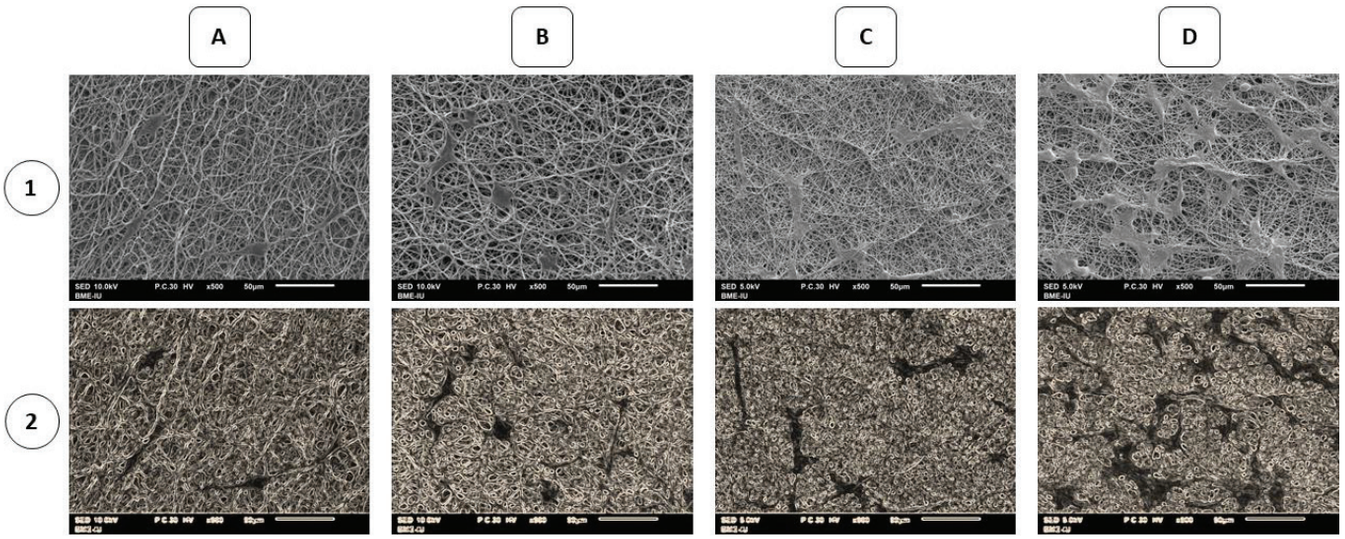

Fig. 17. The proliferation ability of BAECs on PCL scaffold. BAECs on PCL scaffold after **(A)** 1, **(B)** 2, **(C)** 3, and **(D)** 4 d of culture.

Figure 16B shows the cells in the process of spreading onto the attachment surface. At this point, the cell has a rounded tip and the surrounding part begins to spread and mix with the ECM, which is secreted by the cell itself and neighbouring cells. Here, the boundary between the cell and the ECM is indistinguishable. One of the features that helps us see the attachment site of the cell is that the cell-ECM structure hides the underlying matrix and the fibrous structure and voids are gone.

The SEM image in Fig. 16C shows that the substrate is rough and slimy. Between them, there are small grooves consisting of zigzag lines that cross each other. This is one of the demonstrations showing the compatibility of PCL for animal cells in general, or bovine artery endothelial cells - the main subject of this study.

3.7. Proliferation of BAECs on PCL scaffold

SEM images were recorded through days 1, 2, 3 and 5 (Fig. 17-1), and the image shows that the cells spread on the scaffold increase in density over time. SEM images were contrast processed in Microsoft PowerPoint to increase the prominence of cells on the substrate (Fig. 17-2). On day 1 (Fig. 17A), the cells spread in very small numbers. Cells retained their elongated, dendritic shape on subsequent observation days (Figs. 17B, 17C, and 17D).

The results showed that the adhesion and proliferation of BAECs on PCL scaffolds were highly effective. Over the culture period, cells adhered evenly to the surface of the scaffold structure. On the other hand, the cell's ability to attach to the scaffold was highly influenced by the pore size of the scaffold and by the binding between receptors and ligands.

The above results showed that *in vitro* cultures of BAECs on PCL scaffolds do not cause changes to the structure of the scaffold and the data portrays stable spread and proliferation of this cell line. These outcomes suggest the possibility that PCL scaffolds can be used for long-term *in vitro* culture.

4. Conclusions

We designed and fabricated the basic components of an electrospinner. Of these components, a variable high voltage DC power supply that ranges between 5 kVDC and 30 kVDC with display of current and voltage was constructed. Second, a collector system (mandrel) that ejects polymer fibres out of a solution and evaporates solvents to fabricate PCL scaffolds, which are the structure that facilitates cell attachment and growth to develop artificial blood vessels. Finally, the syringe pump system that integrates three needles on the system and an integrated reciprocating mechanism to increase the homogenous coverage of the nanofibers on the collectors. Electrical designs were developed on ORCAD software, mechanical designs were developed on SOLIDWORKS, INVENTOR software. These programs make it easier for engineers to calibrate and develop versions of the machine later.

Given the heat-sensitive characteristics of medical synthetic polymers (i.e., the low melting point of 60^{o}C for PCL), the process of fabricating polymer fibres by electrospinning should not cause fibre fractures or changes in chemical or crystal structure by manipulation at room temperature. Therefore, in the fibre forming process, the polymer is mixed in organic solvents at a temperature lower than the melting point (50^{o}C). The

solvents used for dissolution are highly volatile solvents, so the polymer fibres will almost immediately dry when collected at the collector at room temperature. The *in vitro* results of BAEC cultures on PCL tubes fabricated from our electrospinner showed that the cells exhibited excellent spreading and proliferative ability over time, which demonstrated that our electrospinning PCL tubes exhibit promising cytocompatibility.

CRediT author statement

Hiep Thi Nguyen: Data analysis and Interpretation, Writing and Manuscript revising; Binh Thanh Vu, Thai Minh Do: Method, Data analysis and Writing.

ACKNOWLEDGEMENTS

This research was funded by Vietnam National University, Ho Chi Minh city (VNU-HCM) under grant number C2020-28-08.

COMPETING INTERESTS

The authors declare that there is no conflict of interest regarding the publication of this article.

REFERENCES

[1] E.C. Filipe, M. Santos, J. Hung, et al. (2018), "Rapid endothelialization of off-the-shelf small diameter silk vascular grafts", *JACC: Basic to Translational Science*, **3(1)**, pp.38-53.

[2] Z.M. Huang, Y.Z. Zhang, M. Kotaki, et al. (2003), "A review on polymer nanofibers by electrospinning and their applications in nanocomposites", *Composites Science and Technology*, **63(15)**, pp.2223-2253, DOI: 10.1016/S0266-3538(03)00178-7.

[3] D. Li, Y. Xia (2004), "Electrospinning of nanofibers: reinventing the wheel?", *Advanced Materials*, **16(14)**, pp.1151-1170, DOI: 10.1002/adma.200400719.

[4] N. Tran, A. Le, M. Ho, et al. (2020), "Polyurethane/polycaprolactone membrane grafted with conjugated linoleic acid for artificial vascular graft application", *Science and Technology of Advanced Materials*, **21(1)**, pp.56-66, DOI: 10.1080/14686996.2020.1718549.

[5] D. Lukas, A. Sarkar, L. Martinova, et al. (2009), "Physical principles of electrospinning (electrospinning as a nano-scale technology of the twenty-first century)", *Textile Progress*, **41**, pp.59-140, DOI: 10.1080/00405160902904641.

[6] S. Ramakrishna, K. Fujihara, W.E. Teo, et al. (2006), "Electrospun nanofibers: Solving global issues", *Materials Today*, **9(3)**, pp.40-50, DOI: 10.1016/S1369-7021(06)71389-X.

[7] N. Zhu, X. Chen (2013), "Biofabrication of tissue scaffolds", *Advances in Biomaterials Science and Biomedical Applications*, IntechOpen, DOI: 10.5772/54125.

[8] N.M.P. Tran, T.L. Huynh, B.N. Phan, et al. (2020), "Conjugated linoleic acid grafting improved hemocompatibility of the polycaprolactone electrospun membrane", *International Journal of Polymer Science*, **2020**, DOI: 10.1155/2020/8127570.

[9] ViTREK 4700 Operating and Maintenance manual (2018), https://vitrek.com/downloads/4700/4700_Operating_Manual.pdf, 55pp.

DOI: 10.31276/VJSTE.64(2).95-98

Conformational changes of exogenous deposited fibronectin on decellularized aortic conduits after implantation

Khon Huynh*

School of Biomedical Engineering, International University, Quarter 6, Linh Trung Ward, Thu Duc City, Ho Chi Minh City, Vietnam

Received 27 April 2022; revised 20 May 2022; accepted 2 June 2022

Abstract:

Plasma fibronectin (FN) is produced by hepatocytes and released into circulation as a soluble compact dimer at concentrations of 200-600 µg/ml. Circulating plasma FN is a glycoprotein dimer and multidomain protein with high molecular weight (440-500 kDa) that is folded into a globular compact structure. Its compact structure leads to the inactivation of FN since major functional binding sites are buried. Fibronectin, a pervasive extracellular matrix component, plays a vital role in modulating diverse cellular functions through direct interactions with integrin receptors on cell surfaces. Our previous research demonstrated that fibronectin facilitates the autologous cellular repopulation of implanted decellularized grafts, enhancing adhesion capacity and biocompatibility via fibronectin fibrillogenesis. Interestingly, the supportive effect varied across different regions of the implanted decellularized grafts. This prompted an inquiry into whether there are conformational differences in fibronectin deposited on the luminal and adventitial surfaces of decellularized aortic conduits post-implantation. In this study, we employed a doubly labeled fibronectin with a fluorescent resonance energy transfer (FRET) pair, utilizing it to analyze variations in conformational changes of adsorbed fibronectin at distinct sites within the decellularized aortic conduits. This investigation sheds light on the nuanced interactions between fibronectin and decellularized grafts, offering valuable insights into the intricacies of cellular repopulation dynamics in different regions of implanted conduits.

Keywords: **conformational changes, fibronectin, shear stress.**

Classification number: **3.6**

1. Introduction

Plasma fibronectin (FN) is produced by hepatocytes and released into circulation as a soluble compact dimer at concentrations of 200-600 µg/ml. Circulating plasma FN is a glycoprotein dimer and multidomain protein with high molecular weight (440-500 kDa) that is folded into a globular compact structure. Its compact structure leads to the inactivation of FN since major functional binding sites are buried [1]. However, when needed, plasma FN can interact with cell and platelet receptors by which it is unfolded, assembled into fibrillar matrix with exposed functional binding sites and integrated into the extracellular matrix. Alternatively, an FN fibrillar matrix can also be formed under flow conditions [2-4]. Most of the functions of FN in nature have been reported to be related to fibrillar form. However, the mechanism of FN fibril formation and its biological activities are not yet clearly understood.

The hallmark of understanding biological functions of FN is that these functions are extremely complex and appear to be switched back and forth in specific cases. For instance, FN carries domains that can interact with collagen and fibrin at N- terminus and adhesive sites with RGD sequence at position FNIII10 that is capable of interacting with platelet integrins. Hence, this molecule has been shown to contribute to the process of haemostasis. However, results from previous studies on the effect of FN on adhesion and aggregation of platelets demonstrated that the role of FN would change (either by enhanced or inhibited platelet activities) corresponding to different conditions of interaction with platelets [1]. Results from in vivo studies conducted on mice also agreed with this finding. These contradictory findings have given rise to many hypotheses including one that suggests that the functional switching of plasma FN during cellular processes is related to its conformational changes and fibrillogenesis [1, 5].

FN coatings have been shown to accelerate the autologous cellular repopulation of implanted decellularized aortic conduits by enhancing their adhesion capacity and biocompatibility [6, 7]. However, the supportive effect of deposited FN was shown to be dissimilar in different regions of implanted decellularized grafts. To elucidate the biological mechanism that explains this functional dissimilarity, we labelled FN with two fluorophores for Förster (or fluorescence) resonance energy transfer (FRET) to monitor its conformational changes and study how different structures of FN are distributed along the decellularized conduit grafts.

*Email: hckhon@hcmiu.edu.vn

2. Methods

2.1. FN purification and labelling

Plasma FN was purified using a modified protocol of a previously described procedure and was doubly labelled with two types of fluorescence dyes, Alexa Fluor AF488 (488/514 nm) and Alexa Fluor AF546 (517/570 nm), as donor and acceptor pair, respectively, for the FRET experiments [1]. Briefly, FN was incubated in 4-M GdnHCl solution to expose the four cryptic free cysteine residues, which were specifically labelled by adding AF546 at a molar ratio of 30:1 (dye/FN molecule). The reaction was kept for 1 h at room temperature with gentle rotation in the dark. After that, dialysis was performed against phosphate-buffered saline (PBS) at pH 7.3 overnight to remove unbound dyes. The AF546-conjugated FN (FN546) protein was collected, and the concentration was measured by reading the absorption at 280 nm. Next, amine labelling was performed by adding 0.1 m sodium bicarbonate at pH 8.7 followed by the addition of an 80-fold molar excess of AF488 to FN546 solution. The reaction was incubated for 1 h in the dark at room temperature with gentle rotation. Free dyes were again removed by dialysis against PBS pH 7.3 overnight. Concentrations of conjugated FN and the ratio of FN: dyes were determined by reading absorbance at 280, 496, and 556 nm and calculated according to the user manual.

To confirm the sensitivity of FRET in indicating FN conformation changes, FRET signals from labelled FN in solution with increasing concentration of GdnHCl (0-4 M) were measured. FRET signals were determined as the ratio of donor fluorescence intensity divided by acceptor fluorescence intensity (I_A/I_D). FRET signals of soluble FN in solution without GdnHCl were set at 100%.

2.2. FN coating of aortic conduit grafts

Decellularized aortic conduit (DAC) grafts were obtained from the Department of Cardiovascular Surgery and Research Group for Experimental Surgery, Heinrich Heine University, Germany [6]. Grafts were incubated with 50 µg/ml mixture of doubly labelled FN: unlabelled FN (1:10 ratio) for 24 h at 37ºC. FN-coated grafts were implanted into systemic circulation of recipient rats as previously described [6]. Samples of DACs were fixed with 3.7% formaldehyde and stored in PBS buffer containing 0.1% NaN_3 at 4ºC.

2.3. FRET analysis

At 1, 3, and 6 h after implantation, implanted conduits were thoroughly excised and collected from region A and B corresponding to ascending and descending aortic conduits. Tissue samples were further fixed with 3.7% formaldehyde, cryo-embedded, and sectioned for FRET analysis. For each sample, 15 random ROI from three representative sections 200 µm apart from one another were observed and captured by fluorescence microscopy DM2000 (Leica, Wetzlar, Germany). FRET signals were calculated as the ratio of fluorescence signals of AF488 and AF546 (AF546/AF488) in ROI regions. In parallel experiments, FN-coated conduits were incubated with PBS pH 7.3 buffer or blood plasma for 1, 3, and 6 h followed by FRET analysis without implantation.

3. Results

3.1. FRET changes with FN conformation

In principle, in solution without GdnHCl, FN exposes a compact structure. As GdnHCl in solution increases from 0 to 1, 2, 3, and 4 M, FN molecules become extended either by being partially and completely unfolded (Fig. 1). Accordingly, the average intramolecular distance between donors and acceptors gradually increases leading to the reduction of FRET signals. FRET signals of FN in its compact conformation (0 m GdnHCl) were set at 100% and decreased to 61% as the FN molecule extended in the 1 m GdnHCl solution. Further unfolding of FN at concentrations of 2, 3, and 4 m GdnHCl reduced the FRET signals by 48, 46, and 40, respectively.

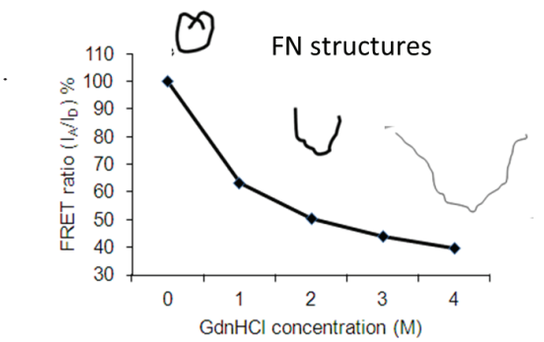

Fig. 1. Conformational changes of FN monitored by FRET.

FN conformation changes in GdnHCl solutions correlated with FRET signals (ratio of I_A/I_D). As GdnHCl concentration in solution increases from 0 to 4 M, causing FN to be partially unfolded or unfolded, respectively, the FRET signal decreases.

3.2. FRET changes upon implantation

Labelled FN was mixed with unlabelled FN at a ratio of 1:10 to prevent energy transfer between adjacent molecules that can influence FRET measurement. To observe the changes in conformation of deposited FN on decellularized aortic conduits (DAC), 50 µg/ml mixture of

labelled and unlabelled FN was used to coat the adventitial and luminal surfaces of DAC. By using fluorescence microscopy to excite donor fluorophores and record both donor and receptor fluorescence emission, we were able to monitor conformational changes of FN on DAC. For better visual observation, microscopic images were set so that regions of high FRET level appeared violet, and regions of low FRET level appeared grey indicating a more compact or more extended state of FN, respectively.

To confirm that the decrease in FRET signals was due to cell invasion after implantation, DAC after FN coating was incubated in PBS buffer pH 7.3 and blood plasma collected from experimental mice (Fig. 2A-B). FRET was monitored within 6 h of incubation. Results showed that while FRET signals of deposited FN did not reduce at the adventitial surface, the FRET signals at the luminal side decreased slightly from 100% to 92±2.6% after 6 h of incubation in PBS (Fig. 2A(b-d)). In blood plasma, at the adventitial side, FRET signals of deposited FN decreased from 100% to 86.2±2.6%. The decrease in FRET signals at the luminal side was less pronounced (from 100% to 94.6±7.9%) (Fig. 2A(e-g)).

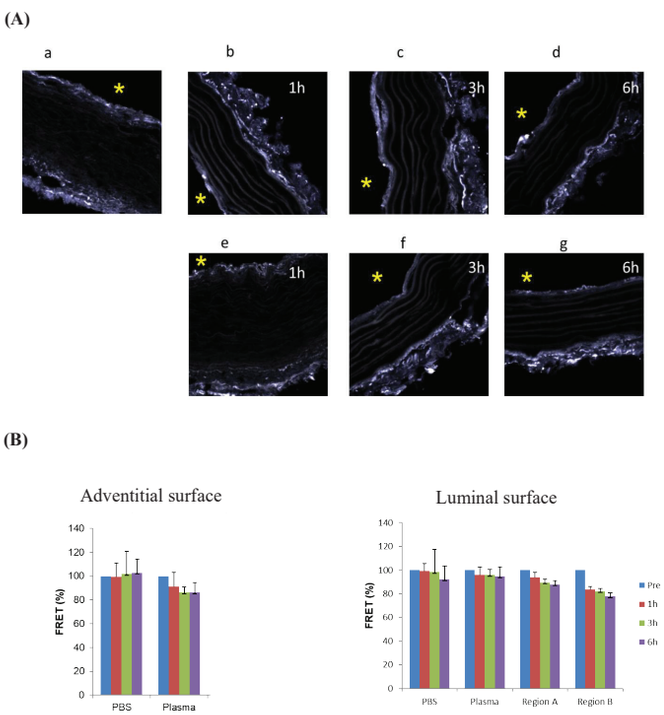

Fig. 2. FRET signal changes of FN incubated in PBS and mouse blood plasma. (A) Representative images of pre-incubation doubly labelled FN (a) and incubated in PBS (b, c, d) and blood plasma (e, f, g) after 1, 3 and 6 h. Areas with high and low FRET signal appear in violet and grey, respectively. Vessel luminal side is indicated by asterisk. **(B)** FRET analysis of FN incubated in PBS and blood plasma at the adventitial (left) and luminal side (right).

To study the conformational changes of deposited FN on DAC after implantation, FRET signals of the adventitial and luminal side at ascending aorta (region A2) and descending aorta (region B1) of DAC were recorded. In contrast to control experiments in which DACs were incubated with PBS buffer and blood plasma (Fig. 2), implanted DACs showed a significant FRET decrease even after 1 h of incubation. The decrement in FRET was pronounced during the first hour of incubation and after that slowed down with only few percent decrement at 3 and 6 h. Among the analysed regions, FRET signals of deposited FN on adventitial side of region A2 showed the most reduction (from 100% to 67.4±4.5%, 63.5±2.6%, and 63.8±3.2% at 1, 3 and 6 h after implantation, respectively). However, in the same region but at the luminal side, FRET decrease was the least going from 100% to only 93.9±4.2%. Changes in FRET signals of the adventitial and luminal sides of region B were similar to each other with about 15% FRET decrement after 1 h followed by 3-5% decrement at every 3 h thereafter (Fig. 3).

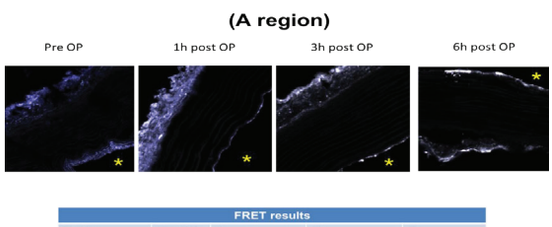

FRET results					
Region		Pre OP	1h	3h	6h
A	out	100 %	67.4 ± 4.5 %	63.5 ± 2.6 %	63.8 ± 3.2 %
	in	100 %	93.9 ± 4.2 %	89.5 ± 2.3 %	87.8 ± 4,1 %

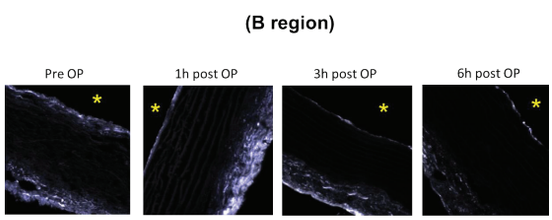

FRET results					
Region		Pre OP	1h	3h	6h
B	out	100 %	85.2 ± 3.5 %	82,7 ± 2.4 %	79.8 ± 2.9 %
	in	100 %	83.6 ± 2.6 %	82.1 ± 2.8 %	77.7 ± 3.5 %

Fig. 3. Changes in FRET signal of adventitial and luminal sides at ascending aorta (region A) and descending aorta (region B).

4. Discussion

Our previous data has shown that FN surface coating of DAC accelerates the autologous *in vivo* recellularization after implantation when compared to the control group without FN coating [6]. The supportive effect of deposited FN was shown to be dissimilar in different regions

of DAC. FN's biological activity is dependent on its conformation and fibrillogenesis [2, 4, 8]. This led us to a question whether there is any difference in conformation of FN deposited on the luminal and adventitial surfaces of DAC after implantation.

FRET measurement was successfully used to monitor conformational changes of FN [1, 9, 10]. The fact that FRET signals of deposited FN did not change during the 6-h time period when DACs were incubated with PBS buffer confirms that coating FN on the surface of DAC did not influence its conformation. However, when blood plasma was used instead of PBS buffer for the incubation, FRET signals of FN on DACs slightly but continuously decreased to 86% and 94.6% during the 6-h observation time at the adventitial and luminal sides, respectively, indicating conformational changes of deposited FN upon contacting with components of the plasma.

In vitro study of FN incorporation into extracellular matrix of NIH 3T3 fibroblasts using FRET measurement showed that within 1-2 h of incubation, cell-bound FN showed initial unfolding and small fibrils formation from the cell edge [11]. Our observation that FRET signals were dramatically decreased after implantation confirms the activity of living cells and the physiological condition on conformation of FN. Our previous study had shown that, during the recellularization process, the cells dominantly invaded from the adventitial side in region A2 but not region B1 of the DAC [6]. This data agrees with the presented FRET data in which we observed that FRET signals of the same region showed a strongest reduction. The effect on FRET decrease can be seen even after 1 h of implantation. The changes of FN conformation can be caused by biomechanical forces generated by invaded cells or the high activity of MMP around the media-repopulating cells. Recent studies have shown the effect of different shear stresses on FN conformation [2-4]. Our data also demonstrates the effect of shear stress on conformation of deposited FN on DACs by the different changes in FRET signals between the adventitial and luminal sides of region A and region B.

5. Conclusions

FRET measurement was successfully used to monitor conformational changes of deposited FN on DACs. The differences in FRET signal reduction between the adventitial and luminal sides of region A and region B demonstrated the effect of shear stress on the deposited FN's conformation. Taken together, our data suggests a morphological-dependent biological activity of FN.

ACKNOWLEDGEMENTS

The author gratefully acknowledge the financial support provided to this study by the Vietnam National Foundation for Science and Technology Development (NAFOSTED) under grant number 108.05-2017.328.

COMPETING INTERESTS

The author declares that there is no conflict of interest regarding the publication of this article.

REFERENCES

[1] K. Huynh, M. Gyenes, C.P. Hollenberg et al. (2015), "Fibronectin unfolded by adherent but not suspended platelets: An in vitro explanation for its dual role in haemostasis", *Thromb. Res.*, **136(4)**, pp.803-812, DOI: 10.1016/j.thromres.2015.08.003.

[2] H. Nguyen, K. Huynh, V.R. Stoldt (2018), "Shear-dependent fibrillogenesis of fibronectin: Impact of platelet integrins and actin cytoskeleton", *Biochem. Biophys. Res. Commun.*, **497(2)**, pp.797-803, DOI: 10.1016/j.bbrc.2018.02.158.

[3] H.T. Nguyen, K.C. Huynh, R.E. Scharf, et al. (2013), "Shear-related fibrillogenesis of fibronectin", *Biol. Chem.*, **394(11)**, pp.1495-1503, DOI: 10.1515/hsz-2013-0183.

[4] P.T.N. Thi, Q.P. Le, V.R. Stoldt, et al. (2020), "Morphologies of fibronectin fibrils formed under shear conditions and their cellular adhesiveness properties", *Molecular & Cellular Biomechanics*, **17(3)**, pp.113-118, DOI: 10.32604/mcb.2020.09643.

[5] Y. Wang, A. Reheman, C.M. Springet al. (2014), "Plasma fibronectin supports hemostasis and regulates thrombosis", *J. Clin. Invest.*, **124(10)**, pp.4281-4293, DOI: 10.1172/JCI74630.

[6] A. Assmann, C. Delfs, H. Munakata, et al. (2013), "Acceleration of autologous *in vivo* recellularization of decellularized aortic conduits by fibronectin surface coating", *Biomaterials*, **34(25)**, pp.6015-6026, DOI: 10.1016/j.biomaterials.2013.04.037.

[7] A. Assmann, M. Struß, F. Schiffer, et al. (2017), "Improvement of the *in vivo* cellular repopulation of decellularized cardiovascular tissues by a detergent-free, non-proteolytic, actin-disassembling regimen", *J. Tissue Eng. Regen. Med.*, **11(12)**, pp.3530-3543, DOI: 10.1002/term.2271.

[8] P. Le, H.N.M. Thi, V.R. Stoldt, et al. (2021), "Morphological dependent effect of cell-free formed supramolecular fibronectin on cellular activities", *Biol. Chem.*, **402(2)**, pp.155-165, DOI: 10.1515/hsz-2019-0402.

[9] W.C. Little, U. Ebneter, V. Vogel, et al. (2008), "Assay to mechanically tune and optically probe fibrillar fibronectin conformations from fully relaxed to breakage", *Matrix Biol.*, **27(5)**, pp.451-61, DOI: 10.1016/j.matbio.2008.02.003.

[10] M.L. Smith, D. Gourdon, W.C. Little, et al. (2007), "Force-induced unfolding of fibronectin in the extracellular matrix of living cells", *PLOS Biol.*, **5(10)**, DOI: 10.1371/journal.pbio.0050268..

[11] G. Baneyx, L. Baugh, V. Vogel (2001), "Coexisting conformations of fibronectin in cell culture imaged using fluorescence resonance energy transfer", *Proc. Natl. Acad. Sci. U.S.A.*, **98(25)**, pp.14464-14468, DOI: 10.1073/pnas.251422998.

DOI: 10.31276/VJSTE.64(2).99-104

Evaluating the effects of chloride on the performance of microbial fuel cells for wastewater treatment

Duyen T. M. To[1], Ngoc Pham[2], Hoa T. Pham[1*]

[1]*School of Biotechnology, International University, Vietnam National University - Ho Chi Minh City, 3 Ly Tu Trong, Ben Nghe Ward, District 1, Ho Chi Minh City, Vietnam*
[2]*Department of Civil Engineering, International University, Vietnam National University - Ho Chi Minh City, 3 Ly Tu Trong, Ben Nghe Ward, District 1, Ho Chi Minh City, Vietnam*

Received 19 April 2021; revised 4 May 2021; accepted 2 July 2021

Abstract:

Water used in many industrial sectors such as processing and agriculture farming contain high salt concentrations. Without prior treatment, effluent discharge containing high salinity and high organic content can have dangerous effects on aquatic life, water portability, and agricultureUp to 5% of wastewater generated worldwide is highly saline effluent. Microbial fuel cells (MFCs) have been considered as a promising saline wastewater treatment, which uses microorganisms to convert organic compounds into electrical energy. This study investigated lab-scale MFCs to evaluate the effect of chloride at different concentrations (0, 5, 10 and 20 g/l NaCl) on the performance of the MFC by examining its electrical generation and wastewater treatment efficiency. Increasing NaCl concentration led to a decrease in power generation with maximum power at 30, 18.7, 18.8, and 5.2 mW/m^2 corresponding to 0, 5, 10, and 20 g/l of NaCl, respectively. The COD removal efficiency of the four treatments did not significantly vary ($p>0.05$) and reached 65.9% to 78.7%. *Acidovorax* spp. was isolated from the treatment without NaCl while *Pseudomonas citronellolis* was isolated from the treatments containing 10 and 20 g/l NaCl. *Pseudomonas citronellolis* can be used as a potential inoculum for MFCs treating highly saline wastewater based on its high electrical generation ability (606.8 mW/m^2) based on inoculation of this pure strain into the mini MFC.

Keywords: ***Acidovorax* spp., chloride, microbial fuel cell (MFC), *Pseudomonas citronellolis*, wastewater treatment.**

Classification number: **5.3**

1. Introduction

Water used in many industrial sectors such as food processing and agriculture farming contain high salt concentrations. Without prior treatment, effluent discharge containing high salinity and high organic content can have dangerous effects on aquatic life, water portability, and agriculture [1]. Therefore, the biological treatment of saline wastewater is an important problem that needs to be solved. In the past, saline effluents have been conventionally treated through physio-chemical treatments as many biological treatments are strongly inhibited by salts (mainly NaCl). However, with the cost of physio-chemical treatments being particularly high, alternative biological systems that reduce cost are increasingly becoming the focus of research.

MFCs are a promising new method due to a combination of effectiveness in wastewater treatment, electricity generation, and low cost in comparison with other methods of wastewater treatment [2]. An MFC is a device that directly converts the energy stored in the chemical bonds of substrates into electrical energy through catalytic reactions of microorganisms [3, 4]. The reaction occurs as a result of two processes in the MFC, as described by [5], and is given by Eqs. (1) through (3) below:

$$\text{Anode oxidation reaction: } (CH_2O)_n + nH_2O \xrightarrow{\text{Microorganisms}} nCO_2 + 4ne^- + 4nH^+ \quad (1)$$

$$\text{Cathode reduction reaction: } 4e^- + 4H^+ + O_2 \rightarrow 2H_2O \quad (2)$$

$$\text{Overall reaction: } (CH_2O)_n + nO_2 \rightarrow nCO_2 + nH_2O + \text{Electrical energy} \quad (3)$$

Added substrates are oxidized under anaerobic conditions by microbes in the anodic chamber of an MFC and release electrons, protons, and carbon dioxide. The electrons are transferred to the anode and transported to the cathode through an external circuit while the protons cross proton exchange membranes (PEMs) or a salt bridge to enter the cathodic chamber where they combine with oxygen to form water [6]. However, this technology is only in early research stages and more investigations are required before domestic MFCs can be made available for commercialization.

The ionic conductivity of the substrate is one of several factors that strongly influences the performance of an MFC [3, 7, 8]. Increasing the conductivity of a substrate could result in improved MFC electrical generation [7, 9]. However, increasing the ionic strength does not always increase MFC performance due to the capacity for salt tolerance of anodophilic bacteria, which are present at the anode of an MFC [10, 11]. Hence, it is important to understand the effect of conductivity and ionic strength on MFC performance in order to optimize bioelectricity production from wastewater treatment.

*Corresponding author: Email: pthoa@hcmiu.edu.vn

Chloride, in the form of NaCl, was used to change the ionic conductivity in this study. NaCl was added into an MFC at different concentrations to evaluate the effects on performance in terms of electrical generation and wastewater treatment efficiency. The microorganisms in the anode at different salt concentrations were evaluated to see the impact to the microbial community.

2. Materials and methods

2.1. Materials

Synthesis wastewater preparation: The microbial fuel cells were fed with artificial wastewater as a substrate following the formula of [12] i.e., glucose 445 mg/l, $NaHCO_3$ 750 mg/l, NH_4Cl 159 mg/l, K_2HPO_4 13.5 mg/l, KH_2PO_4 4.5 mg/l, $CaCl_2.2H_2O$ 125 mg/l, and $MgSO_4.7H_2O$ 32 mg/l. Trace elements supplemented in the synthetic wastewater followed the formula of [13]. The electrolyte solution was comprised of KCl 0.1 mg/l, NH_4Cl 0.2 mg/l, NaH_2PO_4 0.6 mg/l, and $NaHCO_3$ 2 mg/l [14].

Reactor configuration:

- Lab-scale microbial fuel cells (MFCs): Microbial fuel cells were constructed according to the design of [15] with a minor modification using easily available materials to reduce cost (Fig. 1A). Each cell was constructed by using polyvinyl chloride (PVC) pipe. Electrodes were made of round-shaped carbon cloths that were 10 cm in diameter and 5-mm thick sandwiched in between two pieces of stainless steel mesh. The carbon cloth, which had a density of 160±10 g/m^2, a specific surface area of 1200 to 1500 m^2/g, and pore volume of 0.7 to 0.8 ml/g, was purchased from Mien Nam Tec Company, Viet Nam. These components of the electrode were connected together by nuts and bolts that connect to copper wire on the top of the bolt. The disk-shaped anode was located 25 cm from the bottom of the cell and the cathode at the top, which was separated by layers of glass wool and glass beads 30 cm high. The electrodes were filled with granular graphite. The aeration was located just below the cathode chamber to create the aerobic environment. The port for sludge injection was 27 cm from the bottom, just above the electrode. Gravel was placed at the bottom and the top of each cell to prevent the movement of the cell. The anode and cathode were connected by copper wire and to a resistor (1000 Ohm) in order to consume the electricity generation continuously.

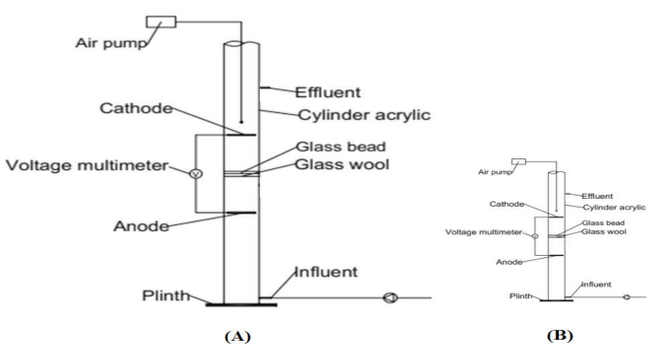

Fig. 1. Schematic of the two MFC models used in the study: (A) the lab-scale MFC (diameter of 10 cm; height of 75 cm) and (B) the mini MFC (diameter of 5 cm; height of 10 cm).

- Small-scale microbial fuel cells (mini MFCs): Mini MFCs were made by scaling down the lab-scale MFC design (Fig. 1B). Its body was also made of PVC in a cylinder shape with 10-cm height. The electrodes were also made of round-shaped carbon cloth with a diameter of 50 mm.

- MFC inoculum, the source of microorganisms: Anaerobic sludge, which was collected from the Brewery Company in district 12, Ho Chi Minh city, was used as an inoculum for all the MFCs. The pH of the inoculum was found to be 7.

2.2. Experimental design

The experiments were comprised of four MFC treatments with different NaCl concentrations (0, 5, 10, 20 g/l) so-called Treatment 1, Treatment 2, Treatment 3, and Treatment 4, respectively. Each treatment was triplicated.

MFCs operation: Firstly, the MFCs were rinsed with electrolyte solution. Then, anaerobic sludge inoculum was injected into the anodic zone of all four treatments with mixed liquor suspended solids (MLSS) 4 g/l. Finally, artificial wastewater with different concentrations of NaCl (0, 5, 10, and 20 g/l) were injected to the anodic zone of the MFCs for Treatments 1, 2, 3, and 4, respectively. All MFC systems were operated in batch mode under room temperature and aerated continuously for 15 days.

Electrogenic bacteria isolation: Microorganisms in the sludge samples of each treatment were withdrawn from the anode after stabilization of the performance. After 15 days, a 1-cm^2 piece of carbon cloth from the anode of each MFC was removed to isolate the electrogenesis bacteria. The carbon cloth samples were placed into a culture bottle (25 ml) containing 20 ml of sterilized GA medium [16]. The suspension of each medium was collected and diluted in 25-ml sterile tubes. Six gradients in triplicate were carried out for the bacteria enrichment. The petri dishes were prepared with agar medium to inoculate bacteria liquids of 10^3 to 10^5 gradients (1 ml). Then, the inoculated bottles were erectly cultivated for 5 days until various single colonies were grown in the medium. Based on the colony's characteristics, target strains were picked out with a sterile needle. Colonies forming on the plates were picked and further purified by quadrant streaking on fresh plates.

Isolated electrogenesis bacteria evaluated with mini MFCs: After isolation, the bacteria strains were enriched in GA medium to densities of 10^6 to 10^8 CFU and then inoculated to the mini MFCs. The mini MFCs were made of PVC cylinders of 10-cm length. The electrodes were made of round-shaped carbon cloth with a diameter of 50 mm. Artificial wastewater was used as the feed substrate. The voltage and current across each pure strain of bacteria was measured after 1 day by a digital multimeter.

2.3. Analytical methods

The pH was measured by a pH Extech 407228. Turbidity was measured by a UV-Vis spectrophotometer (GENESYS 10 UV-Vis, Thermo Fisher Scientific, Inc., USA) at 450 nm using the nephelometric turbidity unit (NTU) as a standard solution. Turbidity removal efficiency was calculated by the difference between outflow and inflow. Chemical oxygen demand (COD) was determined using a closed reflux titrimetric method [17]. Mercuric sulphate was used to eliminate the interference of chlorides at a 10:1 weight ratio of mercuric sulphate to chloride. COD removal rates were calculated by the difference between COD outlet and inlet. Electric current and voltage were measured daily for 15 days. The circuit voltage was measured using a digital multimeter (KYORITSU Model 1009, Japan) with an external resistance of 200 Ohm. The power density (in mW/m^2) was calculated by dividing power by the anode surface area (m^2).

After isolation, the bacteria were gram stained and observed at 100x under microscope to identify gram staining and cell morphology. DNA from the pure bacteria species that generated the highest electricity (verified by inoculating the mini MFCs) was extracted using a DNA kit and subsequent sequencing for specie identification.

2.4. Statistical analysis

The results were statistically analysed by comparing the mean values of the effect of chloride at different concentrations on the performances of the MFCs as a single factor using one-way ANOVA. The statistics were expressed as mean ± standard deviation (SD) with $p<0.05$ as significant. These statistical analyses were performed using the SPSS program (Version 20.0, IBM Corp., USA).

3. Results and discussion

3.1. pH value

Figure 2 shows the pH value of the four treatments during the 15 days of experiment. The pH value of all four treatments were stable with values around 8.5 to 9.0. Statistical analysis showed that the pH value of Treatment 4 was not significantly ($p>0.05$) different with each other. In other words, the change in chloride concentration did not cause much change to the pH value.

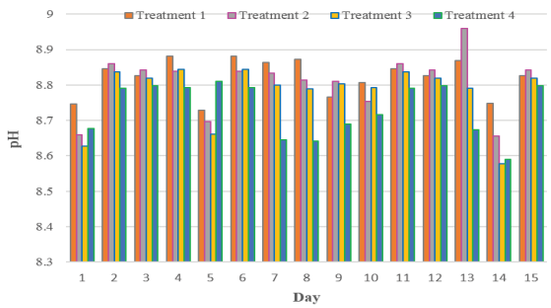

Fig. 2. The pH value of MFCs at different NaCl concentrations over the 15 days of experiments.

3.2. Turbidity

Figure 3 shows the turbidity change over the 15 days of experiments for the four treatments. There was a significant difference ($p<0.05$) between Treatment 1 (without NaCl) and Treatments 2, 3, and 4 (5, 10, and 20 g/l NaCl, respectively). While the turbidity of Treatment 1 increased over 15 days, Treatments 2, 3, and 4, which contain NaCl in artificial wastewater, had reduced turbidity with time during the 15 days.

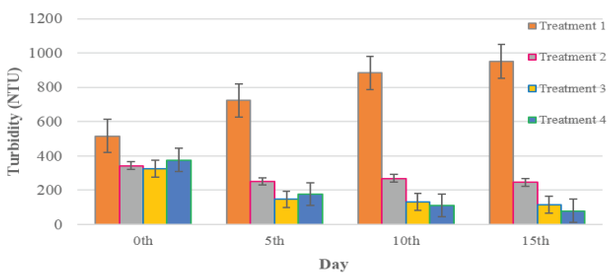

Fig. 3. The turbidity of the MFCs at different NaCl concentrations over the 15 days of experiments. Vertical bars are the standard deviation.

The value of turbidity typically depends on the residue of organic matter inside the feed. After 15 days, the turbidity removal efficiencies were 28.1, 64.7, and 78.7% for Treatments 2, 3, and 4, respectively, which contain 5, 10, and 20 g/l NaCl, respectively. On the other hand, the turbidity of Treatment 1 (without NaCl) increased over the time. The addition of NaCl, as reported by [18], causes decreased turbidity in water during the electrocoagulation process. Hence, the MFC was found as a self-powered electrocoagulation reactor [19]. The increase in turbidity removal with increase of salt concentration in the MFC could occur due to the electrocoagulation process, which might take place inside MFC compartments.

3.3. Electricity generation

Voltage output: Fig. 4 indicates the change of voltage output of the four treatments during the 15 days of experiment. There was a significant difference in voltage output between Treatment 1 (without NaCl) and Treatments 2, 3, and 4 ($p<0.05$), as well as between each treatment. The results showed that increasing NaCl concentration led to a decrease of voltage output. From highest to lowest, the voltage output of all treatments was 0.32 V (Treatment 1), 0.21 V (Treatment 2), 0.12 V (Treatment 3), and 0.11 V (Treatment 4). The maximum voltage recorded for the experiment was approximately 0.32 V, which is lower than 0.53 V obtained in the study of [15] (similar MFC design, but without the addition of NaCl).

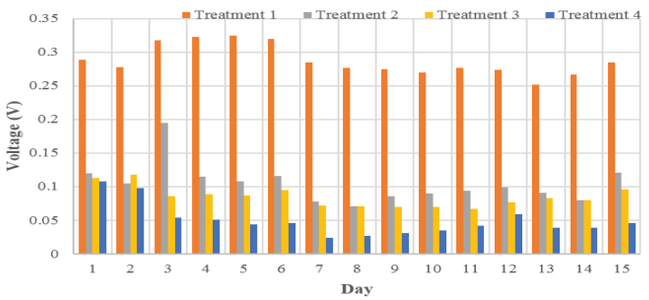

Fig. 4. The voltage output of the MFCs at different NaCl concentrations over the 15 days of experiments.

Power generation: Figure 5 provides the power generated by the four treatments over 15 days. There was a remarkable change in power generation (mW/m^2) from day 1 to day 4. The maximum value of power was attained around day 6 for Treatments 1, 2, and 3, then decreased in the later days. Treatment 4 with 20 g/l of NaCl peaked at day 2 then decreased. There were significant differences ($p<0.05$) in power generation between the treatments, except for Treatments 2 and 3. It was found that the higher concentration of NaCl, the lower power generation attained by the MFCs.

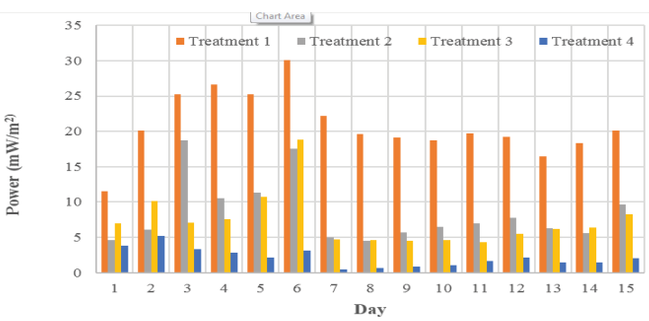

Fig. 5. The current output of MFCs at different NaCl concentrations operated in 15 days of experiments.

The power density widely varied in previous studies and was highly dependent on the configurations of the MFC systems (Table 1). However, the power density obtained in this study was comparable and even in the higher range compared to reports of other studies. For example, the study of [20] that evaluated the effect of NaCl on the anodic bacterial community of MFC reported a reduction in power generation when the salt concentration was higher than 0.1 M (equivalent with 5.85 g/l NaCl). In this study, we also found that power reduced with a salt concentration of 5 g/l.

Table 1. Comparison of MFC performance between different studies.

MFC configuration	Inoculum	e-donor	Anode material	Cathode material	Membrane/ Separation material	Power density (mW.m^{-2})	References
Single chambered	Mixed culture (Anaerobic sludge)	Petroleum sludge	Graphite plates	Graphite plates	Nafion-117	53.11	[21]
Dual chambered	Mixed culture (activated sludge)	Acetate	Toray carbon paper (20% Teflon)	Toray carbon paper (10% Teflon)/Pt coated	Sterion membrane	1.01	[22]
Single chambered	Mixed culture (domestic wastewater)	Acetate	Carbon cloth	Carbon cloth/Pt	Non-woven fabric	1200	[23]
Single chambered	Mixed culture (MFC effluent)	Fermented primary effluent	Graphite fibre brushes	Carbon cloth/Pt	PTFEa	320	[24]
Dual chambered	Mixed culture (Anaerobic sludge)	Acetate	Graphite rod	Graphite rod	Nafion-117	13.59	[25]
Single chambered	Mixed culture (Anaerobic sludge)	Acetate	Carbon cloth	Carbon cloth/Pt	PVA-STAa	58.8	[26]
Single chambered	Mixed culture (Anaerobic sludge)	Glucose	Carbon cloth	Carbon cloth	Gloss wool as separator	30	This study

COD: In order to evaluate the wastewater treatment ability of MFCs, COD was measured at the end of the 15 days of experiment. The COD remarkably decreased over the 15-d period for all treatments. The COD removal efficiency of Treatments 1, 2, 3, and 4 were 68.4, 77.1, 78.7, and 70.5 %, respectively. The results showed that increasing NaCl concentration did not cause any reduction in COD removal efficiency. The statistical analysis showed that there were no significant differences ($p>0.05$) in COD value between the four treatments after 15 days. However, the results of COD removal efficiency in this study are quite low compared to the 85-90% COD removal in the experiment using an MFC in [27]. The difference in COD removal could be caused by different configurations and/or operation conditions (such as influent COD concentration, HRT, specific organic loading rate, and reactor volume) of the MFC models [28], but it does not come from the change in salt concentration.

3.4. Electrogenic microorganism isolation

Anode carbon cloth samples from treatments with the addition of NaCl (Treatments 1, 2, 3, 4) were collected for electrogenesis bacterial isolation. After the isolation

process using GA medium, 5 isolates were obtained from the anode of the MFCs and named No.1 through No.5. There was one isolate from Treatments 1, 3, and 4, while two isolates were extracted from Treatment 2. All isolates were gram negative and had a rod shape. The morphology of isolate No.1 was yellow-brown raised circular, while isolate No. 2 to isolate No.5 were yellow-brown raised circular with slightly wrinkled margins. Microscopic photos were taken for the gram-stained isolates observed at 100x and are presented in Fig. 6.

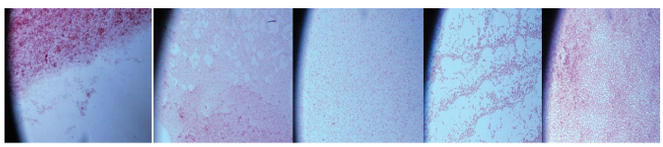

Fig. 6. Microscopic photos taken for the gram-stained isolates observed at 100x. No.1 through No.5 denote the five isolates from four treatments.

The isolates were tested for the electrochemical abilities by inoculating each isolate into the anode of the mini MFC. Artificial wastewater was used as the substrate and electrical generation was measured after the one-day operation.

All five isolates evaluated in the mini MFCs showed higher values of the maximum power generation, which were 10 to 20 times higher than the maximum power generated in the larger scale that was inoculated with anaerobic sludge (Table 2). The maximum electricity generation was obtained from days 3 through 6. This could be due to the different configuration of the MFC, which comes with a different internal resistance. This result points out the potential for using those isolates for treating saline wastewater in MFCs.

Table 2. Power generation with mini MFCs inoculated with isolates obtained from different treatments.

Name	Maximum voltage (V)	Maximum current (mA)	Maximum power (mW/m^2)
No. 1-Treatment 1	0.33	1.48	248.87
No. 2 -Treatment 2	0.48	2.02	494.06
No. 3 -Treatment 3	0.39	1.97	391.49
No. 4 -Treatment 3	0.33	1.49	250.55
No. 5 -Treatment 4	0.52	2.29	606.78

Out of the five isolates, three were selected for molecular identification including isolates No. 1 - Treatment 1 (0 g/l NaCl added), No. 2 - Treatment 2 (10 g/l NaCl), and No. 5 - Treatment 4 (20 g/l NaCl). Isolate No.1 was applicable for no addition of NaCl. Isolate No. 2 and No. 5 showed the highest power output with the addition of NaCl. After sequencing, the results indicated that No. 1 was *Acidovorax* spp. while No. 2 and No. 5 were the same strain, which was *Pseudomonas citronellolis*. *Acidovorax* spp. is the non-pathogenic genus of proteobacteria found in the soil and environment. In this study, Treatment 1 (without NaCl), where the presence of *Acidovorax* spp. was dominant, showed the high power generation (249 mW/m^2). It was a gram-negative rod, which usually occurs singly but occasionally in pairs. *Pseudomonas citronellolis* grows anaerobically in the presence of nitrates over a range of temperature from 25 to 37^{o}C [29]. The wild type of *Pseudomonas aeruginosa* was studied by inoculation into microbial fuel cells by [30]. In their study, the wild type *Pseudomonas aeruginosa* was found to use different electron shuttles that resulted in the enhancement of the maximum current of the MFC. *Pseudomonas citronellolis* was isolated from Treatment 2 and Treatment 4, which contained 5 and 20 g/l NaCl, respectively, and demonstrated that this bacterium had high salt tolerance ability. Therefore, *Pseudomonas citronellolis* can be used as a potential inoculum for MFCs treating highly saline wastewater. This result showed a change in the electrogenesis bacteria due to the change in NaCl concentration. Even *Pseudomonas citronellolis,* which was dominant at higher salt concentrations, possessed good electricity generation and the shift in bacterial community caused a reduction in power at higher NaCl concentration. Along with the study of [20], it is confirmed that a significant change of anodic bacterial community comes with a change of salt concentration.

4. Conclusions

The results from this study showed that chloride had a large impact to the performance of the MFCs. An increasing chloride concentration led to a decrease in power generation. However, the wastewater treatment performance of MFCs are still feasible even at high chloride concentration. The isolated bacteria from the high saline MFC, *Pseudomonas citronellolis*, gave high power density when inoculated into the MFC, which offers this specie as a potential type of inoculum for MFCs treating highly saline wastewater based on its saline tolerant ability and electrical generation.

CRediT author statement

Duyen T. M. To: Data analysis and Interpretation, Writing and Manuscript revising; Ngoc Pham: Method, Data analysis and Writing, Hoa T. Pham: Method, Data analysis and Writing.

ACKNOWLEDGEMENTS

This research is funded by Vietnam National University, Ho Chi Minh city (VNU-HCM) under grant number B2019-28-01.

COMPETING INTERESTS

The authors declare that there is no conflict of interest regarding the publication of this article.

REFERENCES

[1] O. Lefebvre, R. Moletta (2006), "Treatment of organic pollution in industrial saline wastewater: A literature review", *Water Research*, **40(20)**, pp.3671-3682, DOI: 10.1016/j.watres.2006.08.027.

[2] B.E. Logan (2008), *Microbial Fuel Cells*, John Wiley & Sons, 216pp.

[3] J. Heilmann, B.E. Logan (2006), "Production of electricity from proteins using a microbial fuel cell", *Water Environment Research*, **78(5)**, pp.531-537, DOI: 10.2175/106143005X73046.

[4] B.E. Logan, J.M. Regan (2006), "Electricity-producing bacterial communities in microbial fuel cells", *Trends in Microbiology*, **14(12)**, pp.512-518, DOI: 10.1016/j.tim.2006.10.003.

[5] I.-S. Chang, C In-Seop, B Orianna, et al. (2006), "Electrochemically active bacteria (EAB) and mediator-less microbial fuel cells", *Journal of Microbiology and Biotechnology*, **16(2)**, pp.163-177.

[6] K. Rabaey, W. Verstraete (2005), "Microbial fuel cells: Novel biotechnology for energy generation", *Trends in Biotechnology*, **23(6)**, pp.291-298, DOI: 10.1016/j.tibtech.2005.04.008.

[7] H. Liu, S. Cheng, B.E. Logan (2005), "Production of electricity from acetate or butyrate using a single-chamber microbial fuel cell", *Environmental Science & Technology*, **39(2)**, pp.658-662, DOI: 10.1021/es048927c.

[8] C.I. Torres, A.K. Marcus, B.E. Rittman, et al. (2008), "Proton transport inside the biofilm limits electrical current generation by anode-respiring bacteria", *Biotechnology and Bioengineering*, **100(5)**, pp.872-881, DOI: 10.1002/bit.21821.

[9] Y. Fan, E. Sharbrough, H. Liu (2008), "Quantification of the internal resistance distribution of microbial fuel cells", *Environmental Science & Technology*, **42(21)**, pp.8101-8107, DOI: 10.1021/es801229j.

[10] J. Huang, B. Sun, X. Zhang (2010), "Electricity generation at high ionic strength in microbial fuel cell by a newly isolated *Shewanella marisflavi* EP1", *Applied Microbiology and Biotechnology*, **85(4)**, pp.1141-1149, DOI: 10.1007/s00253-009-2259-2.

[11] O. Lefebvre, Z. Tan, S. Kharkwal, et al. (2012), "Effect of increasing anodic NaCl concentration on microbial fuel cell performance", *Bioresource Technology*, **112**, pp.336-340, DOI: 10.1016/j.biortech.2012.02.048.

[12] G. Jadhav, M. Ghangrekar (2009), "Performance of microbial fuel cell subjected to variation in pH, temperature, external load and substrate concentration", *Bioresource Technology*, **100(2)**, pp.717-723, DOI: 10.1016/j.biortech.2008.07.041.

[13] M. Ghangrekar, S.R. Asolekar, S.G. Joshi, et al. "Characteristics of sludge developed under different loading conditions during UASB reactor start-up and granulation", *Water Research*, **39(6)**, pp.1123-1133, DOI: 10.1016/j.watres.2004.12.018.

[14] D. Zhuwei, T. Meng, L. Shaohua, et al. (2008), "Electricity generation using membrane- less microbial fuel cell during wastewater treatment", *Chinese Journal of Chemical Engineering*, **16(5)**, pp.772-777, DOI: 10.1016/S1004-9541(08)60154-8.

[15] J.K. Jang, T.H. Pham, I.S. Chang, et al. (2004), "Construction and operation of a novel mediator-and membrane-less microbial fuel cell", *Process Biochemistry*, **39(8)**, pp.1007-1012, DOI: 10.1016/S0032-9592(03)00203-6.

[16] Y. Kodama, K. Watanabe (2008), "An electricity-generating prosthecate bacterium strain Mfc52 isolated from a microbial fuel cell", *FEMS Microbiology Letters*, **288(1)**, pp.55-61, DOI: 10.1111/j.1574-6968.2008.01326.x.

[17] C. Clescerl (1999), *Standard Methods for Examination of Water & Wastewater (Standard Methods for the Examination of Water and Wastewater) 20th Edition*, American Public Health Association, 1325pp.

[18] N. Rohadi (2019), "Impact of adding sodium Chloride to change of turbidity and iron concentration on treatment wastewater using electrocoagulation process", *Journal of Physics: Conference Series, IOP Publishing*, DOI: 10.1088/1742-6596/1364/1/012062.

[19] I. Gajda, A. Stinchcombe, J. Greenman, et al. (2017), "Microbial fuel cell - a novel self-powered wastewater electrolyser for electrocoagulation of heavy metals", *International Journal of Hydrogen Energy*, **42(3)**, pp.1813-1819, DOI: 10.1016/j.ijhydene.2016.06.161.

[20] M. Miyahara, A. Kouzuma, K. Watanabe, et al. (2015), "Effects of NaCl concentration on anode microbes in microbial fuel cells", *AMB Express*, **5(1)**, pp.1-9, DOI: 10.1186/s13568-015-0123-6.

[21] K. Chandrasekhar, S.V. Mohan (2012), "Bio-electrochemical remediation of real field petroleum sludge as an electron donor with simultaneous power generation facilitates biotransformation of PAH: Effect of substrate concentration", *Bioresource Technology*, **110**, pp.517-525, DOI: 10.1016/j.biortech.2012.01.128.

[22] A.G. del Campo, J. Lobato, P. Cañizares, et al. (2013), "Short-term effects of temperature and COD in a microbial fuel cell", *Applied Energy*, **101**, pp.213-217, DOI: 10.1016/j.apenergy.2012.02.064.

[23] C. Abourached, K.L. Lesnik, H. Liu (2014), "Enhanced power generation and energy conversion of sewage sludge by CEA - microbial fuel cells", *Bioresource Technology*, **166**, pp.229-234, DOI: 10.1016/j.biortech.2014.05.027.

[24] F. Yang, L. Ren, Y. Pu, et al. (2013), "Electricity generation from fermented primary sludge using single-chamber air-cathode microbial fuel cells", *Bioresource Technology*, **128**, pp.784-787, DOI: 10.1016/j.biortech.2012.10.021.

[25] S.-E. Oh, J.Y. Yoon, A. Gurung, et al. (2014), "Evaluation of electricity generation from ultrasonic and heat/alkaline pretreatment of different sludge types using microbial fuel cells", *Bioresource Technology*, **165**, pp.21-26, DOI: 10.1016/j.biortech.2014.03.018.

[26] S. Khilari, D. Pradhan (2018), "Role of cathode catalyst in microbial fuel cell", *Microbial Fuel Cell*, Springer, pp.141-163, DOI: 10.1007/978-3-319-66793-5_8.

[27] U. Abbasi, W. Jin, A. Pervez, et al. (2016), "Anaerobic microbial fuel cell treating combined industrial wastewater: correlation of electricity generation with pollutants", *Bioresource Technology*, **200**, pp.1-7, DOI: 10.1016/j.biortech.2015.09.088.

[28] J.S. Seelam, C.T. Rundel, H.C. Boghani, et al. (2018), "Scaling up of MFCs: challenges and case studies", *Microbial Fuel Cell*, Springer, pp.459-481, DOI: 10.1007/978-3-319-66793-5_24.

[29] W. Seubert (1960), "Degradation of isoprenoid compounds by micro-organisms. I. Isolation and characterization of an isoprenoid-degrading bacterium, *Pseudomonas citronellolis n*. sp", *Journal of Bacteriology*, **79(3)**, DOI: 10.1128/jb.79.3.426-434.1960.

[30] Y.-C. Yong, Y.Y. Yu, C.M. Li, et al. (2011), "Bioelectricity enhancement via overexpression of quorum sensing system in *Pseudomonas aeruginosa* - inoculated microbial fuel cells", *Biosensors and Bioelectronics*, **30(1)**, pp.87-92, DOI: 10.1016/j.bios.2011.08.032.

Vietnam Journal of Science, Technology and Engineering (VJSTE): Manuscript Template

General Instructions on using this template and submitting a manuscript to VJSTE: Thank you for preparing a manuscript for submission to VJSTE. Using this template, or following the guidelines below, will help us in processing your article.

The structure of different types of articles may vary according to the type of study, and the content of the article.

The following are the detailed main components of the original research and review articles submitted to the journal.

Original research

The original research should have three following parts:

Preliminary section: It includes title, list of all contributing authors with their institutional affiliation, and abstract (160-250 words) with at least 3 keywords.

Title: How to format a science article (replace with your real title)

Author(s): List the author name(s) separated by commas. Use superscript numbers to link affiliations, and symbols *†‡ for author notes. For example, Y. Obsie[1*], S.A. Adem[1, 2]

**Corresponding author(s):* Include the email addresses or telephone numbers of the corresponding author(s). Please use the asterisk (*) symbol for the corresponding author information. This information is at the bottom of the manuscript's first page.

Author's affiliation addresses:

[1]Affiliations should be preceded by superscript numbers corresponding to the author list

[2]For any institutions, please provide the institution name, street, district, city, country

Received ; revised ; accepted

Abstract:
Start your abstract here…
Keywords: **keyword 1, keyword 2, keyword 3…**
Classification number(s): **1.1, 3.4, 5.3, etc.**

Abstract: The abstract should range between 160 and 250 words and be structured in a single paragraph following keywords in a separate line. The abstract should represent the main part of the research manuscript. It should reflect a brief and comprehensive background following the aim of the study (main questions to be addressed), methods used for investigating the problem, a summary of significant findings, main conclusions, and implications of the results.

Keywords: They should come immediately after the abstract and contain 3-7 specific and relevant keywords. They should reflect the research study and the relevant field of research.

Classification numbers: Depend on the Journal's Classification Scheme.

Author(s) are encouraged to write a "Highlights" that summarises the most exciting, interesting points from your manuscript.

Manuscript section: It is the main body of the scientific manuscript including: 1) Introduction; 2) Material(s) and method(s); 3) Results and discussion (separation of these two sections is acceptable); 4) Conclusions; 5) Recommendations/Suggestions/ Implications/Study limitations...(if any). These sections may slightly vary depending on the type of research approach and design used in the research. Each section should be numbered.

All of the Figures, Tables, and Equations should be cited in numerical order.

Figures

Fig. #: (Begin each figure caption with a label, "**Fig. 1.**" for example, as a new paragraph).

Fig. 1. The figure caption should begin with an overall descriptive statement of the figure followed by additional text. They should be immediately after each figure. Figure parts are indicated with capital letters **(A)**. If you prefer, you can place both the actual figures and captions logically through the text near where they are cited rather than at the end of the file (but not both). If a paragraph in the main text begins with the name of a figure, write out "Figure" in full (e.g., <para> "Figure 1 shows...").

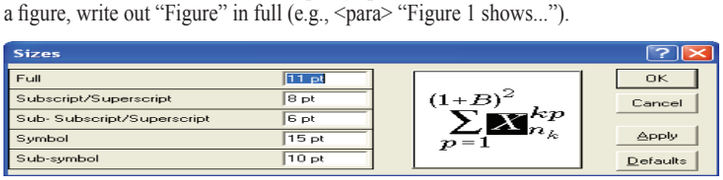

Fig. 1. The figure caption.

Tables

Table #: (Begin each table caption with a label "**Table 1.**", etc. as a new paragraph).

Table 1. Start this caption with a short description of your table. Format tables using the Word Table commands and structures. Do not create tables using spaces or tabs characters.

Table 1. Caption.

a	b	c	d	e
f				
g				
h				

Equations

$$\int_a^b x dx \tag{1}$$

Equations can be included. We do not recommend using the native Word 2007, 2008, 2010 or 2011 equation editor. This can in some cases produce less reliable MathML, the online markup language we use, which may result in display errors. Instead, use the legacy equation editor in Word (Insert menu; select insert object; select word equation) or use MathType (recommended). If you enter equations in simple LaTeX, check that they will convert accurately (Word 2007 and higher can convert simple LaTeX equations).

Closing section: It includes appendices/supplementary materials/data availability statement (if applicable), CRediT author statement (for multiple authors), acknowledgements (if applicable), competing interests, ethics (if any) and a complete list of references corresponding to all the citations given in the text of the manuscript. The appendices/supplementary materials may include data files and other material relevant to the research that should be submitted in separate files if required.

APPENDICES (if any)

The appendices should ideally be under 1000 words (approximately 2 A4 pages) for printing version. With longer appendices, they are only accepted for online publication.

CRediT author statement (for multiple authors)

CRediT offers authors the opportunity to share an accurate and detailed description of their diverse contributions to the published work.

ACKNOWLEDGEMENTS (if applicable)

This section is for the researchers who were funded for the research projects, and it should enclose all sources of financial support.

COMPETING INTERESTS

The author(s) declare(s) that there is no conflict of interest regarding the publication of this article.

REFERENCES

For in-text citation: References should be cited in the bracket with a number [1]. Multiple reference citations are separated by commas [2, 3] or if a series, dashes [4-6]. When citing sources with the author(s) and the year, they should be shortened to the first author's name, followed by et al. (with more than one author) and the year.

For reference list: With less than or equal to three authors, list all the author(s). With more than three authors, the first three should be listed and followed by et al.

References are listed in numerical order, and in the same order in which they are cited in text. The reference list should include all and only those references you have cited in the text. The reference list appears at the end of the article.

The reference consists of: Initial(s) and first/last name of the author(s), author' names separated by commas (Year of publication), "Titles of journal articles or chapter of book", *Title of Journal, Book or Other Publication*, **Volume(Number)** (if any), page numbers (if any), DOI (if any), URL and accessed date (if any) (in its original language if not English).

To cite a website and online/electronic resources, please include the accessed date (day month year).

Example of a reference list:

[1] T. Binzoni, T.S. Leung, D. Boggett, et al. (2003), "Non-invasive laser Doppler perfusion measurements of large tissue volumes and human skeletal muscle blood RMS velocity", *Phys. Med. Biol.*, **48(1)**, pp.2527-2549, DOI: 10.1088/0031-9155-48-15-318.

[2] H.W. Bischoff, H.C. Bold (1963), *Some Soil Algae from Enchanted Rock and Related Algal Species*, University of Texas Publications, 95pp.

[3] R. Busi (2016), "Weedy rice in the Philippines and Vietnam", https://www.aciar.gov.au/publication/technical-publications/weedy-rice-philippines-and-vietnam-final-report, accessed 15 July 2018.

Review articles

They should be different from the original research as they would contain different sections on the literature review. Authors may structure this part as per nature, background, and available literature on the issue argued in the manuscript.

For more detailed instructions, please visit our website: vietnamscience.vn or vietnamscience.vjst.vn

This manuscript template has been used from 2021 onwards.

P-ISSN 2525-2461 • E-ISSN 2615-9937

Vietnam Journal of Science, Technology and Engineering

JUNE 2022 • VOLUME 64 NUMBER 2

EDITORIAL OFFICE

113 Tran Duy Hung Str., Cau Giay Dist., Hanoi, Vietnam

Tel: (84.24) 39436793; Fax: (84.24) 39436794

Email: vjste@most.gov.vn

Website: vietnamscience.vn or vietnamscience.vjst.vn

PUBLICATION LICENCE

No. 459/GP-BTTTT 20th July 2021